University of South Australia

Future Industries Institute

Enhancing Phase Change Material Heat Transfer with Additive Manufacturing for the Thermal Management of High-Powered CubeSat Electronics

by

Artur Medon

BEng Aerospace (Hons)

A thesis submitted for the degree of

DOCTOR OF PHILOSOPHY

January 2023

Research Sponsors:

SMARTSAT
COOPERATIVE RESEARCH CENTRE

Primary Supervisors:

Professor Peter Murphy, University of South Australia

Professor Frank Bruno, University of South Australia

Professor Nikki Stanford, University of South Australia

Dr Kamil Zuber, University of South Australia

External Supervisors:

Professor Kamel Hooman, University of Queensland

Associate Professor Simone Mancin, University of Padua

Contents

List of Figures

List of Tables

Nomenclature

Symbol	Definition	Units
Lower Case		
c_p	Specific heat capacity	J/kg·K
h	Latent heat	J/kg
h_c	Convective heat transfer coefficient	$W/m^2 \cdot K$
m	Mass	g, kg
r_i	Inner radius of the inner taper cylinder	mm
r_o	Outer radius of the outer taper cylinder	mm
t	Time	sec, min
Δx	Wall thickness	mm
Δz	Axial displacement	mm
Upper Case		
A	Surface area	m^2
B	Gyroid base size	mm
E	Young's modulus	Pa
F	View factor	-
G	Power flux	W/m^2
J	Radiosity	W/m^2
k	Thermal conductivity	W/m·K
L	Length	m
Nu	Nusselt number	-
P	Pressure	Pa
Q	Energy	J
$\dot{Q}$	Energy transfer rate	W
R	Radius of taper interface	mm
Ra	Rayleigh number	-
T	Temperature (Absolute temperature)	°C, K
V	Volume	ml, cm^3
W	Weight	N
Greek Symbols		
α	Thermal diffusivity	m^2/s
β	Thermal expansion coefficient	1/°C, 1/K

δ	Radial interference	mm
ε	Emissivity	-
ε	Effusivity	$W\cdot\sqrt{s}/m^2\cdot K$
λ	Liquid Fraction	-
μ	Dynamic viscosity	Pa·s
ν	Viscosity	cP
ρ	Density	kg/m^3, g/cm^3
μ	Poisson's ratio	-
σ	Electrical conductivity	S/m
ϕ	Taper angle	degrees
Constants		
g	Gravitational acceleration	m/s^2
σ	Stefan-Boltzmann constant	$W/m^2\cdot K^4$
L	Lorenz number	$W\cdot\Omega/K^2$

Abbreviations

AM	Additive Manufacturing
BMD	Bound Metal Deposition
CAD	Computer Aided Design
CubeSats	Cube Satellites
DSC	Differential Scanning Calorimetry
EDS	Energy Dispersive Spectroscopy
HEO	High Earth Orbit
ICP-AES	Inductively Coupled Plasma Atomic Emission Spectroscopy
IR	Infrared
LEO	Low Earth Orbit
MEO	Middle Earth Orbit
PCM	Phase Change Material
SEM	Scanning Electron Microscope
SLS	Selective Laser Sintering
TCE	Thermal Conductivity Enhancement
TES	Thermal Energy Storage
TIG	Tungsten Inert Gas
UV	Ultraviolet
VIS	Visible

Abstract

CubeSats (Cube Satellites) are a fast-growing area due to their associated low cost and advancements in capabilities. However, with the increasing levels of power and miniaturisation of electrical components, the heat loads within next generation high-powered CubeSats are increasing. This is a challenge for CubeSats since they have limited surface area available to radiate heat to space due to their small size and limited capacity to manage the transient heat loads within a demanding thermal environment.

Phase Change Material (PCM) heat sinks can provide thermal management for CubeSats by absorbing the peak thermal loads and dissipating the waste heat to space during periods of downtime, thereby enabling the use of high-powered electronics. PCMs use latent heat to store thermal energy, typically in the solid to liquid phase transition. The key advantage of PCMs is their large Thermal Energy Storage (TES) capacity over a narrow temperature range, which allow compact and lightweight PCM heat sinks. For CubeSat applications, PCM heat sinks have been predominately investigated with paraffin PCMs, due to their ideal melting range and high latent heat of fusion per unit weight.

However, paraffin PCMs suffer from inherently low thermal conductivity. To ensure adequate heat dissipation from high-powered electronics, heat transfer enhancement techniques are required. With the expansion of metal additive manufacturing processes, this research investigated the viability of enhancing PCM heat transfer with additive structures. Additive manufacturing offers heat transfer enhancement structures not before possible with traditional manufacturing methods, which have the potential to improve PCM heat transfer whilst minimising the weight of the PCM heat sink.

This research firstly analysed the PCM thermal performance of additive structures using numerical modelling. The traditional fin structure for PCM heat transfer was compared to a struct-based additive structure and a sheet-based organic additive structure. The selected structures were compared for a conceptual 50 W PCM heat sink design and a base size analysis was also performed pushing the limits of allowable additive manufacturing minimum feature sizes. The numerical investigation found that the gyroid sheet-based additive structure demonstrated the best overall heat transfer performance for transferring heat to PCM in three directions. In addition, the numerical modelling also confirmed that smaller base sizes improved the performance of PCM heat sinks.

Secondly, the research explored metal additive manufacturing for PCM heat transfer and containment. This research focused on Bound Metal Deposition (BMD), a recently developed metal

extrusion method. BMD was chosen for this investigation since copper material for high thermal conductivity heat dissipation was recently released and the metal extrusion technique provided the unique capability of fabricating structures without the need to remove fine metal powders from internal cavities. The research investigated the material properties of BMD copper and the printability of the sheet-based gyroid structure. It was found that BMD provided the ability to print the desired gyroid base sizes with a relatively high thermal conductivity (average 353 W/m·K). However, BMD was unable to provide leakproof PCM containment in a vacuum, because of the toolpath porosity inherent in the manufacturing process.

Finally, a hybrid manufacturing solution was evaluated to overcome the challenges identified with the BMD additive manufacturing technique. To provide leakproof PCM containment, a conventional metal case was combined with the benefit of an optimised BMD copper internal additive structure. A prototype PCM heat sink was developed and tested in a vacuum chamber and demonstrated that effective heat dissipation could be achieved from a high heat load using paraffin PCM. A validation model using the numerical methodology employed in this Thesis was also compared with the testing results and showed good alignment for the temperature response at the heat input.

Declaration

This thesis presents work carried out by myself and does not incorporate without acknowledgment any material previously submitted for a degree or diploma in any university; to the best of my knowledge it does not contain any materials previously published or written by another person except where due reference is made in the text; and all substantive contributions by others to the work presented, including jointly authored publications, are clearly acknowledged.

Artur Medon

Acknowledgements

I would like to take this opportunity to express my gratitude to the people who have supported me and contributed to the completion of my thesis. I am extremely indebted to be able to undertake this journey, with the support from the William T Southcott Scholarship, SmartSat CRC and the Future Industries Institute.

Thank you to my supervisory team – Professor Peter Murphy, Professor Frank Bruno, Professor Nikki Stanford, Dr Kamil Zuber, Professor Kamel Hooman and Associate Professor Simone Mancin. Thank you for your guidance, support and challenging me to grow as a scientist. I will be forever thankful I had this time to immerse myself in research and fulfil a lifelong goal of mine.

Also, to those who took the time out to assist with my prototyping and experiments, in particular Bob Chivell, Mark Cherrill, Rodney Pratt, and Anthony Roccisano – without your help I would not have been able to complete my thesis, so thank you. I also thank Ady James and my unofficial PhD mentor Euan Smith for their support, guidance and motivation.

I would also like to acknowledge the facilities of the University of South Australia Industry 4.0 TestLab, the Tango High Performance Computer and the Australian National Fabrication Facility who enabled my research.

Last, but definitely not least, thank you to my family – Sarah and Ava, as well as my friends for all of your support and encouragement. I could not have juggled all of this without having you in my corner and I am very grateful. Thank you for not minding when I spoke obsessively about my thesis and spent most weekends focussed on my research!

1. Introduction

1.1 RISE OF SMALL SATELLITES: CUBESATS

Improvements in satellite technologies are paving the way for high-powered small satellites with increasing capabilities. Small satellites have made major advancements in capability, due to the miniaturisation of component sizes and improvements in solar/battery technologies, allowing small satellites to perform the roles of traditional larger satellites (Kwas et al., 2014).

Compared to traditional larger satellites, small satellites have a lower cost to design, build and launch, and can be developed and manufactured in shorter timeframe (Shinde et al., 2017). Traditional satellites are expensive, large and can have a mass in the order of thousands of kilograms (kg) (NASA, 2020). On the other hand, small satellites generally have a mass of less than 180 kg and are most commonly the size of a shoebox, with a weight of less than 10 kg (NASA, 2020).

The fast-growing area for small satellites is Low Earth Orbit (LEO), with altitudes between 400 to 650 km, as they require low launch capabilities (Facchinetti et al., 2016), (AlenSpace, 2020). The number of small satellites in LEO has significantly increased, especially for small satellites under 50 kg, as shown in Figure 1.1 below. The benefits of LEO include shorter distances for communications and imagery, although satellites in LEO have short windows of operation due to their high orbital periods (Ippolito, 2017).

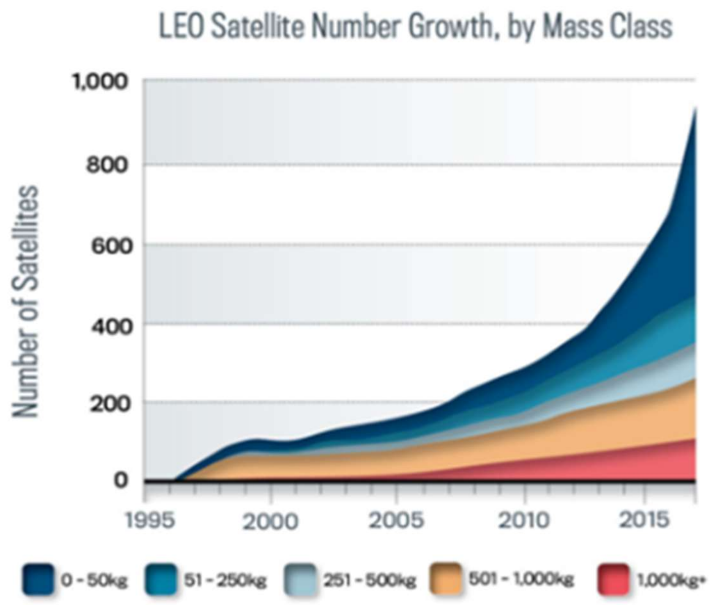

Figure 1.1: Trends in satellite number by mass in Low Earth Orbit (ERG, 2018)

The large increase of small satellites in LEO under 50 kg can be attributed to the rise of a special type of small satellite, namely the Cube Satellite (ERG, 2018). Cube Satellites, also known as CubeSats, are a special class of small satellite designed to conform to standardized cube sizes. The base unit for the CubeSat, referred to a ‘1U’, is defined as 10 cubic centimetres (cm) with a weight of less than 1.33 kg (NASA, 2020). CubeSats come in a range of sizes in multiples of 1U, as shown in Figure 1.2 below. CubeSats were originally developed for research purposes but have since progressed into an industry standard (Facchinetti et al., 2016). The 3U CubeSat has been the most widely used platform to date (Emery et al., 2017).

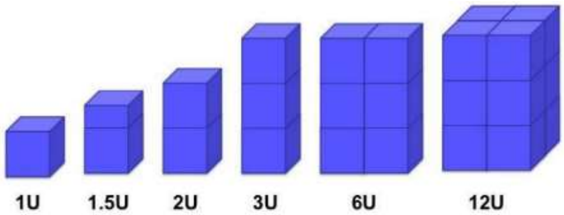

Figure 1.2: CubeSat form factors (NASA, 2020)

Next generation CubeSats are emerging with high power communication and imagery payloads due to advancements in solar panel and battery storage technologies (Hengeveld et al., 2018). With the use of deployable solar panels, orbit average powers of greater than 50 watts (W) are currently commercially available on a 3U CubeSat (Clydespace, 2021). In addition, CubeSat lithium-polymer batteries are also readily commercially available at power densities greater than 150 Wh/kg (National Academies of Sciences, 2016). Figure 1.3 shows a 3U CubeSat with deployable solar panels and also a 0.5U battery pack, which can deliver a peak power up to 160W (Pumpkinspace, 2021).

(a)

(b)

Figure 1.3: (a) 3U solar array (Clydespace, 2021), (b) 0.5U battery pack (Pumpkinspace, 2021)

Next generation CubeSats are opening the possibilities for new space ventures. CubeSats have the potential to disrupt the communications and remote sensing satellite markets with new concepts for LEO constellations, providing new global imagery and communication services (Bryce, 2017).

1.2 CUBESAT THERMAL CHALLENGES

With the increasing levels of power available and miniaturisation of electrical components, the heat loads within next generation CubeSats are increasing (Janzer et al., 2018). The thermal challenges with high-powered CubeSats are managing the high heat loads within a small volume and dissipating the waste heat to space from a limited surface area (Young et al., 2019).

The only mode to dissipate waste heat from a CubeSat in the vacuum of space is by infrared radiation (Remacle, 2018). This is a challenge for CubeSats, since they have limited surface area available to radiate waste heat to space due to their small size (Young et al., 2019). Typically, only 25% of a CubeSats' surface can be used to radiate waste heat (Hartsfield et al., 2020), since not all surfaces are ideal for radiating heat and the CubeSat's surfaces also needs to accommodate solar arrays and RF antennas (Kwas et al., 2014). For example, a 3U CubeSat is only capable of dissipating at best 15 W using the 25% radiator area, which is much less than the peak heat loads from next-generation CubeSats (Hengeveld, D., et al., 2018).

The dissipation of heat loads is important to prevent the overheating of electrical components. Overheating electrical components leads to poor performance and shorter working lives and thus each subsystem of a CubeSat has a specified allowable temperature range (Bouschon, 2018). Table 1.1 demonstrates the allowable temperature range of various subsystems on a CubeSat, adapted from the NASA BOLAS CubeSat (Choi et al., 2019).

Table 1.1: CubeSats allowable temperatures. Adapted from (Choi et al., 2019)

Spacecraft Subsystem	Allowable Operating Temperature (°C)	Allowable Non-Operating Temperature (°C)
Command and Data Handling	-24 to +61	-40 to +85
Electrical Power System	-40 to +85	-
Electrical Power Batteries	0 to +40	-20 to +40
Attitude Control System Star Tracker	+10 to +30	-30 to +70
Communications	-20 to +50	-20 to +50
Propulsion	-20 to +70	-30 to +80
Payloads	Varied	Varied

1.3 PHASE CHANGE MATERIAL HEAT SINKS

Phase Change Material (PCM) heat sinks can provide thermal management for high-powered CubeSats by absorbing the peak heat loads from electronics and then dissipating the waste heat to space during periods of downtime. As shown in Figure 1.4 below, using PCM Thermal Energy Storage (TES), the heat rejection radiators can be designed for the average heat load instead of being designed to radiate the peak thermal loads. This is vital for CubeSats, which have limited surface area for radiators due to their small size.

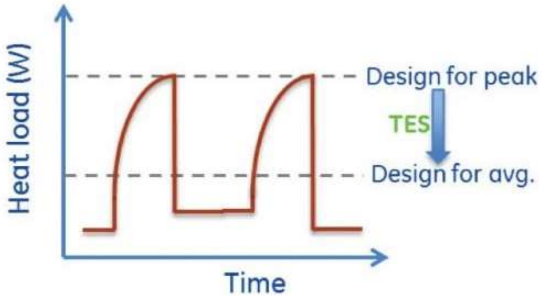

Figure 1.4: Thermal energy storage for duty cycle heat loads (Thiagarajan, 2017)

Furthermore, CubeSats in LEO have short windows of operation due to their quick orbital periods. A CubeSat in LEO completes a full Earth orbit approximately every 90 minutes and has less than 8 minutes line of sight over a particular region (Hartsfield et al., 2020). Therefore, CubeSats have limited time over ground stations and areas of interest. PCM heat sinks can provide heat absorption for a few minutes, which enables the use of high-power electronics during the short windows available.

PCM heat sinks can also provide heat to CubeSat electronics when they are not operating, thus preventing electronics from freezing. In space, thermal radiation is continual, resulting in a mismatch between heat generation and heat rejection. Heaters are typically employed to prevent electronics from freezing (Collette et al., 2011). PCM heat sinks reduce the need for heating power consumption. Figure 1.5 shows a PCM heat sink attached to a CubeSat electronics board.

Figure 1.5: Phase change material heat sink on an electronics board (TMT, 2020)

The key advantage of PCMs is their large thermal energy storage capacity per unit weight, thereby allowing lightweight and compact thermal storage for CubeSats. PCMs use latent heat to store heat energy, typically in a solid to liquid phase change (Ge et al., 2013). A large amount of heat is stored in the solid to liquid phase due to the energy required to change the phase of the material.

A phase change is also isothermal, which allows heat energy to be absorbed at constant temperature. The temperature response for PCMs is shown in Figure 1.6 below, and is compared to the temperature response for sensible heat alone. Both profiles begin with sensible heating, however at the PCM melting temperature, the PCM temperature levels and is maintained during the phase transition. After the PCM has melted, the sensible heating resumes and the temperature increases. Therefore, PCMs offers a large TES capacity over a narrow temperature range, thereby providing stable temperatures for CubeSat electronics.

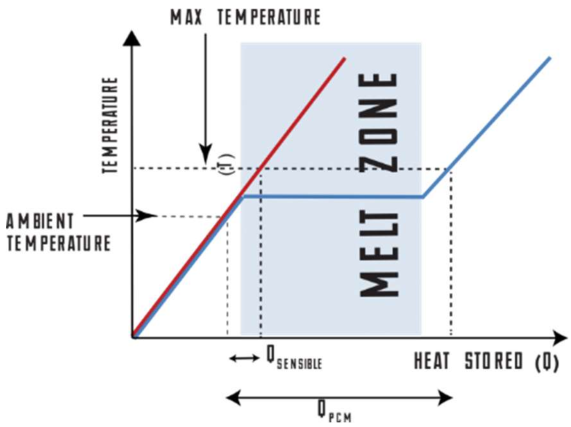

Figure 1.6: PCM temperature response vs and sensible heat alone (ACT, 2021)

PCM heat sinks for CubeSat applications have been predominately studied with paraffin PCMs, due to their high thermal capacity per unit weight and ideal melting temperature range. However, paraffin PCMs suffer from inherently low thermal conductivity (Rathod et al., 2013). For CubeSats applications, efforts have been made to improve heat transfer with paraffin PCM using metal fins (Chen et al., 2016), honeycomb structures (Choi et al.,2018) and carbon fibre encapsulation (Yamanda et al.,2014). Although, these studies pertained predominantly to low power applications of less than 10-20 W.

With trends for higher-power CubeSats applications (Janzer et al., 2018), (Young et al.,2019), (Hengeveld et al., 2019), this research proposes to investigate the use of paraffin PCM heat sinks for higher power applications, namely 50 W for a 3U CubeSat.

1.4 RESEARCH PROBLEM

The challenges with paraffin PCM heat sinks are overcoming the inherently low thermal conductivity of paraffin and containing the PCM volume change during the phase transition (Isaccs et al., 2017). Firstly, overcoming the low thermal conductivity is critical for high-powered electronics to ensure that the heat sink can absorb the high heat loads and maintain the electronics within their operating temperature range. Secondly, containing the PCM volume change is critical to ensure that the PCM heat sink is leakproof and maintains structural integrity at all stages during its lifetime in space.

Of interest in this study is the use of metal additive manufacturing (also known as 3D printing) to maximise PCM heat transfer for high-powered applications. Additive manufacturing offers component design not before possible with traditional manufacturing and allows the optimisation of structures for heat transfer enhancement and mechanical strength. With continual advancements in additive manufacturing, the method is allowing the creation of high surface area structures, which can be applied to for PCM heat transfer.

The use of metal additive manufacturing is of particular interest for this research due to the high thermal conductivity of metals, such as aluminium and copper. However, there has been very limited research regarding the optimal additive structures for maximising PCM heat transfer and there have been very limited studies to investigate the ability of metal additive manufactured parts to provide leakproof and lightweight containment for PCMs in a space environment.

A recent development for additive manufacturing is Bound Metal Deposition (BMD), a metal extrusion process. BMD is cheaper and safer to use compared to the current laser-based metal additive manufacturing processes (Lieberwirth et al., 2017) and features copper material for high thermal conductivity heat dissipation (Desktop Metal, 2020).

However, at present, it is unknown which BMD additive structures are best suited for PCM heat transfer. Also, it is unknown whether BMD printed parts can provide leakproof containment for PCMs and whether they can withstand the PCM volume change during PCM melting and freezing cycles. With this research, new knowledge will be created regarding the suitability of BMD for enhancing PCM heat transfer and containing PCMs for space applications.

1.5 Research Aims and Objectives

This research aims to investigate how additive manufacturing structures can be used to maximise paraffin PCM heat transfer; and the suitability of the Bound Metal Deposition additive manufacturing for CubeSat paraffin PCM heat sinks.

The methodology process to achieve the research aims is shown in Figure 1.7 below. Firstly, numerical modelling is adopted to analyse the PCM thermal performance of additive structures. Secondly, the application of BMD additive manufacturing is explored to manufacture additive TCE structures for PCM heat transfer and containment. Thirdly, the testing of a prototype PCM heat sink is conducted in a vacuum chamber to evaluate the performance.

Figure 1.7: Research methodology process

This research considers a 3U CubeSat with a heat load of 50 W for a period of approximately 5 minutes. The 3U CubeSat, the most widely used CubeSat to date, has orbit average powers of greater than 50 W, however, is unable to utilise due to heat dissipation issues (Hartsfield et al., 2020). Providing heat dissipation for a few minutes enables the use of higher power electronics during the short windows available for communications and for real-time image processing. The following are the research objectives and corresponding research questions, supporting the research aims:

Objective 1:

Investigate the optimal additive manufacturing thermal conductivity enhancement (TCE) structures for PCM heat transfer using thermal numerical modelling.

Research Questions:

- What are the optimal additive TCE structures for PCM heat transfer? How can PCM heat transfer be improved with additive structures?
- Can the low thermal conductivity of paraffin PCMs be overcome to provide cooling of high-power CubeSat electronics of 50 W?

Objective 2:

Explore the BMD additive manufacturing technique to manufacture lightweight TCE structures for PCM heat transfer enhancement and PCM containment.

Research Questions:

- Is BMD additive manufacturing a suitable method for producing structures for PCM heat transfer and what thermal properties can be achieved with BMD additive manufacturing?
- Are BMD additive manufactured parts suitable for containing PCMs in a vacuum for space applications?

Objective 3:

Conduct thermal experiments in a vacuum chamber to evaluate and test the performance of a additively manufactured prototype PCM heat sink.

Research Questions:

- Can additive manufactured PCM heat sinks provide effective cooling for high-powered CubeSat electronics?
- Are additive manufactured PCM heat sinks suitable for high-powered CubeSat space applications?

The performance of PCM heat sinks can be measured by the amount of Thermal Energy Storage (TES) capacity utilised prior to exceeding the specified temperature range. For high heat loads it is not practical to aim for 100% TES utilisation, due to the inherently low thermal conductivity of paraffin PCMs. The role of optimising the metal TCE structure is to ensure the majority of the TES capacity can be utilised using a minimal TCE weight.

For the purposes of this research, the PCM heat sink provides effective cooling if it can utilise over 90% of its TES capacity, however over 80% is reasonable and over 95% is excellent. Noting, the thermal mass of the electronics and CubeSat structure/radiator also provide TES capacity and heat rejection, however for the purposes of this research, the TES capacity and thermal response of the PCM heat sink is investigated in isolation.

1.6 FORMAT OF THESIS

This thesis comprises six chapters as described below:

Chapter 1 contains a brief overview of the research challenge of next generation CubeSats and provides the research aims and objectives.

Chapter 2 comprises the literature review relevant to the current topic, and provides an overview of CubeSat thermal management and PCM thermal storage. The chapter also critically reviews the existing PCM heat sinks developed for CubeSats, and discusses the application of additive manufacturing, including research gaps.

Chapter 3 investigates, using numerical modelling, the optimal TCE structures to enhance PCM heat transfer for the purposes of cooling CubeSat electronics (**Research Objective 1**).

Chapter 4 explores the Bound Metal Deposition additive manufacturing technique to manufacture lightweight TCE structures for PCM heat transfer enhancement and its suitability for PCM containment in a vacuum (**Research Objective 2**)

Chapter 5 considers hybrid manufacturing solutions to overcome the challenges identified with the Bound Metal Deposition for PCM containment in a vacuum; and evaluates and tests the performance of a BMD prototype PCM heat sink in a vacuum environment. (**Research Objective 3**).

Chapter 6 closes with the summary of the work performed, conclusions and recommendations for future work.

2. Literature Review

2.1 Chapter Overview

Chapter 2 reviews the relevant literature pertaining to CubeSat thermal management, in the context of this research. The following areas are broadly reviewed, and the research gap is discussed: CubeSat Thermal Environment; CubeSat Thermal Control Systems; PCM Thermal Storage; PCM Challenges; Existing CubeSat PCM Heat Sinks; and the Application of Additive Manufacturing.

2.2 CubeSat Thermal Environment

CubeSats are generally launched into Low Earth Orbit (LEO) with altitudes between 400 and 650 km (AlenSpace, 2020). In LEO, aerodynamic heating and convective heat transfer are negligible due to the vacuum of space (Savage, 2011). As a result, the thermal environment is dominated by thermal radiation heat transfer.

The thermal environment for a CubeSat in LEO is illustrated in Figure 2.1 below. The CubeSat receives thermal radiation from the Sun and the Earth and emits thermal radiation from its surfaces to space. To prevent the overheating of electrical components, the only mode for a CubeSat to reject heat into its environment is by thermal radiation (Remacle, 2018).

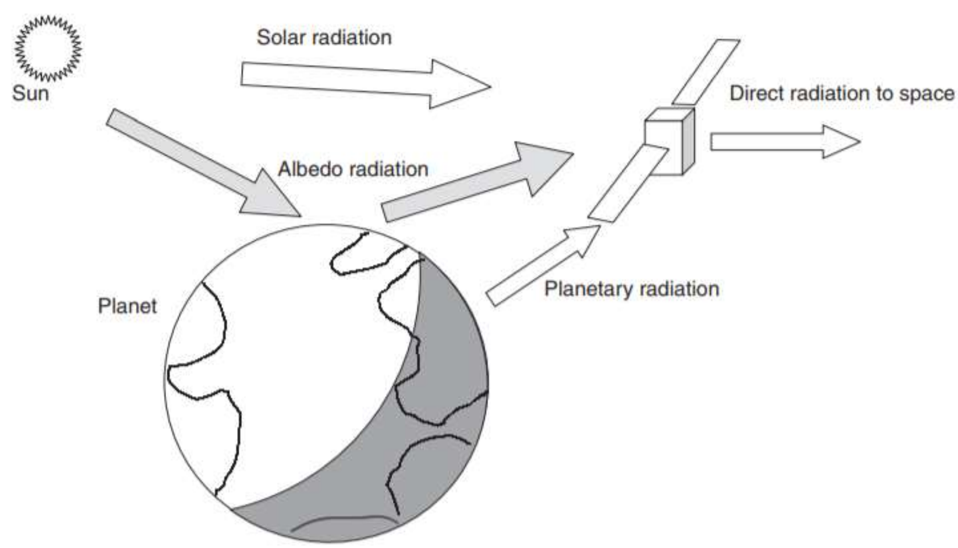

Figure 2.1: Thermal environment for a Low Earth Orbit CubeSat (Savage, 2011)

Thermal radiation is electromagnetic radiation in the ultraviolet (UV), visible (VIS) and infrared (IR) spectra that is emitted from all bodies with a temperature above zero Kelvin (Meseguer et al., 2012). The spectral distribution of emitted thermal radiation depends on the body surface temperature, as shown in Figure 2.2. For example, the Sun with a surface temperature of around 5,800 K predominately emits thermal radiation in the ultraviolet and visible spectrum. Whereas, a CubeSat, with an operating temperature of around 300 K, principally emit thermal radiation in the IR spectrum.

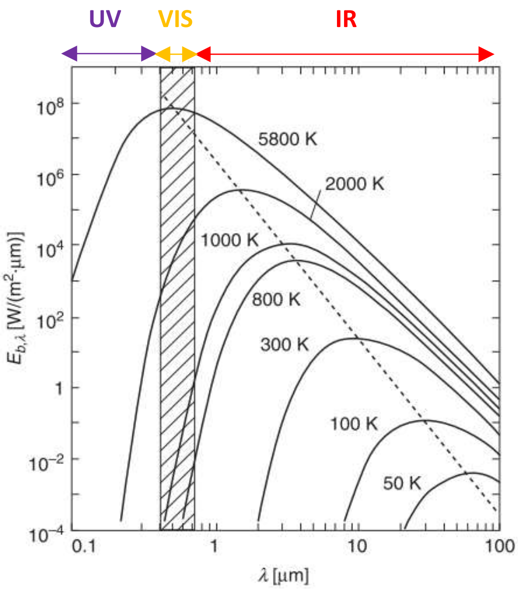

Figure 2.2: Spectral emissive power of a blackbody versus wavelength (Meseguer et al., 2012)

2.2.1 External Thermal Radiation

In LEO, there are three main sources of thermal radiation incident on the CubeSat's surface. These are direct solar radiation, albedo solar radiation and Earth's infrared radiation (Refer to the previous Figure 2.1). Noting, direct solar radiation and albedo solar radiation are only present during the solar exposed portion of the orbit, whilst Earth's infrared radiation is present during both the solar exposed and solar eclipse portion of the orbit.

1. Direct solar radiation is thermal radiation received directly from the Sun, which primarily emits thermal radiation in the ultraviolet and visible spectrums (Remacle, 2018). For LEO, the heat flux for direct solar radiation is around **1400 W/m²** (Reiss, 2012).
2. Albedo is solar radiation which is reflected by the Earth's surface and atmosphere. The amount of solar reflected depends on the terrain, such as reflection from oceans, land, snow or clouds. However, the typical heat flux for albedo in LEO is around **450 W/m²** (Reiss, 2012).
3. Earth's infrared radiation is the thermal radiation emitted by the planet's surface and atmospheric gases, which is mainly in the infrared spectrum (Remacle, 2018). The heat flux for Earth's infrared radiation in LEO varies from **150 to 350 W/m²** (Meseguer et al., 2012).

The radiation transfer reviewed between bodies and surfaces depends on the surface properties, as well as the geometric orientation (Boushon, 2018). To account for geometric orientation, a view factor (F) is given, which is the fraction of radiation leaving the source that reaches a surface, and varies depending on the geometry of the surface with respect to the source, as shown in Figure 2.3 below (Cengel, 2015).

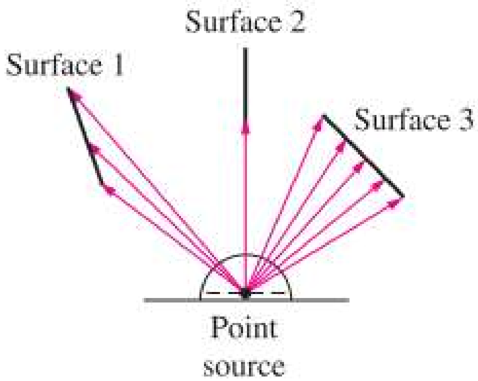

Figure 2.3: View factors from a diffuse point source to various surfaces (Cengel, 2015)

The rate of radiation exchange between surfaces is given by Equation 2.1 below, where A is the surface area, i and j denote the surfaces, F is the view factor and J is the surface radiosity (Cengel, 2015). The surface radiosity (J) represents the rate of radiation leaving a surface and is a function of the surface properties (Cengel, 2015).

$$\dot{Q}_{i-j} = A_j F_{i-j} (J_i - J_j) \qquad \text{Equation 2.1}$$

The orientation of the CubeSat determines which surfaces experience maximum and minimum incoming thermal radiation. However, for CubeSats the incoming thermal radiation is a fraction of the heat rejection required by next generation high-powered electronics. Although, the CubeSats' orientation still needs to be considered for radiator placement to prevent the radiator from excessive solar flux (Remacle, 2018). CubeSats can control their orientation and usually have a specific orientation depending on the stage of the mission, which includes solar battery charging, Earth communications and imagery.

2.2.2 CubeSat Thermal Radiation

CubeSats are designed to operate within temperatures similar to Earth's environment, around 300 K, and accordingly emit thermal radiation in the IR spectral range from its surfaces (Savage, 2011). The amount of energy emitted from a CubeSat surface (Q) is given by Equation 2.2, assuming a view factor of 100% to deep space and negligible deep space temperature, where ε is the surface emissivity, σ is the Stefan-Boltzmann constant, A is the surface area and T is the temperature of radiating surface (Chandrashekar, 2017).

$$\dot{Q} = \varepsilon A \sigma T^4 \qquad \text{Equation 2.2}$$

Heat rejection by a CubeSat is a challenge, since there is limited surface area available, and the temperature is limited by the electronics limit. Figure 2.4 shows the maximum heat rejection possible as a function of temperature, with line graphs provided for standard CubeSat sizes. However, the heat rejection capability of a CubeSat is typically only 25% of the maximum possible, since not all surfaces are ideal for emitting radiation due to the incoming solar radiation and the surfaces also need to accommodate solar arrays, payloads and RF antennas (Kwas et al., 2014).

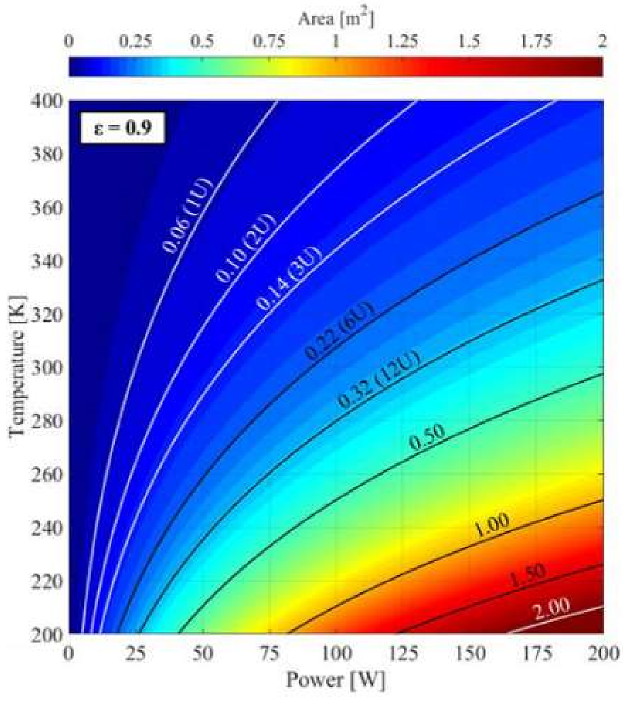

Figure 2.4: Radiator area as a function of power and temperature (Hengeveld et al., 2018)

The thermal radiation from the CubeSat is continual, since the CubeSat's surfaces will continue radiating heat to space as long as the CubeSat has a temperature above zero Kelvin, thus leading to electrical components freezing when not operation if not managed properly (Chandrashekar, 2017).

2.3 CUBESAT THERMAL CONTROL SYSTEMS

The purpose of CubeSat thermal control is to maintain the components of the satellite within their operating temperature range (Meseguer, 2012). When designing the thermal control system, balance is needed to ensure that components do not overheat or become too cold (Chandrashekar, 2017). Typically, to ensure thermal requirements are achieved, a hot case and cold case are both examined, which are the extreme temperature environments that a CubeSat will endure (Boushon, 2018). The hot case corresponds to the maximum heat dissipation from electrical components together with the highest values of solar radiation, and the cold case corresponds to periods of satellite downtime during solar eclipse (Boushon, 2018).

The thermal problem for a CubeSat is transient, since the heat generated by the electronics is variable and the solar flux environment also varies (Meseguer, 2012). As a result, steady-state heat transfer control systems cannot be used in isolation. Therefore, CubeSats utilise a combination of methods to ensure temperatures are regulated. The following section provides an overview of the thermal control methods used by CubeSats, which include surface coatings for exterior protection, thermal straps and heat pipes to transport heat from electrical components, radiators and louvers to dissipate heat to space, electrical heaters for temperature control and PCM heat sinks for heat management.

2.3.1 Surface Coatings

Surface coatings are used to protect CubeSats from external radiation. For CubeSats, surface paints and metallized tapes are the most common methods for providing thermal protection (NASA, 2018). Surface paints are designed to provide low solar absorptance and high emissivity in the infrared spectrum. An example is AZ-93 white thermal paint for space applications from AZ Technology, which provides only 14-16% of the solar absorption, while emitting 89-93% of infrared heat (AZ, 2020). Metallized tapes are second surface mirrors that provide low solar absorptance and high thermal emittance. An example of metalized tape is silvered FEP tapes, which consist of an aluminium surface covered by fluorinated ethylene propylene film, as shown in Figure 2.5 below (Sheldahl, 2020). Surface coatings provide the function of shielding the CubeSat from external thermal radiation, however, they do not provide direct thermal management for electronics.

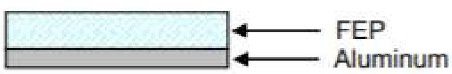

Figure 2.5: Metallized tape second surface mirrors (Sheldahl, 2020)

2.3.2 Thermal Straps

Thermal straps provide heat conduction paths within a CubeSat and provide a method of transferring heat from the electronics to the heat rejection radiator. Thermal straps typically consist of two rigid end terminals separated by a flexible middle section, constructed from either multiple fibres, braids or layers of conductive material. Examples of thermal straps are shown in Figure 2.6 below, and include braided copper, pyrolytic graphite film and aluminium layer thermal straps. High rates of heat transfer can be achieved, especially with graphite film (McKinley et al., 2016). However, thermal straps are limited by how much heat can be radiated to space. For high heat loads, the thermal bottleneck for CubeSats is rejecting heat to space due to their small form factor (Hengeveld et al., 2018).

Figure 2.6: Braided copper, pyrolytic graphite film and aluminium film straps (Wilson et al., 2017)

2.3.3 Heat Pipes

Heat pipes also provide heat transfer paths within a CubeSat and can efficiently transfer heat at high rates (Jafari et al., 2018). As an example, the FlexCool flat panel heat pipe has three times the thermal conductivity of copper at one-third of its density (Isaacs, 2017). A heat pipe transfers heat by evaporating a working fluid on the heated side and transporting the heated vapour to the heat sink/radiator, where it condenses into liquid releasing latent heat. The liquid then returns to the heated source by capillary action. Figure 2.7 shows a heat pipe connected to CubeSat electronics. Although, similarly to thermal straps, heat pipes are also limited by how much heat can be rejected by the CubeSat radiator.

Figure 2.7: CubeSat heat pipe (Hengeveld et al., 2019)

2.3.4 Radiators

Radiators are used to dissipate waste heat to space from overheating electrical components. The most common radiators are body mounted radiators. Although, for CubeSats deployable radiators are being developed to increase surface area to dissipate more heat. An example of a deployable radiator concept is the reversible thermal panel (RTP) deployable radiator, shown in Figure 2.8 below. The radiator can increase heat dissipation by opening the radiator during the hot case, and for the cold case, heat dissipation is decreased by folding the radiator (Akizuki et al., 2020).

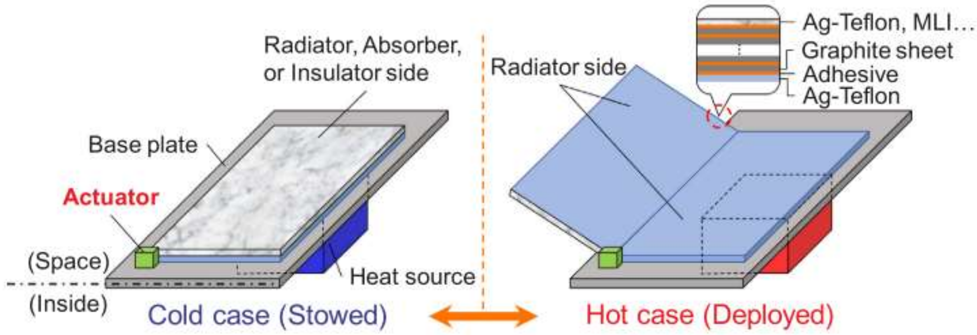

Figure 2.8: Reversible thermal panel radiator (Akizuki et al., 2020)

Another concept for a deployable radiator is the origami inspired radiator concept, as shown in Figure 2.9 below. During the hot case, the radiator expands allowing maximum heat rejection and during the cold case, the radiator contracts thus maintaining a steady temperature (Badagavi, 2017). Deployable and retractable radiators can control the transient temperature of the CubeSat, although, they have a higher risk compared to static body mounted radiators due to the movement and deployment mechanisms. In addition, oversized radiators are still required to manage the peak thermal heat loads from high-powered electronics.

Figure 2.9: Shape shifting radiator concept (Badagavi, 2017)

2.3.5 Louvers

Louvers are mechanical devices integrated into radiators to control the effective emittance. Louver systems typically consist of a frame with a series of reflective blades, which move to shield the radiator thereby changing the effective emissivity (Meseguer, 2012). Figure 2.10 shows louvers installed on the side of a 6U CubeSat, where the louver design uses bimetallic spring actuators to control the position of the blades based on the radiator temperature. When the temperature of the radiator increases, the louvers open to allow increased dissipation. Louvers are passive and work without any power consumption. However, their use on CubeSats has been challenging (NASA, 2018). Furthermore, louvers still require oversized areas to operate, and the mechanical movement adds risk to CubeSats.

Figure 2.10: Louvers on 6U CubeSat (NASA, 2018)

2.3.6 Heaters

Electrical resistance heaters are typically used on CubeSats to maintain temperatures of electronics above the minimum allowable temperature during the cold case (Hengeveld, 2019). The most common electrical heaters are flexible strip heaters, which have electrical resistance filaments sandwiched between layers of flexible insulating material, as shown in Figure 2.11 below. Flexible strip heats have fast warm up and simple control, however they consume power budget (Minco, 2020). CubeSats are typically cold biased, so that the platform remains under positive heater control (Young et al., 2019). However, this results in power budgets needed to operate electrical heaters (Collette et al., 2011).

Figure 2.11: Flexible strip heaters (Minco, 2020)

2.3.7 PCM Heat Sinks

PCM heat sinks are used in CubeSats to thermally manage electrical components which operate with 'on' and 'off' cycles. PCMs use thermal energy storage to absorb the peak thermal loads generated by electronical components and dissipate the heats slowly to space thereby maintaining thermal control. In addition, using thermal energy storage, the CubeSat radiator can be sized for the mean heat removal requirement instead of being sized for peak thermal energy loads (Collette et al., 2011). Additionally, with thermal storage, maintaining temperatures above the minimum operating temperature is also less reliant on electrical heaters.

For CubeSats, the limiting factors for thermal control methods are allowable Size, Weight and Power, known as SWaP (llis et al., 2014). The key advantage of PCMs is their large thermal energy storage capacity per unit weight, thereby allowing lightweight and compact thermal storage for CubeSats. PCM heat sinks also have a passive operation as they do not rely on electrical power to operate. For CubeSat applications, PCM heat sinks have predominantly utilised paraffin PCMs, due to its high latent heat per unit weight. Figure 2.12 below shows a PCM heat sink attached to an electronics board.

Figure 2.12: PCM thermal storage unit by Thermal Management Technologies (TMT, 2020)

Importantly, PCM heat sinks have the potential to enable the use of high-powered electronics for CubeSats, by absorbing the high peak thermal loads, which otherwise would not have been able to be dissipated due to limited surface area. For high heat loads, the thermal bottleneck for CubeSats is rejecting heat to space due to the small form factor (Hengeveld et al., 2018). My research therefore focused on this technology option. In the following sections, PCM thermal storage and PCM challenges are discussed, including a review of existing PCM heat sinks developed for CubeSat applications.

2.4 PCM Thermal Storage

PCM heat sinks utilise Thermal Energy Storage (TES) to absorb the peak heat loads from electronics, and then dissipate the waste heat to space during periods of downtime. The following section reviews the different types of thermal energy storage and the different categories of PCMs available, including their associated advantages and disadvantages.

2.4.1 Thermal Energy Storage Types

Thermal Energy Storage (TES) can be in the form of sensible heat, latent heat and thermochemical heat (Liu et al., 2016). These different types of energy storage for materials are briefly described and their application to CubeSats discussed.

Sensible heat is the heat energy stored in materials by increasing its temperature. The amount of thermal energy stored (Q) is given by Equation 2.3 below, where m is the material's mass, C_p is the specific heat capacity and ΔT is the change in temperature (Liu et al., 2016). Sensible heat is of interest when a large temperature range can be adopted.

$$Q = m\, C_p\, \Delta T \qquad \text{Equation 2.3}$$

Latent heat is the heat energy required to change the phase of a material, without a change of temperature. The amount of thermal energy stored in a phase change (Q) is given by Equation 2.4 below, where m is the material's mass and h is the phase change enthalpy (Liu et al., 2016). A phase change can be any change of state, for example solid state to liquid state, or liquid sate to gas state.

$$Q = m\, h \qquad \text{Equation 2.4}$$

Thermochemical heat is the heat stored as chemical potential energy through reversible endothermic and exothermic chemical reactions. The amount of thermal energy stored (Q) is given by Equation 2.5 below, where m is the mass of the reactants, a_r is the fraction reacted and ΔH is the heat of reaction per unit mass (Liu et al., 2016). The reactants are stored separately until recombination to release back the heat via exothermic chemical reaction.

$$Q = m\, a_r\, \Delta H \qquad \text{Equation 2.5}$$

For CubeSats, the allowable temperature range for electronics is relatively narrow for thermal energy storage. Sensible heat energy storage is useful, however has limitations since the thermal capacity for sensible heat is low over a narrow temperature range. Latent heat is of particular interest as a large amount of heat energy can be stored by the phase change of the material at a constant temperature, consistent with the design objectives of CubeSats. Thermochemical heat is not practical for CubeSats since chemical separation is needed, which adds complexity and volume.

Phase change materials (PCMs) use sensible heat and latent heat to store heat energy. Although, over a narrow temperature range, the majority of the thermal energy storage is in the form of latent heat. For practical purposes, PCM heat sinks commonly feature solid to liquid phase transitions, instead of liquid to gas phase transitions (Collette et al., 2011). Figure 2.13 below illustrates the heat absorption of a solid to liquid PCM. The PCM firstly absorbs energy as sensible heat as the temperature increases. When the phase change temperature is reached, the PCM absorbs energy as latent heat at near constant temperature until the phase is changed (Collette et al., 2011). After phase change, the energy is absorbed again with sensible heat.

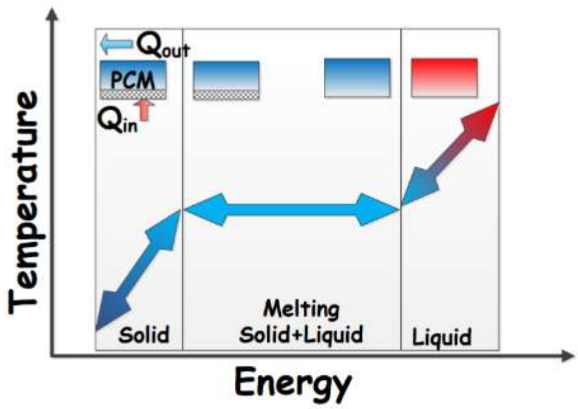

Figure 2.13: Phase change material energy storage (TMT, 2020)

2.4.2 Phase Change Materials (PCMs)

The following section discusses PCM selection and reviews the different categories of PCMs available, including their associated advantages and disadvantages.

2.4.2.1 PCM Selection

The first aspect to consider when selecting a PCM for CubeSat thermal control is the phase change transition temperature. The PCM's melting temperature needs to be within the temperature range of the electrical component for the PCM to be of practical value.

However, there are many factors to consider when assessing the PCM feasibility, which include the PCM's thermo-physical, kinetic and chemical properties (Rathod et al., 2013). Table 2.1 summarises the desirable properties of PCMs for space applications (Hale et al., 1971), (Collette et al., 2011).

Table 2.1: Desirable PCM properties for space applications

Thermo-physical: • High heat of fusion • High thermal conductivity • High specific heat • High density • Low volume change during melting • Low surface tension • Low vapour pressure	Chemical: • Nontoxic • Long term stability during cycling • Compatible with container • Compatible with filler materials
Kinetic: • Dependable melting/freezing behaviour • Reversible solid to liquid transition	Economic: • Affordable • Readily available

In particular, a high heat of fusion per unit weight and volume is desirable to minimise the weight and size of the PCM heat sink for a CubeSat. Also, a high thermal conductivity is desirable for the thermal performance of the PCM heat sink. Furthermore, a low volume change during melting is desirable to reduce the mechanical stresses imposed on the PCM heat sink container in a vacuum environment.

There is however no perfect PCM that has all the ideal properties, and thus trade-offs are required when designing PCM systems (Ge at al., 2013). In addition, to benefit from the specific advantages of PCMs, two or more PCMs can be utilised and the PCMs can be selectively arranged for optimal configuration (Moraga et al., 2016).

In the next section, different categories of PCMs with suitable melting points are reviewed, including their associated advantages and disadvantages. Noting, PCM heat sinks for CubeSat applications have predominantly utilised paraffin PCM, due to their high latent heat per unit weight.

2.4.2.2 PCM Categories

The following section provides an overview of the different categories of PCMs, and Figure 2.14 below shows the general categories of PCMs by their chemical classes. PCMs in their respective categories generally share the same associated advantages and disadvantages (Shamberger et al., 2020). The following section provides an overview of the different classes of PCMs, with suitable examples from each class summarised in Table 2.2, based on their melting points (page 41).

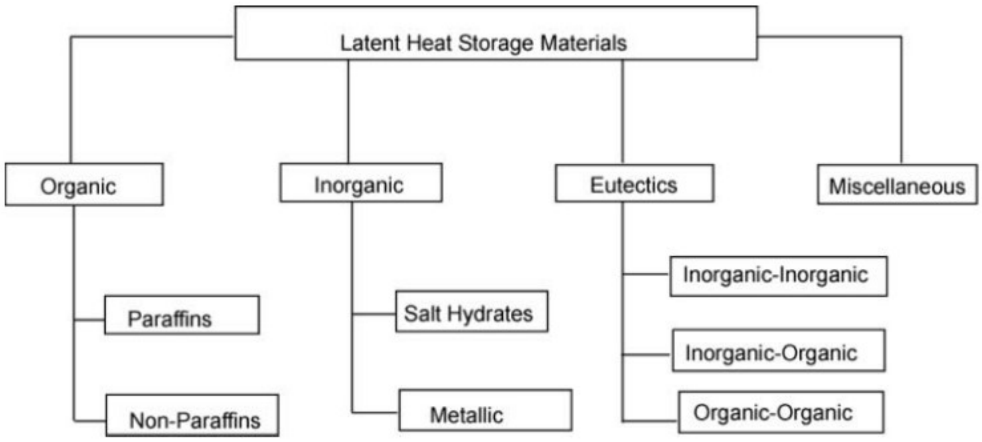

Figure 2.14: PCM Categories (Sharma and Sagara, 2005)

Organics: Paraffins

Organic paraffins are made from a mixture of alkanes of C_nH_{2n+2} hydrocarbons and have very similar properties within their class (Sharma et al., 2005). Paraffins are safe, chemically stable and compatible with all metal containers. The main advantage of paraffins is their high heat of fusion on a weight basis (not volume basis) and their repeatable solidification characteristics with low tendencies to supercool (Rathod et al., 2013). However, paraffins have low thermal conductivity and do not have a well-defined melting point (Rathod et al., 2013). For CubeSat applications, PCM heat sinks have predominantly utilised paraffins, due to their high latent heat per unit weight. However, their main challenge has been overcoming the inherently low thermal conductivity of paraffin PCMs.

Organics: Non paraffins

The non-paraffin organics class contains a variety of subgroups with highly varied properties, and include organic PCMs such as fatty acids, alcohols and glycols (Sharma et al., 2005), (Rathod et al., 2013). In general, non-paraffin organics have a high latent heat and have a well-defined phase transformation, although, they are mildly corrosive and flammable (Khan et al., 2016). Their thermal conductivity is generally low, however their properties vary widely within this category (Khan et al., 2016). This class of PCMs presents an opportunity for further investigation for CubeSat applications, although may need to be discarded due to corrosion problems (Collette et al., 2011).

Inorganic: Salt Hydrates

Salt hydrates are compounds of inorganic salt and water of general formula AB_nH_2O (Khan et al., 2016). Salt hydrates have high latent heat per unit weight and volume and exhibit low volume change during melting (Rathod et al., 2013). Their thermal conductivity is generally low, but higher than paraffins and non-organic paraffins (Khan et al., 2016). However, the issues with salt hydrates are corrosion with metallic containers, supercooling and phase segregation (Collette et al., 2011). Phase segregation occurs during melting, where other hydrates and dehydrated salts are formed which tend to segregate and reduce the active amount of PCM available for heat storage (Khan et al., 2016). Since salt hydrates are corrosive with metal containers and suffer from phase segregation, this class of PCMs has limited application for space based PCM heat sinks.

Inorganic: Metallics

Metallic PCMs suitable for electrical components are primarily Gallium, and eutectics of Gallium (Ga) with combinations of Indium (In), Zinc (Zn) and Tin (Sn). Pure Gallium has a melting point at 29.8 °C, whereas eutectics of Gallium have melting points in the temperature range of 10 to 25 °C (Shamberger et al., 2020). Gallium and its eutectics key strength is their high thermal conductivity, making metallic PCMs very attractive. However, Gallium is corrosive with metal containers, such as for aluminium, copper and steels, making it difficult to contain with conductive materials (Shamberger et al., 2020). Gallium containment is a possibility with Titanium (Mingear et al., 2017). However, Titanium may present a challenge for CubeSats, since Titanium components may not completely disintegrate during re-entry and therefore become a hazard. Another issue with Gallium is supercooling, although nucleating agents such as silicon dioxide powder can improve performance (Ge et al.,2013).

Miscellaneous: Water

Miscellaneous PCMs are materials that do not directly align with the other general categories. One such example is water (Hale et al., 1971). Water is advantageous for space applications as it has the highest latent heat of fusion on a weight and volume basis, and also has very high specific heat capacity (Hansen et al., 2014). In addition, water is non-toxic, stable and non-combustible. The thermal conductivity of water is also relatively high compared to non-metal PCMs and water is compatible with most metal containers (Hale et al., 1971). However, compared to paraffins, water expands when frozen, which can cause issues for rigid containers. The expansion upon freezing can result in water becoming hydraulically locked, thereby causing damage to the PCM container (Hansen et al., 2014).

Table 2.2: PCMs of interest from each class of materials – Properties: (s) solid, (l) liquid

[A] (Ge at al., 2013), [B] (Collette et al., 2011), [C] (Hale et al., 1971), [D] (Sharma et al., 2005), [E] (Moraga et al., 2016), [F] (Shamberger et al., 2020), [G] (Khan et al., 2016), [H] (Amin et al., 2017)

PCM	Melting Point (˚C)	Thermal Conductivity (W/m·K)	Heat of Fusion (kJ/kg)	Specific Heat (kJ/kg·K)	Density (kg/m^3)
Organics: Paraffins					
Tetradecane ($C_{14}H_{30}$)	5.5 [C]	0.15 [C]	228 [C]	(s) 2.070 [C]	(s) 825 [C]
Hexadecane($C_{16}H_{34}$)	16.7 [C]	0.15 [C]	237 [C]	(s) 2.110 [C]	(s) 835 [C]
Octadecane($C_{18}H_{38}$)	28 [B]	0.15 [C]	244 [B]	(s) 2.160 [C]	(s) 814 [C]
Nonadecane($C_{19}H_{40}$)	32 [B]	-	187 [B]	-	-
Eicosane ($C_{20}H_{42}$)	37 [B]	0.15 [C]	246 [B]	(s) 2.210 [C]	(s) 856 [C]
Organics: Non paraffins					
Polyethylene Glycol 600	20-25 [B]	0.16 [C]	146 [B]	(s) 2.250 [C]	(s) 1100 [C]
Acetic Acid	17 [B]	0.18 [C]	187 [B]	(s) 2.040 [C]	1050 [D]
Capric Acid	31.4 [E]	0.153 [D]	153 [E]	(s) 2.096 [E]	884 [E]
Myristic Acid	54 [D]	-	199 [D]	(s) 1.590 [C]	844 [D]
Bees Wax	62.28 [H]	0.25 [H]	141.49 [H]	0.508 [H]	(s) 819.8 [H]
Inorganic: Salt Hydrates					
Calcium chloride hexahydrate ($CaCl_2$ $6H_2O$)	29 [B]	(s) 1.088 [G] (l) 0.54 [G]	190.8 [G]	-	(s) 1802 [G]
Lithium Nitrate Trihydrate ($LiNO_3$ $3H_2O$)	30 [G]	-	296 [G]	-	(s) 1550 [C]
Sodium sulfate decahydrate (Na_2SO_4 $10H_2O$)	31 [B]	(s) 0.554 [G]	254 [G]	-	(s) 1485 [G]
Zinc nitrate hexahydrate ($Zn(NO_3)_2$ $6H_2O$)	36 [G]	(l) 0.469 [G]	147 [G]	-	(s) 1937 [G]
Sodium phosphate dibasic dodecahydrate (Na_2HPO_4 $12H_2O$)	37 [B]	(s) 0.514 [G]	280 [G]	(s) 1.690 [C]	(s) 1522 [G]
Inorganic: Metallics					
67Ga-20.5In-12.5Zn	10.7 [F]	30.7 [F]	67.2 [F]	-	-
78.6Ga-21.4In	15.7 [F]	25.8 [F]	69.7 [F]	-	-
82Ga-12Sn-6Zn	18.8 [F]	27.8 [F]	86.5 [F]	-	-
86.5Ga-13.5Sn	20.55 [F]	25.5 [F]	81.9 [F]	-	-
96.5Ga-3.5Zn	25 [F]	27.3 [F]	88.5 [F]	-	-
Pure Gallium, Ga	29.8 [A]	29.4 [A]	80.12 [A]	0.37 [A]	5907 [A]
Miscellaneous: Water					
Water (H_2O)	0 [B]	(s) 2.2 [C] (l) 0.567 [C]	333 [B]	(s) 2.040 [C] (l) 4.210 [C]	(s) 916.8 [C] (l) 999.8 [C]

2.5 PCM CHALLENGES

The main challenges with PCM systems is the need to overcome their low thermal conductivity and contain the solid to liquid volume change of the PCM (Kandasamy et al., 2008). Thus, the role of the PCM container is twofold: (1) to provide effective heat transfer and (2) to provide leakproof containment.

2.5.1 PCM Heat Transfer Enhancement

Firstly, to provide effective heat transfer with PCMs, heat transfer enhancement techniques are employed, which generally involve techniques for extending the heat exchange area and increasing the bulk thermal conductivity (Zhang et al., 2020).

2.5.1.1 Extending Heat Exchange Area

Extending the heat exchange area for PCM heat sinks is achieved with Thermal Conductivity Enhancement (TCE) structures. The most popular method for extending the PCM heat transfer area with TCEs are fins (Gil et al., 2018). Fins have been widely studied in terms of fin configuration, fin size, fin shapes, fin interval spacing and fractal geometries (Mahdi et al., 2019). (Huang et al., 2017). (Laing et al., 2013). Although, fin designs have limited scope for improvement with traditional manufacturing methods (Shamvedi et al., 2018). Figure 2.15 below shows a CubeSat PCM heat sink with metal fins heat transfer enhancement. The main disadvantage of fins is they reduce the volume available for the storage PCM and increase the weight of PCM systems. This research investigated the use of additive manufacturing to optimise TCE structures for PCM heat transfer. A review of additive structures for PCM heat transfer enhancement is presented in the additive manufacturing section at the end of this literature review.

Figure 2.15: Fins extending heat exchange area

2.5.1.2 Increasing Bulk Thermal Conductivity

Increasing bulk thermal conductivity methods for PCMs include metal foams and dispersed conductive particles. Metal Foams, shown in Figure 2.16 below, can enhance heat transfer rates within PCM systems by increasing the overall thermal conductivity of the PCM-foam combination. Foams are typically produced from copper and aluminium, although non-metallic materials such as porous graphite have also been investigated (Wei et al., 2018). Foams are manufactured by injecting foaming gas to produce porous structures (Mahdi et al., 2019) . Due to this manufacturing method, the pores are randomly oriented in shape and size, and are difficult to optimise for PCM heat transfer enhancement (Mahdi et al., 2019).

Figure 2.16: Metal foam PCM heat sink (Mancin et al., 2015)

Conductive particles dispersed within the PCM can also enhance the heat transfer performance of PCMs. Conductive particles investigated with PCMs have been mainly carbon particles (Choi et al., 2014) and copper oxide nanoparticles (Sheikholeslam, 2018). The addition of highly conductive additives into PCMs can increase the overall thermal conductivity of PCMs, Studies It is finally concluded that Graphite flake is the most promising additive for heat transfer enhancement of stearic acid among three carbon additives, shown in Figure 2.17. Although PCM systems with additives can reduce in performance overtime with particle agglomeration (Zhao et al., 2020).

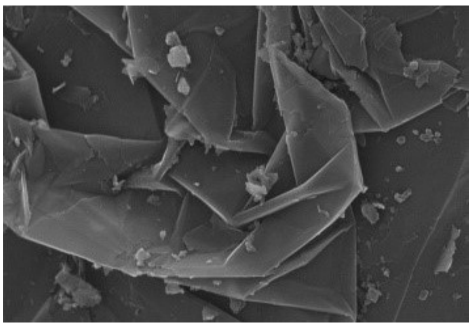

Figure 2.17: FE-SEM images of Graphite flake (Choi et al., 2014)

2.5.2 PCM Containment

Secondly, to provide leakproof containment for PCMs in space, the PCM container must also be capable of withstanding the repeated volume changes of the melting and freezing cycles. (Kandasamy et al., 2008). The PCM volume change depends on the PCM type. For example, paraffins, fatty acids and salt hydrates expand during melting, whereas gallium and water expand during solidification (Khan et al., 2016). Table 2.3 shows the volume change percentages for PCMs of interest.

Table 2.3: PCM volume change characteristics

[A] (Collette et al., 2011), [B] (Hale et al., 1971)

PCM	Density Solid (kg/m^3)	Density Liquid (kg/m^3)	Volume Change (%)
Paraffin: Octadecane	865 [A]	780 [A]	+ 11 (liquid expansion) [A]
Metallic: Gallium	5903 [B]	6093 [B]	- 3 (solid expansion) [B]
Miscellaneous: Water	920 [A]	1000 [A]	- 9 (solid expansion) [A]

A void volume is necessary to accommodate the PCM expansion in rigid containers. The void region in Figure 2.18 is shown at the top of the heat sink, which would occur under gravity. However, in micro-gravity, the void volume would occupy different regions of the container. When a liquid is free from gravitational effects, the intermolecular and surface tension forces, known as the Marangoni Effect, play a large role on the motion of the fluid within the container (Hale et al., 1971).

Void management and heat distribution is also critical to minimising the mechanical stresses in the container and ensuring high heat transfer rates through contact with the PCM. Flow configurations that allow PCM expansion to move freely during melting can reduce high pressure gradients as the PCM melts and expands (ACT, 2020). Also, enhancing the heat spreading throughout the PCM device can uniformly melt the PCM, which in turn increases the heat transfer rate and also reduces high localised pressures as the PCM melts (ACT, 2020).

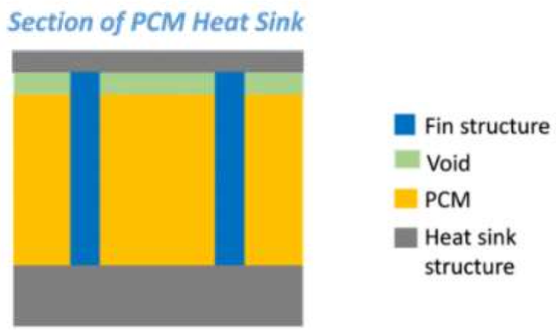

Figure 2.18: PCM heat sink with void volume (ACT, 2020)

The PCM container also needs to be constructed from suitable thermally conductive materials to transfer heat into the PCMs. Table 2.4 below provides thermal properties of potential containment materials for PCMs.

Containment materials include metals, such as aluminium, copper, titanium, magnesium and stainless steel. Copper exhibits the highest thermal conductivity from the metals listed. However, copper has a weight penalty based on its high density. Aluminium and magnesium have the best thermal conductivity on a weight basis due to their lower densities. Titanium and stainless steel have much lower thermal conductivities in comparison to aluminium and magnesium, however, titanium and stainless steel have improved resistance to corrosion (Hale et al., 1971).

In addition to metals, carbon fibre reinforced polymers (CFRP) are also suitable due to the excellent thermal properties of graphene and excellent strength to weight ratio of CFRP (Ivanov et al., 2019). Although, whilst CFRP can achieve high thermal conductivities in the direction of the carbon film (in plane), their out of plane thermal conductivities are much lower (Yu et al., 2015). Due to their low out of plane thermal conductivity, CFRP may be challenging for transferring heat with PCMs. Also, polymers for space applications need to consider outgassing considerations in a vacuum environment.

Table 2.4: Thermal properties of containment materials

[A] (*Incropera et al., 2007*), [B] (*Yu et al., 2015*), [C] (*TCPoly, 2019*)

Material	Thermal Conductivity (W/m·K)	Density (kg/m^3)	Specific Thermal Conductivity (W·m^2/kg·K)	Specific Heat (J/kg·K)	Thermal Diffusivity (mm^2/s)
Metals					
Aluminium	237 [A]	2702 [A]	0.088 [A]	903 [A]	97.1 [A]
Copper	401 [A]	8933 [A]	0.045 [A]	385 [A]	117 [A]
Stainless steel, 316	13.4 [A]	8238 [A]	0.0016 [A]	468 [A]	3.48 [A]
Titanium	21.9 [A]	4500 [A]	0.0049 [A]	522 [A]	9.32 [A]
Magnesium	156 [A]	1740 [A]	0.090 [A]	1024 [A]	87.6 [A]
Non-Metals					
Carbon fibre reinforced polymers	In plane, 119 [B] Out of plane, 0.86 [B]	1430 [B]	In plane, 0.083 [B] Out of plane, 0.0006 [B]	-	-
TCPoly thermoplastic carbon filament	In plane, 8 [C] Out of plane, 2.5 [C]	1550 [C]	In plane, 0.005 [C] Out of plane, 0.002 [C]	1300 [C]	-

In the next section, PCM heat sink containers for CubeSat applications found in the literature are presented and discussed.

2.6 CubeSat PCM Heat Sinks

This section provides an overview of existing PCM heat sinks investigated in literature for CubeSat applications. These include the following:

1. FORMOSAT-5 PCM Device (Taiwan)
2. Roccor Thermal Energy Management Panels (USA)
3. NASA Mini Paraffin Packs (USA)
4. Carbon Fibre Reinforced Polymer Heat Storage Panel (Japan)
5. Advanced Cooling Technologies PCM Heat Sink Module (USA)
6. Thermal Management Technologies Thermal Storage Unit (USA)

2.6.1 FORMOSAT-5 PCM Device (Taiwan)

The Format-5 PCM device, shown in Figure 2.19, was investigated for the Taiwanese Earth observation CubeSat. The proposed placement for the PCM device was between the X-band transmitter and the radiator. The PCMs investigated were paraffins and the PCM device was constructed using aluminium 6061-T6 alloy. Pin fins were used as the PCM heat transfer enhancement technique (Chen et al., 2016).

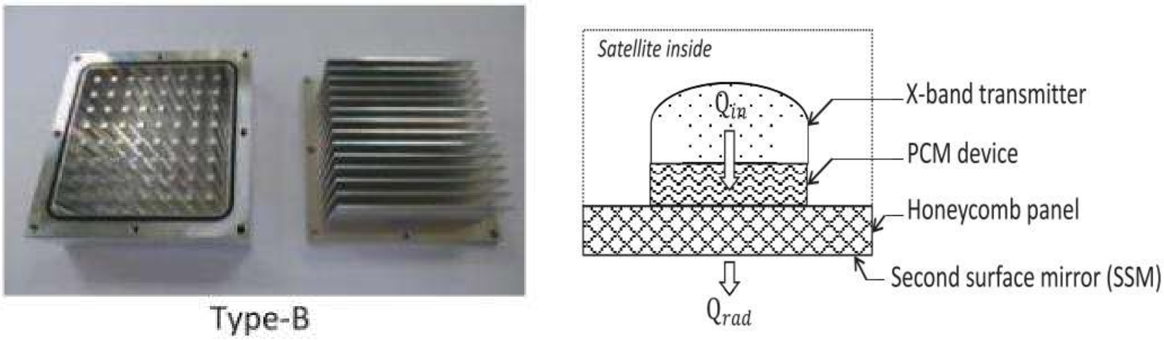

Figure 2.19: PCM device and cross section view of the satellite unit (*Chen et al., 2016*)

The device was experimentally tested under ambient conditions (atmospheric pressure and temperature). The experimental setup was a foil heater (1 in^2 size) attached to the bottom of the PCM container and a thermocouple installed adjacent to the heater. The heating power applied was 9 W for a duration of 40 minutes and the device was cooled by natural convection (Chen et al., 2016).

The test results, shown in Figure 2.20, show the temperature response for Type A (no pin fins) and Type B and C (pin fins). The test results shown are for eicosane (T_{Fus}=37˚C). The results showed that the Type B and C pin fins maintained a temperature at around the PCM melting point and then increased after phase change. The testing was however limited to low powers and it is unknown how the aluminium pin fins with paraffin would manage with higher heat fluxes.

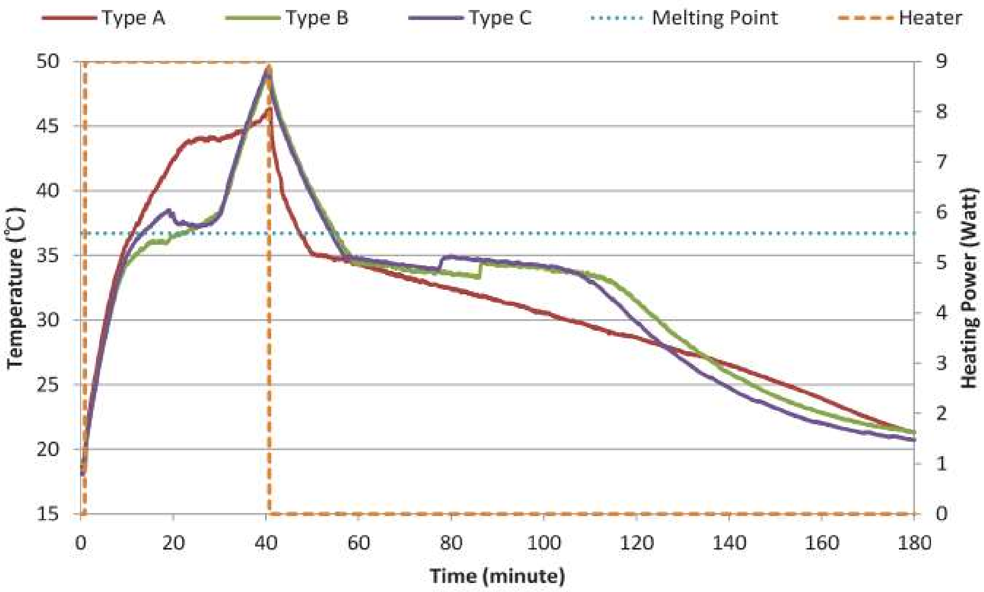

Figure 2.20: Experimental results for eicosane (Chen et al., 2016)

2.6.2 Roccor Thermal Energy Management Panels (USA)

The Roccor thermal management panel is a thin PCM panel designed to be placed on the exterior of a CubeSat, shown in Figure 2.21. The PCMs investigated for this device were paraffins, namely octadecane (T_{Fus}=28˚C) and eicosane (T_{Fus}=37˚C). The panel was constructed using aluminium and the PCM heat transfer enhancement was achieved using pin fins. The panel was additively manufactured using selective laser sintering and sealed with gasketed screws top and bottom (Isaacs et al., 2017).

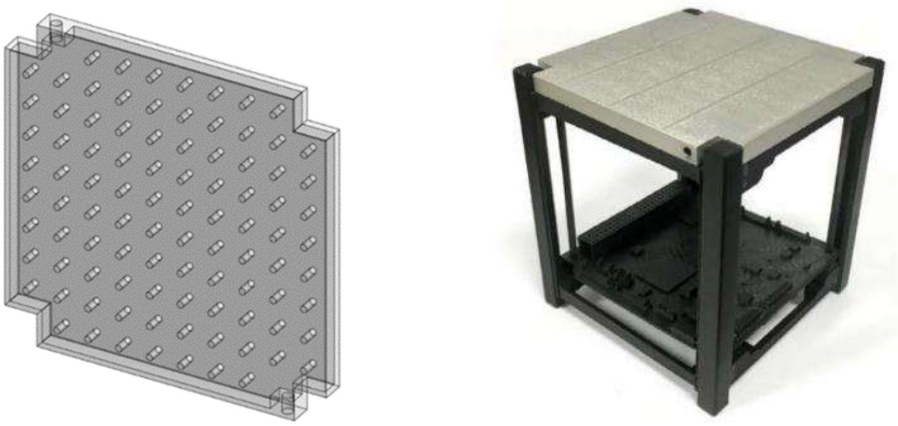

Figure 2.21: Roccor thermal panel and panel for 1U CubeSat (Isaacs et al., 2017).

The Roccor panel was experimentally tested in a vacuum chamber held at a pressure of $1x10^{-3}$ torr. For the experiment, a flexible heater pad was placed on top of the panel. Two power levels were applied for 1 hour, namely 3.8 W and 5.5 W, and then the device was left to cool. The result shown in Figure 2.22 are for the device filled with octadecane. The results showed a higher temperature response for the 5.5 W load compared to the 3.8 W load.

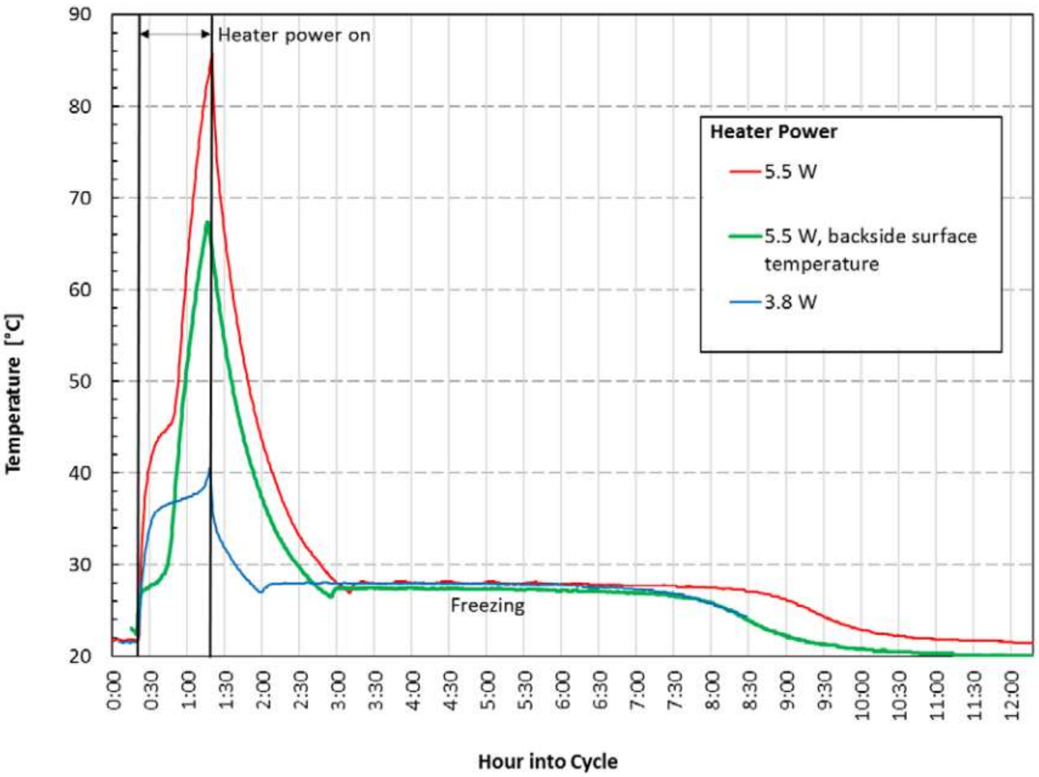

Figure 2.22: PCM panel surface temp profile during melting and freezing (Isaacs et al., 2017)

The Roccor panel was also subjected to 25 thermal cycles and the structural panel did not leak or deform (Isaacs et al., 2017). The additively manufactured panel demonstrated the possibilities of using selective laser sintering to contain PCM. Although, further refined geometries were not investigated to increase heat exchange area and improve the thermal performance for higher powered electronics.

2.6.3 NASA Mini Paraffin Packs (USA)

The NASA mini paraffin packs developed for the ICECUBE 3U CubeSat are shown in Figure 2.23. The PCMs used in the device were also paraffins. To meet the 20˚C temperature requirement for the Mizer LO Assembly (MLA) and Intermediate Frequency Assembly (IFA), the paraffin hexadecane (T_{Fus}=18˚C) was selected (Choi et al., 2015). The proposed placement of the paraffin packs was around the MLA and IFA as shown in Figure 2.23. The mini paraffin packs were constructed using aluminium 6061-T6 alloy and the PCM heat transfer enhancement was achieved using a fine pore aluminium honeycomb core embedded with K1100 carbon fibres (Choi et al., 2015). The internal design details of the honeycomb structures were not provided.

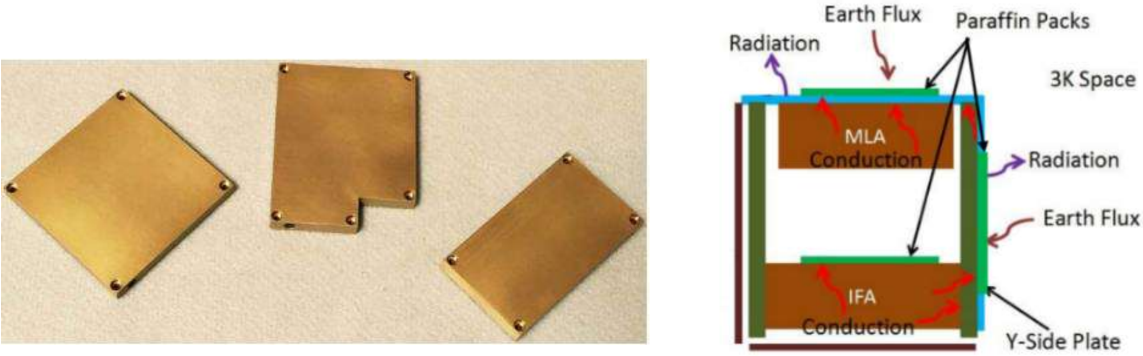

Figure 2.23: NASA mini paraffin packs (Choi et al., 2019) and satellite placement (*Choi et al., 2015*)

Ground testing details for the paraffin mini packs are not provided, however, flight test data is provided for the ICECUBE satellite in orbit. The flight temperature telemetry data is shown in Figure 2.24 for a few orbit cycles. The instrument was powered on for 56 minutes, and then powered off for 37 minutes in each orbit (Choi et al., 2018). The power dissipation from the MLA and IFA were 3.07 W and 1.15 W respectively (Choi et al., 2018). The results show that the paraffin PCM mini packs were able to maintain the instrument temperatures stable close to the 18˚C PCM melting point. The MLA and IFA were however low power devices of less than 5 W. It is unknown how the mini paraffin packs would respond for higher power electronics.

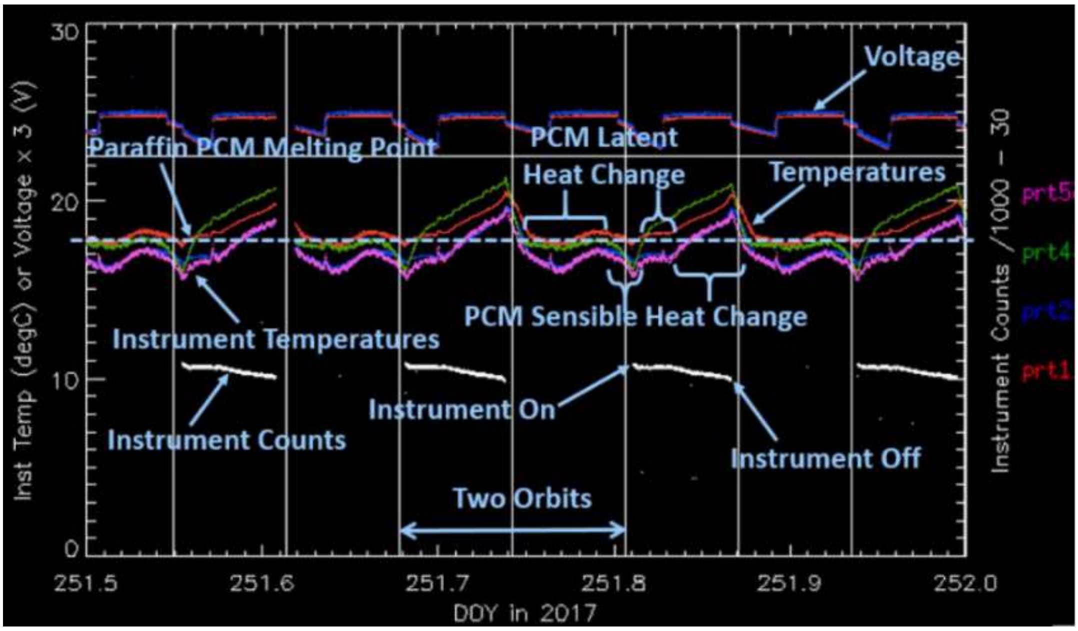

Figure 2.24: Flight temperatures on ICECUBE from Day of Year 251-252 (Choi et al., 2018)
Temp. sensors: PRT-1 (IFA Isolator), PRT-2 (IFA Detector), PRT-4 (MLA), PRT-5 (+Y Plate Interior)

2.6.4 Carbon Fibre Reinforced Polymer Heat Storage Panel (Japan)

The Heat Storage Panel (HSP), shown in Figure 2.25, was developed for the Japanese CubeSat called Hodoyoshi-4 (Yamada et al., 2015). The HSP is a thin carbon fibre reinforced polymer (CFRP) panel with PCM injected between the layers. The HSP's proposed configuration within the CubeSat is shown in Figure 2.25, where the panel is placed adjacent to the battery pack, which has the narrowest allowable temperature range. To radiate excess heat to space, a mini loop heat pipe transports the heat from the HSP to the radiator for heat rejection (Ueno et al., 2017). The PCMs investigated were paraffins, namely eicosane (T_{Fus}=37˚C) (Yamada et al., 2015) and hexadecane (T_{Fus}=16.7˚C) (Ueno et al., 2017). The PCM heat transfer enhancement was achieved with the high thermal conductivity carbon fibres throughout the PCM panel (Yamada et al., 2015). The specific construction details of the carbon fibre encapsulation are not provided.

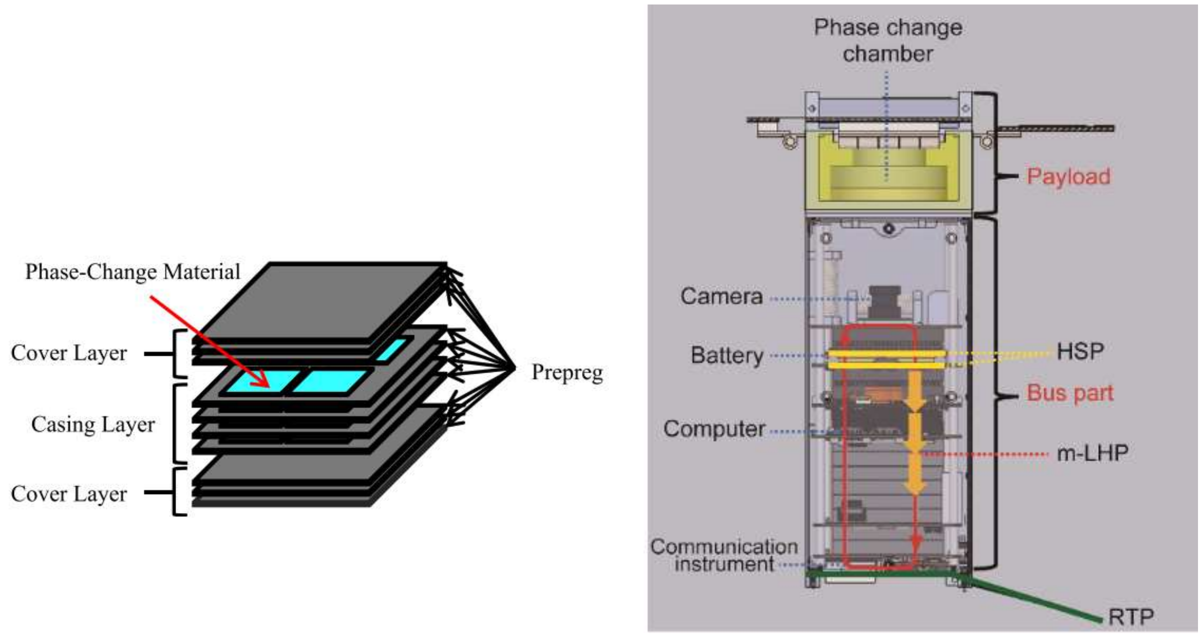

Figure 2.25: Structure of HSP (Yamada et al., 2014) and CubeSat configuration (Ueno et al., 2017)

The HSP was tested in a space chamber with a pressure of 10^{-6} Pa and with a thermal shroud temperature maintained below -180˚C. For testing, an irregular heat load program was applied to the panel, with maximum heat load of approx. 22 W, that simulated the heat output from the CubeSat instruments. The results are shown in Figure 2.26 for the HSP with eicosane and the HSP without any inserted PCM. The panel without any PCM experienced severe temperature fluctuations, whereas the panel with eicosane had a level temperature close to the melting temperature of the PCM.

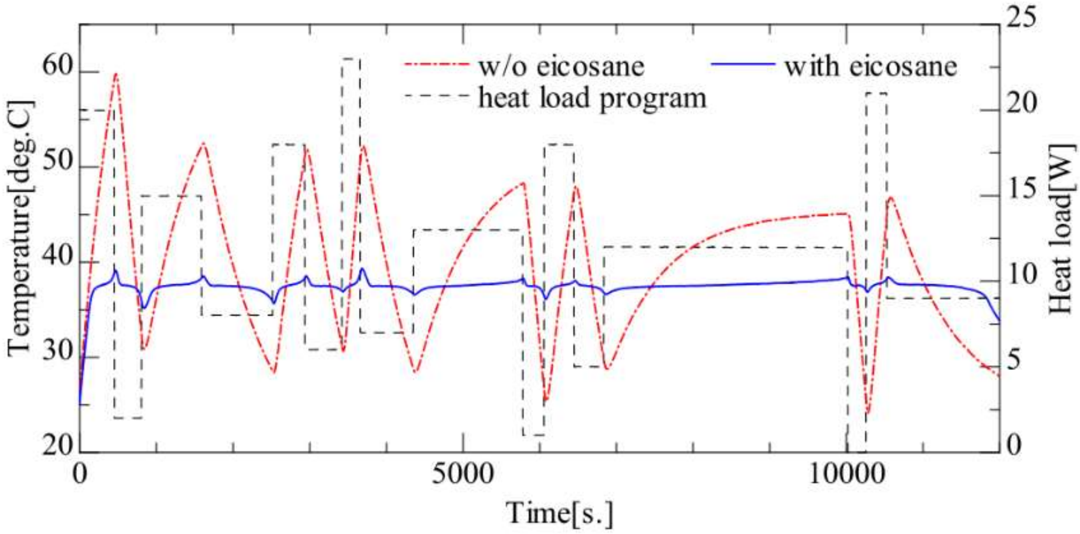

Figure 2.26: Experimental result of simulated program heating test (Yamada et al., 2015)

2.6.5 Advanced Cooling Technologies PCM Heat Sink Module (USA)

Advanced Cooling Technologies (ACT) is a commercial provider of PCM heat sinks for military, aerospace and industrial applications. According to ACT, paraffins are the most common PCM for electronics thermal management since they are chemically compatible with most metals, provide dependable cycling and have a large melting point selection range available (ACT, 2020). The most common materials used by ACT for PCM heat sink containment is aluminium, although ACT has also used copper, steel, and magnesium (ACT, 2020). To overcome the low thermal conductivities of paraffins, ACT uses folded fin structures, as shown in Figure 2.27 (ACT, 2020). Specific testing details are not available for this design.

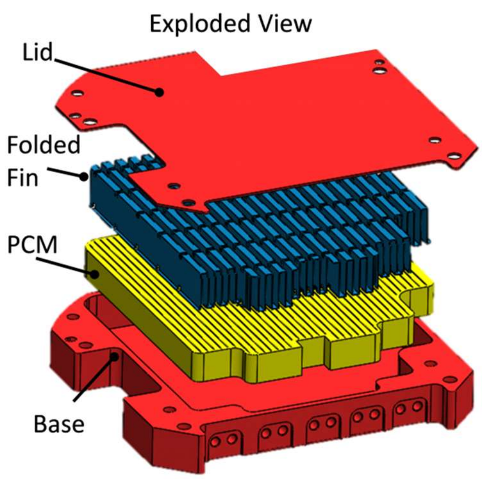

Figure 2.27: PCM heat sink module by Advanced Cooling Technologies (ACT, 2020)

2.6.6 Thermal Management Technologies Thermal Storage Unit (USA)

Thermal Management Technologies (TMT) also provides commercially ready PCM heat sinks for use in space applications. TMT has developed standardised PCM thermal storage units for CubeSat applications to keep costs low and to reduce lead times (TMT, 2020). The PCMs used in the device can be a range of paraffins to suit mission type. The TMT thermal storage unit is shown in Figure 2.28, although there are no details available regarding the design of the device and no testing details with applied heat loads are provided.

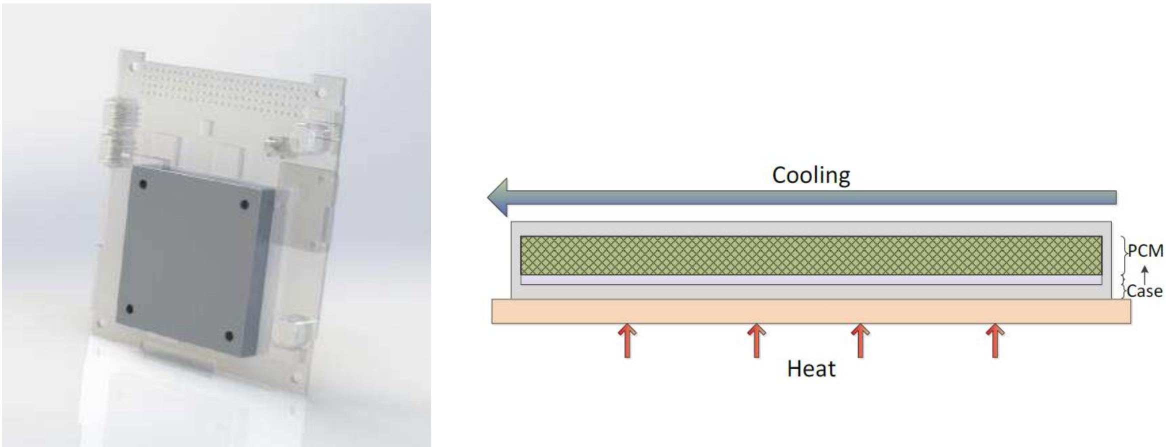

Figure 2.28: Thermal storage unit by Thermal Management Technologies (TMT, 2020)

2.6.7 Concluding Remarks

CubeSat PCM heat sinks have predominantly utilised paraffin PCM, due to its high latent heat per unit weight. However, the studies included in this section pertained predominantly to low power applications of less than 10-20 W. With trends for higher power CubeSat applications (Janzer et al., 2018), (Young et al., 2019), this research investigates paraffin PCM heat sinks for higher power applications.

Of interest in this study is the use of additive manufacturing to maximise paraffin PCM heat transfer for high-powered applications. Additive manufacturing offers new innovative geometries to extend the heat exchange area beyond the traditional manufacturing designs. My research therefore focused on this technology option. Additive manufacturing techniques are reviewed in the next section.

2.7 APPLICATION OF ADDITIVE MANUFACTURING

Additive Manufacturing, also known as 3D Printing, is the process of fabricating three-dimensional objects layer by layer from computer-aided design (CAD) models (Huang et al., 2015). There are many forms of additive manufacturing methods, summarised in Table 2.5 below, which are characterised by the mode the layers are deposited and bonded together (Vyavahare et al., 2019). The available material groups for each process are also provided in Table 2.5, which generally include metals, polymers and ceramics.

Table 2.5: Additive manufacturing processes, Adapted from (Huang et al., 2015)

Process	**Description**	**Materials**
Material Extrusion	Material dispensed through a nozzle	Thermoplastics Metals
Powder Bed Fusion	Material powder bed fused with lasers	Thermoplastics Metals
Vat Photopolymerization	Liquid photopolymer cured by light	UV Curable Resins Waxes, Ceramics
Sheet Lamination	Sheets of material bonded together	Thermoplastics Metals
Directed Energy Deposition	Material fused during deposition	Metals
Material Jetting	Droplets of build material deposited	UV Curable Resins Waxes
Binder Jetting	Bonding agent deposited to join powder	Polymers, Ceramics Metals

Of interest to this research is the use of metals due to their high thermal conductivity and strength. The metal additive manufacturing methods reviewed in this section are Powder Bed Fusion and Material Extrusion. The remaining metal additive methods listed above in Table 2.5 are not reviewed on the following basis: (1) Directed energy deposition is typically used to repair or add additional metal material to existing components and is not suitable for PCM heat sinks; (2) Sheet lamination is more suited for larger two-phase heat exchangers; and (3) Binder jetting is still in development with thermally conductive metals.

2.7.1 Powder Bed Fusion

The most used process for metal additive manufacturing heat sinks has been Powder Bed Fusion, in particular Selective Laser Sintering (SLS) (Nafis et al., 2020). SLS produces three-dimensional objects by depositing layers of fine metal powder and selectively sintering each layer with a laser fusing it to the previous underlying layer (Martin et al., 2017). Figure 2.29 shows the SLS process whereby a selective area of metal power is irradiated and sintered by a laser, and then a powder layer of controlled thickness is evenly spread over the working surface to repeat the sintering process (Sola et al., 2019).

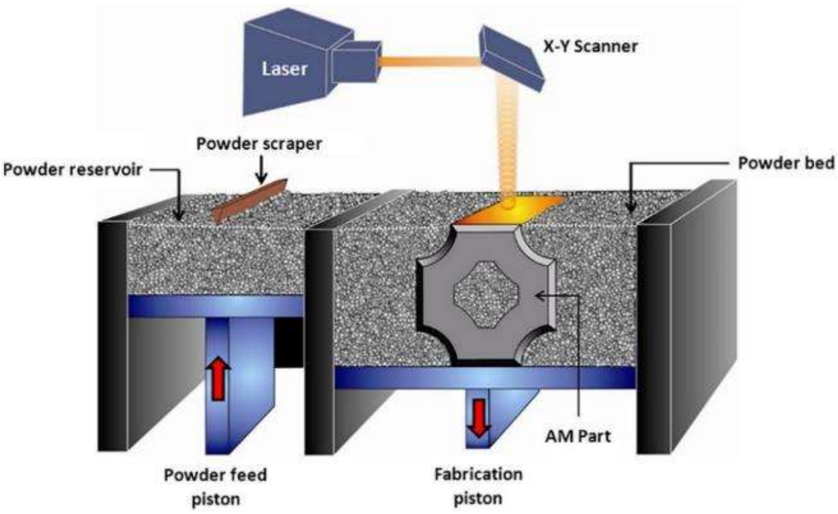

Figure 2.29: Schematic of laser-based powder bed fusion process (Sola et al., 2019)

SLS can manufacture intricate geometries that very closely resemble the 3D design, since the lasers accurately fuse the metal to the desired shape (Nafis et al., 2020). However, post processing requires the removal of the remaining fine metal powder within the structures, as shown in Figure 2.30 below. SLS has had more success with steel, titanium and aluminium, whereas the process has been difficult with copper, due to its high reactivity with oxygen and low absorptivity of lasers (Nafis et al., 2020).

Figure 2.30: Post processing of the laser-based powder bed fusion process (Protolabs, 2020)

Porosity is a common issue with Powder Bed Fusion, as the porosity is caused by large thermal gradients resulting from the repeated and rapid melting and solidification (Ning et al., 2020). Figure 2.31 shows polished 316L additive manufactured samples with irregular shaped pores characterised by the lack of fusion (Ronneberg et al., 2020). Porosity effects the mechanical properties of the material depending on the shape, size, orientation and distribution of the pores (Ronneberg et al., 2020). Porosity in metal samples can also have an adverse effect on the thermal conductivity of the material depending on the level of porosity present (Vincent et al., 2012).

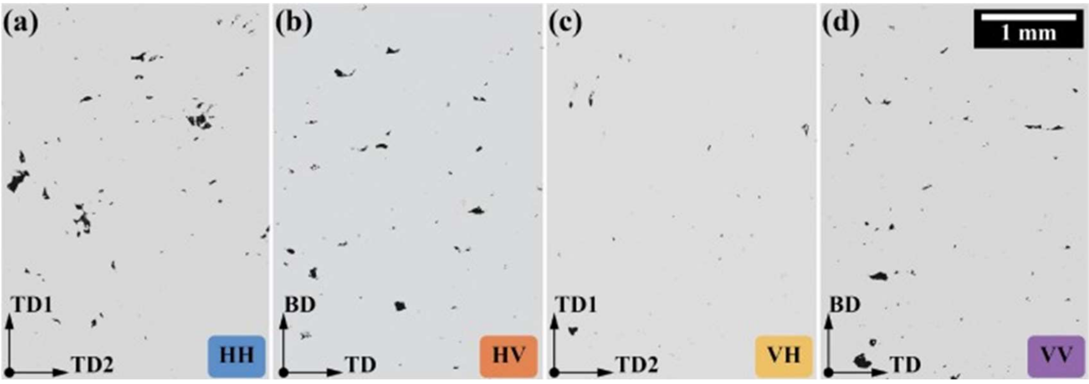

Figure 2.31: Optical micrographs, H-horizontal V-vertical (Ronneberg et al., 2020)

2.7.2 Material Extrusion

A recently developed process for metal additive manufacturing is Metal Extrusion. Metal Extrusion produces three-dimensional objects by extruding material layer by layer onto a build plate, as shown in Figure 2.32 below. The metal filaments extruded typically comprise of a metal powder and binder mixture, allowing the material to be extruded at temperatures well below the metal's melting temperature (Lieberwirth et al., 2017). Post processing stages are required to remove the binder from the printed part and then fusing the metal powder together using a sintering process in a high temperature furnace to produce the final part (Nurhudan et al., 2021).

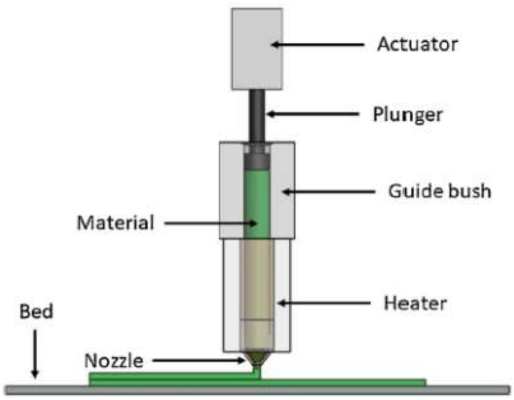

Figure 2.32: Material extrusion additive manufacturing (Nurhudan et al., 2021)

A propriety process that uses the Metal Extrusion technique is Bound Metal Deposition (BMD) by Desktop Metal. BMD is a three-stage process on the Desktop Metal Studio System, shown in Figure 2.33 below. The part is firstly printed by extruding the material layer by layer from the extrusion nozzle. Once the part is printed, the polymer binder is removed from the printed part by immersing the part in the de-bind fluid. The final stage is to sinter the part in the furnace at temperatures approaching the melting point of the metal, allowing the metal powder to fuse together to form the finished part. The metals currently available are 316L stainless steel, 17-4PH stainless steel, H13 tool steel, 4140 chromoly steel, titanium, and copper (DM Materials, 2020).

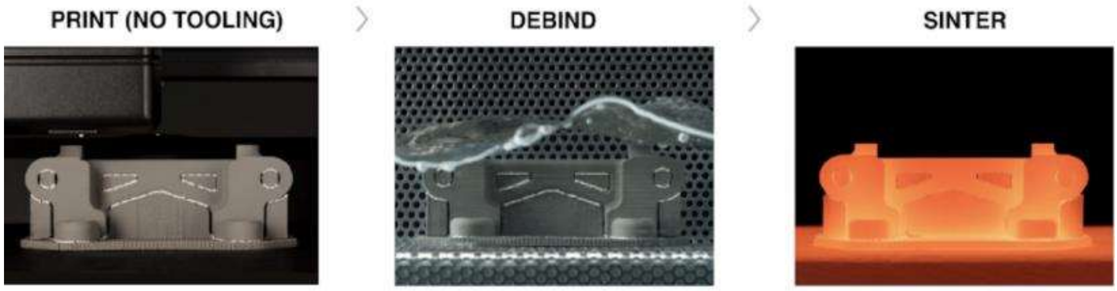

Figure 2.33: Bound metal deposition process (DM Knowledge Base, 2020)

BMD parts are sintered under inert gas atmosphere (Argon with 2.5% Hydrogen). The part shrinks during the sintering process as the metal binds together. Scaling factors are applied by the printing software during the setup stage, and are between 17% and 25%, depending on the print material (DM Design Guide, 2020). The density of sintered parts is high, although similarly to metal injection moulding, micro-pores are present in the sintered material. The volume of micro pores typically comprises 2-5% of the volume of the solid part (DM Knowledge Base, 2020). In addition to micro-porosity, toolpath macro-porosity is also present in the final part, caused by the round shape of the extrusion nozzle bead and the path of the print head. As a result, some geometries and features may have small voids of material. Figure 2.34 shows the tool path macro-porosity and the micro-porosity from the sintering process.

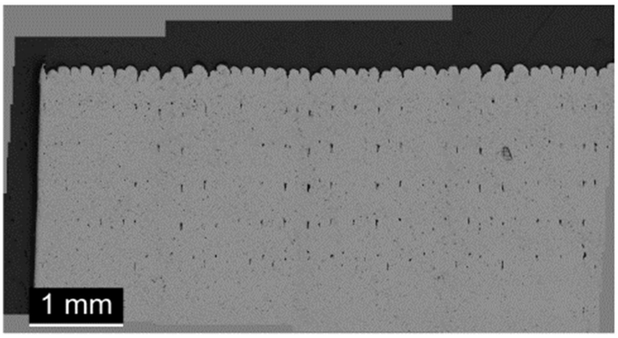

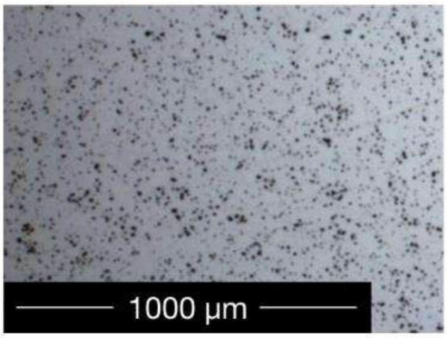

Figure 2.34: Toolpath macro-porosity and sintered micro-porosity (DM Knowledge Base, 2020)

2.7.3 Additive Manufacture and Structural Strength

Additive manufactured structures are primarily gaining attention for improving mechanical performance and weight optimisation (Soro et al., 2018), (Podrousek et al., 2019). Additive offers lightweight lattice structures, which can be optimised for structural strength. For example, bone-like porous 3D patterns have been investigated, shown in Figure 2.35, to provide lightweight and strong internal structures (Wu et al., 2017). The key advantage of additive manufacturing is that is allows optimised lightweight structures to be manufactured.

Figure 2.35: Bone-like optimised infill (Wu et al., 2017)

Another example of additive manufacturing structures investigated for mechanical strength are the sheet-based TPMS additive structures. The TPMS structures, shown in Figure 2.36 below, include the Diamond, Gyroid and Primitive, which are mathematical repeating truss geometries with ultralow density (Han et al., 2017). Recent studies on TPMS structures showed that they offer improved mechanical properties compared to other structures (Alketan et al., 2019).

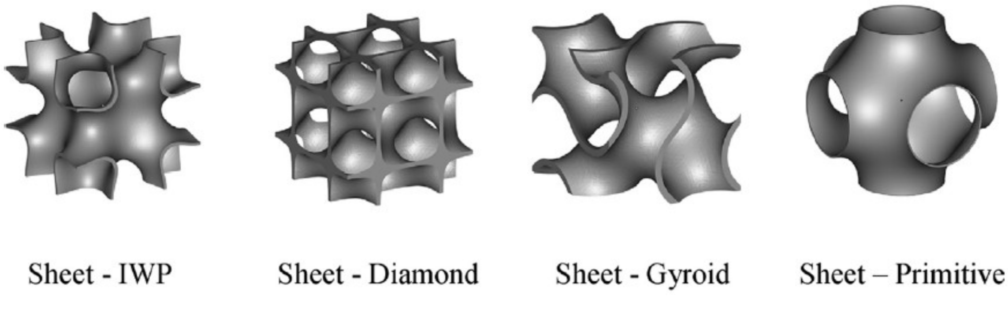

Figure 2.36: TPMS sheet-based cellular structures (Alketan et al., 2018)

This section provided a very brief review of additive manufacturing and structural strength to highlight the benefit of additive structures. However, this research is primarily focused on additive structures for PCM heat transfer enhancement, which is reviewed in the next section.

2.7.4 Additive Manufacture and PCM Heat Transfer

Additive manufacturing is attractive for PCM heat transfer research, since the manufacturing method offers heat transfer enhancement structures, which can be optimised not previously possible with traditional manufacturing. As shown in the CubeSat PCM heat sink review, the Roccor thermal management panel demonstrated the possibilities of using additive manufacturing to contain PCM. The panel was additively manufactured using aluminium selective laser sintering, and investigated paraffin PCM thermal enhancement with pin fins, as shown in Figure 2.37 below (Isaacs et al., 2017). Although, further additive geometries were not investigated to increase the heat exchange area and improve the thermal performance.

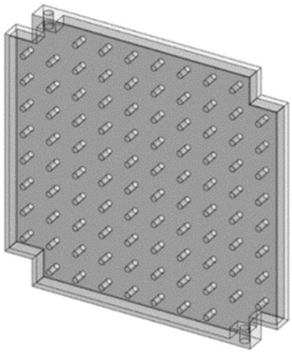

Figure 2.37: Roccor thermal panel (Isaacs et al., 2017)

Recent research conducted for metal additive manufactured PCM heat sinks is shown in Figure 2.38 below. The geometries investigated were the body centered cubic truss structures at various base sizes, at constant PCM volume fraction. These heat sinks were manufactured with the SLS additive manufacturing method. Three different base sizes were considered, namely 10, 20, and 40 mm. The smallest base size of 10 mm had a struct diameter of 1 mm. The key outcome was that smallest base size of 10 mm provided improved thermal performance and more homogenous melting (Righetti et al., 2020). The Authors concluded that smaller base sizes could lead to better results, although noted a 1 mm struct pin diameter limitation with SLS (Righetti et al., 2020).

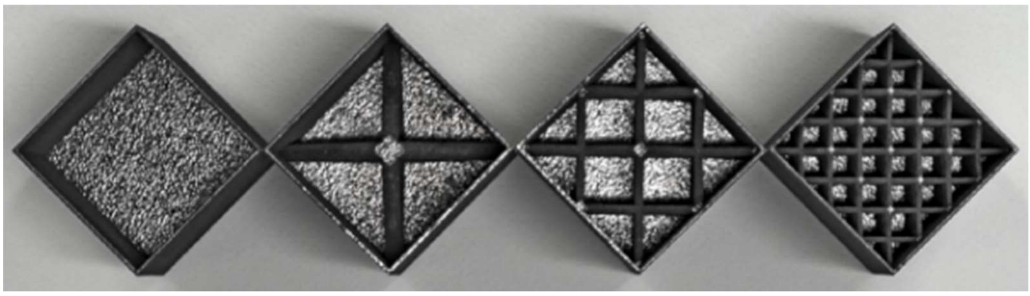

Figure 2.38: 3D metal printed PCM heat sinks (Righetti et al., 2020)

Further recent research conducted for metal additive manufactured PCM heat sinks is shown in Figure 2.39 below. The geometries were optimised using density-based topology to improve heat flow and heat distribution (Nafis et al., 2020). The designs featured 30% metal with respect to 70% PCM. The heat sinks were also manufactured using the aluminium SLS additive manufacturing method. The key outcome was that the topology optimised designs improved PCM performance in comparison with the traditional fin designs (Iradukunda et al., 2020). Although, the Authors also noted a 1 mm minimum fin thickness limitation imposed on the density topology optimisation model, to facilitate manufacturing with the SLS additive method (Iradukunda et al., 2020).

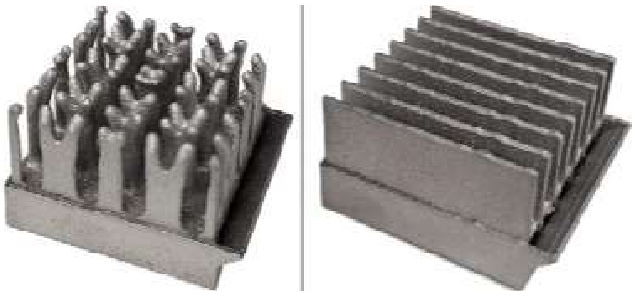

Figure 2.39: Topology optimisation and traditional fin design (Iradukunda et al., 2020)

Another study performed on additive manufactured period structures conceptually analysed the cubic periodic structure, as shown in Figure 2.40. The study numerically investigated the effect of various enhancement materials and pore sizes on the thermal performance with PCMs. The numerical results indicated that for high thermal conductivity materials, such as copper and aluminium, decreasing the pore size improved melting of the PCM. However, for relatively low thermal conductivity materials, such as stainless steel, decreasing the pore size did not have as great as an effect on PCM melting, and instead natural convection in the PCM melting was more important (Zhao et al., 2021).

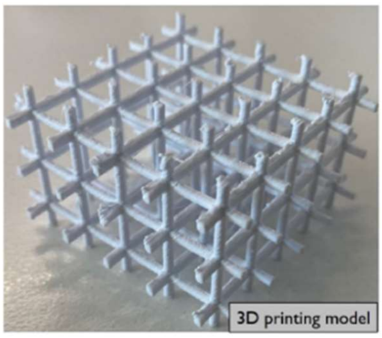

Figure 2.40: Periodic structure for PCM heat transfer enhancement (Zhao et al., 2021)

As seen by the literature review for PCM heat transfer enhancement with additive structures, there has been very limited research on the optimal additively manufacturing structures for PCM heat transfer. Therefore, there is scope for further investigation as presented in the following research gap.

2.8 RESEARCH GAP

PCM heat sinks for CubeSat applications have been predominately studied with paraffin PCMs, due to paraffin's high thermal capacity per unit weight and ideal melting points. However, paraffin PCMs suffer from inherently low thermal conductivity. For CubeSat applications, efforts have been made to improve heat transfer with paraffin PCM using metal fins (Chen et al., 2016), honeycomb structures (Choi et al., 2018) and carbon fibre encapsulation (Yamanda et al.,2014). Although, the studies pertained predominantly to low power applications of less than 10-20 W. With trends for higher power CubeSat applications (Janzer et al., 2018), (Young et al., 2019), (Hengeveld et al., 2019), this research aims to investigate the use of paraffin PCMs for higher power electronics.

To provide thermal management for high power electronics, heat transfer enhancement techniques are required to overcome the inherently low thermal conductivity of paraffin PCMs. Additive manufacturing offers a rethink of current design strategy for enhancing PCM heat transfer and allows new innovative geometries to extend the heat exchange area that would have otherwise been difficult to achieve with traditional manufacturing methods (Becedas et al., 2018). Additive also allows open cell structures to be manufactured which can be easily filled with PCM within an enclosed container, which can also provide strength for PCM containment (Alketan et al., 2019). Additive manufacturing provides a unique opportunity to combine the advantages of heat transfer performance, mechanical strength, and lightweight structures for PCM containment.

However, there has been very limited research on the optimal additively manufacturing structures for PCM heat transfer and also limited research on whether additively manufactured metal parts can provide leakproof containment for PCMs. Accordingly, the focus of this research are additive manufactured structures, which can provide effective PCM heat transfer, as well as being able to provide lightweight leakproof PCM containment for space applications. Of interest in this study is the use of metal additive manufacturing, due to the high thermal conductivity and strength of metals.

Bound Metal Deposition (BMD) is proposed for this investigation since copper material has been recently released for high thermal conductivity heat dissipation. However, it is unknown which additive structures are possible with the BMD extrusion and sintering processes. Moreover, the thermal performance of BMD printed parts has not been investigated and the mechanical properties of BMD printed parts to contain PCMs in a vacuum environment has also not been investigated. It is unknown whether BMD printed parts can provide leakproof containment for PCMs and whether they can withstand the PCM volume change during PCM melting and freezing cycles. With this research, new knowledge will be created regarding the optimal additive structures for PCM heat transfer and the suitability of BMD as an additive manufacturing method for enhancing PCM heat transfer and containing PCMs for space applications.

3. Numerical Investigation of Additive TCE Structures for CubeSat PCM Heat Sinks

3.1 INTRODUCTION

This Chapter investigates the optimal additive geometries to enhance PCM heat transfer using numerical modelling, for the purposes of cooling CubeSat electronics (Research Objective 1). To enhance PCM heat transfer for electronics cooling, Thermal Conductivity Enhancement (TCE) structures are required. Additive manufacturing geometries offer new innovative structures to extend the heat exchange area with PCMs that would have otherwise been difficult to achieve with traditional manufacturing.

Additive geometries, shown in Figure 3.1 below, can generally be categorised as strut-based structures, where lattices are created by truss segments, and sheet-based TPMS structures, where structures are created from organic Triply Periodic Minimal Surfaces (TPMS).

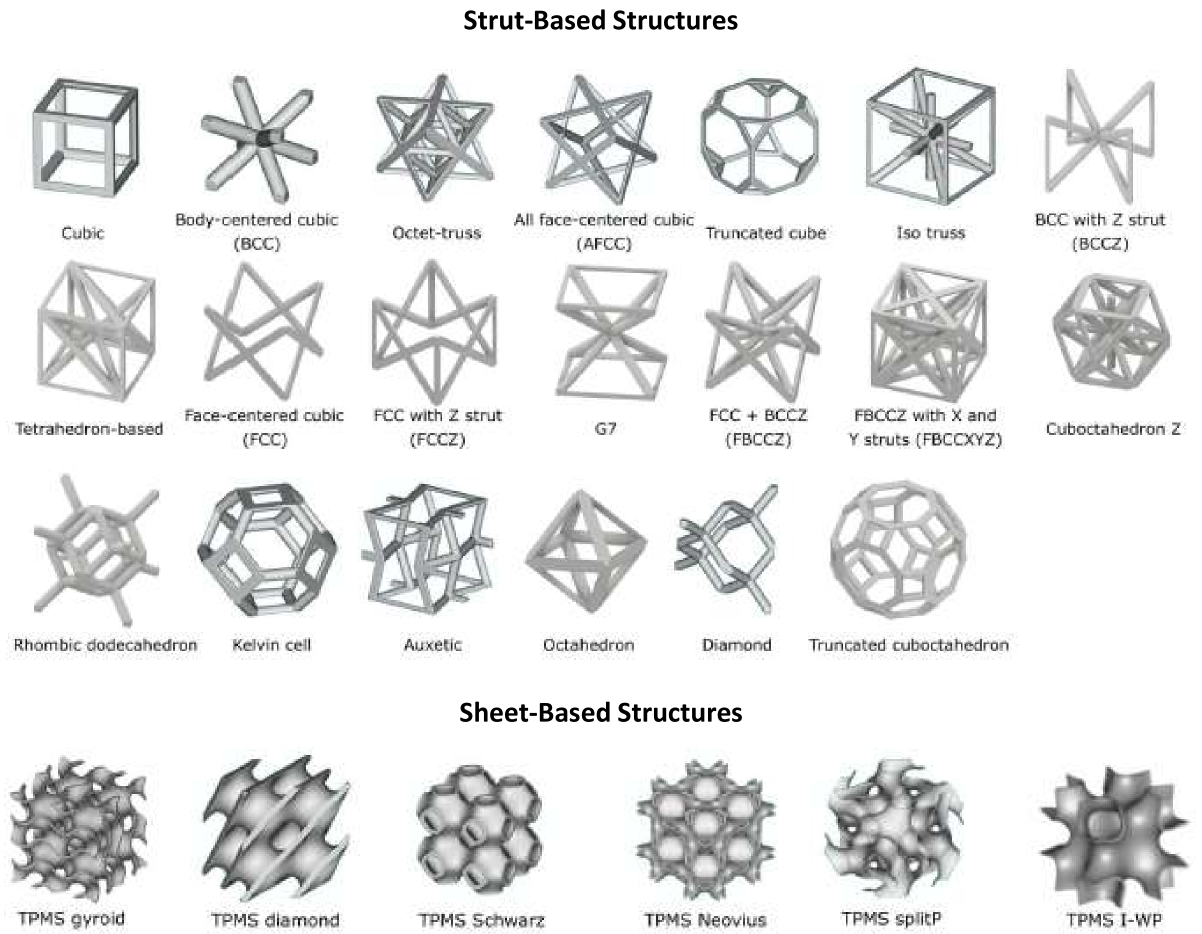

Figure 3.1: Strut-based and TPMS sheet-based additive structures (Benedetti et al., 2021)

The research questions to be answered in this chapter were the following:

What are the optimal additive TCE structures to enhance PCM heat transfer and can the low thermal conductivity of paraffin PCMs be overcome with additive TCE structures to adequately cool CubeSat high-power electronics?

For this analysis, the traditional fin structure for PCM heat transfer was compared to one **strut-based** additive structure and one **sheet-based** TPMS additive structure. The selected structures for this comparison were the body centred cubic truss (strut-based) and the TPMS gyroid (sheet-based). The unit cells for the selected structures are shown in Figure 3.2 below. To the Author's knowledge, PCM heat transfer has yet to be investigated with TPMS structures, such as the gyroid.

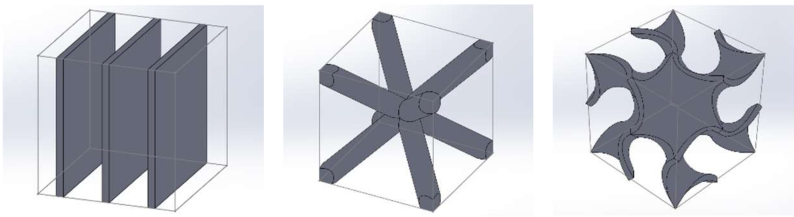

Figure 3.2: Fins, truss and gyroid structures

The selected structures were compared for a conceptual 50 W heat sink design, with two electronic cooling configurations. Firstly, dissipating heat directly from the heat source, and secondly, dissipating heat transferred from a heat pipe. For the two configurations, the heat transfer performance of the selected structures was compared, and the effect of base size/surface area was also investigated.

Thermal numerical modelling was performed using the solidification/melting model in ANSYS Fluent. Initially, a sensitivity analysis on the effects of mesh size, time step and convergence was performed to establish model independence. In addition, a model validation was performed on experimental testing performed by the University of Padua, which investigated the body centered cubic truss 3D structure (Righetti et al., 2020).

3.2 CONCEPTUAL PCM HEAT SINK DESIGN

To investigate the heat transfer performance of the selected TCE structures, a conceptual PCM heat sink was designed. The design parameters included the following:

- Heat load dissipation
- Heat sink materials
- Heat sink size

- Electronic cooling configurations
- TCE internal dimensions

The conceptual PCM heat sink design in this section formed the basis of the numerical modelling in this chapter to investigate and compare the PCM heat transfer performance of the selected structures.

3.2.1 Heat Load Dissipation

The electronics heat load chosen for this analysis was 50 watts (W). A widely used CubeSat, the 3U CubeSat, has orbital average powers greater than 50 W (National Academy of Sciences, 2016). However, due to heat dissipation issues, the 3U CubeSat is capable of dissipating at best 15 W (Hartsfield et al., 2020).

The heat sink was designed to absorb the 50 W heat load for a period of approx. 5 minutes. A CubeSat in Low Earth Orbit has less than 8 minutes line of sight over a particular region (Hartsfield et al., 2020). Providing heat dissipation for a few minutes enables the use of higher power electronics during the short windows available, such as higher power communications with ground stations.

To absorb the 50 W heat load for 5 minutes, a thermal energy storage capacity of 15 kJ was required. Noting, the electronics and CubeSat radiator would also provide minimal thermal capacity and heat rejection, however, to simplify the analysis, the PCM heat sink storage was viewed in insolation.

The heat sink was designed to operate from an initial temperature of 15°C to a limit of 50°C. The temperature limit represents the maximum allowable operating temperature for CubeSat electronics (such as for communications, refer to Table 3.1), and the initial temperature for the PCM heat sink was midway between the allowable temperature range.

Table 3.1: CubeSat allowable temperatures. Adapted from (Choi et al., 2019)

Spacecraft Subsystem	Allowable Operating Temperature (°C)
Command and Data Handling	-24 to +61
Electrical Power – System	-40 to +85
Electrical Power – Batteries	0 to +40
Attitude Control System – Star Tracker	+10 to +30
Communications	-20 to +50
Propulsion	-20 to +70

3.2.2 Heat Sink Materials

The phase change material selected for this analysis was paraffin octadecane ($C_{18}H_{38}$), due to its ideal melting point (~28°C) for maintaining electronics below 50°C and high latent heat of fusion per unit weight (~244 kJ/kg) for lightweight space applications (Collette et al., 2011). The thermophysical properties of paraffin octadecane are provided in Table 3.2.

Table 3.2: Properties of octadecane near melting point (Velez et al., 2015)

Thermal Cond. W/m·K	Density kg/m^3	Specific Heat J/kg·K	Latent Heat J/kg	Melt Range °C
0.3 (solid) 0.15 (liquid)	865 (solid) 776 (liquid)	2,240	243,680	25.52 - 29.20

To overcome the low thermal conductivity of octadecane, the metals selected for the TCE structures were copper and aluminium, due to their high thermal conductivity. Metal properties vary depending on manufacturing process. However, for the purposes of this comparative analysis, high conductivity copper alloy and aluminium 6063 alloy were utilized, with the material properties listed in Table 3.3.

Table 3.3: Copper 110 HC (Conex, 2020) and Aluminium 6063 (Atlas Steels, 2013)

	Thermal Cond. W/m·K	Density kg/m^3	Specific Heat J/kg·K
Copper	391	8940	385
Aluminium	209	2700	900

The main disadvantage of TCE structures is that they reduce the volume available for the storage PCM and increase the weight of PCM systems. The volume ratio of PCM to Metal TCE is known as the PCM volume fraction (Φ), calculated by Equation 3.1 below, where V_V is the void volume and V_T is the total volume. For this analysis, the volume ratio of PCM to Metal TCE chosen was 85%. Noting, PCM volume fractions vary in literature from 70% (Iradukunda et al., 2020) to 95% (Righetti et al., 2020).

$$\Phi = \frac{V_V}{V_T} \qquad \text{Equation 3.1}$$

For this analysis, the 85% PCM volume fraction was selected for the internal volume of the heat sink and did not include the metal case. The metal case reduced the overall PCM volume fraction, however the reduction was dependent on the size of the PCM heat sink and case thickness.

3.2.3 PCM Heat Sink Size

The heat sink size selected for this investigation was 60x60x20 mm, with a case thickness of 1 mm. The selected PCM heat sink size (60x60 mm footprint, 20 mm height) relative to a 3U CubeSat structure is shown in Figure 3.3 below. Noting, the CubeSat footprint (100x100 mm) allowed for a wider and shorter heat sink, however, reducing the height and increasing the footprint ultimately created a heat sink. For example, halving the height to 10 mm, required a footprint size of 89x89 mm for the same internal capacity, which resulted in 63% more metal case compared to the 20 mm height.

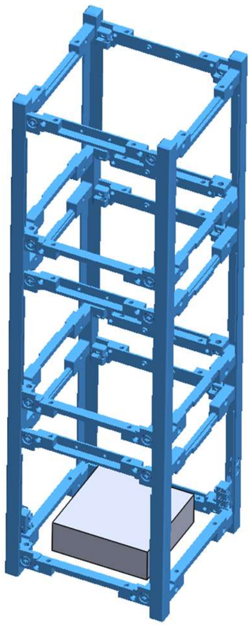

Figure 3.3: PCM heat sink within 3U CubeSat frame

The weight and thermal energy storage (TES) breakdown of the selected PCM heat sink size is provided in Table 3.4 below. Values are provided for both copper and aluminium, with octadecane PCM. The bulk TES capacity is provided by the PCM, whilst the remainder is provided by the metal sensible heat. Aluminium provides slightly less energy storage compared to copper, however, is substantially lighter. The total TES over the temperature range is 15.4 kJ for the copper PCM heat sink and 14.7 kJ for the aluminium PCM heat sink (Target was 15 kJ).

Table 3.4: Weight and energy storage breakdown of the PCM heat sink (ΔT 15-50°C)

*Internal volume of PCM heat sink 58x58x18 mm (60.5 ml)

	Description	Weight (g)	TES (kJ)
PCM	85% of Internal Vol.*	40 [octadecane]	12.9 [octadecane]
Metal TCE	15% of Internal Vol.*	81 [copper], 24 [aluminium]	1.1 [copper], 0.8 [aluminium]
Metal Case	1 mm Thickness Case	102 [copper], 31 [aluminium]	1.4 [copper], 1.0 [aluminium]

3.2.4 Electronic Cooling Configurations

Two electronic cooling configurations were investigated. Firstly, dissipating heat directly from the heat source (Direct Cooling), and secondly, dissipating heat transferred from a heat pipe (Heat Pipe Cooling). Noting, a heat pipe is beneficial when there is limited room around the electronics for a PCM heat sink.

For the direct cooling analysis, a 30x30 mm heat input size was considered. The heat input size represents the dimensions of the electronics' Integrated Heat Spreader (IHS), which facilitate heat transfer to the heat sink (Elliott et al., 2022). The heat input was centred at the base of the PCM heat sink, as shown in Figure 3.4 below (heat input area highlighted in green).

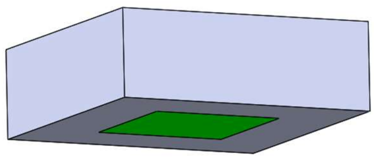

Figure 3.4: Direct cooling configuration

For the heat pipe cooling analysis, a 6 mm diameter heat pipe with a 30 mm evaporator/condenser length was chosen, capable of transferring 50 W (ACT, 2021). The heat pipe had side entry into the heat sink to cater for the 30 mm condenser, as shown in Figure 3.5. Noting, the weight of the case was slightly increased, and the TES capacity was slightly reduced due to the inner tube for the heat pipe (1 g less octadecane PCM).

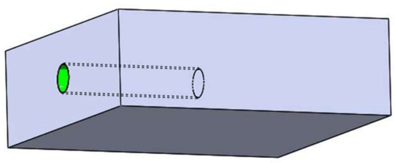

Figure 3.5: Heat pipe cooling configuration

For the two configurations, the weights and TES capacities are provided in Table 3.5 below. The TES capacity is expressed in kilojoules (kJ), but also in the amount of time that the PCM heat sink can absorb the applied heat load of 50 W (i.e. the maximum cooling time available).

The role of the TCE internal metal structures is to ensure that the PCM heat sink utilises the majority of its TES capacity before reaching the 50°C temperature limit. Due to the low thermal conductivity of paraffin octadecane PCM, over 90% TES utilisation was considered effective.

Table 3.5: Weight and TES capacity of the PCM heat sinks (ΔT 15-50°C)

*For an applied heat load of 50 W

	Copper PCM Heat Sink		**Aluminium PCM heat Sink**	
	Total Weight	TES Capacity	Total Weight	TES Capacity
Direct Cooling Configuration	223 g	15.4 kJ **5.1 min***	95 g	14.6 kJ **4.9 min***
Heat Pipe Cooling Configuration	226 g	15.1 kJ **5.0 min***	96 g	14.3 kJ **4.8 min***

3.2.5 TCE Dimensions

The TCE structures investigated were fins, truss and gyroid. The unit cells are shown and described in Figure 3.6 below. The truss represented the strut-based additive structures and the gyroid represented the sheet-based additive structures.

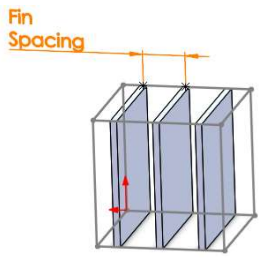

- Fins are characterised by their wall thickness and spacing between the fins.

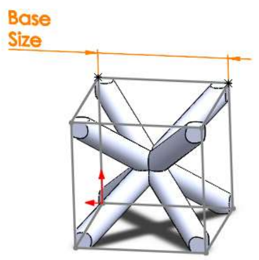

- The body centred cubic truss is characterised by its radial struct thickness and cube base size.

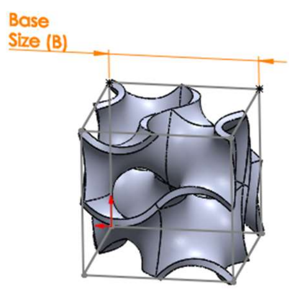

- The gyroid is characterised by its wall thickness and base element (B), with mathematical formula provided by Equation 3.2 (Alketan et al, 2019). Note, the gyroid channel size is half the base element (i.e. ½B).

$$\cos\left(\frac{2\pi x}{B}\right)\sin\left(\frac{2\pi y}{B}\right)+\cos\left(\frac{2\pi y}{B}\right)\sin\left(\frac{2\pi z}{B}\right)+\cos\left(\frac{2\pi z}{B}\right)\sin\left(\frac{2\pi x}{B}\right)=0 \qquad \text{Equation 3.2}$$

Figure 3.6: Units cells for fins, truss and gyroid

The TCE dimensions were created based on the typical feature sizes possible with metal additive manufacturing, for methods such as metal extrusion and powder bed fusion. For powder bed fusion, the feature size is limited by the laser spot size and for metal extrusion, the feature size is limited by the nozzle extrusion diameter.

Feature sizes for additive manufacturing are typically specified by the minimum wall thickness and allowable pin diameter, as shown in Figure 3.7 below. Generally, for powder bed fusion the minimum wall thickness is 0.3-0.4 mm and a minimum reliable struct pin diameter is 1 mm (EOS, 2021). For metal extrusion, the wall thickness and pin radial thickness are given by the nozzle diameter, which are between 0.25-0.4 mm (Desktop Metal, 2020). Noting, a circular extrusion, two nozzle diameters thick, is required for a cylindrical strut.

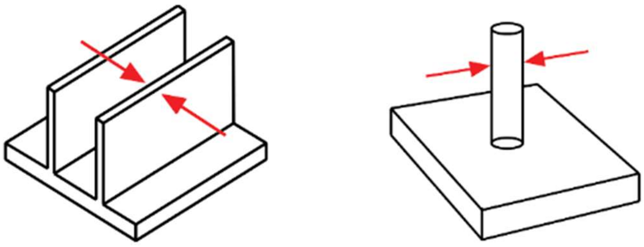

Figure 3.7: General feature dimensions of metal additive manufacturing (Petrak et al., 2022)

For this analysis, a 0.4 mm wall thickness was used for the fins and gyroid and a 0.4 mm radial thickness was used for the truss (i.e. 0.8 mm diameter struct). Although, wall and radial thicknesses of 0.3 and 0.5 mm were also investigated in the base size analysis.

Table 3.6 provides the TCE dimensions created for a wall and radial thickness of 0.4 mm (Noting, the 85% PCM volume fraction was achieved within a 0.5% tolerance). Figure 3.8 illustrates the 0.4 mm TCE structures for the direct cooling and heat pipe cooling configurations.

Table 3.6: Fins, truss and gyroid TCE dimensions – 0.4 mm thickness

	TCE Thickness	**TCE Dimensions**
Fins	Wall thickness 0.4 mm	Fin Spacing 2.55 mm
Gyroid	Wall thickness 0.4 mm	Gyroid Channel Size 4.0 mm
Truss	Radial thickness 0.4 mm	Truss Cube Size 4.5 mm

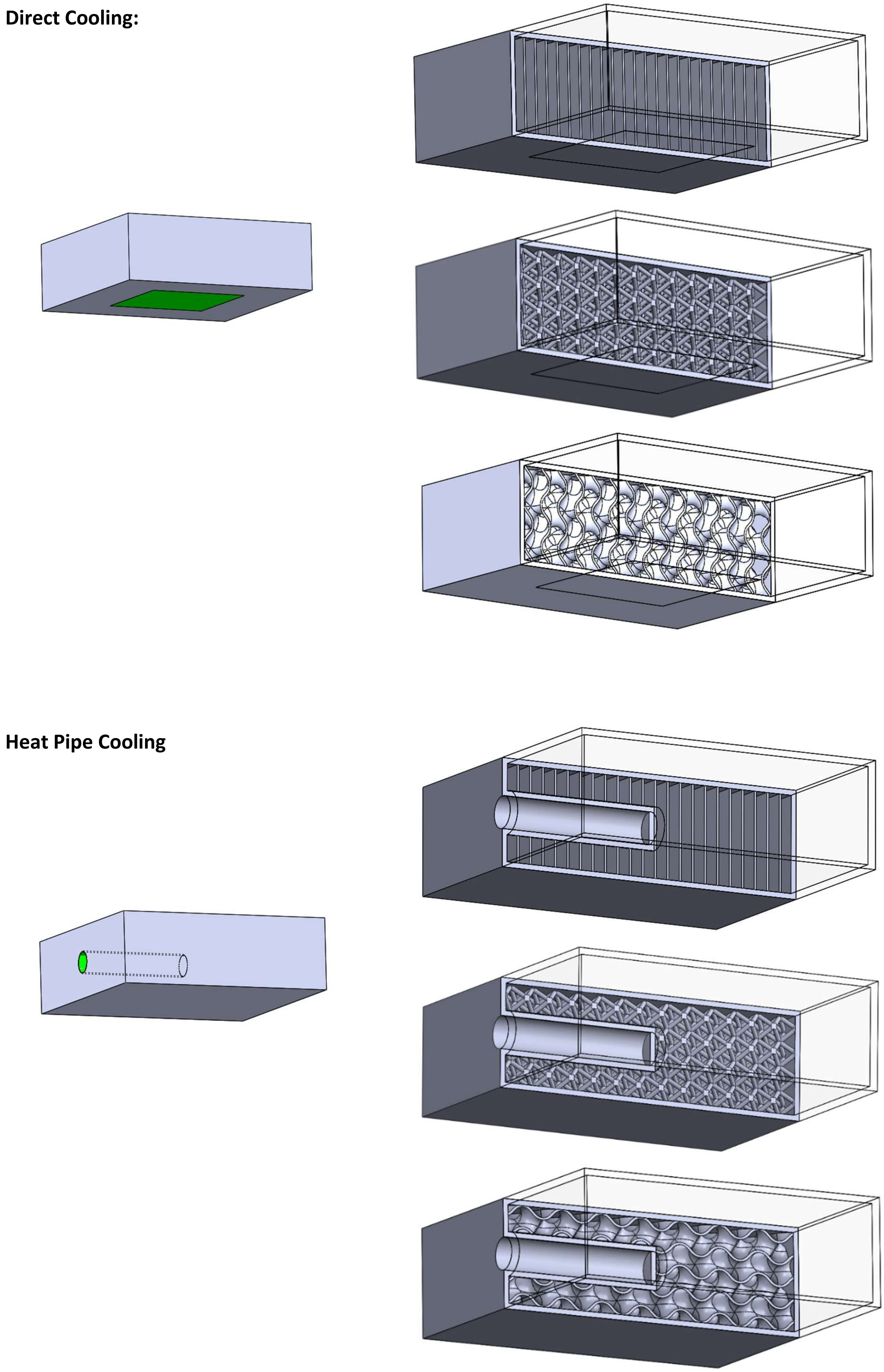

Figure 3.8: Electronic cooling configurations, 0.4mm internal TCE structures

3.3 NUMERICAL METHODOLOGY

ANSYS Fluent numerical methodology was utilised to investigate the heat transfer performance of the selected TCE structures. ANSYS Fluent was selected, since it contains a suitable model to simulate the melting and solidification of PCMs, namely the solidification/melting model. The following describes the ANSYS Fluent numerical model adopted, and the sensitivity analysis conducted to establish model independence.

3.3.1 ANSYS Fluent Solidification/Melting Model

ANSYS Fluent uses a control-volume-based technique that involves dividing the domain into discrete cells using a computational grid, known as the mesh, and then applying the governing equations of mass, momentum and energy (ANSYS Theory Guide, 2021). The solidification/melting model uses an enthalpy porosity method, where the phase change is represented as a liquid fraction in each cell of the fixed grid from solid to liquid. (ANSYS Theory Guide, 2021). The limitation of this fixed grid method was that the model could not simulate the volume change of the PCM during melting and solidification (ANSYS Theory Guide, 2021). However, the purpose of the model was a thermal analysis and not a structural analysis, thus the volume change was not of interest.

3.3.1.1 Modelling Assumptions

The following assumptions were made with the ANSYS Fluent numerical simulation:

1. The PCM density and PCM volume were assumed constant. Due to the fixed grid enthalpy porosity method of the solidification/melting model, the PCM volume change was not modelled and the PCM density was assumed constant. For this analysis, the liquid density was used to represent the amount of PCM in the system encompassing the entire void volume.
2. The PCM flow was assumed to have zero velocity. For CubeSat applications, the effect of gravity is negligible and therefore buoyancy convective heating is not applicable. In microgravity, the motion of the PCM liquid is caused by surface tension forces, known as the Marangoni Effect (Hale et al., 1971), although, this motion was not modelled for this analysis.
3. The heat absorption stage of the PCM heat sink was investigated without thermal radiation to space. This represented the hot case, in which the maximum electronics heat load is experienced combined with the highest values of incoming solar radiation, thus limiting heat rejection capability.

4. The electronics and CubeSat radiator were not modelled for this analysis. Noting, the electronics and CubeSat radiator would also provide minimal thermal energy storage capacity via sensible heat, however, for the purposes of this analysis only the PCM heat sink was modelled to compare the performance of the TCE structures.

3.3.1.2 Governing Equations

For this analysis, only the conservation of energy was solved, since a zero-velocity PCM field was assumed. Accordingly, the conservation of mass and momentum equations were not applicable. The conservation of energy equation for the solidification/melting model with a zero-velocity flow field is given by Equation 3.3 below, where ρ is the density, k is the thermal conductivity, T is the temperature, S is the energy creation source term and H is the enthalpy (ANSYS Theory Guide, 2021).

$$\frac{\partial}{\partial t}(\rho H) = \nabla(k\nabla \mathrm{T}) + S \qquad \text{Equation 3.3}$$

The enthalpy of the material (H) is calculated by Equation 3.4 below, where h is the sensible enthalpy and ΔH is the latent heat enthalpy (ANSYS Theory Guide, 2021).

$$H = h + \Delta H \qquad \text{Equation 3.4}$$

The sensible enthalpy (h) is calculated by Equation 3.5 below, where c_p the specific heat, h_{ref} is the reference enthalpy and T_{ref} is the reference temperature (ANSYS Theory Guide, 2021).

$$h = h_{ref} + \int_{T_{ref}}^{T} c_p dT \qquad \text{Equation 3.5}$$

The latent heat enthalpy (ΔH) is calculated by Equation 3.6 below, where λ is the liquid fraction and L is the latent heat of the material (ANSYS Theory Guide, 2021).

$$\Delta H = \lambda L \qquad \text{Equation 3.6}$$

The liquid fraction (λ) is given by Equation 3.7 below, where T_{solid} is the solidus temperature and T_{liquid} is the liquidus temperature (ANSYS Theory Guide, 2021).

$$\begin{aligned} \lambda &= 0 && if \quad T < T_{solid} \\ \lambda &= 1 && if \quad T > T_{liquid} \\ \lambda &= \frac{T - T_{solid}}{T_{liquid} - T_{solid}} && if \quad T_{solid} < T < T_{liquid} \end{aligned} \qquad \text{Equation 3.7}$$

Noting, the liquid fraction is 0 when the PCM is a solid, 1 when the PCM is a liquid, and between 0 to 1 in the melting zone, known as the mushy zone (ANSYS Theory Guide, 2021).

3.3.1.3 Numerical Scheme

The coupled solver was utilized for the solidification/melting model. Although, with the flow equations turned off, the solution for temperature was essentially an iteration between the energy equation (Equation 3.3) and the liquid fraction equation (Equation 3.7) (ANSYS Theory Guide, 2021). The iterations were monitored using the energy residual to ensure convergence. To aid convergence, under-relaxation factors (α) were used to control the change of a given variable (∅), as described by Equation 3.8 (ANSYS Theory Guide, 2021). For this analysis, the under-relaxation factor for the energy equation was set to 1 and the under-relaxation factor for the liquid fraction update was set to 0.8.

$$\emptyset_{new} = \emptyset_{old} + \alpha\,\Delta\emptyset \qquad \text{Equation 3.8}$$

Discretisation schemes are utilised in ANSYS Fluent to set up the energy equation for the solver. The temporal term, $\partial/\partial t(\rho H)$, was discretised with a second-order fully implicit scheme and bounded to provide better stability (Silva et al., 2020). The diffusion term, $\nabla(k\nabla T)$, was discretised with a central-differencing scheme and was second-order accurate (ANSYS Theory Guide, 2021). To iterate the temperature gradient (∇T) between the cells for the diffusion term, the Least Squares Cell Based approach was implemented

3.3.1.4 Model Domain and Material Properties

The PCM heat sinks were modelled with quarter symmetry to reduce computational effort, as shown in Figure 3.9. Noting gyroids do not have a symmetry plane, and instead are a repeating structure. Thus, the effect of utilising a symmetry plane for the gyroid was investigated in the sensitivity analysis.

The model featured two distinct volume zones, namely the metal solid zone and the PCM fluid zone. Noting, for the metal solid zone, the latent heat enthalpy did not apply and thus the liquid fraction equation (Equation 3.7) was not applicable. The metal solid zone was modelled with constant values for density, specific heat and thermal conductivity. Refer to Table 3.3 for the copper and aluminium material property values utilised.

The PCM zone was modelled with constant values for density, specific heat, and latent heat. Refer to Table 3.2 for the octadecane material property values utilised. Noting, the liquid phase density was selected to represent the amount of PCM in the system encompassing the entire void volume.

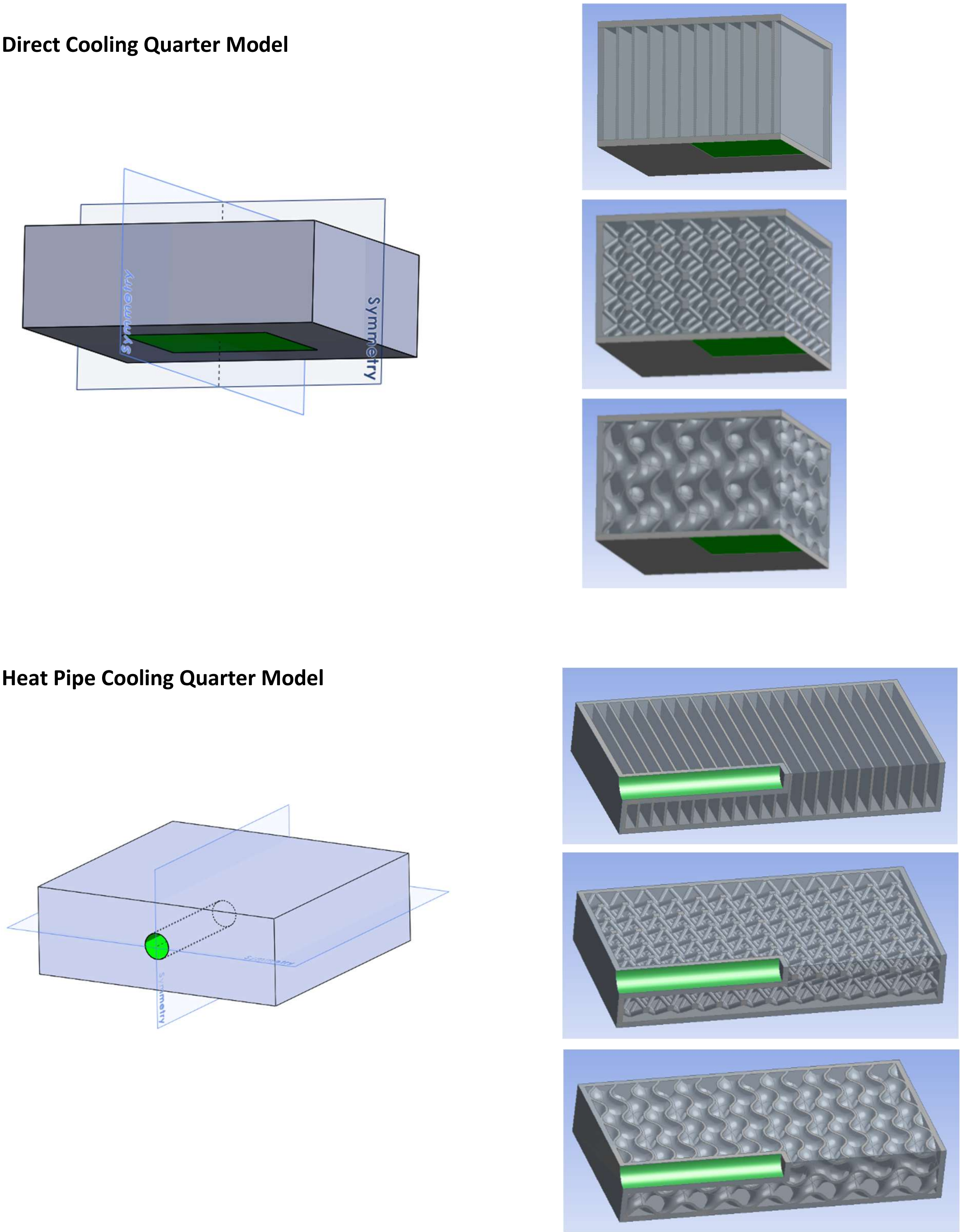

Figure 3.9: Quarter models (Green highlighted area represents the heat input area)

The melting range for the PCM was specified by the solidus temperature (T_{solid}), and the liquidus temperature (T_{liquid}). The lower value of the melting range was specified as the liquidus temperature, and the higher value was specified as the liquidus temperature. The thermal conductivity for the PCM was represented as a step function, with the solid thermal conductivity applying below the solidus temperature, the liquid thermal conductivity applying above the liquidus temperature, and in between a linear gradient.

3.3.1.5 Model Boundary Conditions

The thermal boundary condition between the metal zone and the PCM zone was specified as thermal coupled, to allow heat transfer between the two zones. It was assumed that the PCM and metal had direct contact and therefore the boundary did not include thermal resistance. The thermal boundary condition for the heat input was modelled with a constant heat flux distributed over the heat input area. It was assumed that the electronics and heat pipe transferred the full 50W.

The symmetry walls were specified with symmetry conditions. Noting, a symmetry boundary condition assumes a zero normal flux of all quantities across the boundary condition (ANSYS User Guide, 2021). All other external walls were modelled with a zero-heat flux thermal boundary condition (adiabatic wall) providing for no heat loss. The initial temperature of the metal and PCM zones was set to 15°C (the starting temperature of the system). At this initial temperature the PCM zone was solid (liquid fraction equalling zero).

3.3.1.6 Model Mesh

The metal and PCM zones were meshed with tetrahedral volume mesh elements, and then converted to polyhedral mesh using ANSYS Fluent. The polyhedral conversion improved mesh quality and reduced the overall cell count by a factor of 3-5, since a cluster of tetrahedral cells were used to create each polyhedral cell around the original nodes (ANSYS User Guide, 2021). The mesh quality was checked during the meshing process to ensure acceptable mesh values to prevent solver instabilities. The tetrahedral mesh was checked for cell skewness and the polyhedral mesh was checked for orthogonal quality. Cells with values deemed as 'Bad' and 'Unacceptable' were avoided, refer to Figure 3.10 below.

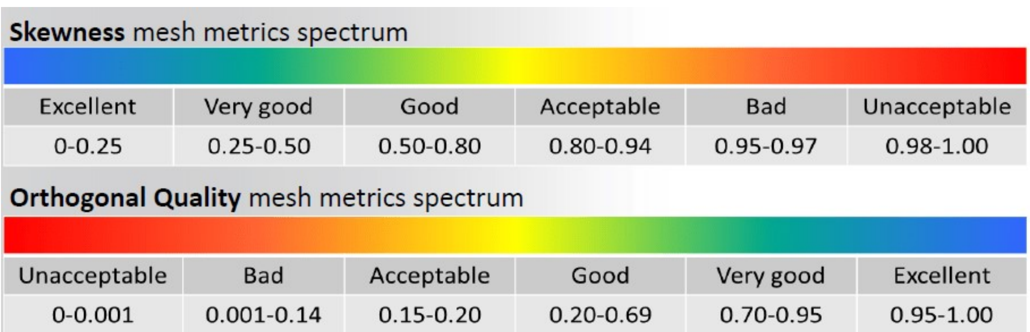

Figure 3.10: Skewness and orthogonal mesh metrics spectrums (Fatchurrohman et al., 2017)

3.3.2 Sensitivity Analysis

To establish model independence, a sensitivity analysis on the effects of mesh size, timestep and convergence criteria was firstly performed. Due to computational limitations of high resolution meshes, a representation section of 20x20x10 mm was investigated for the gyroid, truss and fin structures sensitivity analysis, as shown in Figure 3.11 below.

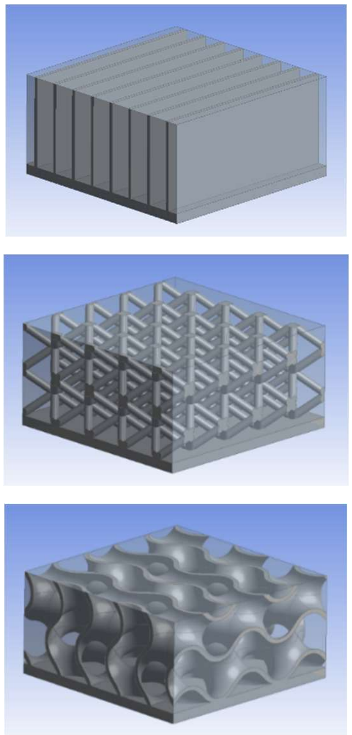

Figure 3.11: Sensitivity analysis – Fins, gyroid and truss 20x20x10 mm representative sections

The base was provided with a heat input of 50 W, assuming an overall footprint of 60x60 mm. The four side walls were specified with symmetry conditions and the top wall was specified with no heat loss. Noting, the effect of utilising a symmetry plane for the gyroid structure was also investigated in this sensitivity analysis.

For the sensitivity analysis, copper was used for the metal zone and octadecane for the PCM zone. For each timestep of the simulation, the heat input junction temperature was recorded, which represented the electronic component temperature of interest.

For the mesh size, timestep and convergence sensitivity analysis, the results for the fins case are presented. However, the same trends were observed with the truss and gyroid, as summarised in Appendix A.

3.3.2.1 Mesh Size Analysis

The mesh sizes investigated were:

- 0.1 mm tetrahedral mesh ('**0.1 mm Tetra**')
- 0.1 mm polyhedral mesh ('**0.1 mm Poly**')
- 0.2 mm polyhedral mesh ('**0.2 mm Poly**')
- 0.1-0.2 mm polyhedral mesh with 20% growth rate ('**0.1-0.2 mm Poly**')

The mesh sizes were investigated with a 0.1 second timestep and 20 iterations per timestep to monitor convergence. Figure 3.12 shows the heat input junction temperature results for the fins case. The results showed a similar temperature profile for all the different mesh sizes, thus demonstrating model mesh independence. Focussing into the PCM melting temperature, the results showed that the temperature response slightly increased with an increased mesh size. However, all temperature profiles were within 0.1°C of each other.

The 0.1 mm mesh was only practicable for this mesh study and required too many cells to be used for any of the heat sink geometries. The 0.1-0.2 mm poly mesh was adopted for this study, since it provided the most versatility for meshing geometries with various thicknesses. However, the 0.2 mm poly mesh was used for the larger volume simulations, where the variable 0.1-0.2 mm mesh could not be used, such as for the Padua validation experiment model and the gyroid symmetry analysis.

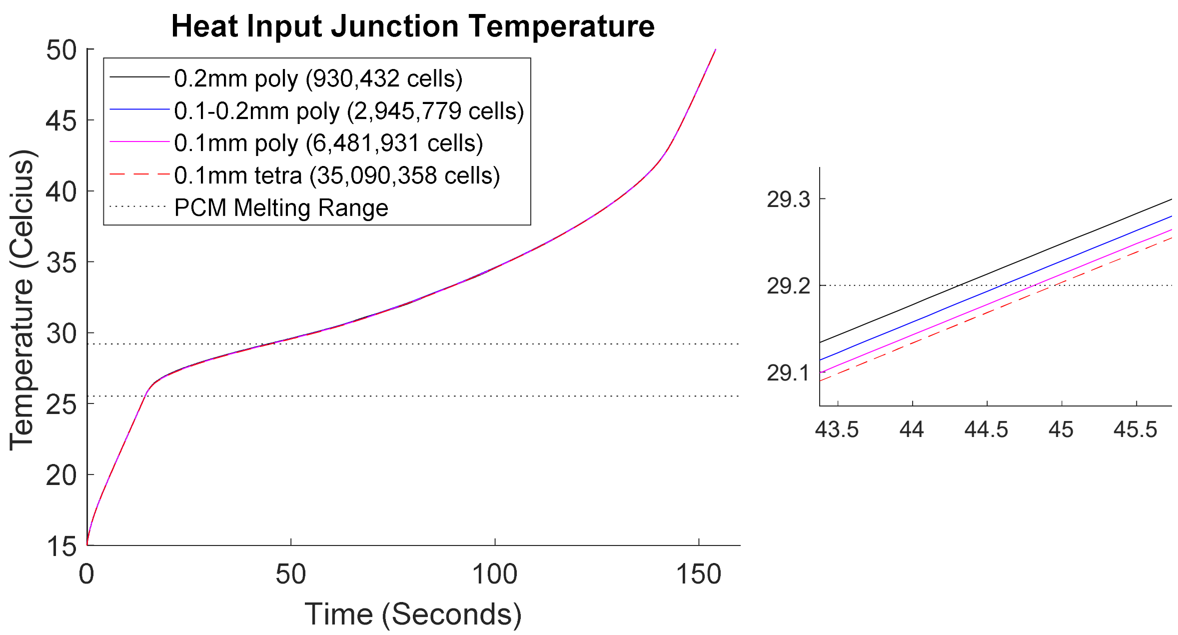

Figure 3.12: Mesh size study – Fins case

3.3.2.2 Timestep Analysis

The 0.1-0.2 mm poly mesh was investigated with timesteps of 0.05, 0.1 and 0.2 seconds. For each timestep, 20 iterations were performed to monitor convergence. Figure 3.13 shows the heat input junction temperature results for the fins case. The results showed a similar temperature profile for each timestep, thus demonstrating model timestep independence. Focussing into the PCM melting temperature, the results showed that the temperature response slightly reduced with an increased timestep. However, the decrease was very minor as all temperature profiles were within 0.01°C. Accordingly, the 0.2 second timestep was used for this study, since it halved the computation time compared to the 0.1 second timestep.

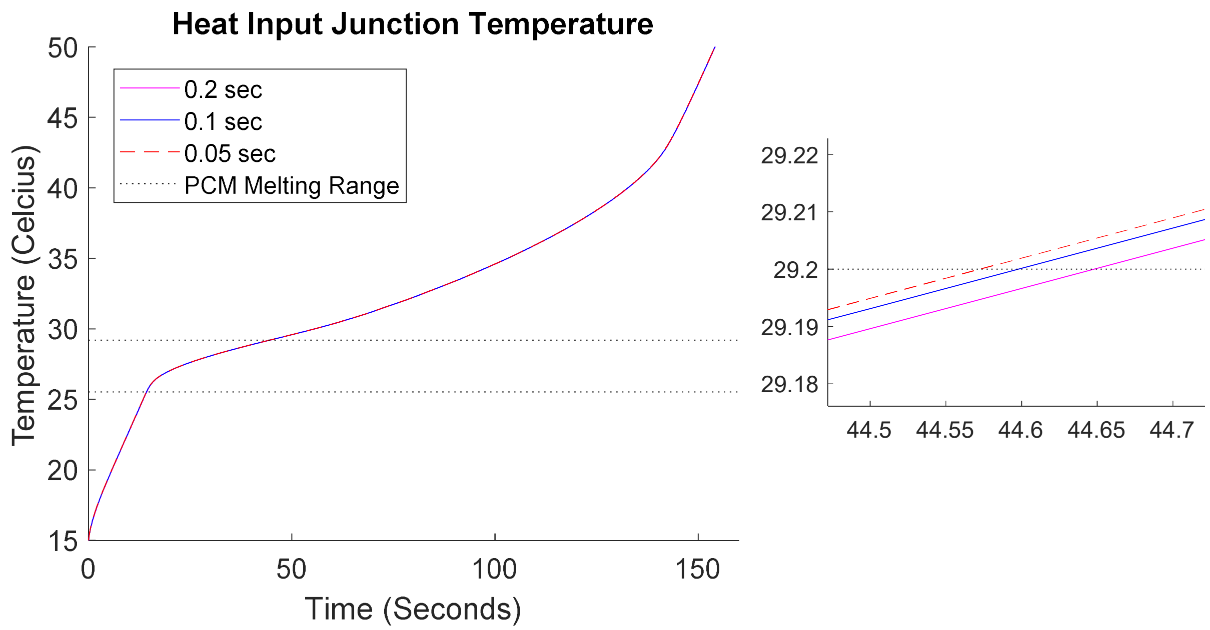

Figure 3.13: Timestep study – Fins case

3.3.2.3 Convergence Analysis

The 0.1-0.2 mm poly mesh was investigated with convergence criteria of 5, 10 and 20 iterations per timestep. The timestep utilised was 0.2 seconds. Figure 3.14 shows the heat input junction temperature results for the fins case. The results for 10 and 20 iterations provided almost identical results. The results for 5 iterations had a slightly reduced temperature profile, however only deviated by a very small temperature fraction (0.001 °C).

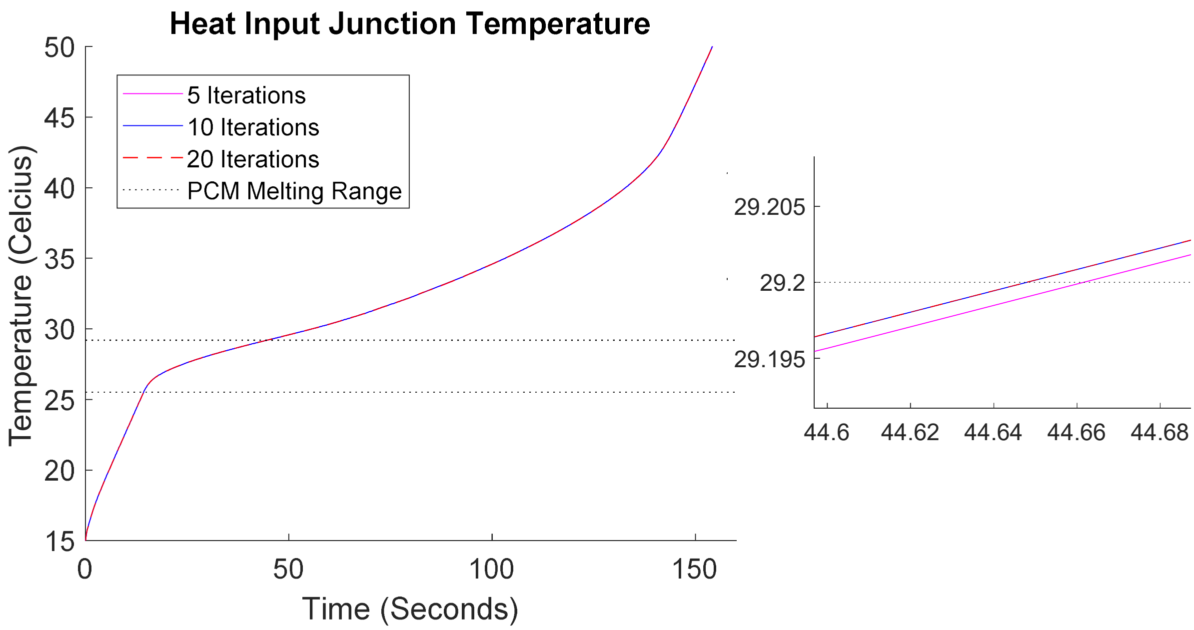

Figure 3.14: Convergence study – Fins case

Figure 3.15 shows the final energy residual at the end of each timestep for the convergence analysis. The results for 20 iterations converged below 10^{-14}, the results for 10 iterations converge under 10^{-12}, and the results for 5 iterations converged below 10^{-8}. For this analysis 10 iterations per timestep was selected to ensure that the results did not have any solver instabilities, and converged below a final energy residual value of 10^{-12}.

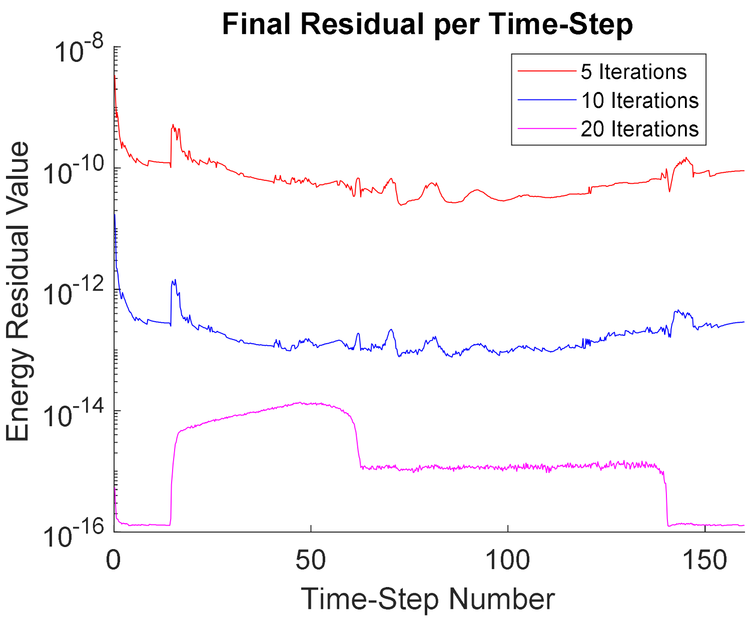

Figure 3.15: Convergence study residuals – Fins case

3.3.2.4 Gyroid Symmetry

The effect of utilising a symmetry plane for the gyroid model was investigated for a heat sink of size of 60x60x10 mm (i.e. half the size of the PCM heat sink size selected for this analysis).

The quarter model of the heat sink was compared to the full model. The heat input was at the base of the heat sink. Figure 3.16 shows the heat input junction temperature results for the quarter model compared to the full model. The results show that the quarter model accurately represents the results of the full model. Focussing in on the 50°C temperature limit, the temperature response of the quarter model was slightly higher than the full model. However, the results were within 0.2°C and the time was 0.5 seconds apart.

The results demonstrated that a quarter model could be used to accurately represent the results of a gyroid full model. This was necessary since the cell count would have been prohibitively high on the full model of the gyroid PCM heat sink.

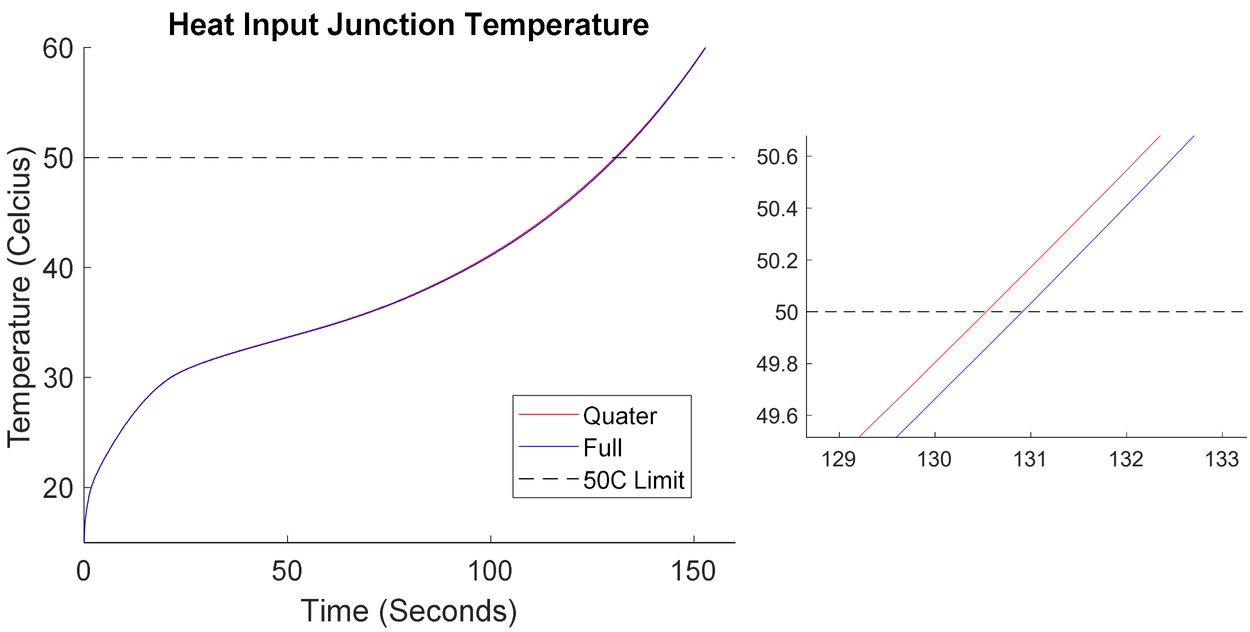

Figure 3.16: Gyroid quarter model vs Full model

3.4 VALIDATION MODEL

The numerical model was applied to experimental testing conducted by the University of Padua. The University of Padua conducted experimental testing on a PCM heat sink with the body centered cubic truss structure (Righetti et al., 2020), see Figure 3.17. The heat sinks were additively manufacturing using aluminium selective laser sintering. The heat sink footprint was 42x42 mm with an internal structure height of 40 mm. The body centered cubic truss investigated featured a cube base size of 10 mm and a strut radius of 0.5 mm. The internal PCM volume fraction was 95%.

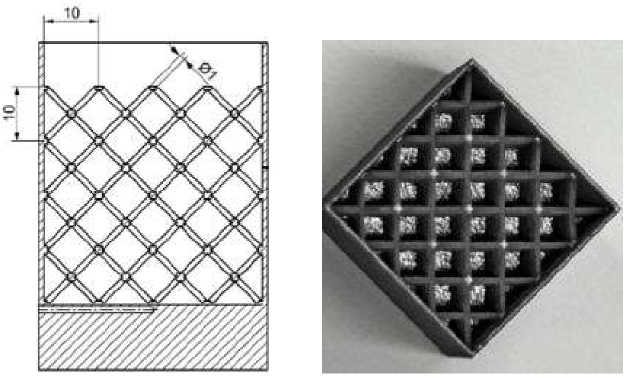

Figure 3.17: Padua body centered cubic heat sink with base size 10 mm (Righetti et al., 2020)

The test setup and thermocouple placement are shown in Figure 3.18. The heat sink was placed on top of an aluminium heater block and surrounded by 25 mm rock wool insulation (Righetti et al., 2020). The aluminium heater block had an 8 mm diameter cartridge heater, which supplied a power loading of approx. 30 W to the heat sink. Noting, thermocouple T3 represented the electronics temperature (Righetti et al., 2020).

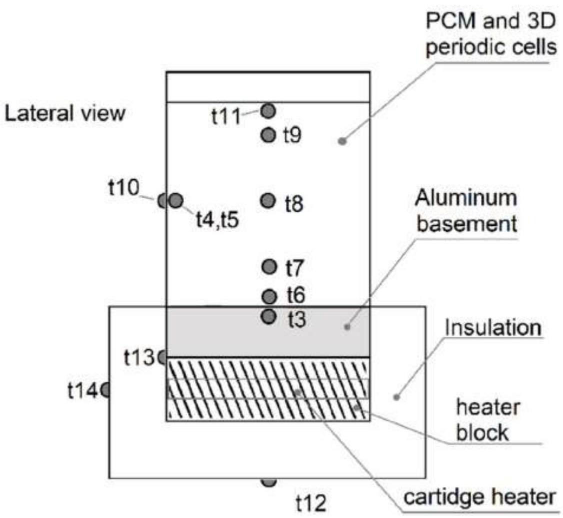

Figure 3.18: Padua test setup and thermocouple placement (Righetti et al., 2020)

3.4.1 Numerical Validation Model

The heat sink test setup was modelled with quarter symmetry to reduce computational effort, as shown in Figure 3.19 below. The metal and PCM zones were meshed with a 0.2 mm Poly mesh. The surrounding 25 mm thick rook wool insulation was also included due to its thermal mass.

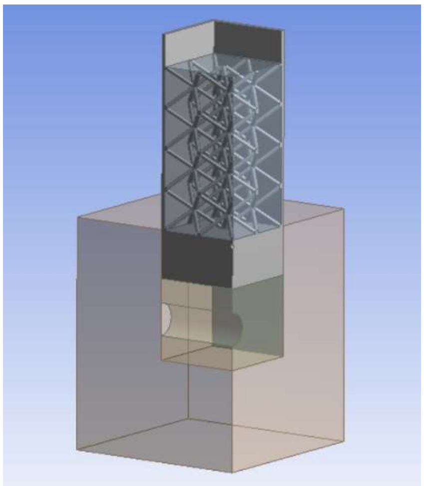

Figure 3.19: Padua test setup and thermocouple placement (Righetti et al., 2020)

3.4.1.1 Model Material Properties

The PCM used in the experiment was Rubitherm RT55, refer to Table 3.7 for material properties. Noting the liquid density of the PCM was utilised, as per the solidification/melting modelling assumptions specified in subsection 3.3.1 of the numerical modelling methodology.

Table 3.7: Properties of PCM RT55 (Righetti et al., 2020), (Rubitherm, 2021)

Thermal Cond. (W/m·K)	Density (kg/m^3)	Specific Heat (J/kg·K)	Latent Heat* (J/kg)	Melt Range (°C)
0.2 (both phases)	880 (solid) 770 (liquid)	2000	170,000 ± 7.5%	48 - 57

* Includes sensible heat over the melting range

The heater block used for the experiment was aluminium. The material properties utilised for the heater block were a thermal conductivity of 205 W/m·K, a density of 2700 kg/m^3 and a specific heat of 900 kJ/kg. (Righetti et al., 2020), (Atlas Steels, 2013).

The heat sink was additively manufactured with aluminium alloy (ALSi10Mg-0403) using selective laser sintering (SLS) (Righetti et al., 2020). The material properties utilized for the heat sink were a thermal conductivity of 110 W/m·K, a density of 2670 kg/m^3 and a specific heat of 915 kJ/kg. Noting, the thermal conductivity utilised was half-way between the SLS build and transverse directions, and the thermal conductivity reported by the Authors (EOS, 2014), (Righetti et al., 2020).

The insulation utilised for the experiment was rock wool. The material properties utilized for rock wool were a thermal conductivity of 0.034 W/m·K, a density of 80 kg/m^3 and a specific heat of 1030 kJ/kg (Rodrigues et al, 2020).

3.4.1.2 Model Boundary Conditions

The heat input for the heater block was supplied by a cartridge heater, which had an average heat load of 29.8 W for the experiment. The heat input was modelled as a constant heat flux distributed over the heat input area of the cartridge heater void.

The symmetry walls were specified with symmetry conditions. The heat loss due to natural convection was included for the experiment. The heat loss was specified for all external walls of the model using a heat transfer coefficient and free stream temperature. For this analysis, the convective heat transfer coefficients were estimated using the Nusselt number and Raleigh number (Cengel, 2002). For the vertical walls of the model, a heat transfer coefficient of 13.5 W/m^2·K was utilised and for the horizontal walls, a heat transfer coefficient of 12.5 W/m^2·K was utilised (Refer to Appendix B).

The thermal boundary conditions between the metal, insulation and PCM zones were specified as thermal coupled, to allow heat transfer between the zones. It was assumed that the PCM and metal had direct contact with the metal and therefore the boundary did not include thermal resistance. A contact resistance was applied to the boundary between the heater block and heat sink. The contact resistance was simulated with a virtual surface, using a wall thickness (Δx) and wall thermal conductivity (k_w), as per Equation 3.9.

$$Contact\ Reistance = \frac{\Delta x}{k_w} \qquad \text{Equation 3.9}$$

Contact resistance is dependent on material properties, surface characteristics and contact pressure (Fletcher, 1993). For this analysis, a nominal contact resistance of 0.001 m^2·C/W was applied to the boundary. The contact resistance assumed a smooth-rough aluminium contact with a low contact pressure. Refer to Appendix B for the contact resistance.

3.4.2 Results Comparison

Figure 3.20 shows two temperature profiles comparing the numerical validation model to the experimental data. The first is the temperature profile for thermocouple T3, which is situated at the base of the PCM heat sink, representing the electronic component temperature of interest. The second is the temperature profile for the average PCM temperature. The average PCM temperature is helpful to compare the PCM melting, since the PCM liquid fraction of the experiment is difficult to quantity. The average PCM temperature of the experiment was obtained by averaging the 7 internal PCM thermocouples.

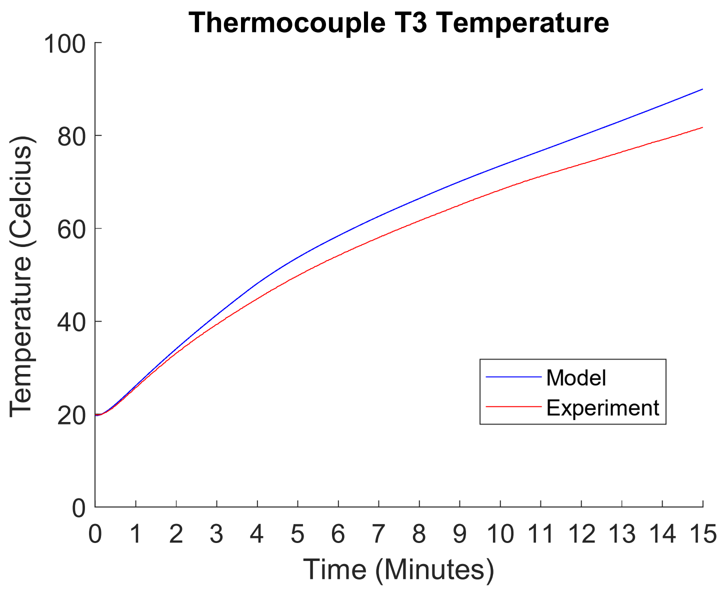

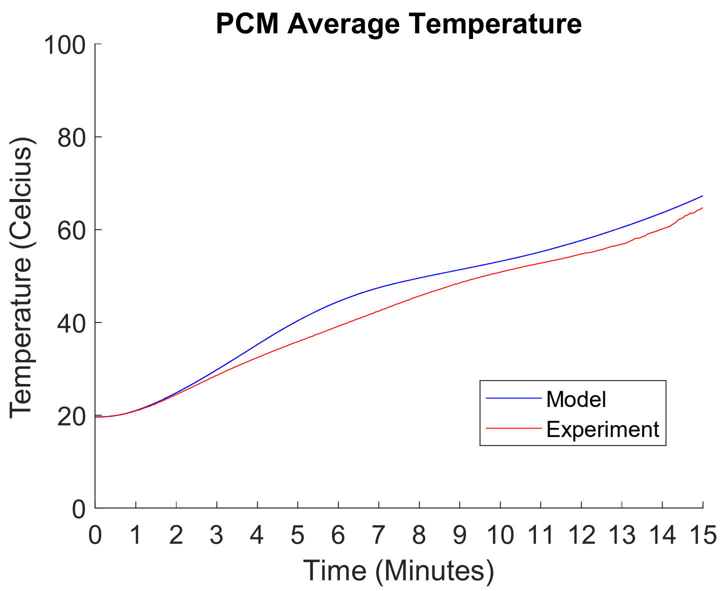

Figure 3.20: Thermocouple T3 and Average PCM temperature

The temperature results in Figure 3.20 show that the model predicts a slightly higher temperature compared to the experiment. The results diverged at around 2.5 minutes, although, the temperature profiles featured the same trends. The mean difference over the course of the 15 minutes experiment was 4.2°C for thermocouple T3 and 2.7°C for the PCM average temperature. The difference at the end of the experiment was 8.1°C for thermocouple T3 and 2.5°C for the PCM average temperature.

Figure 3.21 provides the top view of the experiment every 3 minutes. It is difficult to quantify when the PCM first began to melt and how much PCM had melted at each interval. However, there appears to be PCM variation already at 3 minutes. The PCM melting was gradual until 12 minutes, however in the last three minutes of the experiment, the PCM melting was very rapid. At the end of the experiment, there was still a fraction of PCM still solid (approx. 5%).

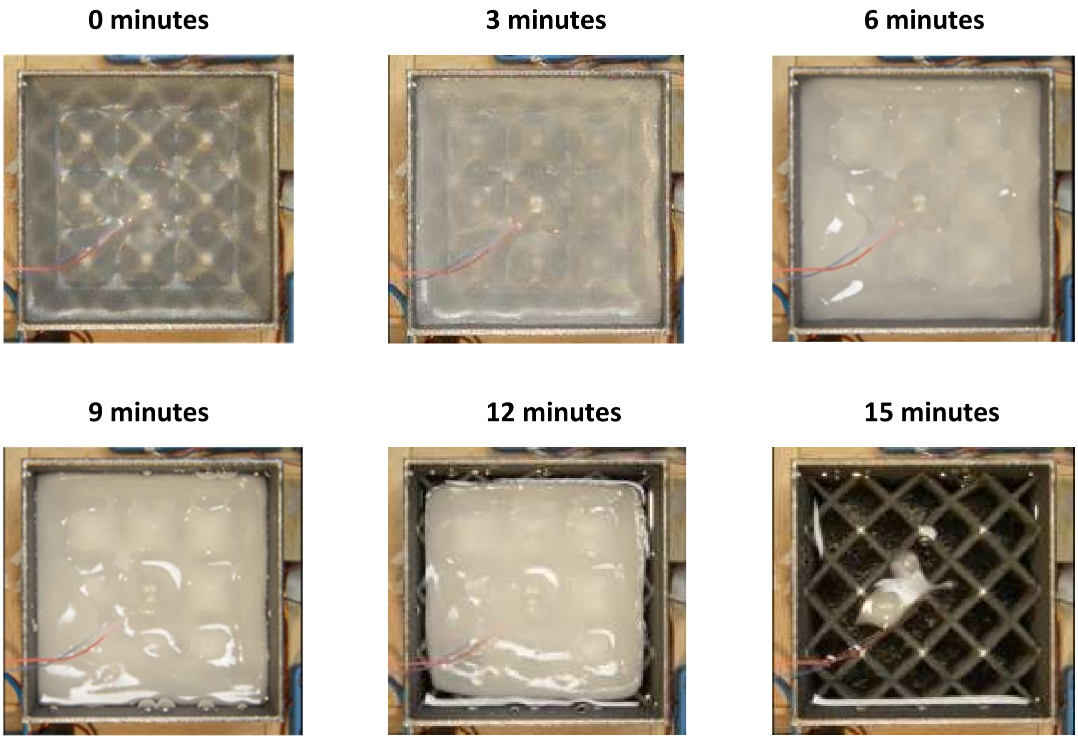

Figure 3.21: Experiment PCM melting

Figure 3.22 shows the PCM liquid fraction for the numerical model, which provides the model's PCM melting rate. The PCM in the model began to melt at approx. 4.5 minutes. The PCM melt was almost linear until approx. 12 minutes, and then slightly declined until the end at 15 minutes. The PCM in the model was 90% melted at the end of the experiment.

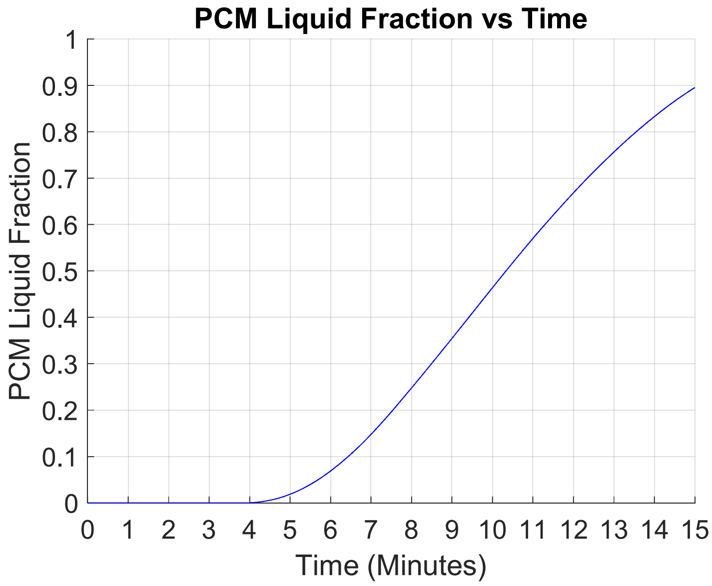

Figure 3.22: Model validation PCM liquid fraction

Figure 3.23 provides a cross-section view of the model at 9, 12 and 15 minutes. The model and experiment fairly align at 9 and 12 minutes in terms of PCM melt distribution. At 9 minutes, the model is 36% melted, and at 12 minutes, the model is 67% melted. However, at 15 minutes, the model underpredicts the amount of melted PCM. At 15 minutes, the model is 90% melted, however, the experiment appears over 95% melted from Figure 3.21.

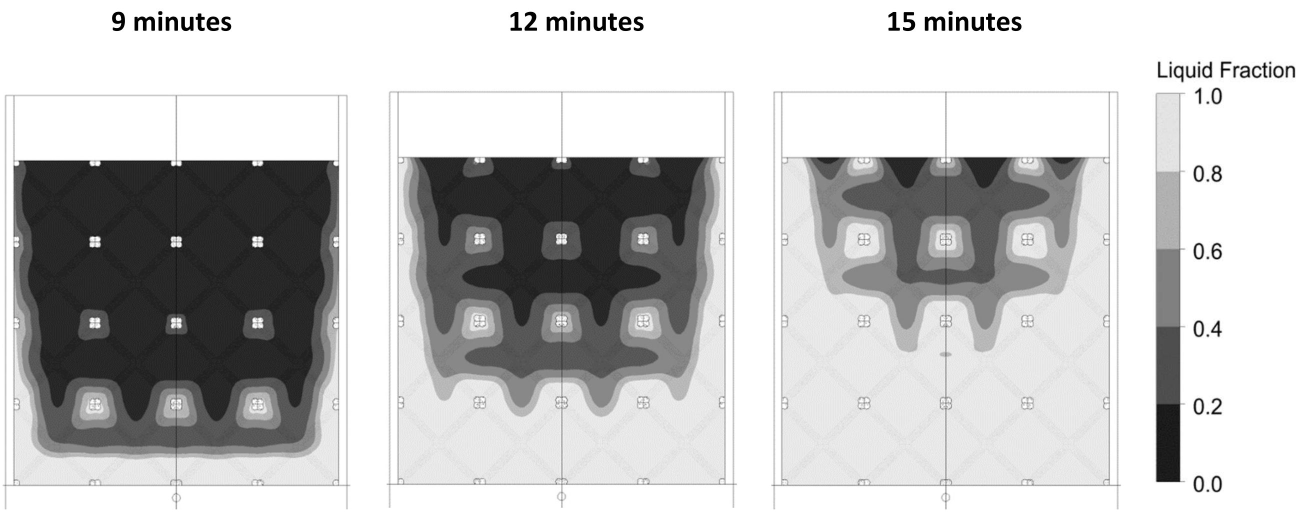

Figure 3.23: Model validation PCM melting side view

In summary, the model predicts the temperature performance of the PCM heat sink with a good degree of accuracy (4.2°C mean difference for the temperature of interest). However, in general, the model is slightly hotter than the experiment, and the PCM does not melt as quickly, especially towards the end of the experiment.

The differences may be attributed to the role of natural convection and the PCM melting properties. Firstly, the role of natural convection is particularly dominant towards the end of the experiment, as the PCM becomes more liquid and freer for motion. In the final 3 minutes of the experiment, the PCM melts rapidly and the average PCM temperature increases with fluctuations. Whereas the model relies solely on heat conduction, and in the final 3 minutes, the PCM melting slows down as the heat flow is encumbered by the low thermal conductivity of the PCM. This results in slower melting towards the end and a higher base temperature since less heat is absorbed by the PCM. Although, for CubeSat applications natural convection does not occur, and thus a slower melt towards the end would be expected.

Secondly, another factor is the PCM melting properties. The model assumed a well-defined PCM melting range and a constant liquid PCM density. However, in reality the melting point for paraffin PCM is not as well-defined and the solid PCM has a higher density. The high density PCM would allow faster heat transfer as the heat conductance required a shorter distance of travel. Also, due to the wide-ranging melting point of paraffin RT55, the PCM may have begun melting and absorbing heat earlier than predicted. The net effect would be a lower temperature of heat sink and PCM, as the PCM absorbs heat earlier. This was observed in the results comparison, where the temperatures diverged at 2.5 minutes, prior to the PCM melting in the model at 4.5 minutes.

In conclusion, the model provided a conservative result for the temperature response of the PCM heat sink, since the temperature in the experiment was lower than predicted by the model. Noting, the TCE structures proposed for this investigation have a smaller base size and a higher thermal conductivity than the heat sink analysed in the validation model. As a result, the slow melting towards the end may not be as prominent, since the role of natural convection is reduced for smaller base sizes and higher thermal conductivity structures (Zhao et al., 2021). In addition, the PCM heat sinks proposed for this investigation uses high purity octadecane paraffin, which may have a more well-defined melting performance over RT55 paraffin.

3.5 RESULTS

The following presents the numerical modelling results for the conceptual PCM heat sink designs (direct cooling and heat pipe cooling), shown in Figure 3.24 below, with the additive internal TCE structures (truss, gyroid and fins). The results are firstly presented for the direct cooling configuration and then for the heat pipe cooling configuration using the TCE wall and radial thickness of 0.4 mm. To conclude, a base size analysis is presented for both configurations which compared TCE thicknesses of 0.3, 0.4 and 0.5 mm, whilst maintaining the internal PCM volume fraction of 85%.

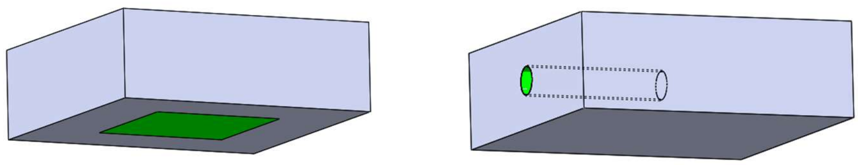

Figure 3.24: Direct cooling and heat pipe cooling configurations

The performance of the TCE structures was measured based on their utilisation of the TES capacity. To recap from the conceptual PCM heat sink design (Section 3.2), the TES capacities for the PCM heat sink configurations, expressed in minutes for the 50 W heat load are provided in Table 3.8 below for both the copper and aluminium PCM heat sinks. Noting, aluminium provided slightly less TES capacity compared to copper and the heat pipe cavity slightly reduced the TES capacity for the heat pipe cooling configuration.

Table 3.8: TES capacity of the PCM heat sink configurations for a 50 W heat load (Temperature range of 15-50°C)

	Copper PCM Heat Sink	Aluminium PCM Heat Sink
Direct Cooling Configuration	5.1 min	4.9 min
Heat Pipe Cooling Configuration	5.0 min	4.8 min

The TES utilisation was determined measured by the amount of time that the heat input was maintained below the 50°C limit relative to the TES capacity. Noting, due to the inherently low thermal conductivity of paraffin PCM, it was not practical to aim for 100% TES utilisation and over 90% TES utilisation was considered effective cooling, however over 80% was also reasonable.

3.5.1 Direct Cooling Results (0.4mm Structures)

Figure 3.25 below shows the results for the direct cooling copper PCM heat sink (TES: 5.1 minutes). Two graphs are provided, firstly the temperature response (i.e. heat input junction temperature) and secondly the PCM melting rate (i.e. PCM liquid fraction). The temperature response results showed that the fins maintained the lowest heat input junction temperature, close to 30°C, followed closely by the gyroid and then the truss. The PCM melting results showed that all geometries had a similar continuous melt rate, with only a reduced slow down towards the end above a liquid fraction of 0.95, and that all PCM was melted at approximately 4.5 minutes for all geometries.

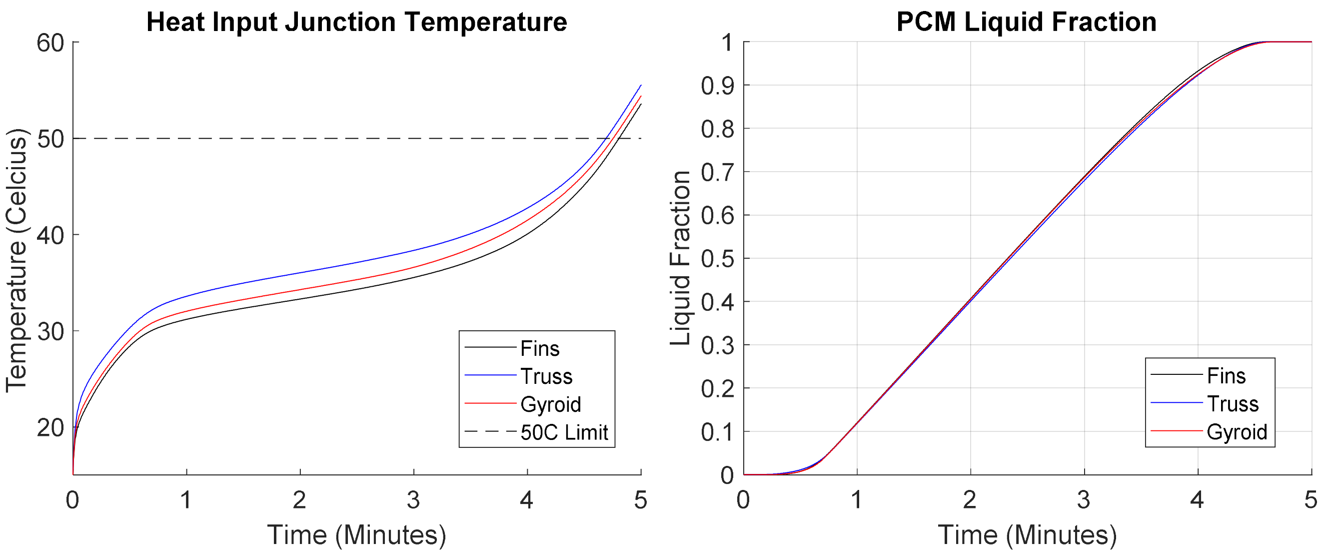

Figure 3.25: Copper PCM heat Sink, Direct cooling at 50 W

Table 3.9 below provides the key results for the direct cooling copper PCM heat sink. The overall performance of the geometries was similar and all geometries provided over 4.5 minutes cooling and close to 95% TES utilisation. The results demonstrated that effective cooling was achievable with paraffin octadecane PCM for a 50 W heat load.

Table 3.9: Key results for the copper PCM heat sink (direct cooling)

	Time at 50°C Limit	TES Utilisation at 50°C Limit
Fins	4.8 minutes	94%
Truss	4.7 minutes	92%
Gyroid	4.8 minutes	94%

Figure 3.26 below shows the results for the direct cooling aluminium PCM heat sink (TES: 4.9 minutes). For the aluminium heat sink, the differences between the structures became more evident. Again, the fins provide the lowest heat input junction temperature response, close to 35°C, followed closely by the gyroid. However, the worst performing structure was the truss. All geometries had a similar continuous melt rate. However, compared to the copper PCM heat sink, the aluminium PCM heat sink began to melt earlier due the higher temperature response at the heat input (i.e. less heat dissipation for the aluminium heat sink). The PCM melting results showed that all PCM was melted also at approximately 4.5 minutes for all geometries.

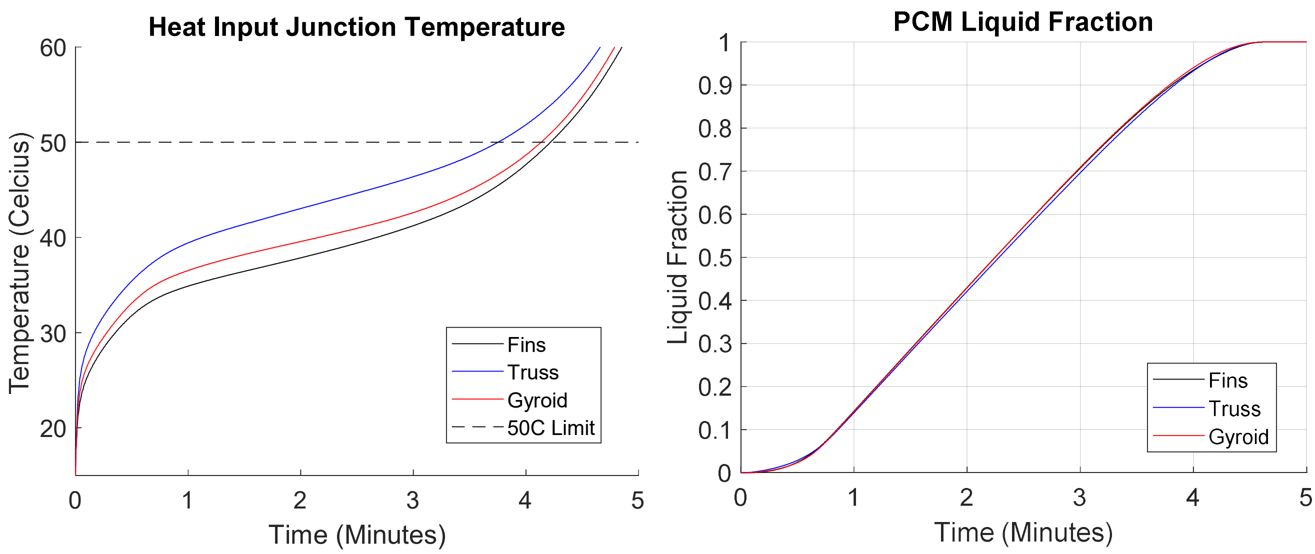

Figure 3.26: Aluminium PCM heat sink, Direct cooling at 50 W

Table 3.10 below provides the key results for the direct cooling aluminium PCM heat sink. The fins and gyroid provided over 4.0 minutes of cooling and utilised approximately 85% of the TES capacity, which was a reasonable result. However, the truss did not exceed 80% of the TES capacity, despite the same overall PCM melt rate.

Table 3.10: Key results for the aluminium PCM heat sink (direct cooling)

	Time at 50°C Limit	TES Utilisation at 50°C Limit
Fins	4.2 minutes	86%
Truss	3.8 minutes	77%
Gyroid	4.1 minutes	84%

PCM Melt Distribution – Direct Cooling

Figure 3.27 below shows a cross-section view of the PCM melt distribution inside the quarter model aluminium PCM heat sink at the melting halfway point (2.5 minutes). Whilst the melt rate was similar for all geometries (as shown in Figure 3.26 above), the melt distribution within the PCM heat sink was different, which indicates why there was a different temperature response. The melt distribution was best within the fins structure, due to the short distance between the fins. The melt distribution in the gyroid was also well distributed, although the channel size is larger than the fins which resulted in a larger concentrated of areas of un-melted PCM. The melt distribution in the truss was not well distributed, with the melting concentrated around the heat load.

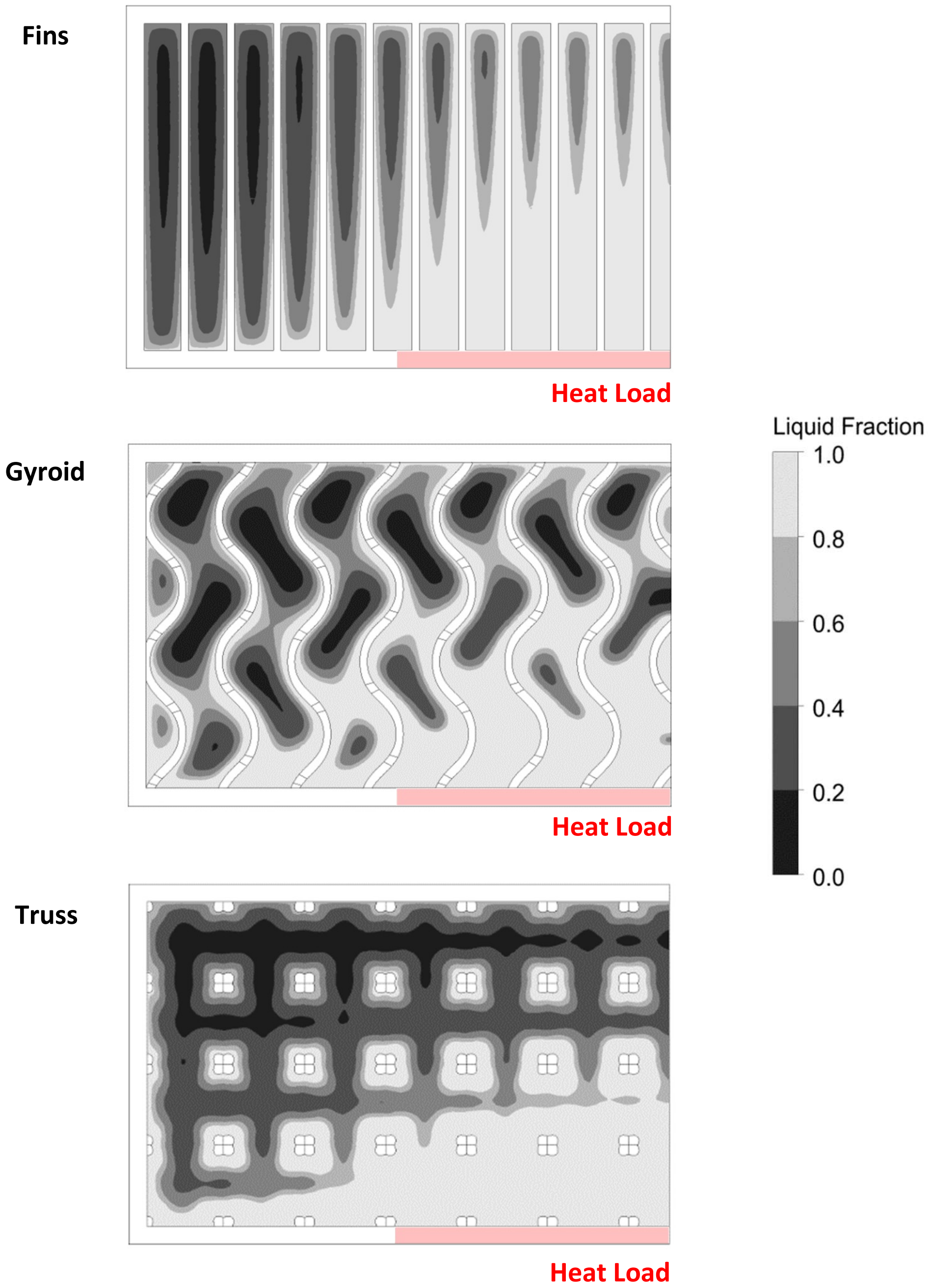

Figure 3.27: PCM melt distribution in aluminium direct cooling quarter model at halfway point

3.5.2 Heat Pipe Cooling Results (0.4mm Structures)

Next the results are presented for the heat pipe cooling configuration using the same internal TCE structures. Figure 3.28 below shows the results for the copper PCM heat sink (TES: 5.0 minutes). For the heat pipe cooling configuration, the gyroid provided the best temperature response. The fins provided a good response initially, however half-way through the temperature response increased. The truss temperature response was consistent, but higher than both the gyroid and the fins. Regarding the PCM liquid fraction, all geometries started with a similar melting rate, but the gyroid continued with the slightly faster melting rate. The truss and especially the fins slowed down after the halfway point.

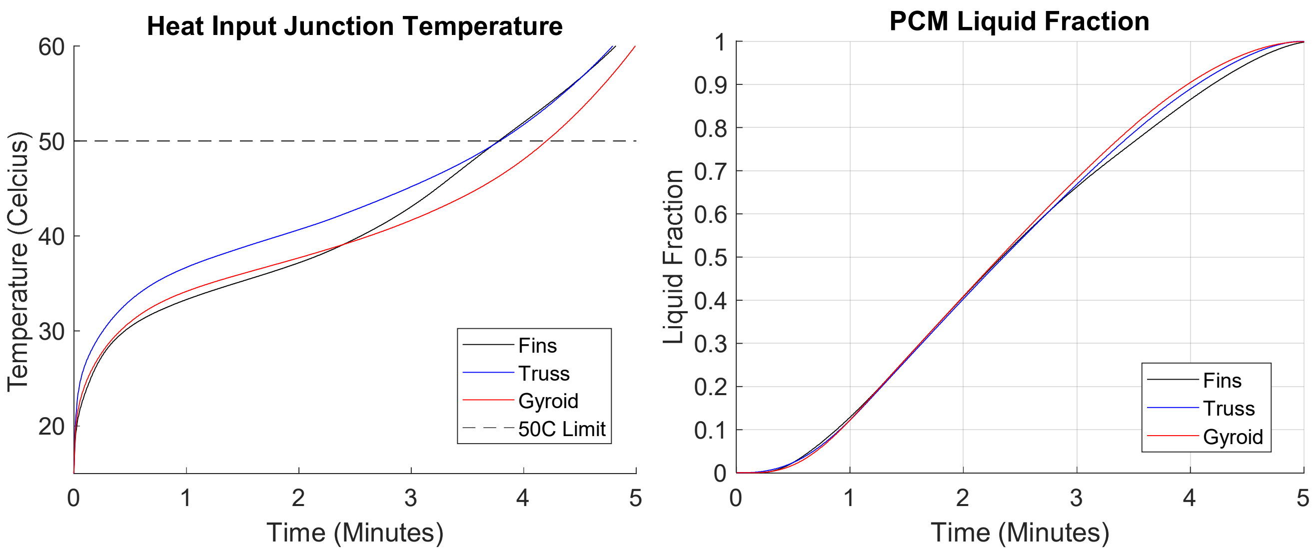

Figure 3.28: Copper PCM heat sink, Heat pipe cooling at 50 W

Table 3.11 below provides the key results for heat pipe cooling copper PCM heat sink. Noting, only the gyroid TCE geometry provided over 4.0 minutes of cooling capacity and close to 85% TES utilisation, which was a reasonable result. The fins and truss were unable to utilise above 80% of the TES capacity of the PCM heat sink.

Table 3.11: Key results for the copper PCM heat sink (heat pipe cooling)

	Time at 50°C Limit	TES Utilisation at 50°C Limit
Fins	3.8 minutes	76%
Truss	3.8 minutes	76%
Gyroid	4.2 minutes	84%

Figure 3.29 below shows the results for the heat pipe cooling aluminium PCM heat sink (TES: 4.8 minutes). Using aluminium, the geometries were unable to dissipate the heat load from the heat pipe and already exceeded the 50°C limit at the halfway point. The gyroid had the more consistent temperature response for the heat load, and again, the fins performed well at the beginning and then increased sharply. The truss was unable to dissipate the high heat load and had the highest temperature response. Regarding the PCM liquid fraction, the geometries started with a similar melting rate, but only the gyroid continued with a faster melting rate as observed with the copper heat sink.

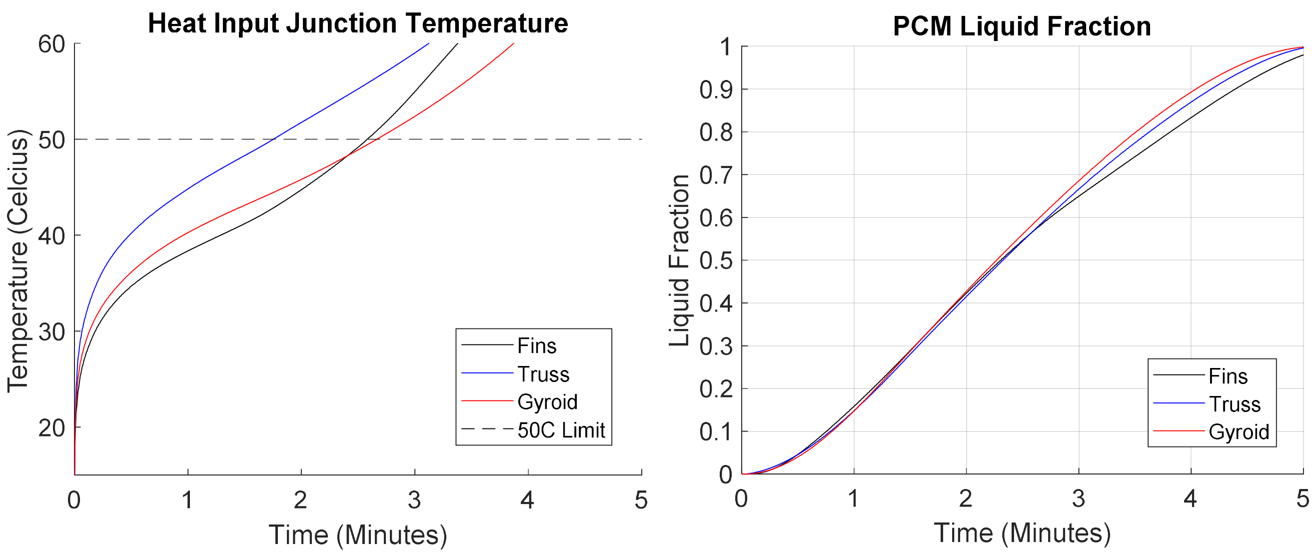

Figure 3.29: Aluminium PCM heat sink, Heat pipe cooling at 50 W

Table 3.12 below provides the key results for the heat pipe cooling aluminium PCM heat sink. The gyroid provided the longest cooling, however only utilised 56% of the TES storage capacity, which demonstrated that the 50 W heat load was too high for the aluminium PCM heat sink.

Table 3.12: Key results for the aluminium PCM heat sink (heat pipe cooling)

	Time at 50°C Limit	TES Utilisation at 50°C Limit
Fins	2.6 minutes	54%
Truss	1.8 minutes	37%
Gyroid	2.7 minutes	56%

PCM Melt Distribution

Figure 3.30 below shows a cross-section view of the PCM melt distribution inside the quarter model copper heat pipe cooling PCM heat sink at the melting halfway point (2.5 minutes). The gyroid showed the best melt distribution, since the PCM melt was being utilised on both sides of the heat sink, although more strongly on the heat pipe side. For the fins, the PCM melt was solely on the heat pipe side, and thus showed that the fins were unable to utilise the PCM effectively on the far side of the PCM heat sink. The truss melt was mainly around the heat pipe and showed that the truss structure was not as good at transporting heat from the source as the gyroid and fins.

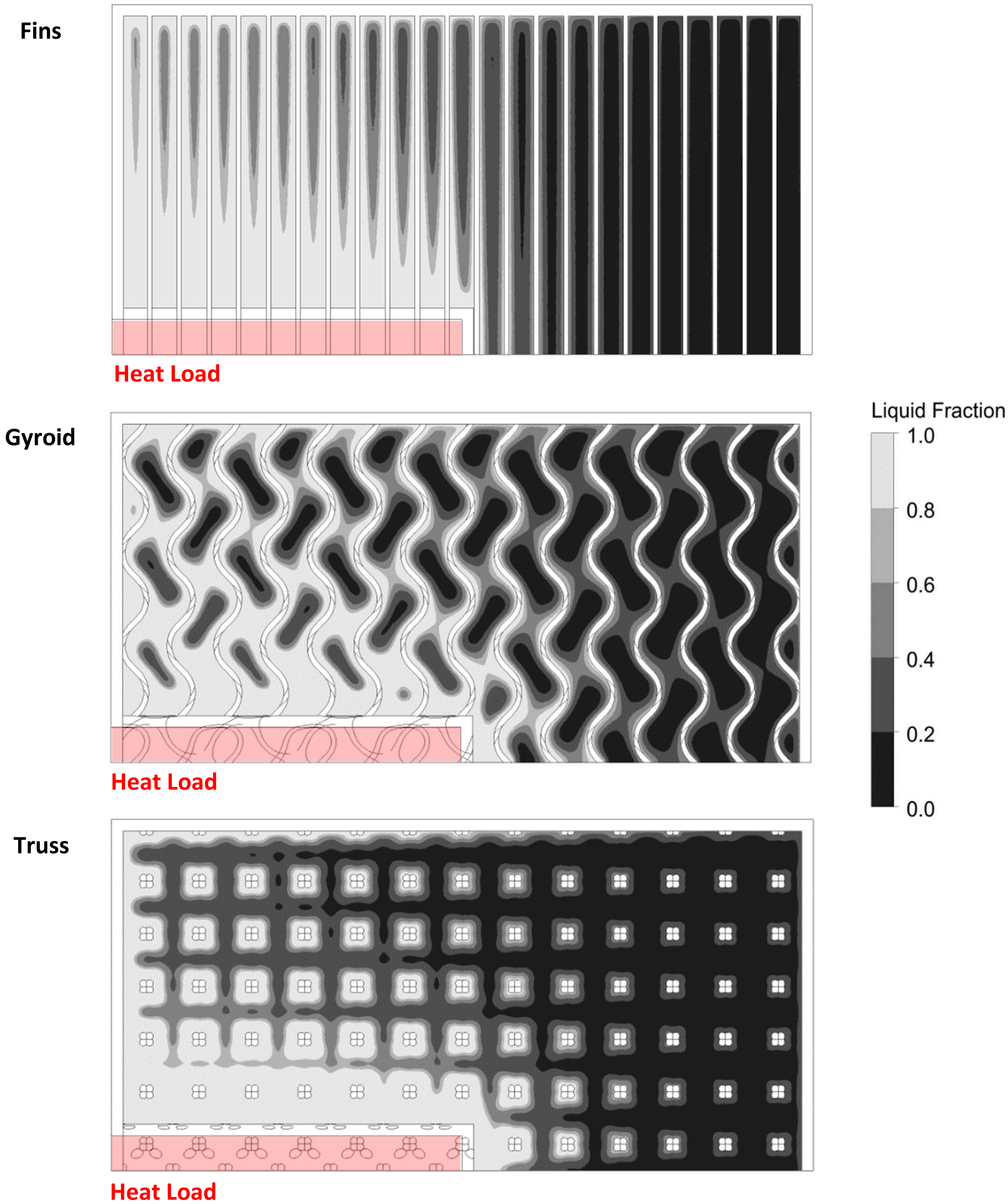

Figure 3.30: PCM melt distribution in copper heat pipe cooling quarter model at halfway point

3.5.3 Base Size Analysis Results

A base size analysis was performed on the direct cooling and heat pipe cooling configurations, which investigated the effect of changing the TCE structure thickness and unit dimensions. The original wall and radial thickness of 0.4 mm was compared to thicknesses of 0.3 and 0.5 mm. To maintain the 85% internal PCM volume fraction, the TCE unit dimensions (base sizes) were smaller for the 0.3 mm thickness and larger for the 0.5 mm thickness.

Table 3.13 provides the base sizes created for the wall and radial thicknesses of 0.3, 0.4 and 0.5 mm. (Noting, the 85% PCM volume fraction was achieved within a 0.5% tolerance). The surface area to volume ratio of the structures are also provided in Table 3.13 below. Noting, the fins and gyroid had the same surface area to volume ratio. However, the surface area to volume ratio of the truss was slightly less than the fins and gyroid for each respective base size. The performance of the TCE base sizes were therefore compared relative to their surface areas as the baseline. The base size quarter models are illustrated in Appendix C.

Table 3.13: Fins, truss and gyroid base sizes

	0.3 mm	**0.4 mm**	**0.5 mm**
Fins	Fin Spacing 1.95 mm Surface Area Ratio **6.6:1**	Fin Spacing 2.55 mm Surface Area Ratio **5:1**	Fin Spacing 3.1mm Surface Area Ratio **4:1**
Gyroid	Gyroid Channel Size 3.0 mm Surface Area Ratio **6.6:1**	Gyroid Channel Size 4.0 mm Surface Area Ratio **5:1**	Gyroid Channel Size 5.0 mm Surface Area Ratio **4:1**
Truss	Truss Cube Size 3.3 mm Surface Area Ratio **6:1**	Truss Cube Size 4.5 mm Surface Area Ratio **4.5:1**	Truss Cube Size 5.5 mm Surface Area Ratio **3.6:1**

The direct cooling base size results are presented in Figure 3.31 below for the aluminium and copper PCM heat sinks. The results showed that for each TCE structure, increasing the surface area improved the performance of the heat sink. The results also showed that the fins were the best performing structure for the direct cooling configuration, followed closely by the gyroid, and then lastly the truss. However, the results showed that the performance of the structures converged as the base sizes were reduced. In particular, the gyroid performance matched the fins performance for the smallest structure thickness of 0.3 mm. For the copper heat sink, the performance was better than the aluminium, although the performance improvement for the copper heat sink was marginal, since the performance was approaching the limits of its maximum TES capacity.

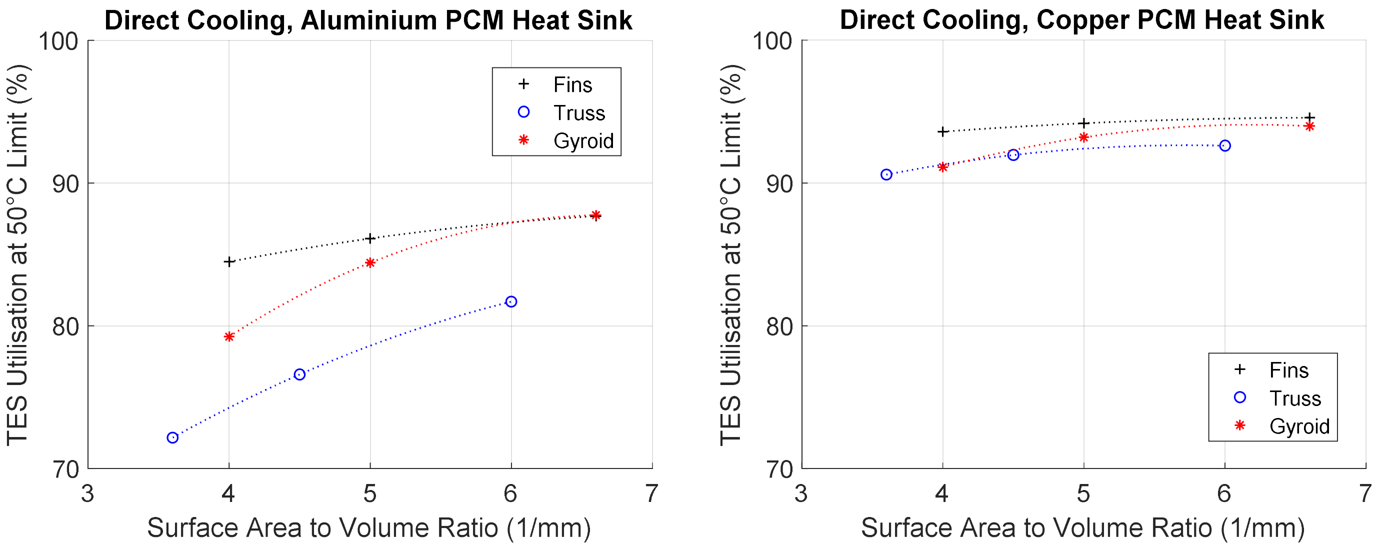

Figure 3.31: Base size analysis, Direct cooling

The heat pipe cooling base size results are presented in Figure 3.32 below. The results are presented only for the copper PCM heat sink, since the aluminium PCM heat sink could not dissipate the heat load required. Again, the results showed that increasing the surface area improved the performance of the heat sink. For the heat pipe cooling, the best performing structure was the gyroid. For the fins, increasing the surface area did not have a large impact, since the fins were unable to effectively utilise the PCM in the entire heat sink. For the truss, reducing the base size improved the performance, however, the truss was not as good as dissipating heat as the sheet-based gyroid structure for all surface area to volume ratios.

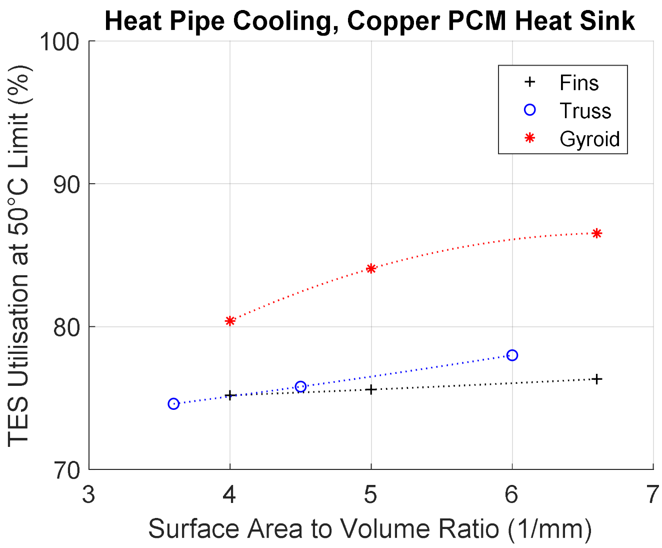

Figure 3.32: Base size analysis, Heat pipe cooling

3.6 DISCUSSION

The modelling results demonstrated that effective heat dissipation could be achieved with paraffin PCM, for both the direct cooling and heat pipe cooling configurations with a 50 W heat load. The following discusses the results in terms of the TCE geometries, TCE materials and TCE base sizes. Concluding remarks are provided for additive manufacturing methods and the next Chapter of this Thesis.

3.6.1 TCE Geometries

For the direct cooling, the fin structure provided the best results, followed very closely by the gyroid structure. The fins demonstrated a better PCM melt distribution due to the small distance between the fins. The gyroid channel size was slightly larger than the fins, which provided fins with the small gain. The truss PCM melting was concentrated around the heat source and showed that the strut-based truss was not as effective at dissipating heat as the sheet-based fins and gyroid.

For the heat pipe cooling, the gyroid structure provided the best results. The copper gyroid structure demonstrated the best PCM melt distribution and capability to dissipate heat in all directions. The fins, on the other hand, could only effectively utilise the PCM melting on one side due to its one directional geometry. The truss PCM melt was again concentrated around the heat source and could not dissipate heat as well as the gyroid structure.

Overall, the gyroid demonstrated the best performance, since it was effective for both configurations. Whilst the fins showed optimal performance for PCM melting in one direction, the fins failed to distribute heat in all directions for the heat pipe cooling. For both configurations, the gyroid structure was better at dissipating heat than the truss structure.

3.6.2 TCE Materials

For the direct cooling, the copper PCM heat sink provided better performance than the aluminium PCM heat sink, due to copper’s superior thermal conductivity. However, the aluminium heat sink provided reasonable results with the fins and gyroid, compared to the copper heat sink (approx. 85% vs 95% TES utilisation respectively). Since the aluminium heat sink is over 50% lighter, from a weight perspective it would be better to make use of the aluminium PCM heat sink and investigate whether a 10% larger PCM heat sink would provide the same cooling time as the copper PCM heat sink. Although, it is suspected that the copper PCM heat sink could be applied to higher heat loads for direct cooling, whereas the aluminium PCM heat sink was at its limits with the 50 W heat load.

For the heat pipe cooling, the aluminium heat sink could not dissipate the required heat load. The copper heat sink was needed to dissipate the heat from the heat pipe condenser. The dissipation of heat was more demanding due to the small heat input area of the heat pipe condenser, compared to the larger heat input area for the direct cooling. Thus, high thermal conductivity copper was needed to dissipate the 50 W heat load. Although, the copper PCM heat sink is heavy, and ways to reduce the copper content are needed, whilst still maintaining good performance. For example, reducing the case thickness, which is the dominant weight of the heat sink (over 50% of the metal mass). However, this reduction is dependent on how well additive parts can contain PCMs in a vacuum.

3.6.2 TCE Base Sizes

The base size analysis showed that thinner structures with smaller base sizes improved the performance of the PCM heat sink. The performance improved due to the increased surface area for PCM heat transfer, but also because of the smaller distance between the PCM and metal structure.

For the direct cooling, the base size results confirmed that the fins were the best structure, followed closely by the gyroid and the least performing structure was the truss. The results also showed that the performance of the structures converged as the base sizes were reduced. In particular, the gyroid matched the performance of the fins at the smallest structure thickness of 0.3 mm, and provided 88% TES utilisation for the aluminium heat sink and 95% TES utilisation for the copper. Noting, the copper PCM heat sink performance did not vastly increase with reduced base size, since the heat sink was operating at a high performance (95%).

For the heat pipe cooling, the results showed that reducing the base size for the gyroid and truss structures improved the performance. However, for the fins, reducing the base size did not have a large impact, since the fins were unable to effectively utilise the PCM in the entire heat sink. In addition, the results confirmed that the gyroid structure was better at dissipating heat than the truss, and was not as result of the lower surface area to volume ratio of the pin struts. The gyroid was the only geometry that could utilise above 80% TES utilisation, with the smallest base size achieving close to 90% TES utilisation.

In summary, the gyroid showed the best performance with the heat pipe cooling, with the largest gyroid base size outperforming the smaller base sizes for the truss and fins. For the direct cooling, the gyroid matched the fins for the smallest base size. Therefore, the gyroid would also make the better choice for direct cooling, since there are other benefits that additive structures provide. These include improved mechanical properties (Alketan et al., 2018), easier PCM filling with open cell geometries and manufacturability of small base sizes.

3.6.4 Additive Manufacturing

Metal additive manufacturing with aluminium and copper depends on the additive process available. For aluminium additive manufacturing, the most prominent method is selective laser sintering (SLS), which is a powder bed fusion method. The minimum wall thickness specified for SLS is 0.3-0.4 mm, however the thermal conductivity with no heat treatment is approx. 50% less than aluminium 6063 alloy (110 W/m·K vs 209 W/m·K) (EOS, 2021). Thus, at present for direct cooling, traditionally manufactured fins may be the best approach. A new method recently released for aluminium additive manufacturing is liquid metal printing, which is a metal extrusion method. However, due to the challenges of liquid metal printing, the minimum wall thickness with this method is 3 mm, which is not suitable for the application (Basiliere, 2022).

For the heat pipe cooling, high thermal conductivity copper was required. Copper additive manufacturing is currently only available with the metal extrusion method, such as Bound Metal Deposition (BMD) by Desktop Metal. The extrusion nozzle diameters available with BMD are 0.4 mm and 0.25 mm (Desktop Metal, 2020). However, it is unknown which gyroid base sizes and thicknesses are possible with the BMD extrusion and sintering processes. Also, the thermal performance of BMD printed parts has not been reported and it is unknown whether BMD parts are suitable for PCM containment in a vacuum. Since the gyroid outperformed the fins and truss for the heat pipe cooling, this new manufacturing method with copper was explored in the next Chapter for PCM heat sink applications.

4. Application of BMD Additive Manufacturing for CubeSat PCM Heat Sinks

4.1 Introduction

This Chapter explores the application of the Bound Metal Deposition (BMD) additive manufacturing for CubeSat PCM heat sinks applications (Research Objective 2). BMD was chosen for this investigation since copper material was recently released for high thermal conductivity heat dissipation and new geometries were possible with the additive manufacturing philosophy for PCM heat transfer enhancement.

BMD is a metal extrusion additive manufacturing technique by Desktop Metal, which produces three-dimensional objects layer by layer by extruding material. In this investigation, the gyroid structure from Chapter 3 was explored, which demonstrated the best overall PCM heat transfer performance for dissipating heat in all three directions. However, the BMD process was new with copper, and it was unknown how well thin-walled structures, such as the gyroid, could be customised. Furthermore, the thermal properties of BMD were not yet explored in the literature, and it was unknown whether BMD parts could provide leakproof containment for PCMs.

The research questions to be answered in this chapter were the following:

Is BMD additive manufacturing a suitable technique for producing 3D structures for PCM heat transfer and is BMD additive manufacturing suitable for containing PCMs in a vacuum for space applications?

To the Author's knowledge, the BMD manufacturing process had never been applied to enhance PCM heat transfer or provide PCM containment. To determine the BMD viability for space PCM heat sink applications, the following four experimental investigations were untaken in this Chapter 4:

1. **Porosity:** The porosity was investigated to quantity the type and level of the porosity present in the manufacturing process and its predicted effect on the thermal properties.
2. **Thermal Conductivity:** The thermal conductivity was tested to quantify the thermal performance of BMD parts for heat dissipation.
3. **Gyroid Printability:** The manufacture of the gyroid structure was explored to determine the wall thickness/base sizes possible with BMD.
4. **PCM Containment:** The leakproof integrity of BMD parts in a vacuum was tested to determine if the method was suitable for space applications.

4.2 OVERVIEW: BMD DESKTOP METAL STUDIO SYSTEM

The BMD investigations in this Chapter were undertaken with the Studio System, shown in Figure 4.1 below, using the high resolution printhead. The following provides an overview of the Studio System manufacturing process, main printing parameters, and known material properties of BMD copper.

Figure 4.1: Studio system, Left to Right: Printer, de-binder and furnace (DM Design Guide, 2020)

4.2.1 Manufacturing Process

BMD is a three-stage process on the Desktop Metal Studio System, which includes printing, debinding and sintering, as shown in Figure 4.2 below. The part is firstly printed layer by layer onto the build plate via the extrusion printer. The feedstock is a mixture of metal powder and polymer binder, which allows the material to be extruded at temperatures well below the metal's melting temperature (DM Knowledge Base, 2020).

After the part is printed, the second stage is to remove the polymer binder by immersing the part in the de-bind fluid. The final stage is to sinter the part in the furnace at temperatures approaching the melting point of the metal, allowing the metal powder to fuse together to form the finished part. During sintering, BMD parts shrink by approx. 20% in size, and therefore parts are automatically printed larger by the printing software using scaling factors (DM Design Guide, 2020). BMD parts are also printed on a raft base layer to facilitate shrinking during the sintering process.

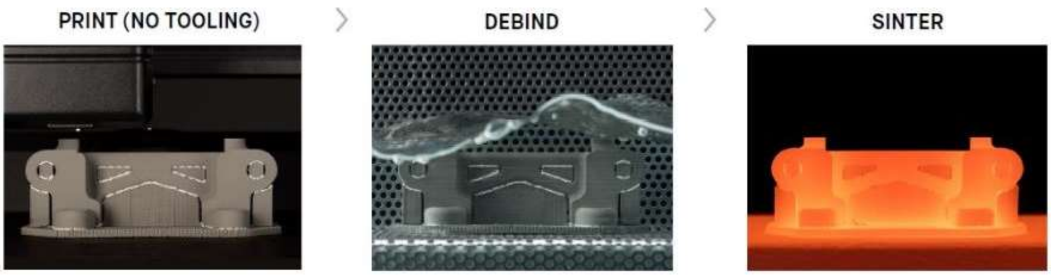

Figure 4.2: Bound metal deposition process (DM Knowledge Base, 2020)

4.2.2 Printing Parameters

BMD parts are designed to be printed with a shell and infill, as shown in Figure 4.3 below. The main printing parameters are the extrusion layer width, layer height, shell thickness and infill.

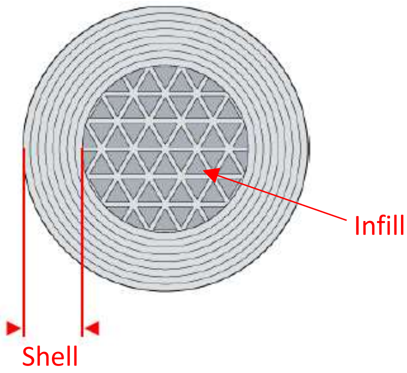

Figure 4.3: Shell thickness and infill (DM Design Guide, 2020)

The layer width is the horizontal thickness of the extrusion bead, and generally corresponds to the extrusion nozzle diameter. For the high resolution printhead (diameter 0.25 mm) on the Desktop Metal Studio System, the default layer width is 0.3 mm (DM Fabricate Settings, 2020).

The layer height is the vertical thickness of the extrusion bead. The layer height is a trade-off between surface quality and print time, with finer layer heights better for parts with fine features. For the high resolution printhead, the default layer height is 0.1 mm (DM Fabricate Settings, 2020)

The shell thickness is the width of the printed part wall. Increasing the shell thickness increases the strength of the part, although, also increases the weight of the part. The standard shell thickness is 1mm, and the maximum advised is 10 mm (DM Design Guide, 2020).

The infill is the interior structure of the printed part. The Desktop Metal Studio System currently only prints copper using 2D triangular infill as standard (DM Knowledge Base, 2020). Although, an alternative approach is to model the internal structure directly using computer aided design and then print the part as solid.

For the customised internal structure approach, the printing software required the internal walls to be at least two toolpaths wide for printing (DM Design Guide, 2020). It was unknown which thin-walled additive structures, such as the gyroid, could be customised using this approach for PCM heat transfer.

4.2.3 Material Properties

The stated composition of BMD sintered copper is 99.9% copper and 0.01% oxygen (DM Material Data Sheet, 2020). However, the BMD method is affected by porosity due to the printing and sintering process. The total volume of porosity typically comprises 2-5% of the solid part (DM Knowledge Base, 2020).

Table 4.1 below provides the known material properties of BMD copper compared to traditionally manufactured high conductivity copper alloy. In comparison, the density of BMD copper is 2% less, the ultimate tensile stress is 30% less, the electrical conductivity is 16% less and the coefficient of thermal expansion is 2% less. Noting, the thermal conductivity of BMD copper was not reported, and it was unknown how it was affected by porosity.

Table 4.1: Material properties of BMD copper and high conductivity copper alloy (DM Material Data Sheet, 2020), (Conex, 2020)

	BMD Copper Studio System	High Conductivity Copper Alloy
Density (kg/m^3)	8750	8940
Ultimate Tensile Strength (MPa)	195	280
Electrical Conductivity	85.2 %IACS*	101 %IACS*
Coefficient of Thermal Expansion (/◦C)	17.43E^{-6}	17.7E^{-6}
Thermal Conductivity (W/m·K)	-	391

*IACS - International Annealed Copper Standard

4.2.4 Knowledge Gaps

Due to the porosity and reduced material property values, it was unknown how the thermal conductivity was affected, and thereby the thermal performance of BMD parts. It was also unknown which thin-walled additive structures, such as the gyroid, could be printed for PCM heat transfer enhancement. Furthermore, it was also unknown whether BMD parts could provide leakproof vacuum integrity for PCM containment. These aspects were experimentally investigated in this Chapter using the Desktop Metal Studio System. The BMD copper printing was investigated with the Studio System high resolution nozzle, to achieve the smallest base size and thinnest structures possible for gyroid.

4.3 PorOSITY INVESTIGATION

The porosity of BMD was firstly investigated to quantity the type and level of the porosity present in the manufacturing process. In addition, thermal models were also created, based on the porosity observed, to estimate the effect on the thermal conductivity.

4.3.1 Methodology

The porosity was investigated using optical microscopy and scanning electron microscopy. Two BMD copper samples were dissected and polished to a mirror finish to investigate the internal porosity. One sample was printed horizontally to investigate the porosity between the print layers, and one sample was printed vertically to investigate the porosity within the print layers.

The BMD printed samples were rectangular blocks with a cross-section of 10x10 mm and a height of 30mm, as shown in Figure 4.4. The printing parameters utilized were a 0.3 mm layer width, 0.1 mm layer height, 4 wall line count shell thickness and solid infill to allow cutting. The porosity was investigated within the 4 wall line extrusions, as shown in Figure 4.4.

4.3.1.1 BMD Sample Preparation

The block samples were cut in half across the 10x10 mm section using an aluminium oxide blade and the samples were secured in round discs of a cold curing resin (Technovit 4006) for metallographic grinding and polishing. The contemporary preparation method for copper metallographic testing was followed (Vander Voort, 2000), with the five-step method used to prepare the samples shown in Table 4.2 below. The first two steps were grinding processes using the Struers TegraForce5 and the final three steps were polishing processes using the Presi Mecatech 250 SPC.

Table 4.2: Method for copper sample preparation

Step	Surface/Abrasive	RPM	Direction	Load (N)	Time (min)
1	320-grit SiC	300	Complementary	15	Until flat
2	500-grit SiC	300	Complementary	15	1
3	3um diamond paste on cloth pad	150	Complementary	22	2
4	1um diamond paste on cloth pad	150	Complementary	22	2
5	Colloidal silica on micro cloth pad	150	Opposite	22	2

The BMD samples for the porosity investigation are shown in Figure 4.4 below, and includes the toolpath profile, printed blocks, sintered blocks, and final cut and polished samples.

(a)

(b)

(c)

(d)

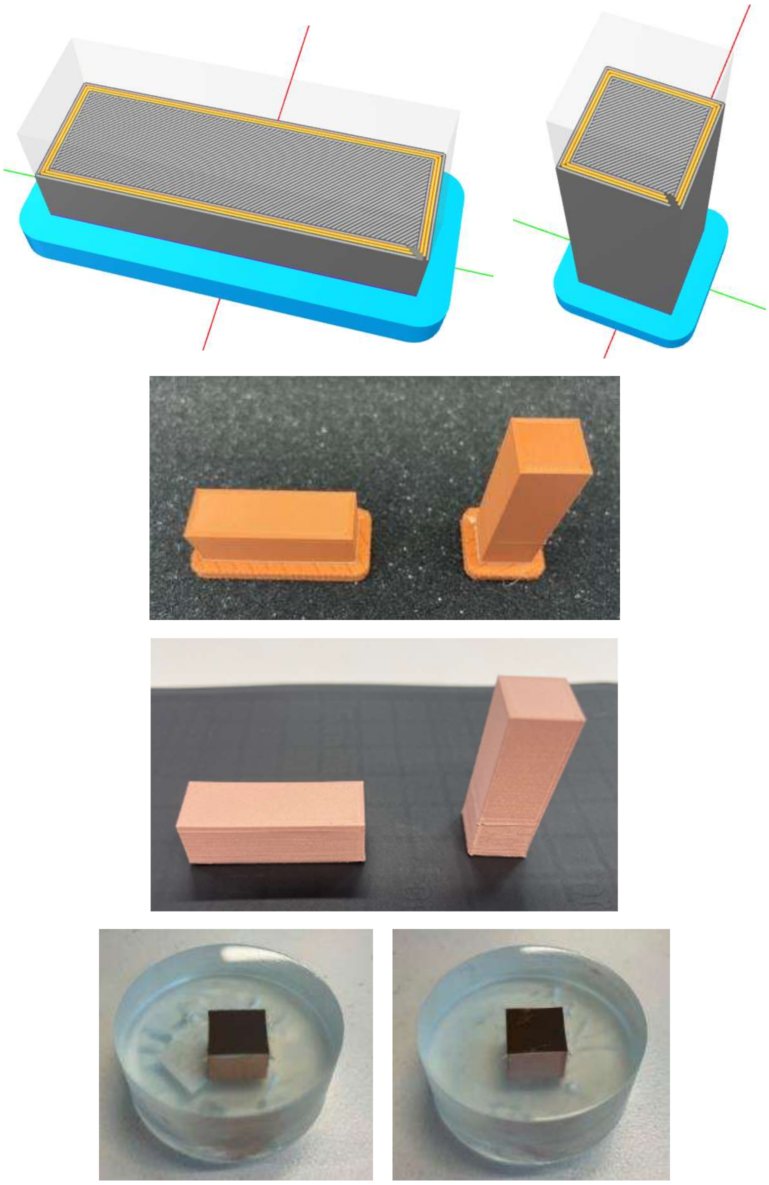

Figure 4.4: Horizontally (left) and vertically (right) printed blocks for the porosity investigation (a) toolpath profile, (b) printed blocks, (c) sintered blocks, (d) final cut and polished samples

4.3.1.2 Optical Microscopy

The porosity in the printed samples was investigated using optical microscopy. The apparatus utilised was the Olympus SC50 and the images were analysed using the ImageJ software. The sizes of the pores were measured, and the porosity percentages were calculated. The porosity percentages were calculated from the highlighted pore regions using the threshold tool. The red colour channel of the image was utilised for the threshold tool since it provided the most contrast between the mirror material and the non-reflective pores. The threshold was adjusted to capture the pore regions.

4.3.1.3 Scanning Electron Microscopy

The porosity in the samples was also investigated using a scanning electron microscope (SEM) to confirm the pore regions were in fact pores and not particles due to the limits of visual optical methods. The scanning electron microscopy, Carl Zeiss Microscopy Crossbeam 540 with GEMINI II column, equipped with a field emission gun was operated at 15 kV. The images were obtained with an Everhart-Thornley secondary electron detector. In addition, the Energy Dispersive Spectroscopy (EDS) method was used to investigate the material elemental composition of the pore regions. With EDS, a region of porosity was selected and irradiated with electrons resulting in the emission of X-rays. The X-ray signal detected were displayed as a map sum spectrum and EDS map, allowing the chemical elements of the sample area to be identified.

4.3.1.4 Mass-Spectrometry

A sub-section of the BMD copper sample was also externally tested using mass-spectrometry to provide the composition of the sample material tested, since the SEM-EDS method was very targeted to a particular area of interest.

4.3.1.5 Thermal Model

The porosity observed was translated into numerical models to investigate the effect of the porosity on the thermal conductivity. A steady-state analysis was performed using ANSYS Fluent, with the energy equation as stated in Equation 4.1 below, where k is the material thermal conductivity, T is the temperature and S is the energy source term (ANSYS Theory Guide, 2021).

$$\nabla(k\nabla\mathrm{T}) = S \qquad \text{Equation 4.1}$$

A temperature difference (ΔT) was applied to the model boundaries and the heat flux at each boundary was output from the model. The effective thermal conductivity (k_{eff}) of the model was then calculated using Equation 4.2 below, where L is the model distance, ΔT is the temperature difference and $\dot{Q}/A$ is the area weighted heat flux at each boundary (Cengel, 2002).

$$\frac{\dot{Q}}{A} = \frac{k_{eff}\Delta T}{L} \qquad \text{Equation 4.2}$$

The effective thermal conductivity (k_{eff}) was compared to the material thermal conductivity (k) to determine the effect of the porosity on the model.

4.3.2 Results of Porosity Investigation

The following section presents the porosity observed for the BMD samples, as well as the thermal numerical results based on the observed porosity. Two types of porosity were observed in the BMD printed block samples. Firstly, macro porosity due to the extrusion printing process, and secondly, micro porosity due to the sintering process. Refer to the BMD process (printing, debinding and sintering) illustrated in the previous Figure 4.2.

The results are firstly presented for the macro and micro porosity observed with optical microscopy, followed by the results for the scanning electron microscope energy dispersive spectroscopy and mass spectrometry. Under the optical microscope light, the porosity in the samples was revealed as dark regions and dense metal appears as light and reflective (GE, 2021). Lastly, the thermal modelling results are presented based on the observed macro and micro porosity.

4.3.2.1 Macro Porosity

The macro porosity due to the extrusion printing process is shown in Figure 4.5 below for the vertically printed sample. The image shows the top-down view of the 4-line extrusion shell wall. The measured extrusion widths were on average 265 Micron. The porosity between the extrusion widths is clearly visible. The measured porosity gaps between the extrusions were on average 30 Micron at their largest. Refer to Appendix D for measurements. The percentage of the macro porosity is measured only for the horizontally printed sample in the next section, sine the overall macro porosity percentage in the 4-line extrusion wall was better represented by the horizontal slicing of the sample.

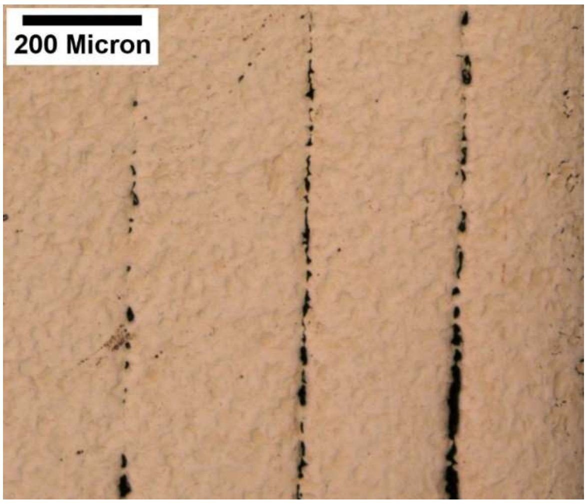

Figure 4.5: Toolpath macro-porosity (vertical sample)

The macro porosity from the horizontally printed sample is shown in Figure 4.6 below. The image shows the side view of the 4-line extrusion shell wall and consists of 10 stacked layers. The measured extrusion heights were on average 85 Micron. The porosity at the corners of each extrusion bead is clearly visible. The measured porosity gaps between the stacked layers were on average 20 Micron at their largest. The percentage of macro porosity observed ranged from 1.25% to 1.50%, with an average macro porosity of 1.38%. Refer to Appendix D for measurements.

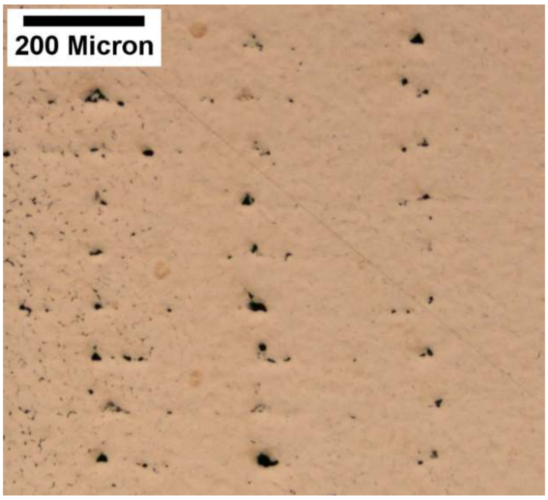

Figure 4.6: Toolpath macro-porosity (horizontal sample)

Using the observed toolpath dimensions from the vertically and horizontally printed samples, a 1x1x1 mm 3D model was created with voids representing the toolpath porosity, as shown in Figure 4.7 below. Based on the toolpath dimensions, the calculated porosity in the 3D model was 1.45%, which was comparable to the observed average macro porosity of 1.38% in the horizontally printed sample. The 3D toolpath model was used to estimate the effective thermal conductivity due to toolpath porosity, which is presented at the end of the porosity results.

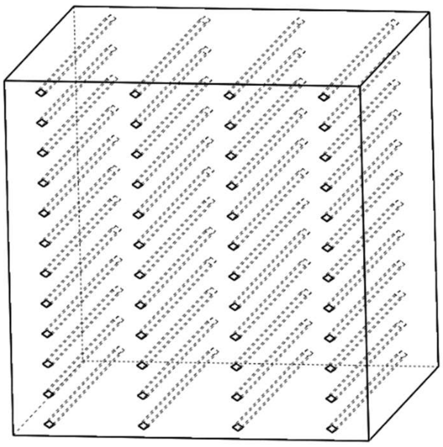

Figure 4.7: 3D model (1x1x1 mm) toolpath porosity

4.3.2.2 Micro Porosity

The micro-porosity due to the sintering process was observed throughout the entire material for both the vertically and horizontally printed samples. Figure 4.8 shows the representative micro-porosity observed using the optical microscope. The image below was taken from the vertically printed sample. Ten images of the micro porosity were analysed from each of the vertically printed and horizontally printed samples. For the horizontally printed sample, the porosity percentage observed ranged from 0.72% to 1.26%, with an average porosity value of 0.95%. For the vertically printed sample, the porosity percentage observed ranged from 0.80% to 1.28%, with an average porosity value of 1.03%. Refer to Appendix D for the porosity percentages measured.

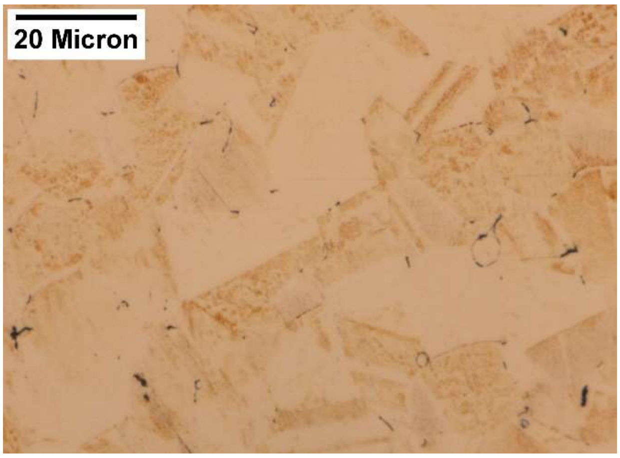

Figure 4.8: Micro-porosity (vertical sample)

Based on the observed micro-porosity (Average 0.99%), a 1x1 mm 2D model was created. The 2D porosity model was sketched from a typical image (100x100 Micron), as shown in Figure 4.9 below, and then used to create a 1x1 mm 2D model with approximately 1.00% porosity. The 2D micro porosity model was used to estimate the effective thermal conductivity, which is presented along with the macro porosity at the end of the porosity results.

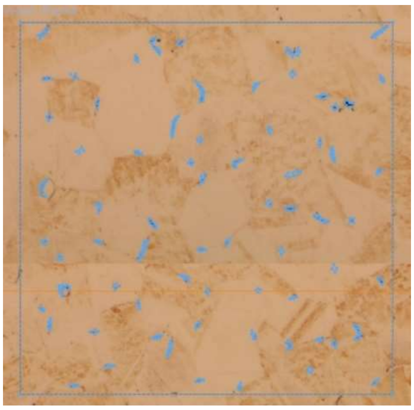

Figure 4.9: 2D model (1x1 mm) micro-porosity

4.3.2.3 Scanning Electron Microscope Energy Dispersive Spectroscopy

The micro-porosity in the samples was investigated with SEM-EDS (Scanning Electron Microscope Energy Dispersive Spectroscopy) to further examine the micro-porosity due to the limits of optical microscopy. Figure 4.10 below shows the typical micro-porosity observed on the scanning electron microscope with the image obtained using the Everhart-Thornley secondary electron detector. The image shows micro-pores of less than 1 micron in length to 2 microns in length.

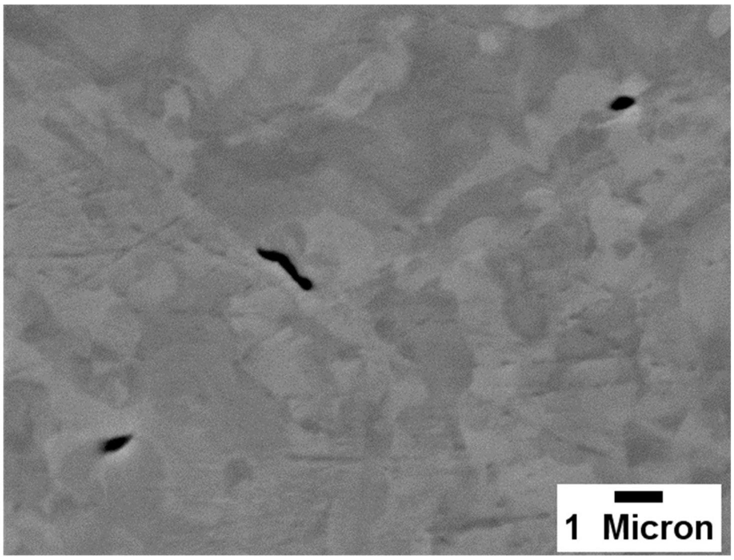

Figure 4.10: SEM image of micro-porosity, magnification 5000

The Energy Dispersive Spectroscopy (EDS) method was used to investigate the material elemental composition of the micro-pore regions to establish that the dark regions in the sample images were in fact pores and not inclusions or foreign particles. Figure 4.11 below shows the area of micro-porosity selected for EDS mapping and also shows the EDS mapping results with the copper elemental composition overlay.

The EDS mapping results showed that the only chemical element detected of significance was copper. Therefore, it was concluded that the dark regions were micro porosity present in the sample due to the sintering process as the copper particles fused together. Note, the EDS map sum spectrum results for the EDS mapped area is provided in Appendix E.

(a)

(b)

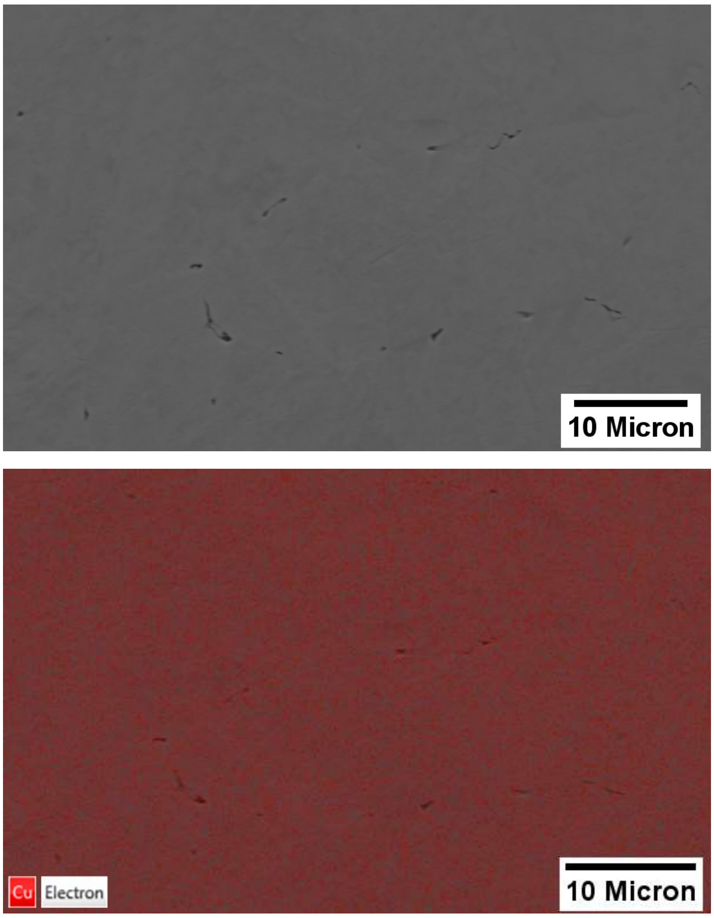

Figure 4.11: SEM-EDS material elemental composition (a) EDS site, (b) EDS copper mapping

4.3.2.4 Mass-Spectrometry

A section of the BMD copper was also externally tested using mass spectrometry to provide the overall composition of the sample. The results were obtained by ICP-AES (Inductively coupled plasma atomic emission spectroscopy) and are provided in Table 4.3 below. The results provide that over 99.9% of the sample was copper, with only a 0.003% oxygen content. The results are consistent with high conductivity copper, which typically contains an oxygen content of 0.001% to 0.003% and an impurity level of 0.03% (Walton, 2017). Whilst the composition of BMD copper is consistent with high conductivity copper, the porosity needs to be however considered for the thermal conductivity.

Table 4.3: Mass spectrometry results by ICP-AES

Cu (%)	Si (%)	Fe (%)	Zn (%)	Pb (%)	C (%)	Ni (%)	Mn (%)	Sn (%)	Al (%)	P (%)
Bal	0.005	0.037	0.004	0.001	0.001	0.004	0.002	<0.001	0.003	<0.002

As (%)	Sb (%)	Be (%)	Cd (%)	Bi (%)	In (%)	Ag (%)	Te (%)	Ti (%)	Zr (%)	O (%)
<0.001	<0.001	<0.001	<0.001	0.002	<0.001	<0.002	<0.002	0.008	0.002	0.003

4.3.2.5 Porosity Thermal Modelling Results

The following effective thermal conductivity results were obtained with the 3D model created for the macro toolpath-porosity (Refer to Figure 4.7) and the 2D model was created for micro-porosity (Refer to Figure 4.9). To recap, the porosity percentage was 1.45% for the macro-porosity model and 1.00% for the micro-porosity model. Thus, equating to a total porosity of 2.45%.

For the 3D macro porosity model, the effective thermal conductivity was examined both along the extrusion layers (XY-direction) and through the extrusion layers (Z-direction). For the 2D micro porosity model, it was assumed the same in all directions.

Incremental temperature difference from 0.01 to 1 degree Celsius were applied to the 1 mm length models. The results showed that the effective thermal conductivity reduced due to the porosity and for all temperature differences the results achieved were the same. Table 4.4 below provides a summary of the results. It was assumed that the total reduction was the addition of the macro and micro porosity models.

The results showed that the thermal conductivity was the best along the extrusions layers (i.e. in the horizontal XY-direction). The results also showed that the micro-porosity also had a large effect on the thermal conductivity. Overall, the thermal conductivity reduction through the extrusion layers (i.e. in the vertical Z-direction) was 3% higher than along the extrusion layers.

Table 4.4: Effective thermal conductivity reduction relative to material thermal conductivity

	3D Model Macro Porosity Reduction	2D Model Micro Porosity Reduction	**Total Reduction**
XY-Direction (Along the layers)	1.4%	5.2%	**6.6%**
Z-Direction (Through the layers)	4.4%	5.2%	**9.6%**

4.4 THERMAL INVESTIGATION

The thermal conductivity of BMD copper was experimentally tested in this next investigation to verify and quantify the thermal performance of BMD parts for heat dissipation.

4.4.1 Methodology

The thermal conductivity was tested using the Transient Plane Source (TPS) method, which measures a temperature response when a heat signal was applied (C-Therm, 2020). Two BMD copper samples were printed using the Desktop Metal Studio System. One sample was printed horizontally to measure the thermal conductivity in the XY-print direction and the one sample was printed vertically to measure the thermal conductivity in the Z-print direction.

4.4.1.1 Transient Plane Source Method

The apparatus utilised was the C-Therm Trident instrument. For high thermal conductivity metals (greater than 90 W/m·K), the Trident TPS method required a solid cylindrical test sample, with a minimum height of 38.1mm and a precise diameter of 17.76 ± 0.05 mm, corresponding to the sensor dimensions for minimal heat loss. The accuracy specification for high thermal conductivity metals was 5% (C-Therm, 2020).

The test setup for high conductivity metals is shown in Figure 4.12 below. The copper cylinder samples were placed on top of the one-sided sensor/heater. A plastic holder sleeve was utilised to ensure the samples were centered and a weight was placed on top of the samples to ensure good contact with the sensing element. The contact agent between the sensor/samples was three drops of water on the sensor as specified by C-Therm for high thermal conductivity metals (C-Therm, 2020).

Figure 4.12: Test setup for copper samples

4.4.1.2 BMD Samples

The BMD copper cylinders were printed horizontally and vertically. The horizontally printed cylinder was used to measure the thermal conductivity along the print layers (XY-direction) and the vertically printed cylinder was used to measure the thermal conductivity through the print layers (Z-direction).

The cylinders were printed 2 mm oversize and then machined to the high dimensional tolerances required by the C-Therm Trident instrument. The printing parameters utilised were a 0.3 mm layer width, 0.1 mm layer height, 4 wall line count shell thickness and solid infill. The BMD copper cylinder samples are shown in Figure 4.13 below, and includes the toolpath profile, printed parts, sintered parts, and final machined samples. Note, the infill profile were diagonal extrusions.

(a) (b) (c) (d)

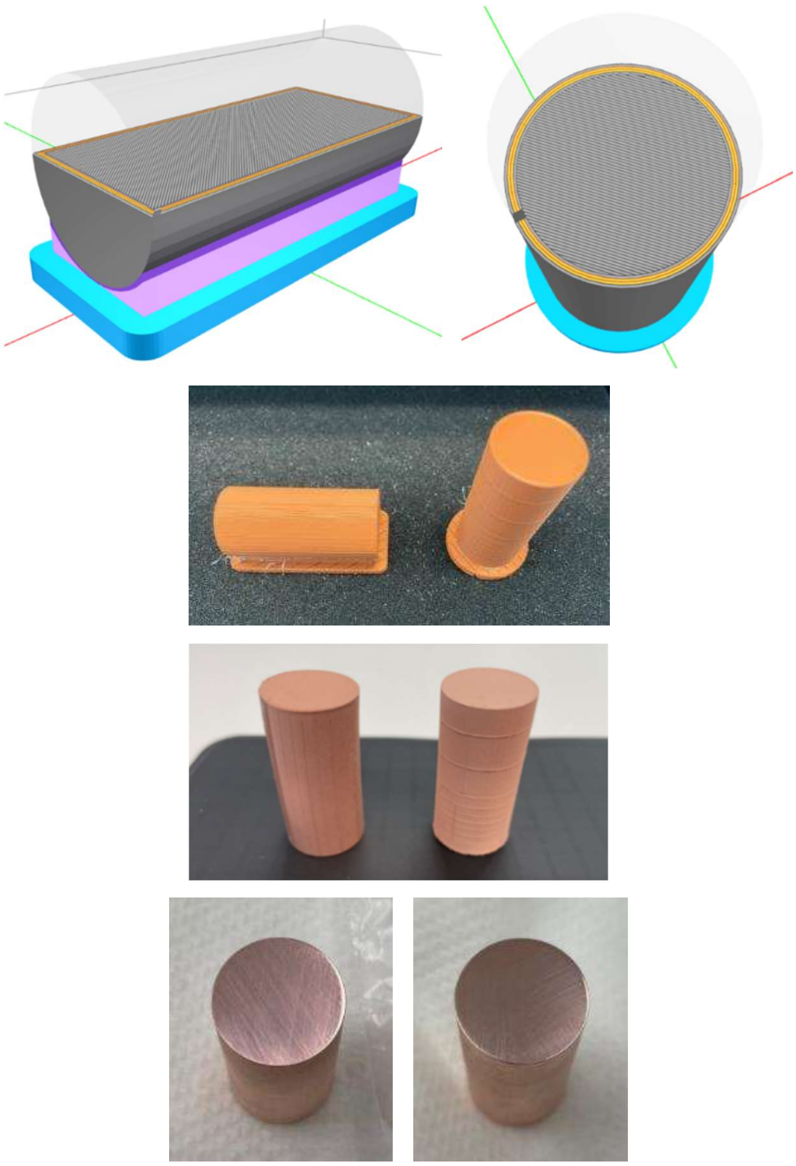

Figure 4.13: Horizontally and vertically printed cylinders for thermal conductivity testing
(a) toolpath profile, (b) printed parts, (c) sintered parts, (d) final machined samples

4.4.1.3 Thermal Conductivity/Effusivity

The C-Therm Trident instrument measured the effusivity of the material, which is the material's ability to exchange thermal energy. The instrument calculated the effusivity (ε) using Equation 4.3 below, where G is the power flux supplied to the sensor, ΔT is the change in sensor surface temperature and t is the time measured from the start of the process (C-Therm, 2020). The methodology assumed no thermal contact resistance at the interface between the sensor and the sample, and therefore sample contact with the sensor surface was critical. The method conformed to ASTM D7984 (C-Therm, 2020).

$$\Delta T = \frac{1.1284\, G\sqrt{t}}{\varepsilon_{sensor} + \varepsilon_{sample}} \qquad \text{Equation 4.3}$$

The thermal conductivity (k) of the sample material was then calculated from the effusivity (ε) using Equation 4.4 below, where ρ is density and c_p is the specific heat. Accordingly, the density and specific heat capacity of BMD copper were also investigated.

$$k = \frac{\varepsilon^2}{\rho\, c_p} \qquad \text{Equation 4.4}$$

4.4.1.4 Density

The densities of the BMD test cylinders were obtained using hydrostatic weighing, by comparing the dry weight and submerged weight of the samples. The density (ρ) was calculated using Equation 4.5 below, where W_g is the weight of the sample in air, W_a is the apparent weight of the sample submerged in water and ρ_w is the water density (Davis, 2021). Ultrapure water from the ELGA PURELAB with very low levels of impurities was utilised.

$$\rho = \frac{W_g}{W - W_a}\rho_w \qquad \text{Equation 4.5}$$

4.4.1.5 Specific Heat Capacity

The specific heat capacity of BMD copper was measured using differential scanning calorimetry (DSC). The apparatus utilised was the Netzsch Pegasus DSC 404. Due to the small nature of the test samples required for DSC, the BMD test cylinders were not measured directly.

The ideal samples were 6 mm diameter flat disks for good contact (Netzsch, 2021). Two BMD copper discs were printed, with a diameter of 6 mm and height of 1.2 mm. The disc samples were printed with solid infill and after sintering, the disc samples were polished to ensure good thermal contact with the crucible floor. Figure 4.14 shows the two BMD copper discs prepared for DSC.

Figure 4.14: BMD copper discs 1 and 2

The Pegasus DSC held two small graphite crucibles in a temperature-controlled furnace. The first crucible was empty and was used as a reference, and the second crucible contained the sample material. The reference and sample were heated to a controlled temperature program. The temperature difference between the reference and sample was measured and converted to specific heat using a calibration. A sapphire disc was used for the calibration and was subjected to the same temperature-controlled program. In addition, a baseline correction was performed with the two empty crucibles to account for any small variations between the two crucibles.

The controlled temperature program utilised is provided in Table 4.5 below. The heating rate used was 20 K/min from 25°C to 150 °C. Prior to the heating stage, the temperature was held constant for 20 minutes (Isothermal Phase) to allow the material and chamber to stabilise, which helped reduce the accumulation of thermal lag (Netzsch, 2021).

Table 4.5: DSC heating program

Phase	Time Start (min)	Time End (min)	Temperature Start (°C)	Temperature End (°C)	Heating Rate (K/min)
Start Up	0:00	1:00	Room Temp.	25	-
Isothermal	01:00	21:00	25	25	-
Heating	21:00	27:00	25	150	20
Isothermal	27:00	47:00	150	150	-

4.4.2 Results of Thermal Investigation

The following section presents the thermal conductivity results for the horizontally and vertically printed cylindrical copper samples. To begin with, the density and specific heat capacity results of the BMD copper samples are firstly presented, which were used as an input for the BMD copper thermal conductivity calculations.

4.4.2.1 Density

Figure 4.15 shows the density results for the BMD copper horizontally and vertically printed cylinders. The densities were calculated using the average measured dry and submerged weights. Refer to Appendix F. The error in the average calculated density was ± 0.01 g.

The results were compared to the reported density of BMD copper (DM Material Data Sheet, 2020) and the reported density of cast high conductivity copper (Conex, 2020). Noting, the reported density of BMD copper is 2% less than copper. However, the level of porosity in BMD parts is ultimately dependent on the part geometry and toolpath, and typically the total volume of porosity in BMD parts comprises 2-5% of the solid part (DM Knowledge Base, 2020).

The results showed that the density of the vertically and horizontally printed cylinders was 3.5-4% less than the density of cast high conductivity copper, and 1.5-2% less than the reported density of BMD copper. Accordingly, the densities of the printed cylinders were still within the reported 2-5% volume reduction exhibited in BMD parts.

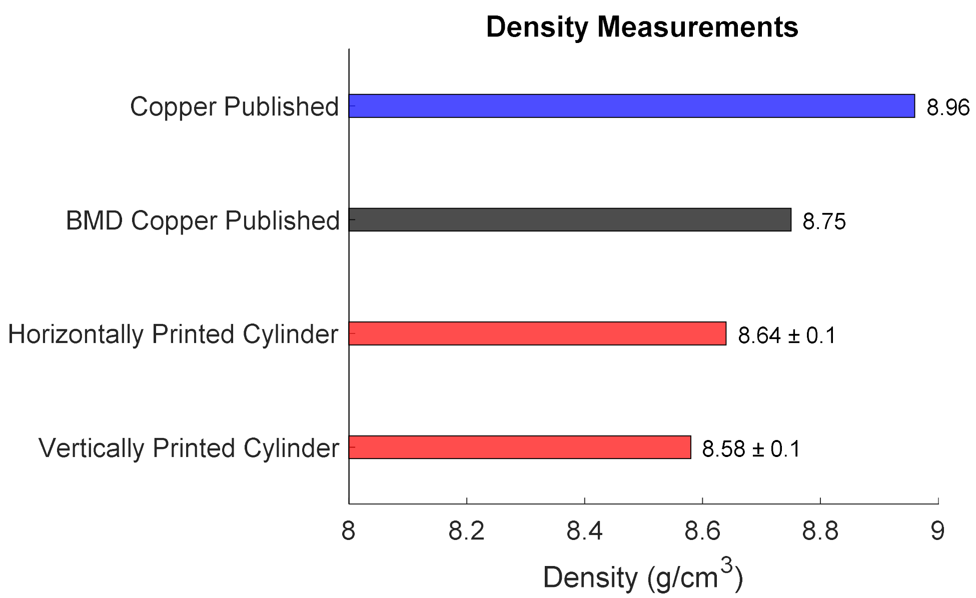

Figure 4.15: Density results

4.4.2.2 Specific Heat Capacity

Figure 4.16 shows the specific heat results for the BMD copper samples 1 and 2. The specific heat results were obtained from the DSC heating phase. The DSC voltage outputs for the BMD copper samples, including sapphire calibration are summarised in Appendix G.

The specific heat results are shown for the temperature range of 80°C to 120°C, where the DSC values stabilised. The mean difference between the BMD copper samples was 1.3%. The results in Figure 4.16 were compared to the literature values for pure copper (White et al., 1984). The results show that the BMD samples were within a 1% error margin of the literature mean.

Since the DSC results were within a reasonable error of the published data, the published data for the copper specific heat capacity at 20°C was utilised for the thermal conductivity calculation, namely 385 J/Kg°C (White et al., 2014).

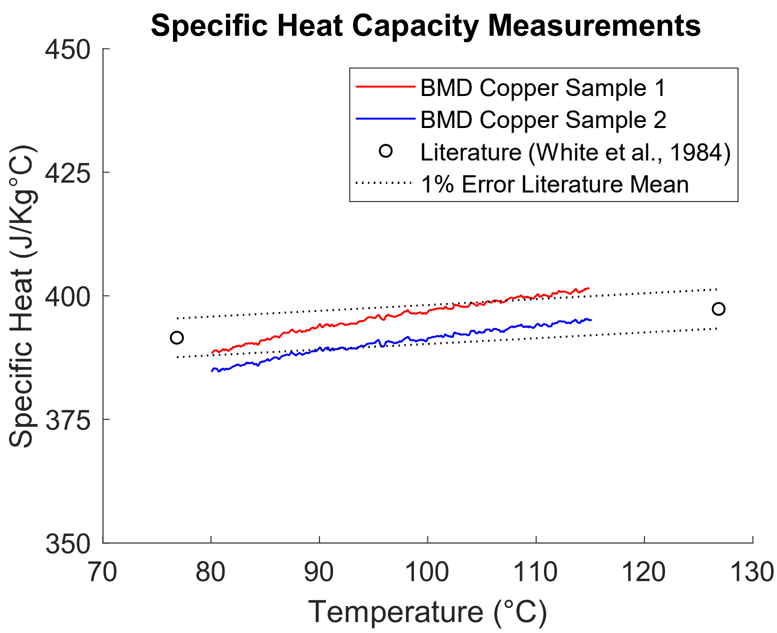

Figure 4.16: Specific heat capacity results

4.4.2.3 Thermal Conductivity

The thermal conductivity results are presented in Figure 4.17 for the horizontally and vertical printed BMD samples. The BMD samples were compared to a reference copper cylinder provided with the instrument, which had a reported thermal conductivity of 398 W/m·K (C-Therm, 2020). Noting, the purpose of the copper reference material was to verify the function equipment and did change the pre-loaded calibration (C-Therm, 2020).

One calibration test was performed for the reference copper cylinder to verify accuracy. The average thermal conductivity measured was 384.6 W/m·K, resulting in a 3.4% lower thermal conductivity compared to the reported reference value (398 W/m·K). However, the average measurement was within the 5% accuracy specification for high thermal conductivity metals (C-Therm, 2020).

For the BMD samples, three tests were performed for each sample with eight measurements per test. The standard deviation is included in Figure 4.17 below. Noting, the recommended number of measurements per test was 5-10 (C-Therm, 2020). The full test results are provided in Appendix H.

The average thermal conductivity of the horizontally printed sample was 349.5 W/m·K, which represented a 9.1% reduction compared to the reference test. Whereas the average thermal conductivity of the vertically printed sample was 333.3 W/m·K, which represented a 13.3% reduction compared to the reference test. Thus, the thermal conductivity along the print layers (horizontally printed sample) was 4.2% higher than the thermal conductivity through the print layers (vertically printed sample), which aligned well with the thermal porosity models in the previous investigation.

The overall thermal conductivity of the BMD copper was 341.4 W/m·K (average of all horizontal and vertical results), representing a 11.2% reduction compared to the reference measurement. Based on the reported reference copper thermal conductivity (398 W/m·K), the adjusted thermal conductivity for the BMD copper was 353.3 W/m·K (11.2% reduction).

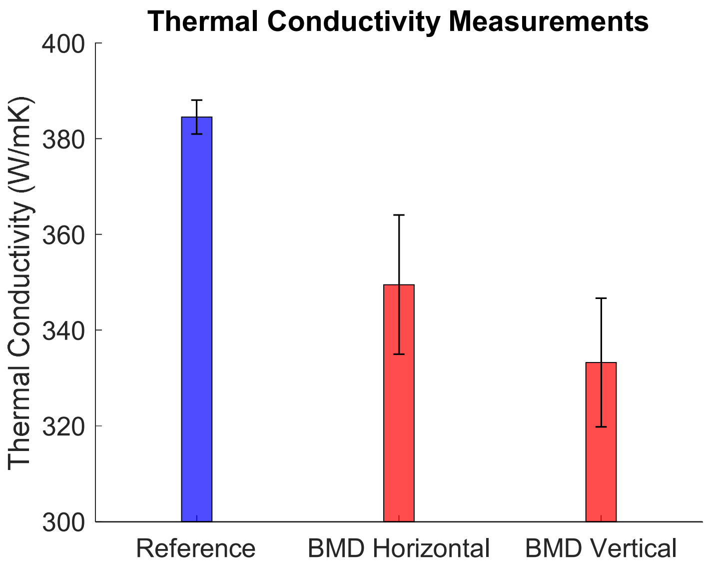

Figure 4.17: Thermal conductivity results

4.5 GYROID PRINTING INVESTIGATION

In the next investigation, the printing of the gyroid structure was explored with BMD to determine the smallest wall thickness and base size achievable. In chapter 3, the gyroid structure demonstrated the best overall PCM heat transfer performance for transferring heat in all three directions. In particular, the results also showed that smaller base sizes with thinner structures improved the PCM heat transfer performance. Accordingly, lightweight small base size gyroid structures were pursued with BMD on the Desktop Metal Studio System.

4.5.1 Methodology

The method used to print the gyroid was to model the structure directly using computer aided design, and then print the part as solid using BMD copper. This methodology firstly describes the process used to create the gyroid using computer aided design (CAD), and then the printing parameters utilised to print the gyroid on the Desktop Metal Studio System.

4.5.1.1 Gyroid - Computer Aided Design (CAD)

The gyroid structure was created in CAD by importing the gyroid base surface from Matlab into SolidWorks. The smallest surface that was needed to create the gyroid unit cell was the 1/8 surface, as shown in Figure 4.18 below. Using then 1/8 surface, the gyroid unit cell could be evolved using the process shown, whereby the 1/8 surface was rotated and translated into the eight positions.

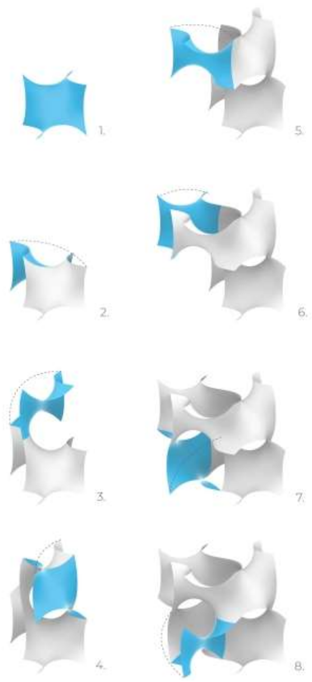

Figure 4.18: Evolution of a gyroid surface (Whitehead, 2019)

The 1/8 gyroid surface was created in Matlab using Equation 4.6, which is the mathematical representation of the sheet-based gyroid minimal surface, where B is the dimension of the gyroid unit cell (Alketan et al., 2019). The gyroid is a minimal surface, meaning that the surface has a mean curvature of zero at every point.

$$\cos\left(\frac{2\pi x}{B}\right)\sin\left(\frac{2\pi y}{B}\right)+\cos\left(\frac{2\pi y}{B}\right)\sin\left(\frac{2\pi z}{B}\right)+\cos\left(\frac{2\pi z}{B}\right)\sin\left(\frac{2\pi x}{B}\right)=0 \qquad \text{Equation 4.6}$$

The 1/8 gyroid minimal surface was then exported from Matlab using the ‘triangulation’ command. Figure 4.19 show the triangulated surface in SolidWorks. The triangulated surface was used to create a new surface in SolidWorks, which could be used to build the gyroid internal structure. The new surface was created in SolidWorks by using the ‘surface fill’ command with 6 boundary sketches and 3 internal guide sketches, as shown in Figure 4.19 below.

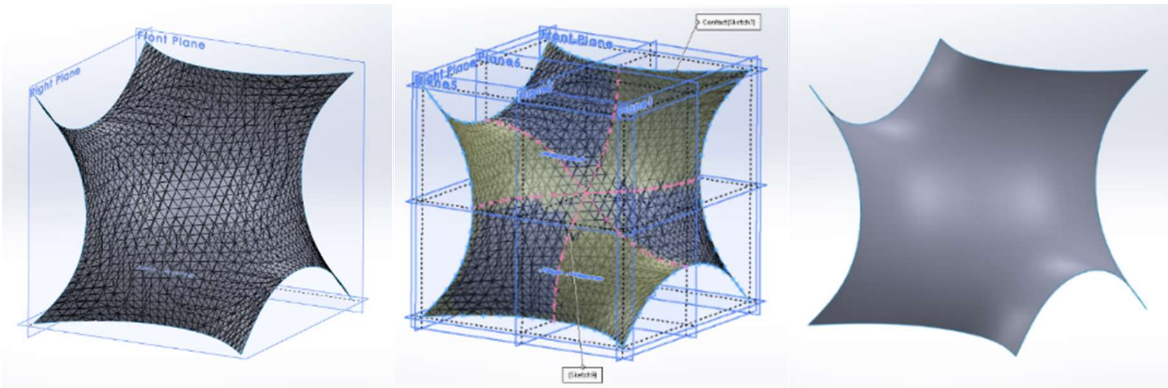

Figure 4.19: Triangulated surface, bounding sketches and final surface

The gyroid unit cell was then created using the eight-step process, and copied and translated in all XYZ directions to the required size, as shown in Figure 4.20 below. Noting, the gyroid structure is triply periodic, meaning that the gyroid unit cell repeats in all three axes. The gyroid surfaces were then given a wall thickness in SolidWorks and then exported as an STL file for printing.

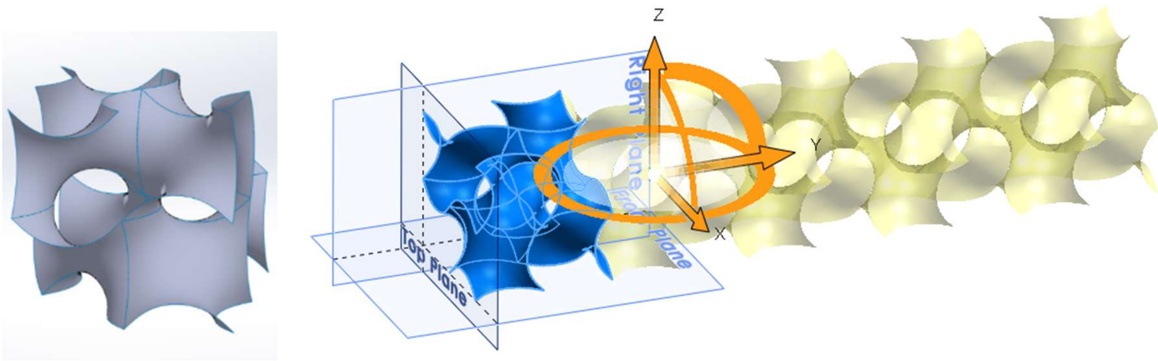

Figure 4.20: Gyroid unit cell translation

4.5.1.2 Gyroid BMD Printing

Initially, to investigate the gyroid printing on the Desktop Metal Studio System, open rectangular containers of size 40x40x10 mm with an outer wall thickness of 1 mm, as shown in Figure 4.21 below, were printed. Two gyroid base sizes were investigated, namely unit cell sizes of 8 mm and 10 mm. Note, the gyroid channel size is half the unit cell size (i.e. gyroid channel sizes of 4 mm and 5 mm).

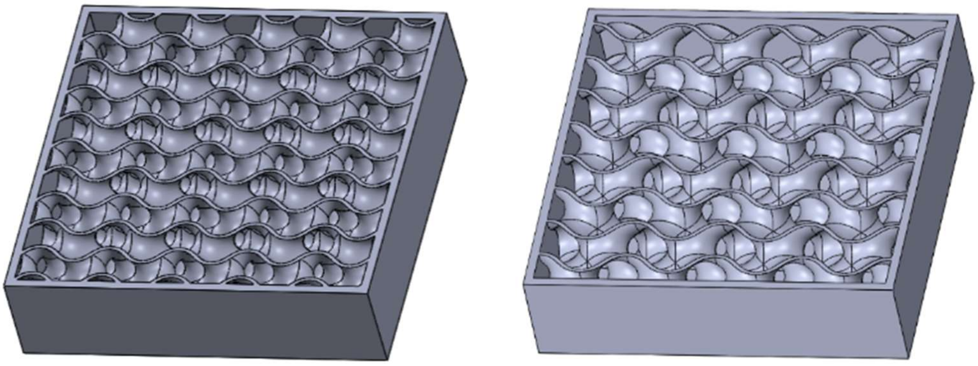

Figure 4.21: Gyroid rectangular containers – Left: Channel size 4 mm, Right: Channel size 5 mm

In Chapter 3, these base sizes were modelled with a wall thickness of 0.4 mm and 0.5 mm respectively to maintain the same PCM volume fraction. However, in this investigation, both gyroid base sizes were modelled using a 0.4 mm wall thickness and printed using the 0.25 mm high resolution printhead.

The toolpath program for the gyroid structure is shown in Figure 4.22 below. The gyroid structure was printed with sinusoidal extrusions layer by layer and the intermediatory gyroid layers were printed with closed loops. The printing parameters used were a 0.3 mm layer width and a 0.1 mm layer height. The gyroid walls were printed with 2 extrusion lines (i.e. pre-sintered layer width of 0.6 mm). Noting, the minimun wall thickness on the Desktop Metal Studio System was 2 extrusion lines. The outer walls were printed with 4 extrusion lines (i.e. pre-sintered layer width of 1.2 mm).

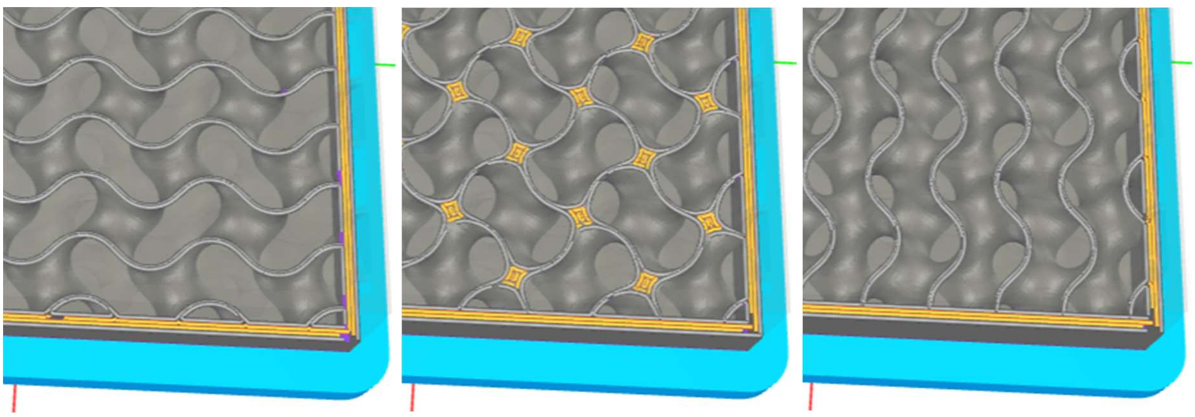

Figure 4.22: Gyroid print layer toolpath program

During sintering, the printed wall thicknesses reduced in size due to the sintering shrinking process. To account for the reduction, scaling factors are automatically applied by the printing software and BMD parts are printed oversize. The sintering scaling factors for BMD copper are 18% in the XY-direction and 19% in the Z-direction.

Based on the 18% XY-sintering factor, the estimated outer wall thickess (4 extrusions) was approx. 0.98 mm (~1 mm) and the estimated gyroid layer thickness (2 extrusions) was approx 0.49 mm. However, the gyroid walls were printed at an angle relative to the build direction. As a result, the gyroid effective wall thickness was a function of the wall angle, as shown in Figure 4.23 below for a diagonally printed wall with 2 side by side extrusions into the page.

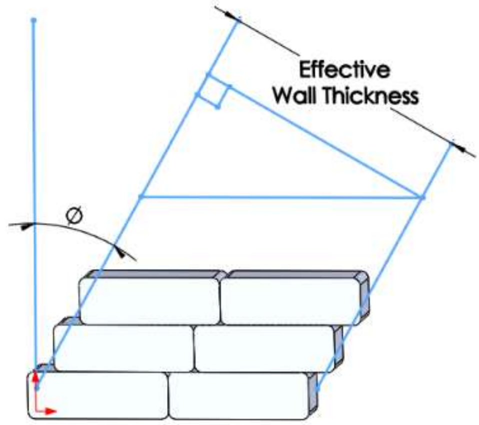

Figure 4.23: Effective wall thickness (2 parallel extrusions into the page)

Generally, BMD additive parts can be printed with wall angles of 0-45 degrees, which provides a potential wall thicknesses of 0.49 mm (at 0 degrees) to 0.35 mm (at 45 degrees), based on two extrusions. To estimate the effective wall thickness of the gyroid structure, small gyroid cubes of size 20x20x20 mm were printed without the case, as shown in Figure 4.24 below. The effective wall thickness was estimated by comparing the actual printed weight of the gyroid cubes with the CAD volume weight.

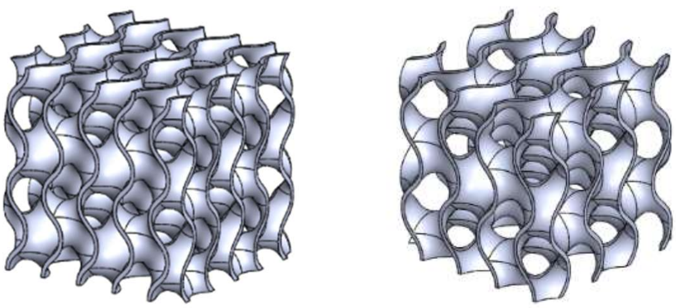

Figure 4.24: Gyroid cubes – Left: Channel size 4 mm, Right: Channel size 5 mm

4.5.2 Results of Gyroid Printing Investigation

The following section presents the outcomes of the BMD gyroid printing on the Desktop Metal Studio System. Firstly, the printed gyroid open rectangular containers are presented, which demonstrated the concept of the gyroid PCM heat sink container. Secondly, the gyroid cubes without the case are presented to determine the weight and effective wall thickness.

4.5.2.1 Gyroid Containers

Figure 4.25 below shows the open rectangular containers initially investigated for the gyroid printing, and includes the printed parts and sintered parts. The containers feature internal gyroid unit cell sizes of 8 mm and 10 mm (i.e. gyroid channel sizes of 4 mm and 5 mm). The sintered containers demonstrated the ability to print the desired gyroid base sizes in a containment structure.

(a)

(b)

Figure 4.25: Gyroid containers - Left: Channel size 4 mm, Right: Channel size 5 mm
(a) printed parts, (b) sintered parts

The dimensions of the sintered rectangular parts were within 0.25 mm of the required XY dimensions and within 0.15 mm of the Z dimensions. Although, the sintering caused the rectangular containers to slightly warp, since they were not completely square in the XY and Z axes. The corners of the containers tended to lift from the raft and the sides tended to bend inwards. However, the tolerances were within the specified range of ±0.5 mm as given by Desktop Metal for parts under 60 mm due to the variance induced by the printing and sintering process (Knowledge Base, 2020). Note, for high tolerance parts, such as holes and flat surface, it recommended to print 0.5 mm oversize and then machine to the correct dimensions.

The surface of the sintered gyroid structure is shown in Figure 4.26 below for the 4mm gyroid channel size. The individual print layers and extrusions are visible. The gyroid walls featured a corrugated grooved surface finish. The grooved effect inadvertently increased the surface area of gyroid, which increased the surface area available for PCM heat transfer.

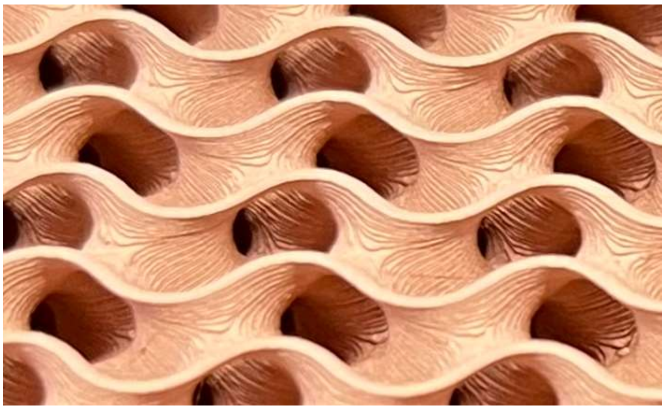

Figure 4.26: Surface quality of BMD gyroid

A gyroid open rectangular container was also filled with a red dye liquid (water-based with a viscosity of 8 ± 0.5 cP and a surface tension of 40 ± 5 mN/m) to investigate if the BMD container was leakproof, as shown in Figure 4.27 below. The red dye was maintained for several days, with top ups added due to evaporation. There were no signs of leakage onto the white absorption paper underneath and the exterior walls of the container did not feature any red colouration. The outer wall thickness used for the test was a 3-line extrusion, instead of a 4-line extrusion wall thickness. The test demonstrated the ability to provide a thinner lighter wall for leakproof containment.

Figure 4.27: Red dye liquid leakproof test

4.5.2.2 Gyroid Cubes

Figure 4.28 shows the 20x20x20 mm gyroid cubes, and includes the printed parts and sintered parts. The gyroid cubes shown are the 4 mm and 5 mm gyroid channel sizes. The gyroid cubes were printed with two extrusions lines for the structure walls.

(a)

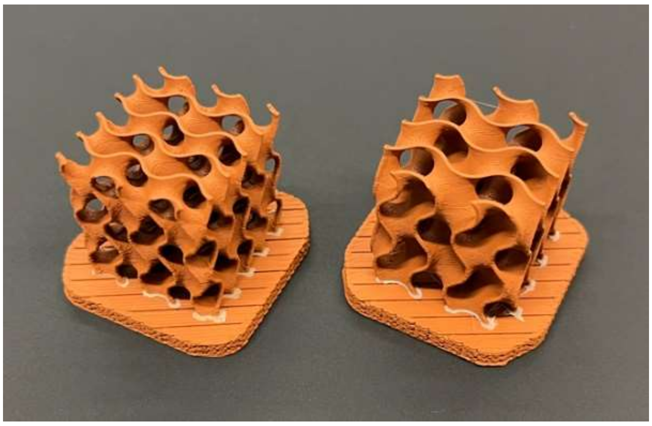

(b)

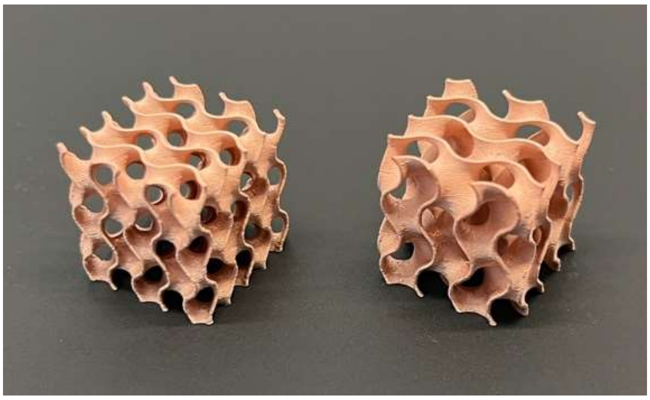

Figure 4.28: Printed and sintered cubes - Left: Channel size 4 mm, Right: Channel size 5 mm

(a) printed parts, (b) sintered parts

Three of each gyroid size were printed and the average printed weights were compared to the estimated CAD weights to estimate the effective wall thickness. For the 4 mm gyroid channel size, the weights of the three cube samples were 11.05, 11.08 and 11.09 g (average 11.07 g). For the 5mm gyroid channel size, the weights of the three cube samples were 8.86, 8.88, 8.89 g (average 8.88 g).

The weight results are summarised in Table 4.6 below, which compares the average printed weights with the estimated CAD weights. The estimated CAD weights were determined using the volume from the CAD model using a gyroid wall thickness of 0.4 mm and a BMD copper density of 8750 kg/m^3 (DM Material Data Sheet, 2020).

The results show that the 4 mm gyroid print weight was 1.7% more than the estimated CAD weight and the 5 mm gyroid print weight was 3.4% more than the estimated CAD weight. Based on these percentages, this equated to an effective wall thickness of 0.407 mm for the 4 mm gyroid and 0.414 mm for the 5 mm gyroid.

Table 4.6: Gyroid cube printed vs estimated CAD weights

*Estimated weight based on 0.4 mm wall thickness

Gyroid Base Size	Printed Weight Average (g)	CAD Weight Estimated (g)	Printed Percent Difference	Effective Wall Thickness (mm)
4 mm Channel Spacing	11.07	10.88	1.7% Increase	0.407
5 mm Channel Spacing	8.88	8.59	3.4% Increase	0.414

The 4 mm gyroid effective wall thickness was slightly lower than the 5 mm gyroid size, since the 4 mm gyroid is more compressed. As a result, the wall angles relative to the layer height are slightly higher and therefore provide a thinner effective wall thickness.

The 4 mm gyroid size was utilised for the PCM heat sink prototype, since the PCM heat transfer performance in Chapter 3 was greater with the smaller base sizes. For the Chapter 3 PCM heat sink (size 60x60x20 mm), the predicted weight of the 4 mm gyroid structure is 83.8 g based on these results. Overall, the printed 5 mm gyroid size is approximately 20% lighter than the 4 mm gyroid size, however this only equates to a difference of 16.6 g.

In comparison, reducing the Chapter 3 PCM heat sink case thickness from 1 mm (4-line extrusion wall) to 0.5 mm (2-line extrusion wall), reduces the case weight from approximately 102 to 50 g. Thus, reducing the case thickness has a better improvement, and therefore was the aim of the PCM containment investigation.

4.6 PCM CONTAINMENT INVESTIGATION

In the final investigation, the leakproof integrity of BMD parts containing PCMs were tested in a vacuum to determine if the method was suitable for space applications and for PCM thermal cycling.

4.6.1 Methodology

Two containers were printed to investigate the leakproof integrity of BMD copper parts for vacuum and thermal cycling testing. These included a circular cross-section container and a rectangular cross-section container, as shown in Figure 4.29 below. The containers were printed with the 4 mm gyroid channel size internal structure. An outer wall thickness of 1 mm (4-line extrusion wall) was initially investigated. Both parts were printed with a 45 degree top section to ensure cohesion in the container top. The overal size of the circular container was 40x40x40 mm and the overal size of the rectangular container was 60x60x16 mm.

(a)

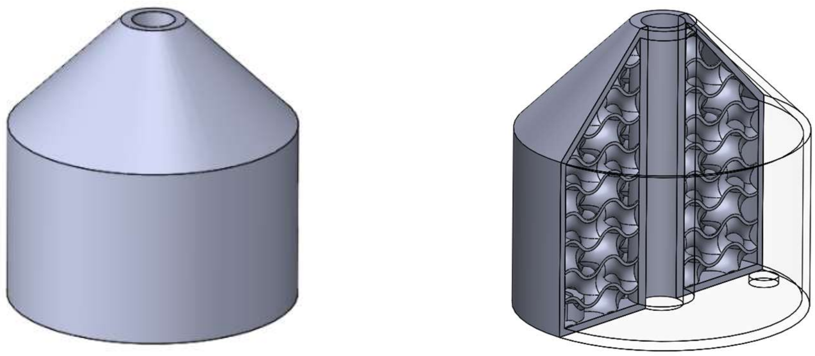

(b)

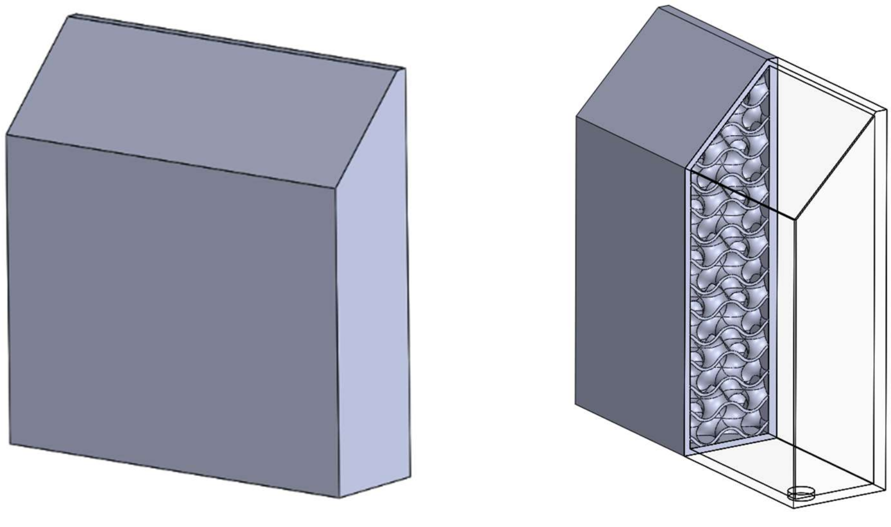

Figure 4.29: Circular and rectangular BMD containers

(a) circular cross-section, (b) rectangular cross-section

The parts were printed with two fill ports (inlet and outlet) to allow PCM filling, as shown in Figure 4.30 below. Noting, the gyroid structure created two separate interconnecting internal volumes. The fill ports covered both internal volumes to allow filling. The interal CAD volumes were 26 ml for the circular container and 35 ml for the rectangular container.

Heating elements were included for theraml cycling of the PCM. The circular container was printed with an oversized circular hole, which was machined to accomadate a heating cartridge. The rectangular container was printed with one oversized wall, which was machined flat to accomadete a heating element pad.

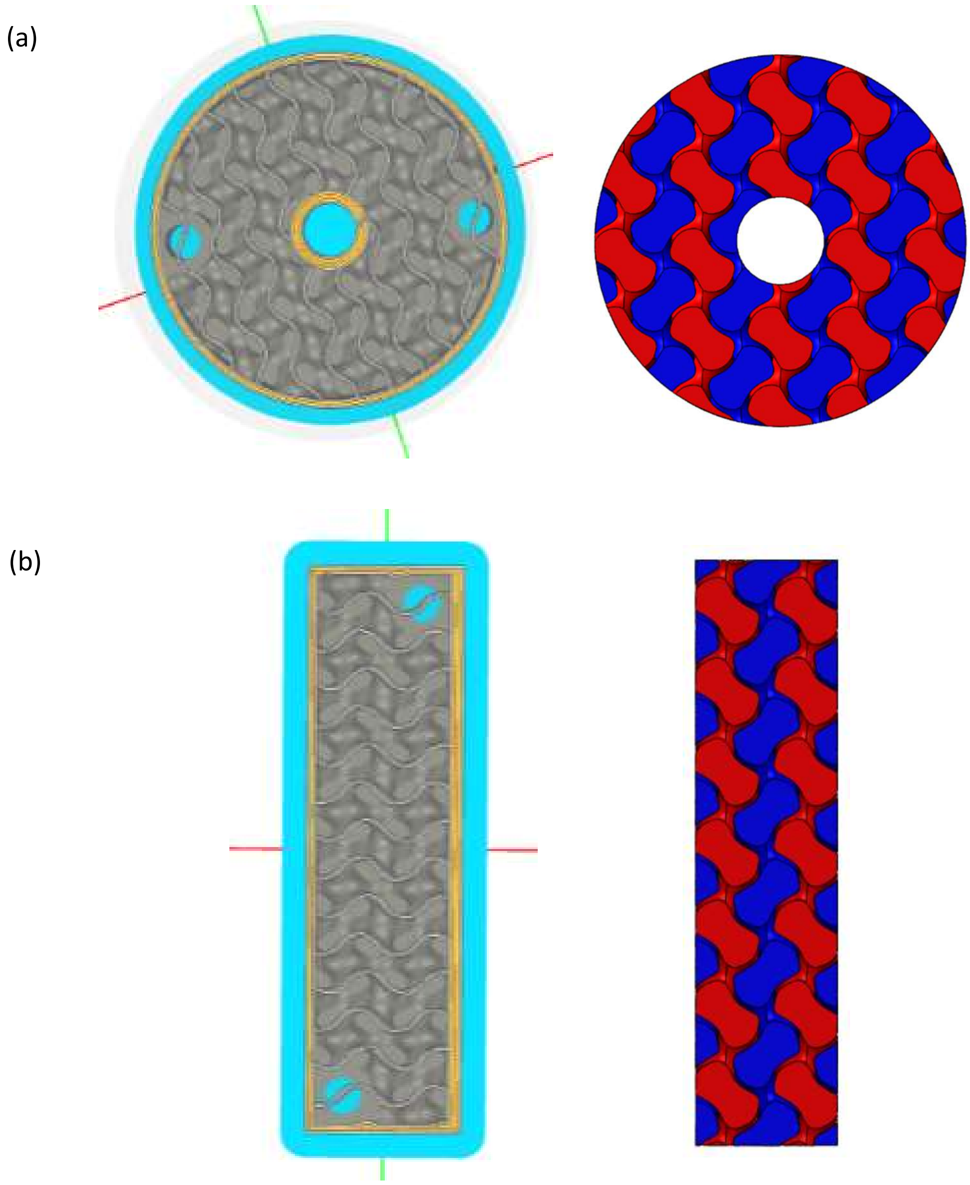

Figure 4.30: Gyroid internal volumes

(a) circular cross-section, (b) rectangular cross-section

Figure 4.31 below shows the circular container, and includes the printed part, sintered part, and machined part. The inner hole was drilled to the required dimensions for the cartridge heater.

(a) (b) (c)

Figure 4.31: BMD circular container

(a) printed part, (b) sintered part, (c) machined part

Figure 4.32 shows the rectangular container, and includes the printed part, sintered part, and machined part. The outer wall was machined flat for the heating element. To achieve a flat surface, a 0.48 mm depth was removed, which was within the tolerance (±0.5 mm) of BMD parts.

(a) (b) (c)

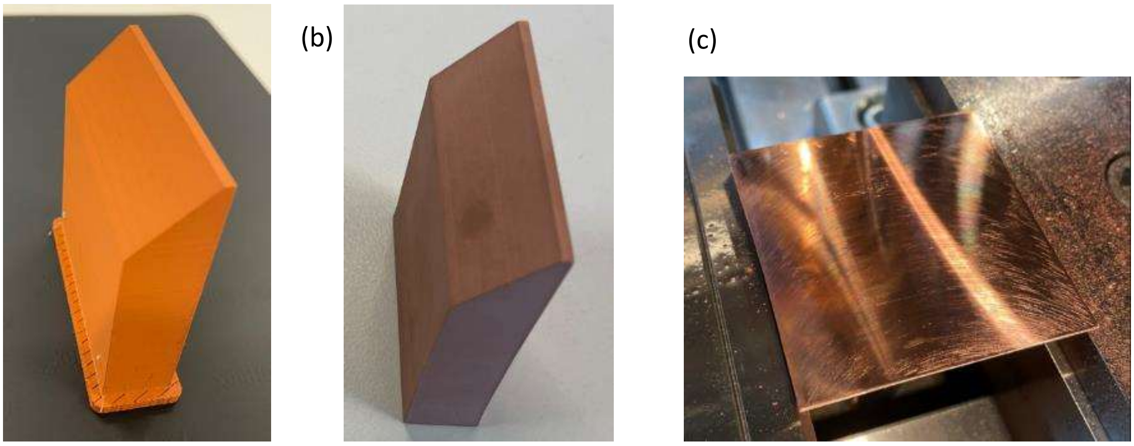

Figure 4.32: BMD rectangular container

(a) printed part, (b) sintered part, (c) machined part

The containers were filled with octadecane PCM, which has a liquid density of 776 kg/m^3, a viscosity of 2.7 cP and a surface tension of 27.5 mN/m (Velez et al., 2015), (Hale et al., 1971). The containers were filled leaving an additional 15% air gap to allow for the PCM volume change. Noting, octadecane volume phase change is a 11% reduction from liquid to solid (Collette et al., 2011). The circular container was filled with 22 ml (17 g) of PCM and the rectangular container was filled with 30 ml (23 g).

The fill ports were sealed with grub screws and thread lock. The containers were placed in a roughing vacuum chamber for leakproof thermal cycling testing and were heated from room temperature (22°C) to 50°C, noting that the melting point of octadecane is approximately 28°C (Velez et al., 2015).

The roughing vacuum chamber reduced the pressure to an order of 10^{-1} millibar. Although, for space applications a secondary test using a high vacuum pump was also needed.

4.6.2 Results of PCM Containment Investigation

The following sections presents the results of the PCM leakproof vacuum testing of the circular and rectangular printed BMD parts. The containers were heated and placed inside the roughing vacuum chamber. Upon operation of the roughing vacuum pump, it was immediately identified that the BMD parts were not able to contain the liquid PCM in a vacuum. The liquid PCM leaked to the surface and covered the entire copper container. Air bubbles from the inside air gap were seen bubbling on the surfaces covered by liquid PCM.

Figure 4.33 below shows images of the containers inside the vacuum chamber, which were taken through the chamber viewport. Quality photos were difficult to obtain through the chamber viewport, however, the photos show the bubbling observed on the container surfaces.

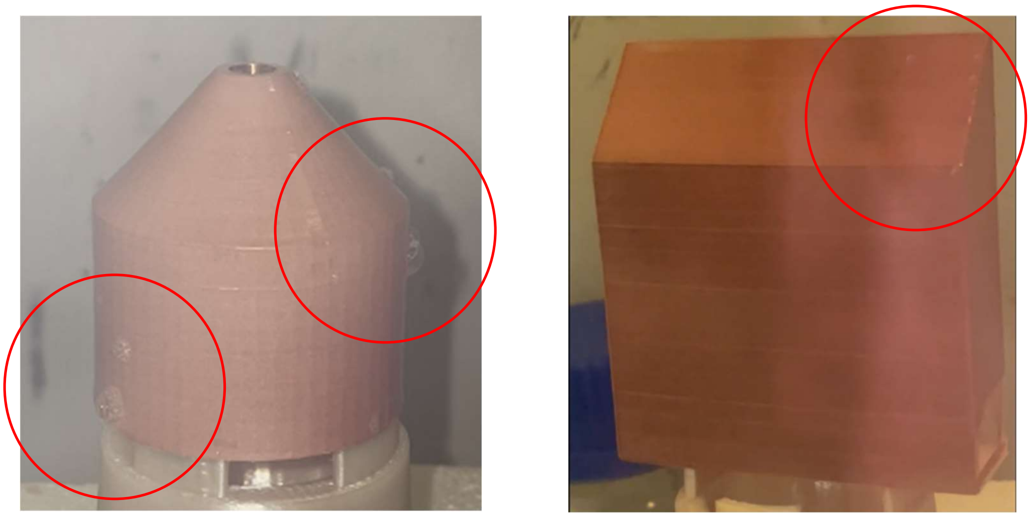

Figure 4.33: Roughing vacuum test

It was concluded that it was not possible to hold PCM in a vacuum using BMD at this wall thickness. Noting the case thickness used was 1 mm (4-line extrusions). Thus, reducing the case thickness to 0.5 mm (2-line extrusions) as planned was discontinued. Thermal cycling testing was also not undertaken since the BMD container failed on the first vacuum test. Furthermore, a higher vacuum test was not performed due to the failure at the roughing vacuum stage. Therefore, an alternate solution was required to provide PCM containment with BMD copper PCM heat sinks.

4.7 DISCUSSION

The results are firstly discussed for the porosity and thermal conductivity investigations, and then for the gyroid printing and PCM containment investigations.

4.7.1 Porosity and Thermal Conductivity

The material composition of BMD copper was consistent with high conductivity copper, however, the porosity needed to be considered for the thermal conductivity measurements.

Thermal numerical models were created based on the observed macro and micro porosity, using the optical microscope average porosity measurements. The porosity percentage was 1.45% for the macro porosity model and 1.00% for the micro porosity model (Total Porosity 2.45%). The numerical results showed that the thermal conductivity reduction was 6.6% along the extrusion print layers and the thermal conductivity reduction was 9.6% through the extrusion print layers.

The thermal conductivity of BMD copper was then experimentally tested with horizontally printed and vertically printed cylinder samples. The test results showed that the thermal conductivity reduction was 9.1% along the print layers and the thermal conductivity reduction was 13.3% through the print layers. Thus, the difference in thermal conductivity was 4.2%, which aligned with the thermal numerical results, which showed a 3.0% difference.

The thermal conductivity reduction was slightly higher for the test results compared to the predicted results from the numerical models. However, the numerical results were based on an average observed total porosity of 2.5%. Whereas the porosity in the thermal conductivity test cylinders was 3.5-4.0% from the density measurements. Therefore, a higher porosity would have led to a higher thermal conductivity reduction.

Furthermore, the test cylinders were printed with diagonal extrusions, which alternated in direction layer by layer. This would have also led to a higher thermal conductivity reduction compared to straight extrusions, which were used for the numerical results.

In summary, the results showed that the porosity was the main cause behind the thermal conductivity reduction. In addition, the results showed that there was thermal conductivity anisotropy in BMD parts due to the way the print layers were deposited.

Overall, the thermal conductivity of BMD copper (average of the horizontal and vertical results) was 11.2% less compared to the copper reference test. Based on the 11.2% reduction, the adjusted overall thermal conductivity for BMD copper was 353.3 W/m·K, using the reported thermal conductivity of the reference copper (398 W/m·K).

Noting, the dominant form of thermal conduction in metals is electron based, since metals have a high concentration of free conduction electrons (Majumdar et al., 2014). Porosity in metals therefore reduces the thermal conductivity since the porosity limits the movement of electrons.

Electrical conductivity in metals is also due to the movement of electrons, and therefore any porosity in metals also corresponds to loss of charge-carrier in the material (Montes et al., 2008). The relationship between thermal conductivity (k) and electrical conductivity (σ) for pure metals is proportional to the Lorenz number (L), given by Equation 4.7, where T is the absolute temperature (Kumar et al., 1993).

$$\frac{k}{\sigma} = LT \qquad \text{Equation 4.7}$$

Whilst the thermal conductivity of BMD copper was not reported, the electrical conductivity of BMD copper was reported as 85.2 %IACS (DM Material Data Sheet, 2020). Noting, IACS is the International Annealed Copper Standard, which is defined as 58 x 106 S/m at 20°C (ASM, 2000). Using Equation 4.7 and the theoretical value of Lorenz number, 2.44 x 10^{-8} W·Ω·K^{-2} (Kumar et al., 1993), the calculated BMD thermal conductivity was 353.5 W/m·K at 20 degrees Celsius. The derived value for thermal conductivity from the electrical conductivity favourably compared to the overall tested thermal conductivity of BMD copper (353.3 W/m·K).

Whilst there was an 11.2 % overall reduction, the thermal conductivity result of BMD copper was relatively high. Compared to aluminium additive manufacturing using Selective Laser Sintering (SLS), the thermal conductivity with no heat treatment is only 110 W/m·K, which is approx. 50% less compared to aluminium (EOS, 2021).

4.7.2 Gyroid Printing and PCM Containment

The gyroid printing demonstrated the ability to print the desired gyroid base sizes and the approach allowed the gyroid base sizes to be customised for the PCM heat sink design. The 4 mm and 5 mm gyroid channel sizes were successfully printed using the high resolution printhead on the Desktop Metal Studio System.

The printing results showed that the 4 mm gyroid effective wall thickness was 0.407 mm and the 5 mm gyroid effective wall thickness was 0.414 mm, based on the weights of the printed cube samples. Noting, the gyroid wall thickness needed to be printed with two extrusion passes, as required by the Desktop Metal Slicing Software.

For the 4 mm gyroid channel size, the printed weight was only 1.7% more than the estimated CAD weight based on a wall thickness of 0.4 mm, which was the thickness used in Chapter 3 for this base size. The 4 mm gyroid channel size was the mid-range base size in Chapter 3, which produced good results for the heat pipe cooling configuration using copper (84% TES utilisation).

However, BMD was not suitable for containing PCM in a vacuum. The printed BMD containers using a 1 mm exterior wall thickness (4 extrusions) leaked PCM throughout the entire container when subjected to a roughing vacuum pressure. Whilst the BMD container was suitable for holding liquid under atmospheric conditions, the BMD containers failed to hold PCM in a vacuum. It was suspected that the macro toolpath porosity led to the failure.

Thus, it was concluded that the BMD method was not suitable as a stand-alone method for containing PCM in a high vacuum space environment. Therefore, other solutions were required to provide PCM containment with BMD copper thermal enhancement, which were explored in the next Chapter 5.

5. Development, Testing and Validation of a BMD Additive Prototype PCM Heat Sink

5.1 INTRODUCTION

This Chapter develops, tests and validates the performance of a BMD additive manufacturing prototype PCM heat sink in a vacuum chamber for space applications (Research Objective 3). In this investigation, a hybrid BMD solution was explored to overcome the challenges identified with the BMD additive manufacturing technique in Chapter 4.

In Chapter 4, BMD provided the ability to manufacture thermal conductivity enhancement (TCE) structures for PCM heat transfer. However, BMD was unable to provide leakproof PCM containment in a vacuum, as a result of the toolpath porosity inherent in the manufacturing process. To provide leakproof PCM containment, a hybrid concept was developed in this Chapter, which combined the benefit of internal BMD additive structures with a conventional metal case.

The hybrid BMD concept was investigated with the heat pipe cooling configuration from Chapter 3, using the gyroid internal structure as shown in Figure 5.1 below. The concept featured a BMD copper internal structure coupled to an aluminium external case to provide PCM containment. The benefit was the ability to optimise the internal additive structure for PCM heat transfer and also reduce the weight by using a lightweight aluminium case.

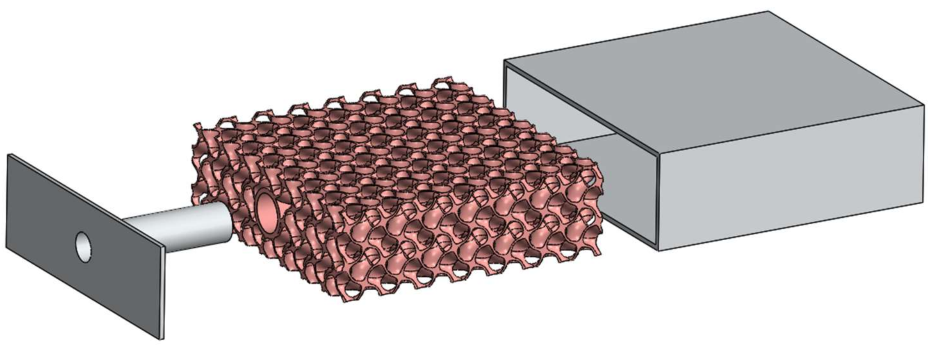

Figure 5.1: Hybrid Concept: BMD Copper Internal Structure and Aluminium Case

In Chapter 3, the heat pipe cooling configuration required the use of copper to achieve adequate heat dissipation. It was unknown whether the hybrid BMD concept using an external aluminium case could deliver the required heat transfer for PCM heat dissipation.

The research questions to be answered in this Chapter were the following:

Can the hybrid additive PCM heat sink provide adequate cooling for high-powered CubeSat electronics and is the hybrid additive PCM heat sink suitable for CubeSat space applications?

The feasibility of the hybrid BMD concept was firstly explored using the numerical modelling methodology from Chapter 3. The feasibility study investigated the performance of BMD copper and the use of an aluminium case, including the role of the contact resistance between the two metals.

Based on the feasibility study, a prototype PCM heat sink was manufactured using BMD and tested in a vacuum chamber. In addition, a numerical validation model using the prototype testing parameters was performed in order to verify the numerical methodology employed in this thesis.

5.2 CONCEPT FEASIBILITY STUDY

This section presents the initial feasibility study performed to investigate if the hybrid PCM heat sink could provide adequate cooling for the heat pipe cooling configuration. The following three feasibility investigations were undertaken:

- Firstly, the effect of the BMD copper thermal conductivity reduction in Chapter 4 was investigated and compared to the material properties used in Chapter 3;
- Secondly, the effect of using an aluminium external case with a BMD copper internal structure was investigated; and
- Thirdly, the effect of the thermal contact resistance between the aluminium case and the BMD copper internal structure was investigated.

The Chapter 3 conceptual PCM heat sink design was utilised as the basis for this feasibility study. In particular, the feasibility study was explored with the heat pipe cooling configuration, which was more demanding than the direct cooling configuration, due to the concentrated heat input area.

To recap from Chapter 3, the overall size of the PCM heat sink was 60x60x20 mm and catered for a 6 mm diameter heat pipe with a 30 mm condenser into the PCM heat sink. The heat pipe cooling configuration was designed to absorb a 50 W heat load for a period of approximately 5 minutes, from an initial temperature of 15°C to a limit of 50°C.

As per Chapter, the PCM modelled was paraffin octadecane, due to its ideal melting point (~28°C) for maintaining electronics below 50°C (Collette et al., 2011). The numerical modelling approach for the feasibility study was the ANSYS Fluent solidification/melting model, in accordance with the Chapter 3 methodology.

To recap from Chapter 3, the modelling assumed a constant PCM volume and a zero-gravity velocity field. Also, the modelling assumed no heat loss and did not consider the thermal mass of the electronics/CubeSat radiator (i.e. the PCM heat sink thermal energy storage was viewed in insolation).

The PCM heat sink was modelled with quarter symmetry, as shown in Figure 5.2 below. For this feasibility study, the gyroid model from Chapter 3 was used, since the gyroid provided the best PCM heat transfer for the heat pipe cooling configuration.

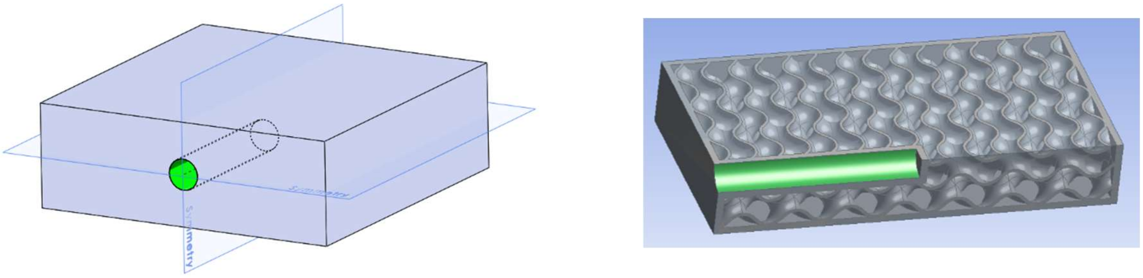

Figure 5.2: Heat pipe cooling quarter model symmetry planes and gyroid quarter model

5.2.1 Impact of BMD Copper Thermal Conductivity Reduction

Firstly, the effect of the BMD copper thermal conductivity reduction in Chapter 4 was numerically investigated and compared to the copper and aluminium material properties used in Chapter 3. Table 5.1 below summarises the material properties of BMD copper and the Chapter 3 material properties used for copper and aluminium.

Table 5.1: Metal TCE Material properties, [A] (Conex, 2020), [B] (Atlas Steels, 2013)

	Thermal Cond. W/m·K	Density kg/m^3	Specific Heat J/kg·K
BMD Copper (Chapter 4)	353	8750	385
Copper [A] (Chapter 3)	391	8940	385
Aluminium [B] (Chapter 3)	209	2700	900

BMD copper had an overall 11% reduced thermal conductivity compared to the reference copper sample in Chapter 4. Whilst BMD exhibited a slightly different thermal conductivity in each print direction (4% variance), the overall thermal conductivity for BMD copper (353 W/m·K) was used, since the ANSYS Fluent model required a constant value.

The mid-size 4 mm gyroid channel size model from Chapter 3 was selected for this study, as shown in Figure 5.3 below. In Chapter 4, the 4 mm gyroid channel size was successfully printed using BMD copper with an effective wall thickness of 0.407 mm, which was only 1.7% more than the 0.4 mm wall thickness used in Chapter 3. For the purposes of this feasibility study, the 0.4 mm model was used for ease of meshing and simplified comparison with the Chapter 3 results.

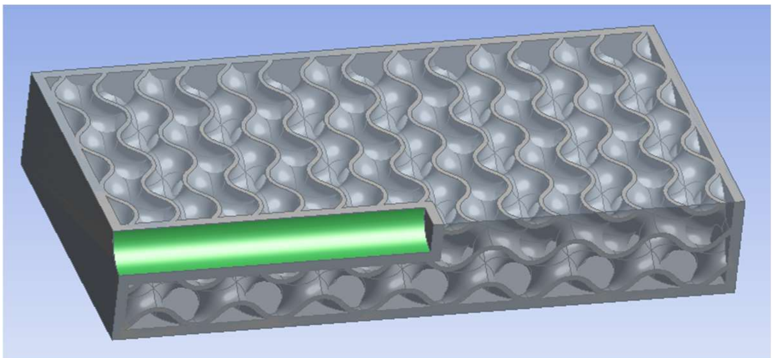

Figure 5.3: Gyroid quarter model, 4 mm gyroid channel size (Single metal design)

The performance of the models were measured based on the Thermal Energy Storage (TES) utilisation prior to exceeding the 50°C limit. In Chapter 3, the copper PCM heat sink achieved 84% TES utilisation and the aluminium PCM heat sink achieved 56% TES utilisation, using the 4 mm gyroid channel size model for the heat pipe cooling configuration. To recap, the weights and TES capacity for the heat pipe cooling configuration is provided in Table 5.2 below for both the copper and aluminium PCM heat sinks. The performance using BMD copper is presented in the following results.

Table 5.2: Weight and TES capacity of the Heat Pipe Cooling PCM heat sink (ΔT 15-50°C)

*For an applied heat load of 50 W

Copper PCM Heat Sink		**Aluminium PCM heat Sink**	
Total Weight	TES Capacity	Total Weight	TES Capacity
226 g	15.1 kJ **5.0 min***	96 g	14.3 kJ **4.8 min***

Results – BMD Copper Investigation

The numerical results for the thermal conductivity investigation are shown in Figure 5.4 below, and compares BMD copper to the Chapter 3 results for copper and aluminium. The results showed that BMD copper had a similar temperature response to copper, and maintained the heat input junction temperature closely with the copper results. The temperature response was much better than the aluminium PCM heat sink, which could not dissipate the heat as well as copper.

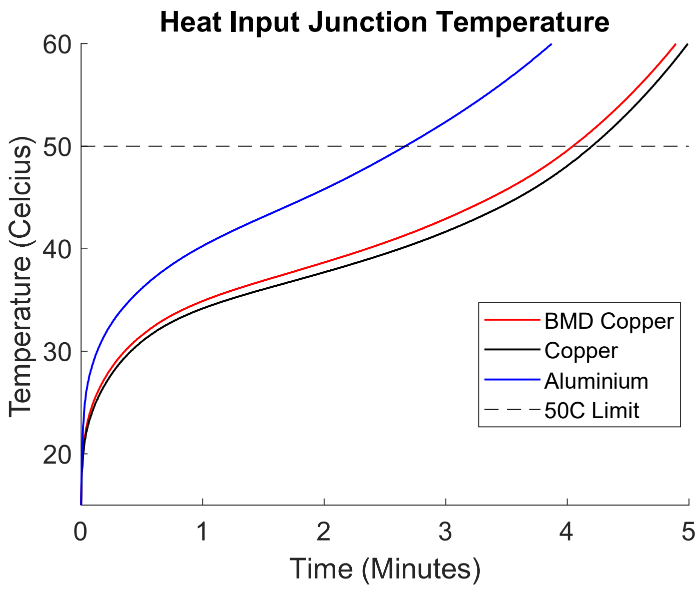

Figure 5.4: Impact of BMD thermal conductivity reduction

Heat Pipe Cooling Configuration – 4mm Gyroid TCE Structure

Table 5.3 summarises the key results for the thermal conductivity investigation. Compared to copper, BMD copper utilised only 2% less TES and also provided over 4.0 minutes of cooling. Accordingly, whilst there was an 11% reduction in the BMD copper thermal conductivity, the BMD copper model demonstrated reasonable heat dissipation for the heat pipe cooling configuration.

Table 5.3: Key results for thermal conductivity investigation

	Time at 50°C Limit	TES Utilisation at 50°C Limit
BMD Copper	4.1 minutes	82%
Copper	4.2 minutes	84%
Aluminium	2.7 minutes	56%

5.2.2 Effect of Hybrid Aluminium Case

Secondly, the effect of using an aluminium case with the BMD copper internal structure was investigated for this feasibility study. The 4 mm gyroid channel size model from Chapter 3 was again selected for this study. However, to investigate the effect of the hybrid design, the metal zone was separated into two further sub regions, namely the outer case and the internal structure, as shown in Figure 5.5 below.

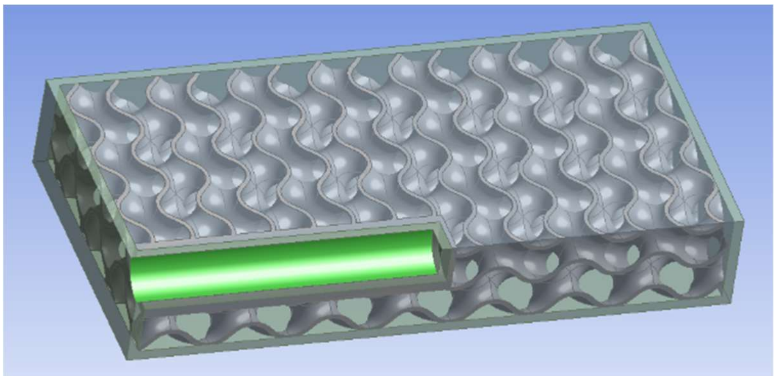

Figure 5.5: Gyroid quarter model, 4mm gyroid channel size (Hybrid design)

To promote heat transfer between the outer case and the internal structure, the internal structure featured a connecting tube with the heat input cylinder. Initially, the hybrid design model assumed no thermal contact resistance between the aluminium case and the internal BMD copper structure.

The hybrid model was simulated with a BMD copper internal structure and a conventional aluminium external case. Refer to the previous Table 5.1 for the material properties used. The weight and TES capacity of the hybrid design is shown in Table 5.4 below. The values for the hybrid design are midway between the values of the copper PCM heat sink and aluminium PCM heat sink. The performance of the hybrid model is presented in the following results.

Table 5.4: Weight and TES capacity of the hybrid design PCM heat sinks (ΔT 15-50°C)

*For an applied heat load of 50 W

Hybrid Aluminium/BMD Copper PCM Heat Sink	
Total Weight	TES Capacity
159 g	14.7 kJ **4.9 min***

Results – Hybrid Aluminium Case Investigation

The numerical results of the hybrid design investigation are shown in Figure 5.6 below, and compares the hybrid model to the results for just using BMD copper and just using aluminium for the metal part. The results showed that the aluminium case reduced the performance, however the temperature response only deviated towards the end. Overall, the temperature response closely aligned with the BMD copper results. Thus, the case metal did not have a large impact on the performance and showed that the internal structure material was dominant.

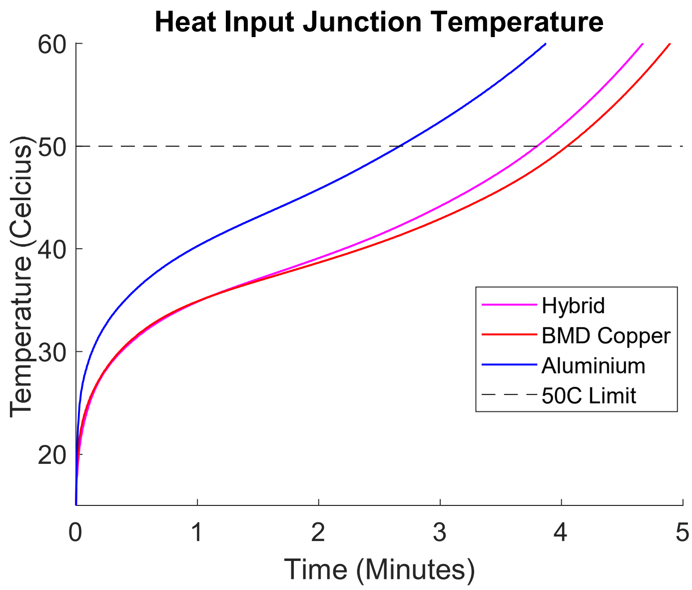

Figure 5.6: Effect of hybrid aluminium case

Heat Pipe Cooling Configuration – 4mm Gyroid TCE Structure

Table 5.5 provides the key results for the hybrid model investigation. The hybrid combination provided 78% TES utilisation compared to 82% TES utilisation using BMD copper, which was a promising solution. However, the hybrid model did not consider the thermal contact resistance between the aluminium external case and BMD copper internal structure, which is further explored in the next feasibility investigation.

Table 5.5: Key results for hybrid aluminium case investigation

	Time at 50°C Limit	TES Utilisation at 50°C Limit
Hybrid	3.8 minutes	78%
BMD Copper	4.1 minutes	82%
Aluminium	2.7 minutes	56%

5.2.3 Effect of Thermal Contact Resistance

Finally, the role of the thermal contact resistance between the aluminium case and the internal BMD copper structure was numerically investigated for this feasibility study. Thermal contact resistance impedes the transfer of heat between two solid bodies, since the actual contact area for heat transfer is smaller than the apparent contact area due to microscopic gaps between the solid surfaces, as shown in Figure 5.7 below (Fletcher, 1993).

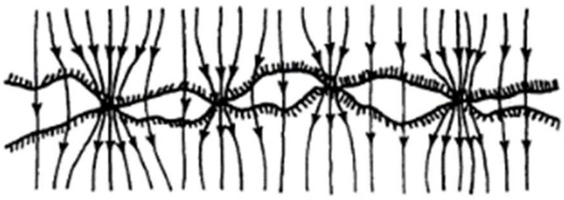

Figure 5.7: Microscopic view of two surfaces in contact (Fletcher, 1993)

Thermal contact resistance between two solids is generally dependent on the material properties, surface characteristics and contact pressure (Fletcher, 1993). Figure 5.8 shows the thermal contact resistance between two aluminium surfaces for various surface roughness's, temperatures and contact pressures. For smooth surfaces, the thermal contact resistance ranged from 0.1 to 0.01 m^2·C/kW, for contact pressures above 1 MPa.

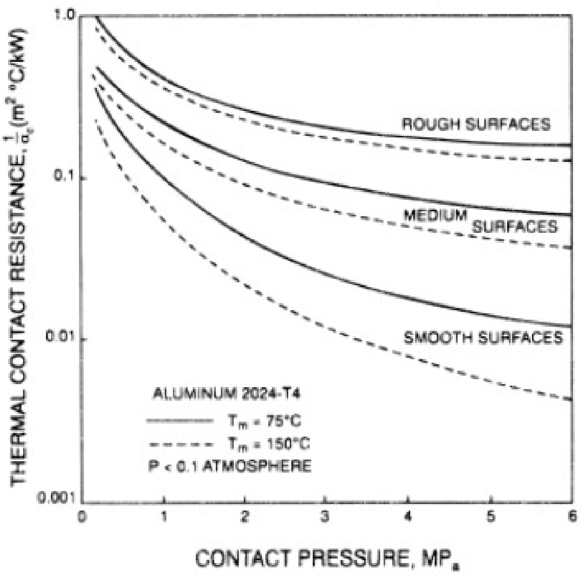

Figure 5.8: Aluminium surfaces contact resistance (Fletcher, 1991)

In this feasibility investigation, it was assumed that smooth surfaces could be achieved between the aluminium and BMD copper. Thus, thermal contact resistance values of 0.1, 0.05 and 0.01 m^2·C/kW were modelled and evaluated. These were compared to the nil contact resistance as previously modelled and presented in the following results.

Results – Thermal Contact Resistance Investigation

The results of the thermal contact resistance investigation for the hybrid model are shown in Figure 5.9 below, and compares the various contact resistance values with the previous nil contact resistance. The results showed that the thermal contact resistance had a large effect on the temperature response throughout the duration. With a greater contact resistance, the temperature response was consistently higher.

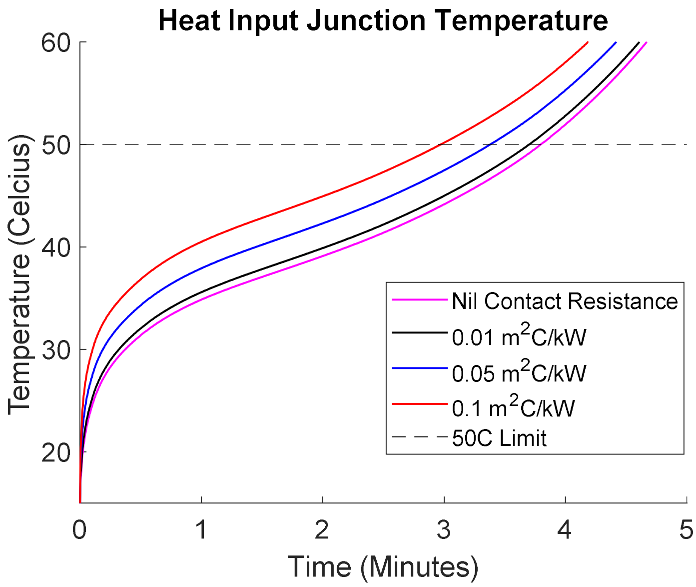

Figure.5.9: Effect of thermal contact resistance results for the hybrid model

Heat Pipe Cooling Configuration – 4mm Gyroid TCE Structure

Table 5.6 provides the key results for the thermal contact resistance investigation. The very low value of contact resistance provided similar performance to the previous nil contact resistance. However, the higher contact resistance provided only 61% TES utilisation, which was near the result for just using aluminium, thus negating the benefit of the copper internal structure. Therefore, a very low thermal contact resistance was required for the hybrid BMD concept to be feasible. This is further explored in the design and manufacture of the prototype hybrid PCM heat sink in the next section.

Table 5.6: Key results for the thermal contact resistance investigation

	Time at 50°C Limit	TES Utilisation at 50°C Limit
Nil Contact Resistance	3.8 minutes	78%
0.01 m^{2}C/kW	3.7 minutes	76%
0.05 m^{2}C/kW	3.4 minutes	70%
0.1 m^{2}C/kW	3.0 minutes	61%

5.3 PROTOTYPE DESIGN AND MANUFACTURE

This section presents the design and manufacture of the prototype PCM heat sink. Firstly, the design of the PCM heat sink is presented, including the interface design between the aluminium case and the BMD copper internal structure. Secondly, the manufacture of the prototype heat sink is presented, including the PCM filling and sealing method. The testing of the prototype PCM heat sink in a vacuum chamber is presented in the next section.

5.3.1 Prototype Design

The cross-section design of the prototype PCM heat sink is shown in Figure 5.10 below. The heat sink design was based on the feasibility study using the gyroid internal structure. However, a tapered connection was selected for the interface between the aluminium case and the BMD copper internal structure, as shown in Figure 5.10 below.

The aim of the tapered connection was to minimise the thermal contact resistance by improving the contact between the two metals and also by applying a pre-loaded contact pressure to the tapered surfaces. The following discusses the design of the taper connection, the method of applying contact pressure and the design dimensions and estimated weights of the prototype design.

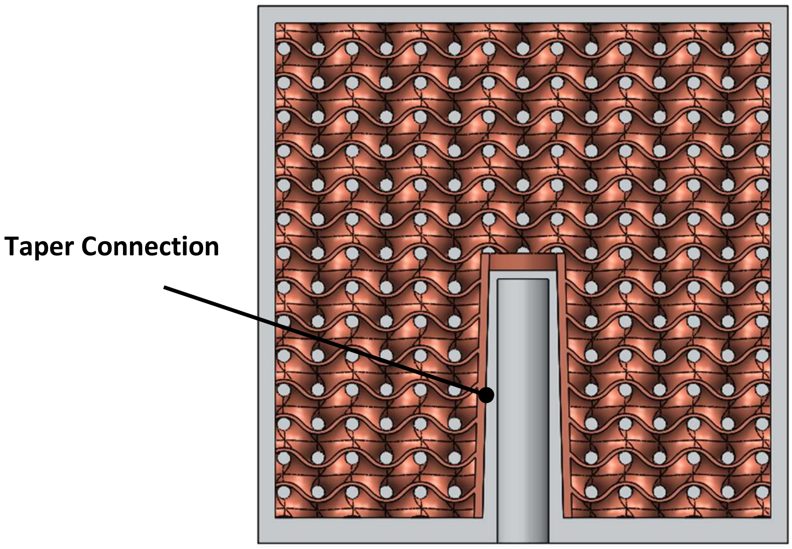

Figure 5.10: Prototype PCM heat sink - Aluminium case, BMD copper internal structure

5.3.1.1 Taper Connection

The tapered connection between the BMD copper internal structure and the aluminium external case was designed with a Morse taper to ensure well-connected surfaces. The Morse taper is a cone in cone construction, with both interconnecting cones uniformly tapered, to provide an intimate contact (Hernigou et al., 2013). The Morse taper typically has a taper angle of 1.23-1.5 degrees, which yields a better fit between cone elements (Rabelol et al., 2015). For the prototype PCM heat sink, a taper angle of 1.5 degrees was selected (i.e. a total cone angle of 3 degrees).

The heat input for the PCM heat sink was a 6 mm diameter 30 mm length heat pipe condenser, as per the Chapter 3 design. The aluminium tapered cone had a minimum wall thickness of 1 mm at the tip and flared out to 1.75 mm thick at the base. The internal copper interfacing cone had a thickness of 1 mm to allow fitment to the aluminium cone. The copper cone was designed slightly higher than the aluminium cone, with a conservative 2 mm difference, so that the internal structure would not interfere with the contact pressure.

5.3.1.2 Contact Pressure

The tapered connection was designed with a contact pressure to further reduce the contact resistance. The aim was to apply a contact pressure between 3 to 6 MPa to achieve a low contact resistance near to 0.01 $m^2 \cdot C/kW$ (Refer to the previous Figure 5.8). For a tapered connection, a contact pressure could be achieved with an interference fit. As shown in Figure 5.11 below, a radial interference (δ) was created by an axial displacement (Δz), which resulted in a radial interference equal to $\Delta z \cdot \tan\phi$, where ϕ is the taper angle (Bozkaya et al., 2003).

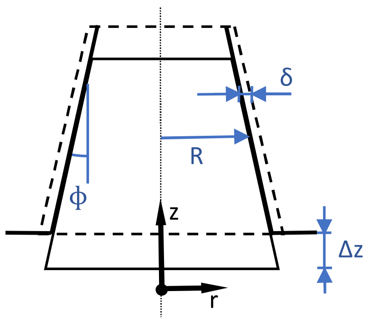

Figure 5.11: Taper fit radial interference

For the purposes of estimating the contact pressure, the tapered interference fit could be assumed as a cylindrical interference fit (Xiao et al., 2015). The contact pressure for a cylindrical interference fit is given by Equation 5.1 below, where δ is the radial interference, R is the interface radius, r_i is the inner radius of the inner cylinder, r_o is the outer radius of the outer cylinder, μ is the Poisson's ratio and E is the Young's modulus (Budynas et al., 2020). The material properties of the outer and inner cylinders are denoted (o) and (i) respectively.

$$P = \frac{\delta}{R\left[\frac{1}{E_o}\left(\frac{{r_o}^2 + R^2}{{r_o}^2 - R^2} + \mu_o\right) + \frac{1}{E_i}\left(\frac{R^2 + {r_i}^2}{R^2 - {r_i}^2} + \mu_i\right)\right]} \quad \text{Equation 5.1}$$

Using Equation 5.1, the radial interference required for a contact pressure between 3 to 6 MPa are shown in Table 5.7 below. The interference was calculated using the base radii of the taper fit and a 1 mm wall thicknesses (Refer to Appendix I for the radial dimensions and properties of the interfacing materials used). The results showed that with an axial z-displacement of 0.1 to 0.2 mm, a contact pressure between 3 to 6 MPa was achievable.

Table 5.7: Axial displacement contact pressure for selected values of δ and Δz

Contact pressure (MPa)	δ (mm)	Δz (mm)
3	0.0023	0.09
6	0.0046	0.18

5.3.1.3 Prototype Design Dimensions and Estimated Weights

The internal dimensions of the prototype PCM heat sink was 58x58x18 mm, consistent with the Chapter 3 design. For the internal TCE structure, the 4 mm gyroid channel size was utilised, which was successfully printed in Chapter 4 with a 0.407 mm effective wall thickness (1.7% larger than the corresponding gyroid base size modelled in Chapter 3).

The aluminium case was designed with a 2 mm outer wall thickness, instead of the 1 mm wall thickness used in Chapter 3, due to the difficulties associated with welding thin aluminium walls. The aluminium base was 3 mm to provide additional wall thickness for the fill ports and sealing screws required for PCM containment. Therefore, the overall size of the PCM heat sink was 63x62x22 mm.

Based on the CAD models, the estimated weight of the copper structure was 87.48 g and the estimated weight of the aluminium case was 70.86 g. The PCM capacity of the heat sink was 38 g of octadecane PCM (48.8 ml), which equated to an internal PCM volume fraction of 83%. This was slightly lower than Chapter 3 (PCM 39 g and 85% internal PCM volume fraction), due to the taper fit and the slightly higher BMD wall thickness.

5.3.2 Prototype Manufacture

The prototype PCM heat sink design was manufactured using the Desktop Metal Studio System as per Chapter 4 and the aluminium case was welded around the BMD copper structure using the TIG welding method (Tungsten Inert Gas). The following discusses the printing of the internal structure, the construction of the aluminium case and the PCM filling and sealing method.

5.3.2.1 Internal Structure

The internal copper structure of the PCM heat sink was firstly printed using BMD. Figure 5.12 shows the toolpath profile and the printed internal structure prior to sintering. The internal structure was printed vertically to allow better printing of the internal taper hole, without the need for an internal printing support structure.

The internal structure and the taper fit were both printed oversized to allow machining after sintering for a high tolerance fit. The overall structure was printed 1 mm larger in the xyz-directions and the taper fit hole was printed with 1 mm more material to allow the precise taper to be machined.

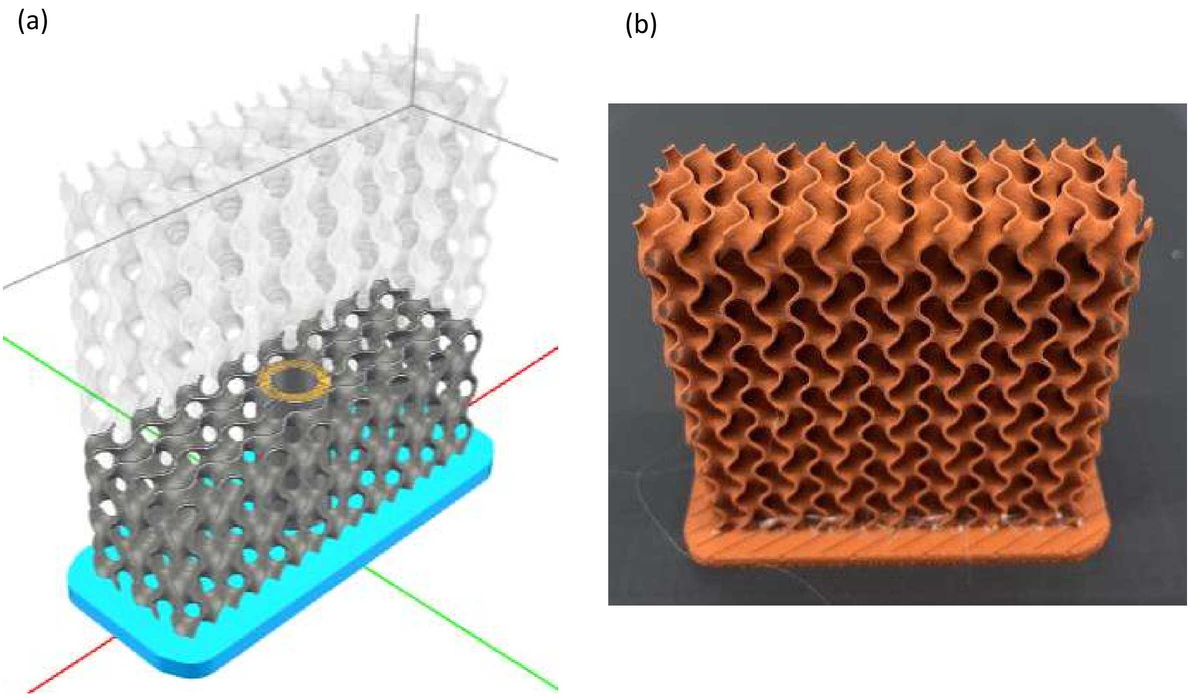

Figure 5.12: BMD internal structure, (a) Toolpath profile, (b) Printed part

The sintered BMD internal structure is shown below. Figure 5.13 (a) shows the internal structure before machining and Figure 5.13 (b) shows the internal structure after machining. The taper fit was machined with a 1.5-degree taper angle. The overall gyroid structure was machined to a size of 58x58x18 mm to fit inside the aluminium welded container.

(a) (b)

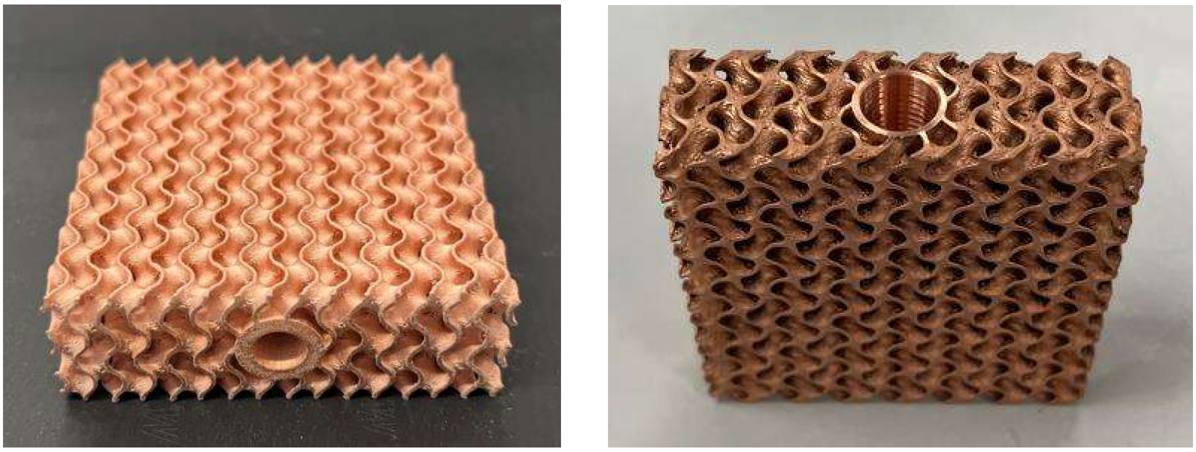

Figure 5.13: Internal structure, (a) As sintered, (b) Machined

The final machined weight of the BMD copper structure was 90.33 g. The internal structure was slightly heavier than the estimated weight from the CAD model (87.48 g), since the machining of the internal taper was not machined through, as to not damage the gyroid structure. However, the marginally higher copper content only reduced the PCM volume by 0.3 ml to 48.5 ml.

5.3.2.2 Aluminium Case

The aluminium case was welded around the BMD copper internal structure. The aluminium case was made using aluminium 6061, which was the best aluminium alloy available at the time of manufacture due to material shortages. The material properties of aluminium 6061 are provided in Table 5.8 below. Noting, the thermal conductivity of aluminium 6061 (167 W/m·K) is 20% lower than aluminium 6063 (209 W/m·K) which was modelled in the feasibility study (Refer to the previous Table 5.1).

Table 5.8: Material properties of aluminium 6061 (Alliance LLC, 2022)

Thermal Cond. W/m·K	Density kg/m^3	Specific Heat J/kg·K
167	2700	896

Figure 5.14 (a) shows the aluminium base machined with the same taper angle as the BMD internal structure. The aluminium taper was machined slightly wider than the BMD copper internal taper, to provide an axial displacement interference of 0.1-0.2 mm. The aluminium base was press fit into the copper structure. Caution was needed not to deflect the internal structure when applying the interference fit. Figure 5.14 (b) shows the final aluminium case welded around the copper internal structure. Two fill ports were added to the base to allow PCM filling.

(a) (b)

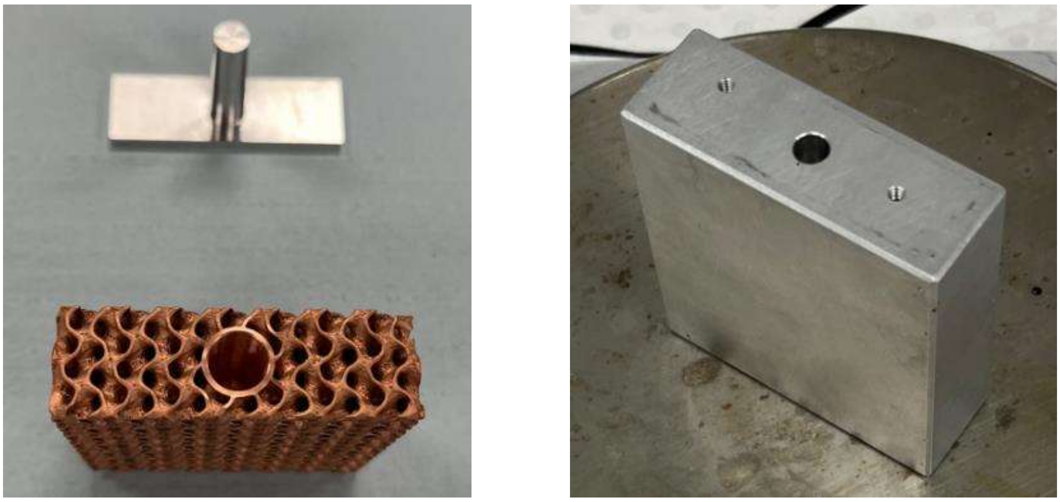

Figure 5.14: Prototype heat sink, (a) Internal taper and structure, (b) Final heat sink

The final weight of the combined copper and aluminium was 159.99 g, providing an aluminium weight of 69.66 g. The weight was slightly less than the estimated weight of the CAD model (70.86 g), since the aluminium case was machined on all sides to remove the excess welds and fill ports were added. The slight reduction did not affect the internal capacity of the heat sink.

5.3.2.3 PCM Filling Method

The last stage was to fill the heat sink with PCM and seal. The PCM chosen was octadecane, as per Chapter 3, due to its ideal melting point (~28°C) for maintaining electronics below 50°C and high latent heat of fusion per unit weight (~244 kJ/kg) for lightweight space applications (Collette et al., 2011). The thermophysical properties of octadecane are provided in Table 5.9 below.

Table 5.9: Properties of octadecane near melting point (Velez et al., 2015)

Thermal Cond. W/m·K	Density kg/m^3	Specific Heat J/kg·K	Latent Heat J/kg	Melt Range °C
0.3 (solid) 0.15 (liquid)	865 (solid) 776 (liquid)	2,240	243,680	25.52 - 29.20

The strategy was to fill the PCM heat sink with liquid PCM, leaving a 5% air gap to cater for the internal pressure change caused by the PCM volume phase change. Noting, the octadecane volume phase change is a 11% reduction from liquid to solid (Collette et al., 2011). The aim was to fill the PCM heat sink with 46 ml of liquid octadecane PCM (95% of the total capacity 48.5 ml), which had a predicted weight of 35.7 g.

Based on the volume change, the PCM would contract to 41 ml when solid. However, the PCM heat sink was sealed when the PCM was still liquid, thereby reducing the pressure in the heat sink when the PCM solidified. The alternative was sealing the heat sink when the PCM was solid, thereby increasing the internal pressure when the PCM melted. The internal pressure change can be estimates by the ideal gas law for a closed system, given by Equation 5.2 below, where V is the air gap volume, P is the internal pressure and T is the system temperature (Roth, 2012).

$$\frac{P_1V_1}{T_1} = \frac{P_2V_2}{T_2} \qquad \text{Equation 5.2}$$

Table 5.10 compares the internal pressure change for both alternatives (i.e. sealing when liquid and sealing when solid). Noting, the initial pressure, P_1, for both cases is the atmospheric pressure of 101 kPa (Engineering Toolbox, 2022). Sealing when liquid results in a decrease of pressure to 31 kPa, and sealing when solid results in an increase of pressure to 328 kPa when melted. Reducing the pressure was the preferred method to be more equalised with the vacuum pressure environment.

Table 5.10: Pressure change inside PCM Heat Sink

	P_1 (kPa)	V_1 (ml)	T_1 (K)	V_2 (ml)	T_2 (K)	P_2 (kPa)
Sealing when Liquid	101	2.5	323	7.5	298	31
Sealing when Solid	101	7.5	298	2.5	323	328

The PCM heat sink was sealed with machine screws and an epoxy sealant (Torr Seal Low Vapor Pressure Epoxy) to ensure no leaking in the vacuum chamber. The final weight of the PCM heat sink was 195.51 g. Minus the weight of the copper (90.33 g), aluminium case (69.66 g) and mounting hardware (0.18 g), the actual weight of the PCM added to the heat sink was 35.34 g. The testing of the prototype heat sink in a vacuum chamber is presented in the next section.

5.4 PROTOTYPE TESTING

This section presents the thermal testing of the prototype PCM heat sink in a vacuum chamber for space applications. The following includes the test setup, test parameters (including the TES capacity of the prototype PCM heat sink), and finally the test results.

5.4.1 Test Setup

Figure 5.15 below shows the test setup schematic for the PCM heat sink. The orientation of the heat sink was vertical to allow the PCM to be concentrated around the heat source. A cartridge heater was used to simulate a heat pipe, which had a diameter of 6 mm and a length of 20 mm. The heater was placed halfway along the internal cavity of the heat sink with thermal paste.

A thermocouple was positioned near the cartridge heater to measure the heat input junction temperature. A 0.5 mm diameter hole was drilled alongside the cylindrical cavity, as shown in Figure 5.15 below, to allow placement of the thermocouple. The thermocouple used was a miniature k-type thermocouple (0.25 mm diameter), ideal to measure the fast transient temperature response.

The heat sink was placed on top of a stand 3D printed with Ultem 1010, a vacuum compatible thermoplastic with a low thermal conductivity of 0.24 W/m·K (Stratasys, 2021). The low thermal conductivity Ultem stand was printed with minimal contact area with the base of the PCM heat sink to ensure minimal heat transfer during the experiment.

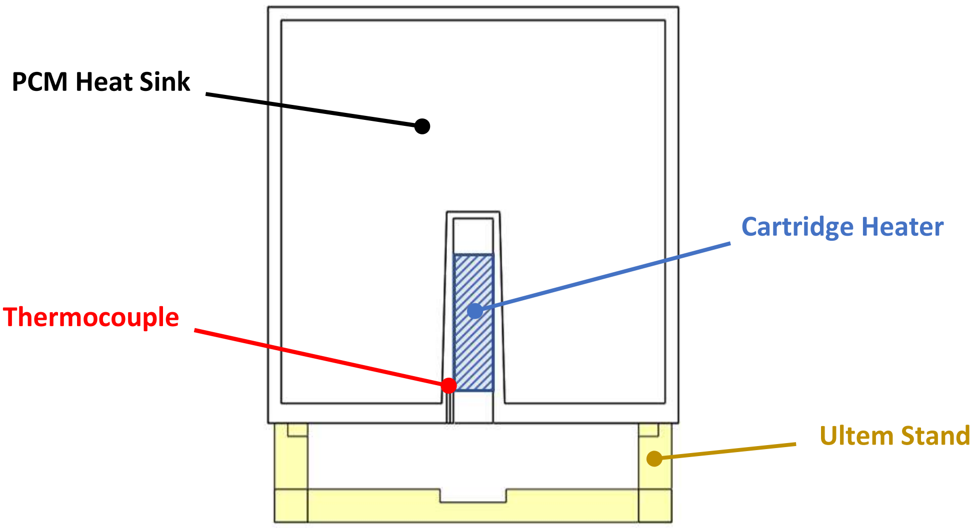

Figure 5.15: Test setup schematic

Figure 5.16 below shows the vacuum chamber used for the testing of the prototype PCM heat sink, with the test setup situated inside the chamber. The chamber featured a cylindrical cross-section with a large view port on the front and was connected to a high vacuum pump, pressure sensor and pressure release value.

The power supply for the cartridge heater and the cables for the thermocouple were connected into the chamber via a sealed through port at the rear of the vacuum chamber. A thermocouple was also placed externally of the chamber as a reference temperature. The sampling rate was every 1 second for the thermocouples and every 5 seconds for the power delivered to the cartridge heater.

The high vacuum pump used was a dual-stage oil sealed rotary vane pump. The aim was to achieve a high vacuum in the chamber, which is defined as a pressure range from 10^{-3} to 10^{-7} Torr (Roth, 2012). The pressure experienced in Low Earth Orbit is towards the low end of this range (i.e. 10^{-7} Torr). However, the higher-pressure values of this range (i.e. 10^{-3} Torr) are suitable for testing the performance of the prototype PCM heat sink (Isaacs et al., 2017).

Figure 5.16: Vacuum chamber test setup

5.4.2 Test Parameters and TES Capacity

The duration of the thermal test was dependent on the operating temperature range, heat load and TES capacity of the prototype PCM heat sink. The environment temperature of the laboratory was maintained between 24-25°C and the temperature limit specified for the PCM heat sink was 50°C. Accordingly, for practical reasons, the prototype PCM heat sink operating range was from 25 to 50°C.

The heat load delivered to the prototype PCM heat sink from the cartridge heater in the vacuum chamber was on average 41.3 W. The cartridge heater was rated for a higher power, however the planned 50 W could not be achieved due to the technical challenges associated with the resistance of the lead connectors through the vacuum chamber port.

The TES capacity of the prototype PCM heat sink for the given operating temperature range (25-50°C), was 12.9 kJ, which equated to a maximum 5.2 minutes of cooling capacity for the given heat load of 41.3 W. The TES capacity breakdown for each material component is provided in Table 5.11 below.

Table 5.11: TES capacity of prototype PCM heat sink
*For an applied heat load of 41.3 W
[A] (Velez et al., 2015), [B] (White et al., 2014). [C] (Alliance LLC, 2022)

	Weight (g)	Specific Heat (J/kg·K)	Latent Heat (J/kg)	TES Capacity (kJ)
Octadecane PCM	35.34	2,240 [A]	243,680 [A]	10.6
BMD Copper TCE	90.33	385 [B]	Nil	0.8
Aluminium Case	69.66	896 [C]	Nil	1.5
			Total	12.9 ***5.2 minutes**

Noting, the TES capacity of the prototype PCM heat sink (12.9 kJ) was approx. 2 kJ less than the TES capacity of the feasibility study heat sink (14.7 kJ) primarily due to the reduced amount of octadecane PCM (i.e. air gap) and the narrower temperature range. However, the cooling time was comparable to the feasibility study (approx. 5 minutes) due to the lower heat load (41.3 W instead of the 50 W simulated). The test results in the vacuum chamber are presented in the next section.

5.4.3 Test Results

Figure 5.17 below provides the thermal test results of the prototype PCM heat sink. The temperature response is shown for the thermocouple situated adjacent to the cartridge heater, which represented the heat input junction temperature.

The thermocouple temperature results are provided for the first 5.2 minutes of the experiment to align with the maximum TES capacity of the PCM heat sink for the given heat load. The temperature response was similar to the numerical modelling performed. At the beginning, a sharp rise in temperature was observed consistent with sensible heating. Then the temperature stabilised between 30 and 40°C as a result of the PCM latent heat. After 4.0 minutes, the temperature again climbed steadily with sensible heating.

At 5.2 minutes, the temperature of the thermocouple reached 53.7°C. Overall, the prototype PCM heat sink maintained the temperature of the heat input below 50°C for 4.7 min and thereby provided 90% TES utilisation of the maximum cooling capacity (5.2 min).

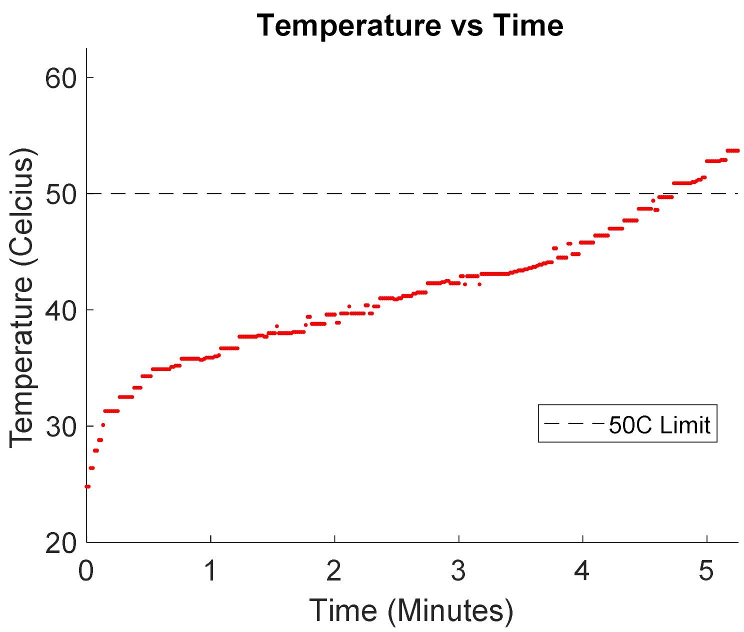

Figure 5.17: Prototype PCM heat sink thermal testing results

The experiment duration was 6.0 minutes, with the full testing results provided in Appendix J, including the reference thermocouple and power supplied to the cartridge heater. The average temperature of the reference thermocouple external to the vacuum chamber was 24.8°C during the experiment and then average power supplied to the cartridge heater was 41.3 W.

The pump down pressure achieved for the vacuum chamber during the experiment was 6 x 10^{-3} Torr, which was near the beginning of the high vacuum pressure range. Towards the end of the experiment, a small leak developed in the top heat sink weld line, as shown in Figure 5.18 below. This leak was noticed by the small air bubbling at the weld seam. As a result of the leak, the vacuum chamber pressure at the end of the experiment increased from 6 x 10^{-3} Torr to 8 x 10^{-3} Torr.

Figure 5.18: Minor weld leak under vacuum

Noting, prior to the experiment, the PCM heat sink was filled with Isopropanol and placed in the vacuum chamber sealed to check for leaks, but none were identified. It is suspected that when the prototype heat sink was filled with PCM, the PCM was drawn into the defect and solidified. Then, during the experiment when the PCM expanded from solid to liquid (11% expansion), the expansion caused the defect to open further and cause a hairline crack.

As a result of the small leak, the prototype PCM heat sink was not thermal cycled in the vacuum chamber for structural integrity. However, the small leak would not have affected the temperature results as it was very minor and developed towards the end of the experiment. In the next section, the test results are compared to the thermal numerical validation modelling, using the prototype testing parameters.

5.5 NUMERICAL MODEL VALIDATION

This section presents the numerical validation model for the prototype PCM heat sink. The purpose of the validation model was to verify the numerical methodology employed in this thesis. Firstly, the validation model is presented and secondly, the numerical results are presented, and finally the numerical results are compared to the experimental test results.

5.5.1 Numerical Validation Model

The numerical modelling methodology from Chapter 3 was applied to the prototype PCM heat sink. The modelling assumptions from Chapter 3 are summarised below, and their validity to the prototype PCM heat sink experiment are discussed.

- Firstly, the PCM volume was assumed constant for the solidification/melting model, and the liquid density was used to represent the amount of PCM in the system for the entire volume. This assumption was a limitation of fixed grid enthalpy porosity method and was also necessary for the validation model. However, the purpose of the model was a thermal analysis and not a structural analysis, thus the volume change was not of interest.
- Secondly, the PCM flow was assumed to have zero velocity, since the effect of gravity was not applicable for space applications, and hence the buoyancy convective heating was ignored. Whilst gravity was present for the experiment, this assumption could also be used for the validation model since conduction is the dominant heat transfer mechanism for such small base size and high thermal conductivity structures, where the role of buoyancy convection can be effectively ignored (Zhao et al., 2021).
- Thirdly, the PCM heat sink was modelled with no heat loss, representing the hot case, where the heat absorption stage was investigated without thermal radiation to space. This assumption could also be used for the experiment since the heat loss was negligible in the vacuum chamber. In addition, the low thermal conductivity Ultem stand had a minimal contact area with the heat sink and thus no heat loss could be assumed.
- Fourthly, the electronics and CubeSat radiator were not modelled. This assumption was also used for the validation model, since a radiator was not attached, and the electronics/heat pipe were simulated with a heating cartridge. Noting, the heating cartridge in the experiment provided additional minimal thermal mass, although was not modelled for the purposes of this analysis and further discussed in the results section.

As per Chapter 3, the prototype PCM heat sink was modelled with quarter symmetry to reduce computational effort, as shown in Figure 5.19 below. The internal volume of the PCM was reduced by 5% to represent the amount of PCM in the system. The void air space was at the top of the heat sink as per the experiment. Noting, the void space was not modelled with air, due its low thermal mass.

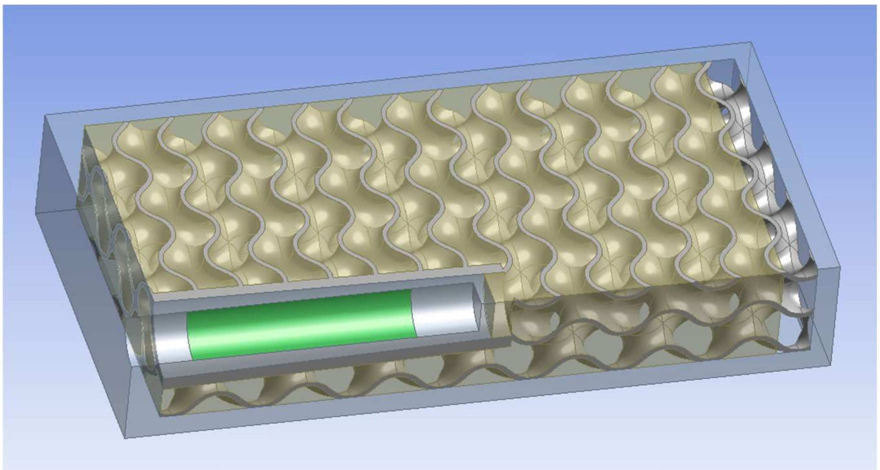

Figure 5.19: Quarter model of experiment heat sink

The material properties used aluminium 6061 for the case (see Table 5.3), BMD copper for the internal structure (see Table 5.1) and paraffin octadecane for the PCM (see Table 5.4). The PCM liquid density was used to represent the amount of PCM in the system (~35.3 g).

The heat input was modelled as a constant heat flux distributed over the heat input area for the cartridge heater, shown highlighted in green in Figure 5.19 above. The thermal boundary conditions between the PCM and the metal zones were specified as thermal coupled, to allow heat transfer between the zones. It was assumed that the PCM had direct contact with the metals and therefore the boundary did not include thermal resistance.

A thermal contact resistance was applied to the boundary between the aluminium case and BMD copper internal structure. Since the contact resistance achieved by the press fit was unknown, a nil contact resistance was modelled as the baseline, in addition to three nominal contact resistance values of 0.1, 0.05 and 0.01 $m^2 \cdot C/kW$, as per the feasibility study.

All zones were meshed with the 0.1 to 0.2 mm polyhedral mesh, with a 20% growth rate from the metal surfaces to the PCM liquid zone, as per Chapter 3. The timestep used with the numerical simulation was 0.2 seconds and 10 iterations were performed per timestep, as per Chapter 3. The energy residual at the end of each timestep converged past an order of magnitude of 10^{-8}.

5.5.2 Numerical Validation Model Results

The validation model numerical results are firstly presented for the PCM liquid fraction (i.e. PCM melting rate) and then secondly for the heat input junction temperature (i.e. temperature response).

Figure 5.20 below shows the PCM melting rate results for the numerical validation. The results are shown for nil contact resistance and contact resistance values of 0.1, 0.05 and 0.01 $m^2 \cdot C/kW$. The results showed that all the PCM had melted by 5.2 minutes, which represented the maximum TES capacity of the prototype PCM heat sink. In addition, the results showed that the PCM melt rate was constant for the first 4.0 minutes until 90% of the PCM was melted. The results also showed that the PCM melt rate was substantially the same for all contact resistance values. However, as shown in the next results, the temperature response varied for the different values of contact resistance.

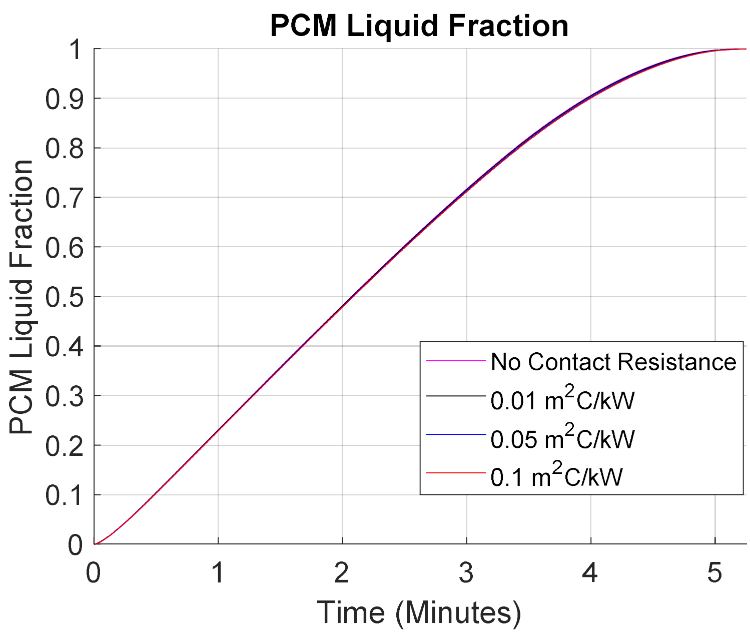

Figure 5.20: Numerical valuation model PCM liquid fraction

Figure 5.21 below shows the temperature response results for the numerical validation. The results all followed the same profile, however, as seen in the feasibility study, the temperature response was consistently higher with a greater value for thermal contact resistance. The results also showed that the temperature response stabilised between 30 and 40°C for the first 4.0 minutes, exhibiting the same trend as the experiment. However, the time at the 50°C limit varied depending on the thermal contact resistance value.

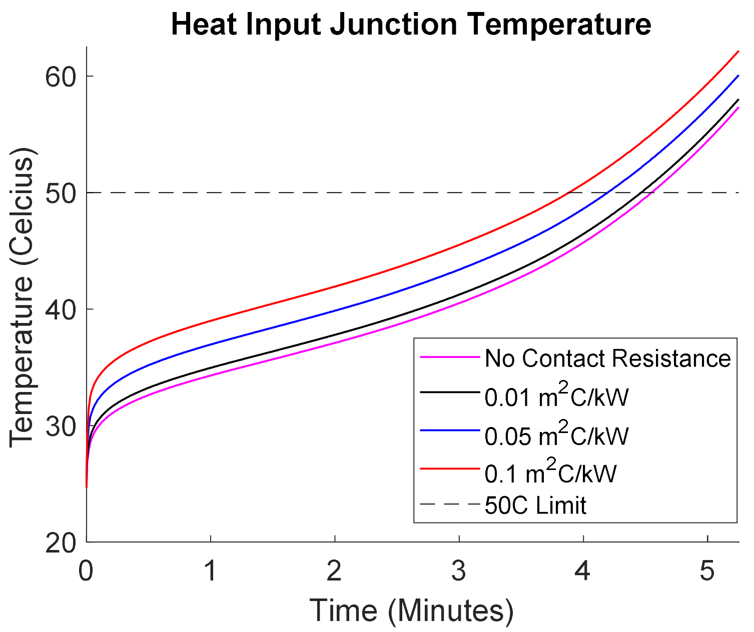

Figure 5.21: Numerical validation model heat input junction temperature

Table 5.12 provides the key results for the numerical validation model. The time at the 50°C limit achieved for the validation model was between 4.0 and 4.6 minutes depending on the thermal contact resistance value, thereby providing a TES utilisation between 77% to 89% accordingly. For the nil thermal contact resistance model, the numerical results (89% TES utilisation) closely aligned with the experimental test results (90% TES Utilisation). However, the comparison between the experimental and numerical results is further discussed in the next section for the prototype PCM heat sink.

Table 5.12: Key results for the numerical validation model

	Time at 50°C Limit	TES Utilisation at 50°C Limit
Nil Contact Resistance	4.6 minutes	89%
0.01 m^{2}C/kW	4.5 minutes	87%
0.05 m^{2}C/kW	4.3 minutes	83%
0.1 m^{2}C/kW	4.0 minutes	77%

5.5.3 Numerical Validation Model Comparison

The following provides a comparison between the experiment results and the numerical validation model results. Noting, only the temperature response results were compared due to the nature of the experiment, since the PCM melting rate was not observable for the experiment within the vacuum enclosed PCM heat sink. Furthermore, the average PCM temperature could not be measured, sine the PCM heat sink was a sealed system in the vacuum chamber.

In terms of performance, the experimental test results (4.7 minutes below 50°C limit) closely aligned with the nil thermal contact resistance modelling results (4.6 minutes below 50°C limit). However, as shown in Figure 5.22 below, the temperature response most closely aligned with the 0.05 $m^2 \cdot C/kW$ thermal contact resistance model.

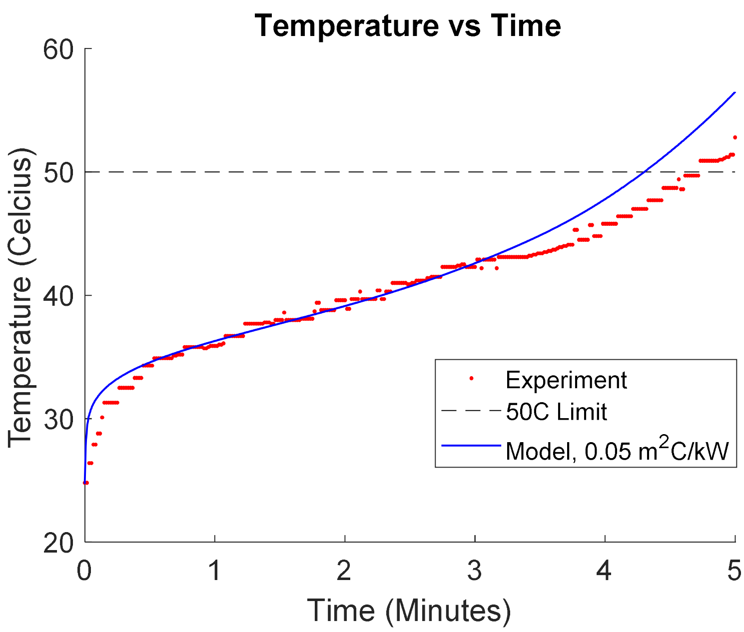

Figure 5.22: Numerical modelling vs experiment results

The 0.05 $m^2 \cdot C/kW$ thermal contact resistance model provided a cooling capacity of 4.3 minutes, which was 0.4 minutes less than the experimental testing results (4.7 minutes). However, there was a lag in the temperature response when comparing the experimental results with the numerical results. The lag at the beginning amounted to approximately 0.2 minutes and the lag at the 50°C limit was 0.4 minutes. The observed lag is further expanded in the discussion.

5.6 DISCUSSION

The test results showed that the hybrid additive PCM heat sink could provide adequate cooling for high heat loads and was a promising solution for space applications. The results are discussed in terms of the prototype testing results and the numerical model validation

5.6.1 Prototype Testing Results

The prototype BMD heat sink provided effective cooling for the 41.3 W heat load. The PCM heat sink maintained the temperature below 50°C for 4.7 min, which was 90% of the maximum TES capacity of the PCM heat sink (5.2 min). Therefore, the hybrid BMD heat sink demonstrated that it could provide adequate cooling for the 41.3 W heat load and therefore was a promising solution for cooling high-powered CubeSat electronics via a heat pipe.

The prototype PCM heat sink performed better than the feasibility study heat sink, which provided 78% TES utilisation for nil contact resistance, however, the heat load for the testing was only 41.3 W and not the planned 50 W. It was unknown how well the prototype PCM heat sink would perform with the higher 50 W load that would be capable with a 6 mm diameter heat pipe (ACT, 2021).

As a result of the small leak towards the end of the experiment, the prototype PCM heat sink was not thermal cycled in the vacuum chamber for structural integrity. Thus, whether the hybrid additive PCM heat sink was suitable for space applications could not be directly answered in this investigation. However, the conventional metal case provided a promising solution for the BMD additive manufacturing PCM containment issue identified in Chapter 4.

Noting, due to availability and prototyping constraints, the aluminium heat sink welds were limited by the skill and experience of the technician. With improved welding by a specialist aluminium welder, it is considered feasible that the case welds would provide leakproof PCM containment. However, the question remains how thin the walls could be and still provide structural integrity. The prototype heat sink was made with 2 mm thick aluminium walls, however, the original plan was to use 1 mm thick walls, which would reduce the aluminium case weight by half.

In terms of weight, the copper internal structure was the heaviest part of the heat sink, which weighed 90.33 g. Whereas, the PCM added was 35.34 g and the aluminium case was 69.66 g. The PCM provides the majority of the thermal capacity, and thus reducing the PCM component is not desired. However, the aluminium case weight could be reduced by further machining the walls, and the copper could be decreased reduced if the structure could be printed with a thinner wall thickness. Although at present, the BMD additive technology for copper was the limiting factor and further research would be required for the optimal wall thickness, if the technology allowed thinner walls.

5.6.2 Numerical Model Validation

There was good agreement between the test results and the numerical validation modelling results. In particular, the temperature response for the mid-range thermal contact resistance model (0.05 m^2·C/kW) aligned closely with the experimental test results. There was however a noticeable lag between the test results and the numerical validation modelling results. The lag at the beginning amounted to approximately 0.2 minutes and the lag at the 50°C limit was 0.4 minutes.

The observed lag could be explained by a few factors, which include the following:

- Firstly, the cartridge heater would have had a warm-up phase at the beginning of the experiment due to its associated thermal mass. This would have caused a temperature lag at the beginning of the experiment compared to the numerical results, since the numerical model simulated the heat input as a constant heat flux over the heat input boundary which began instantaneously.
- Secondly, the cartridge heater heat transfer with the PCM heat sink could have been reduced by the additional thermal contact resistance between the two metal junctions, even with thermal paste. Whereas the heat input was modelled with the full 41.3 W heat load without any thermal contact resistance. This may have also caused a consistent temperature lag throughout the experiment duration.
- Thirdly, the positioning of the thermocouple slightly away from the cartridge heater would have caused a slight delay in the thermal response from the heat input junction temperature to the thermocouple. This would have caused a consistent temperature lag throughout the entire duration.

Noting, for the actual operation of the PCM heat sink on a CubeSat, the electronics and heat pipe would also have an associated thermal mass and would therefore also need to be considered. Thus, there would also be a lag between the electronics heat generation and the PCM heat sink in real-world application during start up. Although, the numerical model provided a conservative prediction since it simulated the highest possible heat transfer.

Furthermore, the CubeSat heat rejection radiator connected to the heat sink would also need to be considered as it too would have a thermal mass and a heat dissipation rate to space. Whilst the heat rejection rate would only be a fraction of the heat load from the electronics, it would however extend the cooling capacity of the PCM heat sink. These matters are further discussed in the next Chapter for the Summary, Conclusions and Future Work.

6. Summary, Conclusions and Future Work

6.1 SUMMARY

The purpose of the research was to enable next generation capability for CubeSats by providing cooling solutions for high-powered electronics. CubeSats are a fast-growing area due to their small size, associated low cost and advancements in capabilities. However, due to their limited surface area available to radiate waste heat, CubeSats have been unable to utilise the increasing levels of power available and the capabilities of high-powered electronics

PCM heat sinks offer lightweight and compact cooling for CubeSats by absorbing the peak thermal loads and dissipating the waste heat to space during periods of downtime. Providing heat dissipation for a few minutes enables the use of high-power electronics during the short line of sight windows available. However, limited research is available for applying PCM heat sinks to high heat loads. The literature review showed that PCM heat sinks for CubeSat applications have been predominately investigated with paraffin PCMs, due to their high latent heat of fusion per unit weight. Although, the studies pertained to low power applications of less than 10 to 20 W.

With trends for higher power CubeSat applications, this research investigated paraffin PCM heat sinks for higher power applications. The main challenge with paraffin PCMs is their inherently low thermal conductivity. This research investigated the viability and application of enhancing PCM heat transfer with additive manufacturing optimisation. With additive manufacturing processes, new and novel methods were available which have the potential to provide cooling for high heat loads. However, there was very limited research on the optimal additively manufacturing structures for PCM heat transfer and also limited research on whether additively manufactured metal parts were suitable for space PCM applications.

Firstly, this research investigated the optimal additive structures for PCM heat transfer enhancement using thermal numerical modelling. The modelling explored how PCM heat transfer could be improved with additive structures and whether the low thermal conductivity of paraffin PCMs could be overcome to provide cooling of high-power CubeSat electronics. This research investigated the strut-based body centred cubic truss and the sheet-based TPMS gyroid structures, and compared to the traditional fin structure, where most of the research for PCM's had been performed. Noting, the gyroid structure had never been applied to PCM heat transfer.

The selected structures were compared for a conceptual 50 W heat sink design with approximately 5 minutes of TES capacity. The initial temperature of the heat sink was 15°C and the temperature limit specified was 50°C. The PCM modelled was paraffin octadecane (melting point approximately 28°C), with an internal PCM volume fraction of 85%. The selected structures were compared for dissipating heat directly from the heat source and dissipating heat transferred from a heat pipe. Two high thermal conductivity metals were investigated, copper and aluminium, to overcome the low thermal conductivity of octadecane. A base size analysis was also performed pushing the limits of allowable additive manufacturing minimum feature sizes. The effect of changing the base size, whilst maintaining the PCM to metal ratios, was analysed for both heat sink configurations, which had not been previously performed with such small base sizes for the strut-based body centred cubic truss and the sheet-based gyroid structures.

Secondly, this research explored the possibilities with the Bound Metal Deposition (BMD) additive manufacturing method for PCM heat sink applications. BMD was investigated since copper material was available for high thermal conductivity heat dissipation. However, there were many unknowns with the recently developed metal extrusion additive method, such as which additive structures were possible and how these structures could be customised for PCM heat transfer, as the process had never been applied to PCMs. Furthermore, it was unknown how the porosity in the process effected the material properties and capabilities, such as the thermal performance and whether BMD printed parts were suitable for space PCM applications.

The BMD porosity was firstly investigated to quantity the type and level of the porosity present in the manufacturing process and a prediction was made for the impact to thermal conductivity. The thermal conductivity was then experimentally tested to quantify the thermal performance of BMD parts. In addition, the manufacture of the gyroid TCE structure was explored to determine the wall thickness/base sizes possible with BMD and the leakproof integrity of BMD parts in a vacuum was tested with a gyroid internal structure to determine if the method was suitable for space PCM applications.

Finally, this research developed, tested and validated a BMD prototype PCM heat sink in a vacuum chamber. To provide leakproof PCM containment, a hybrid manufacturing concept was explored which combined a conventional metal case with the benefit of an optimised BMD copper internal additive structure. The feasibility of the hybrid BMD concept was firstly explored using numerical modelling methodology. The feasibility study investigated the performance of BMD copper and the use of an aluminium case, including the role of the contact resistance between the two metals.

Based on the concept feasibility study, a hybrid prototype PCM heat sink was manufactured using BMD. The prototype PCM heat sink was tested in a vacuum chamber, with a heat load delivered from cartridge heater representing the heat load from a heat pipe. The suitability for space applications was evaluated. In addition, a numerical model using the prototype testing parameters was performed to validate the numerical methodology employed in this thesis.

6.2 CONCLUSIONS

Based on the research performed in this thesis, the following conclusions were reached for each stage of this research. Firstly, in the numerical modelling investigation, this research found the following:

- The sheet-based gyroid structure was better than the strut-based truss structure at dissipating heat to PCM, and demonstrated the best PCM heat transfer in all three directions.
- Whilst the fins showed optimal performance for PCM melting in one direction for direct cooling, the fins failed to distribute heat in all directions for the heat pipe cooling.
- The performance of PCM heat sinks improved for smaller base sizes, using thinner structures to maintain the PCM volume fraction.
- The small base size structures demonstrated that effective cooling could be achieved using paraffin for a heat load of 50 W.
- For the direct cooling, 95% TES utilisation was achieved with copper and 88% TES utilisation was achieved with aluminium using the smallest fins and gyroid base size.
- For the heat pipe cooling, 87% TES utilisation was achieved with copper with the smallest gyroid base size and aluminium proved ineffective.

Secondly, in the BMD additive manufacturing investigated, this research found the following:

- The thermal conductivity of BMD copper was on average 11.2% less compared to the copper reference test, providing a relatively high thermal conductivity of 353 W/m·K for BMD copper.
- The 4 mm and 5 mm gyroid channel sizes were successfully printed using the high resolution printhead on the Desktop Metal Studio System, with an effective wall thickness of 0.407 mm and 0.414 mm respectively.
- The observed macro porosity due to the extrusion printing process was on average 1.4% and the observed micro porosity due to the sintering process was on average 1.0%.
- For the investigated 1 mm case, BMD was unable to provide leakproof PCM containment in a vacuum, due to the toolpath porosity inherent in the manufacturing process.

Thirdly, in the prototype PCM heat sink development and testing, this research found the following:

- Whilst there was an 11.2% reduction of the BMD copper thermal conductivity, the feasibility numerical study showed that BMD copper could provide reasonable heat dissipation for the heat pipe cooling configuration with over 80% TES utilisation at a heat load of 50 W.
- The feasibility numerical study also showed that a very low thermal contact resistance was required between the BMD copper internal structure and the external aluminium case for the hybrid BMD concept to be viable.
- The prototype hybrid PCM heat sink, with a heat load of 41.3 W delivered from a cartridge heater, provided 90% TES utilisation using paraffin octadecane PCM.
- The prototype experiment temperature response was accurately predicted with the numerical model, thereby providing model validation, although the model showed that better modelling of the heat input was required to account for the thermal mass of the system.

6.3 FUTURE WORK

Overall, the research demonstrated that effective paraffin PCM heat dissipation could be achieved for a heat load of 40 W (experimentally) to 50 W (numerically). This research also showed the benefits of additive manufacturing TCE structures for PCM heat transfer. During the research, opportunities for future work were identified and presented below for further discussion.

Firstly, there is scope for further numerical modelling work for different heat loads. This research numerically investigated a heat load of 50 W. However, other heat loads can be investigated and characterised. For example, higher heat loads for direct cooling and smaller electronics sizes can be investigated. It is suspected that for smaller electronics, additive structures would be beneficial since the gyroid was more effective at transferring heat in all directions from a concentrated load. Furthermore, larger diameter heat pipes with higher heat loads can also be investigated. Alternatively, multiple heat pipes from the heat source can also be investigated thereby distributing the heat load over each heat pipe into the PCM heat sink.

In addition, there is scope for further numerical modelling work for different additive structures. This research compared the body centred cubic truss and the TPMS gyroid structures, however there are limitless types of additive manufacturing geometries. Since the sheet-based geometry produced better results, further work could be performed investigating other TPMS sheet-based structures, as shown in Figure 3.1 from Chapter 3. Furthermore, there is scope to investigate additive structures with fractal geometries, where the thickness of the structure increases near the source for improved heat transfer and then decreases away from the heat source. Although, there are limits with additive manufacturing with minimum feature sizes.

Regarding additive manufacturing, there is also scope for further investigations with other additive methods. For example, the application of aluminium additive manufacturing using selective laser sintering (SLS). Aluminium is substantially lighter than copper and produced reasonable results for the direct cooling numerical investigation. Also, whilst the numerical investigated showed that aluminium alone could not provide adequate heat dissipation for the heat pipe cooling configuration, the aluminium heat sink could be investigated with multiple heat pipes from the heat source, thereby lowering the heat load from each heat pipe. However, the suitability of SLS for space PCM applications would also need to be investigated and the thermal conductivity and TCE base sizes possible with the method explored.

Further work could also be performed to investigate the structural strength of additive TCE geometries and whether they would provide benefit for PCM containers to withstand the volume change during the PCM melting and freezing cycles. Although, this heavily relies on the properties of the manufacturing process, as seen for BMD which was unable to contain PCM in a vacuum. Regarding the hybrid BMD concept investigated in this research, further work is necessary to determine if the concept was suitable for PCM thermal cycling. Also, minimising the internal air gap to determine the allowable pressure change. This analysis could not be performed for the prototype BMD heat sink due to the minor weld leak in the aluminium case, however the thermal results were analysed.

Finally, the model validation highlighted the importance of modelling the thermal mass of the heat input, since there was a noticeable lag between the Chapter 5 experiment and the numerical validation model. For this research, the PCM heat sink was viewed in isolation. However, the thermal mass of the CubeSat system also needs to be considered within the operating environment. Firstly, the electronics, radiator and CubeSat structure need to be considered as these all add thermal mass via sensible heating and would prolong the use of the electronics. Although, the amount additional thermal storage depends on the system and notably would be a fraction of the PCM thermal energy storage.

Also, the heat rejection by the radiator also needs to be explored whilst the PCM heat sink is absorbing heat. However, this is a complex interaction with the thermal radiative environment and greatly depends on whether the CubeSat is on the solar exposed or eclipse portion of the orbit. It also depends on the orientation of the CubeSat and the location of its radiators. There are thermal analysis software packages developed for ray tracing during LEO orbits, such as ESATAN-TMS, but these have not been integrated with high fidelity thermal modelling tools such as ANSYS used for this research. Therefore, there is scope to further explore the performance of the PCM heat sink for high-powered electronics within the CubeSat thermal environment.

7. References

ACT. PCM Heat Sink Design Considerations. 2020 20/05/2020]; Available from: https://www.1-act.com/innovations/thermal-storage/pcm-heat-sink-design-considerations/.

ACT, Advanced Cooling Technologies, ACT, PCM Heat Sinks, Accessed 22/05/21, https://www.1-act.com/products/pcm-heat-sinks/.

ACT, Advanced Cooling Technologies, Heat Pipe Calculator, Accessed Online 07/12/2021, Web address: https://www.1-act.com/resources/heat-pipe-calculator/.

Akizuki, Y., et al., Development and testing of the re-deployable radiator for deep space explorer. Applied Thermal Engineering, 2020. 165: p. 114586.

AlenSpace. A Basic Guide to Nanosatellites. 2020 17/04/2020]; Available from: https://alen.space/basic-guide-nanosatellites/.

Alketan O, Rowshan R, Abu Al-Rub R, Topology-mechanical property relationship of 3D printed strut, skeletal, and sheet based periodic metallic cellular materials, Elsevier, Additive Manufacturing, 2018.

Alketan O, Abu Al-Rub R, Multifunctional mechanical-metamaterials based on triply periodic minimal surface lattices: A review. Advanced Engineering Materials, 2019.

Alliance LLC, Aluminium 6061 T6 Material Data Sheet, Accessed online 6 May 2022, Web address link, https://www.allianceorg.com/pdfs/alumext/6061t6.pdf.

Amin, M., et al., Thermal properties of beeswax/graphene phase change material as energy storage for building applications. Applied Thermal Engineering, 2017. 112: p. 273-280.

ANSYS Inc, ANSYS Fluent Theory Guide, Release 2021 R1.

ANSYS Inc, ANSYS Fluent User's Guide, Release 2021 R1.

ASM International, 2000. Electrical and Magnetic Properties of Metals Data Book (#06333G), www.asminternational.org.

Atlas Steels, Data Sheet Aluminium Alloy 6063, Atlas Steels Pty Ltd, 2013.

AZ. AZ-93 White Thermal Control, Electrically Conductive Paint / Coating. 2020 14/05/2020]; Available from: http://www.aztechnology.com/materials-coatings-az-93.html.

Badagavi, P., V. Pai, and A. Chinta. Use of Origami in Space Science and various other fields of science. in 2017 2nd IEEE International Conference on Recent Trends in Electronics, Information & Communication Technology (RTEICT). 2017.

Basiliere P, Metal 3D Printer Selection Begins with the End in Mind, Published Xerox.com, Accessed online 19 July 2022, Web Address: https://www.xerox.com/en-us/innovation/insights/metal-3d-printer-selection

Becedas, J. and A. Caparrós, Additive Manufacturing Applied to the Design of Small Satellite Structure for Space Debris Reduction, in Applications of Design for Manufacturing and Assembly. 2018, IntechOpen.

Benedetti M, Plessis A, Ritchie R, Dallago M, Razavi S, Berto F, 2021, “Architected cellular materials: A review on their mechanical properties towards fatigue-tolerant design and fabrication”, Materials Science & Engineering

Boushon, K.E., Thermal analysis and control of small satellites in low Earth orbit, in Mechanical and Aerospace Engineering. 2018, Missouri University of Science and Technology.

Bozkaya D, Muftu S, 2003, Mechanics of the tapered interference fit in dental implants, Elsevier, Journal of Biomechanics 36 (2003) 1649–1658

Bryce, Global Space Industry Dynamics : Research Paper for Australian Government, Department of Industry, Innovation and Science. 2017, Alexandria (United States) : Bryce Space and Technology LLC.

Budynas R, Nisbett J, 2020, Shigley’s Mechanical Engineering Design, Eleventh Edition, McGraw-Hill Education

Cengel Y, Heat Transfer: A Practical Approach, Second Edition, McGraw-Hill, 2002.

Cengel, Y.A. and A.J. Ghajar, Heat and Mass Transfer: Fundamentals and Applications 5th Edition ed. 2015: Mcgraw-Hill Education.

Chandrashekar, S., Thermal Analysis and Control of MIST CubeSat. 2017, KTH, School of Electrical Engineering (EES).

Choi, D.H., et al., Thermal conductivity and heat transfer performance enhancement of phase change materials (PCM) containing carbon additives for heat storage application. International Journal of Refrigeration, 2014. 42: p. 112-120.

Choi, M.K., Paraffin Phase Change Material for Maintaining Temperature Stability of IceCube Type of CubeSats in LEO. American Institute of Aeronautics and Astronautics, 2015. AIAA 2015-3984.

Choi, M.K. Thermal Assessment of Paraffin Phase Change Material Mini-Packs on IceCube 3U CubeSat in Flight. in 2018 International Energy Conversion Engineering Conference. 2018.

Choi, M.K., Using Paraffin PCM for Thermal Management of BOLAS Planetary CubeSats with Ion Thrusters, in AIAA Propulsion and Energy 2019 Forum. 2019.

Chen, M.-H., J.-D. Huang, and C.-R. Chen. An investigation on phase change device for satellite thermal control. in 2016 7th International Conference on Mechanical and Aerospace Engineering (ICMAE). 2016.

Clydespace, Satellite solar arrays, Accessed 09/09/2021, https://www.aac-clyde.space/satellite-bits/solar-arrays.

Collette, J., et al., Phase change material device for spacecraft thermal control. 62nd International Astronautical Congress 2011, 2011.

Conex, Material Data Sheet High Conductivity Copper Alloy 110, Consolidated Extrusions Pty Ltd, 1994.

C-Therm, Thermal Conductivity Instrument User Manual, Manual Version: 4.1 09/2020.

Davis L, Body Physics Second Edition, Pressbooks, Accessed Online 26/04/22, Web Address: https://openoregon.pressbooks.pub/bodyphysics2ed/chapter/hydrostatic/.

Desktop Metal, Bound Metal Deposition Design Guide Studio System, Version 1.0, 2020.

Desktop Metal, Copper Material Data Sheet, BMD-MDS-COPPER-201203, 2020.

Desktop Metal, Fabricate Settings, Accessed online 02/05/2020, https://fab.desktopmetal.com/studio.

Desktop Metal, Knowledge Base, ‘Density of Studio System Parts’, ‘Tolerances of Studio System Parts’, ‘Strength of Studio System Parts’, Accessed online 03/06/2020, knowledge.desktopmetal.com.

Desktop Metal, Materials Library, Accessed online 03/06/2020; Available online, https://www.desktopmetal.com/materials.

EOS GmbH - Electro Optical Systems, Material Data Sheet: Aluminium AlSi10Mg, 05/2014

EOS GmbH - Electro Optical Systems, Material Data Sheet: Aluminium AlSi10Mg, 05/2021

Elliott J, Lebon M, Robinson A, Optimising integrated heat spreaders with distributed heat transfer coefficients: A case study for CPU cooling, Case Studies in Thermal Engineering, Elsevier, 2022

Emery, W. and A. Camps, Chapter 12 - Remote Sensing With Small Satellites, in Introduction to Satellite Remote Sensing, W. Emery and A. Camps, Editors. 2017, Elsevier. p. 797-810.

Engineering ToolBox, Water Density, Accessed online 23/06/2022, Web Address: https://www.engineeringtoolbox.com/water-density-specific-weight-d_595.html.

Engineering Toolbox, 2022, Atmospheric Pressure vs. Elevation above Sea Level, Accessed Online 12/07/2022, Web address: https://www.engineeringtoolbox.com/air-altitude-pressure-d_462.html.

Engineering Toolbox, 2022, Young’s Modulus Copper and Poisson's Ratio Copper, Accessed Online 24/03/2022, Web address: https://www.engineeringtoolbox.com/young-modulus-d_417.html, https://www.engineeringtoolbox.com/poissons-ratio-d_1224.html.

ERG, Review of Australia's Space Industry Capability. 2018, Report from the Expert Reference Group.

Facchinetti, G., et al., Small Satellites Economic Trends. 2016, Space Industry and R&D Collaborations.

Fatchurrohman N, Chia ST, Performance of hybrid nano-micro reinforced mg metal matrix composites brake calliper: simulation approach, 4th International Conference on Mechanical Engineering Research, 2017

Fletcher LS, Conduction in solids, imperfect metal-to-metal contacts: thermal contact resistance, Section 502.5. Heat Transfer and Fluid Mechanics Data Books, Genium Publishing Company, Schenectady, New York, 1991.

Fletcher LS, Experimental Techniques for Thermal Contact Resistance Measurements, Elsevier Experimental Heat Transfer, Fluid Mechanics and Thermodynamics, 1993.

GE Additive, Frydryk D, 10 March 2021, Porosity in Metal Additive Manufacturing, Accessed online, https://www.ge.com/additive/blog/get-facts-porosity-metal-additive-manufacturing.

Ge, H., et al., Low melting point liquid metal as a new class of phase change material: An emerging frontier in energy area. Renewable and Sustainable Energy Reviews, 2013. 21: p. 331-346.

Ge, H. and J. Liu, Keeping Smartphones Cool With Gallium Phase Change Material. Journal of Heat Transfer, 2013. 135(5).

Gil, A., et al., Experimental analysis of the effective thermal conductivity enhancement of PCM using finned tubes in high temperature bulk tanks. Applied Thermal Engineering, 2018. 142: p. 736-744.

Hale, D.V., M.J. Hoover, and M.J. O'Neill, Phase Change Materials Handbook. NASA CR-61363, 1971.

Han, S.C., et al., A Microscopic Shell Structure with Schwarz’s D-Surface. Scientific Reports, 2017. 7(1): p. 13405.

Hansen, S.W., et al. Water-Based Phase Change Material Heat Exchanger Development. 2014. 44th International Conference on Environmental Systems.

Hartsfield C, Shelton T, Palmer B; O’Hara R, All-Metallic Phase Change Thermal Management Systems for Transient Spacecraft Loads, Journal of Aerospace Engineering, 2020

Hengeveld, D., et al., Thermal Design Considerations for Future High-Power Small Satellites. 48th International Conference on Environmental Systems, 2018. ICES_2018_77.

Hengeveld, D.W., et al., Enabling High-Power SmallSats with Advanced Thermal Management. 2019.

Hernigou P, Queinnec S, Flouzat Lachaniette C, One hundred and fifty years of history of the Morse taper: from Stephen A. Morse in 1864 to complications related to modularity in hip arthroplasty. International Orthopaedics (SICOT) 37, 2081–2088, 2013.

Huang, Y., et al., Additive Manufacturing: Current State, Future Potential, Gaps and Needs, and Recommendations. Journal of Manufacturing Science and Engineering, 2015.

Huang, Z., Y. Hwang, and R. Radermacher, Review of nature-inspired heat exchanger technology. International Journal of Refrigeration, 2017. 78: p. 1-17.

llis, M., et al., Development of a miniature cryocooler system for cubesats. 2014. 18: p. 329-337.

Incropera, F.P., et al., Fundamentals of Heat and Mass Transfer. Sixth Edition ed. 2007: John Wiley & Sons.

Ippolito, L.J., Jr., Satellite Communications Systems Engineering : Atmospheric Effects, Satellite Link Design and System Performance. 2017, Chicester, UNITED KINGDOM: John Wiley & Sons, Incorporated

Iradukunda, A.-C., et al., Transient Thermal Performance using Phase Change Material Integrated Topology Optimized Heat Sinks. Applied Thermal Engineering, 2020: p. 115723.

Isaacs, S., et al. Development of a two-phase heat strap for CubeSat applications. 2016. 46th International Conference on Environmental Systems.

Isaacs, S., D. Arias, and G. Shoukas, Development of a Lightweight and Low-Cost 3D-Printed Aluminum PCM Panel for Thermal Management of CubeSat Applications. 47th International Conference on Environmental Systems, 2017. ICES 2017 108.

Isaacs, S.A., et al., Experimental Development and Computational Optimization of Flat Heat Pipes for CubeSat Applications. Journal of Electronic Packaging, 2017. 139(2).

Ivanov, E., et al., PLA/graphene/MWCNT composites with improved electrical and thermal properties suitable for FDM 3D printing applications. 2019. 9(6): p. 1209.

Jafari, D. and W.W. Wits, The utilization of selective laser melting technology on heat transfer devices for thermal energy conversion applications: A review. Renewable and Sustainable Energy Reviews, 2018. 91: p. 420-442.

Janzer, K., et al., Thermal Control of High Power Applications on CubeSats. 2018.

Kandasamy, R., X.-Q. Wang, and A.S. Mujumdar, Transient cooling of electronics using phase change material (PCM)-based heat sinks. Applied Thermal Engineering, 2008. 28(8): p. 1047-1057.

Kosky P, Balmer R, Keat W, Wise G, Exploring Engineering (Third Edition), Chapter 12 - Mechanical Engineering, Academic Press, 2013,

Khan, Z., Z. Khan, and A. Ghafoor, A review of performance enhancement of PCM based latent heat storage system within the context of materials, thermal stability and compatibility. Energy Conversion and Management, 2016. 115: p. 132-158.

Kumar G, Prasad G, Pohl R, 1993, Review Experimental determinations of the Lorenz number, Journal of Materials Science 28 (1993) 4261-4272.

Kwas, A., et al., Printing Multi-Functionality: Additive Manufacturing for CubeSats. AIAA SPACE 2014 Conference and Exposition, American Institute of Aeronautics and Astronautics, 2014.

Laing, D., et al., Development of high temperature phase-change-material storages. Applied Energy, 2013. 109: p. 497-504.

Lieberwirth, C., A. Harder, and H. Seitz, Extrusion Based Additive Manufacturing of Metal Parts. Journal of Mechanics Engineering and Automation, 2017.

Liu, M., et al., Review on concentrating solar power plants and new developments in high temperature thermal energy storage technologies. Renewable and Sustainable Energy Reviews, 2016. 53: p. 1411-1432.

Mahdi, J.M., S. Lohrasbi, and E.C. Nsofor, Hybrid heat transfer enhancement for latent-heat thermal energy storage systems: A review. International Journal of Heat and Mass Transfer, 2019. 137: p. 630-649.

Majumdar A, Reddy P, Role of electron–phonon coupling in thermal conductance of metal–nonmetal interfaces, Applied Physics Letters, Vol. 84, No. 23, 2004.

Mancin, S., et al. (2015). "Experimental analysis of phase change phenomenon of paraffin waxes embedded in copper foams." International Journal of Thermal Sciences 90: 79-89.

Martin, J.H., et al., 3D printing of high-strength aluminium alloys. Nature, 2017. 549(7672): p. 365-369.

Meseguer, J., I. Pérez-Grande, and A. Sanz-Andrés, Spacecraft Thermal Control. 2012: Woodhead Publishing.

McKinley, I.M., et al., Pyrolytic graphite film thermal straps: Characterization testing. Cryogenics, 2016. 80: p. 174-180.

Minco. Flexible Heaters Design Guide. 2020 28/05/2020]; Available from: https://www.minco.com/~/media/files/minco/instructions/heaters/heater%20design%20guide.ashx .

Mingear, J. and D. Hartl. Corrosion of nickel-titanium, C110, and Al6061 in gallium-based liquid metal alloys. in TMS 2017 146th Annual meeting & exhibition supplemental proceedings. 2017. Springer.

Montes J, Cuevas F, Cintas J, Porosity effect on the electrical conductivity of sintered powder compacts, Applied Physics A 92, 375–380, 2008.

Moraga, N.O., J.P. Xamán, and R.H. Araya, Cooling Li-ion batteries of racing solar car by using multiple phase change materials. Applied Thermal Engineering, 2016. 108: p. 1041-1054.

Nafis, B.M., et al., Additive Manufacturing for Enhancing Thermal Dissipation in Heat Sink Implementation: A Review. Heat Transfer Engineering, 2020: p. 1-18.

NASA. State of the Art of Small Spacecraft Technology. 2018 14/04/2020]; Available from: https://sst-soa.arc.nasa.gov/07-thermal.

NASA. What are SmallSats and CubeSats? 2015 21/03/2020]; Available from: https://www.nasa.gov/content/what-are-smallsats-and-cubesats.

National Academies of Sciences, Achieving Science with CubeSats: Thinking Inside the Box, 2016, Washington, DC: The National Academies Press. https://doi.org/10.17226/23503.

Netzsch, 2021, Differential Scanning Calorimetry DSC 404 F1/F3 Pegasus Method, Technique, Applications.

Ning J, Sievers D, Garmestani H , Liang S, Analytical modelling of part porosity in metal additive manufacturing, International Journal of Mechanical Sciences, Elsevier, 2020.

Nurhudan A, Supriadi S, Whulanza Y, Saragih A, Additive manufacturing of metallic based on extrusion process: A review, Journal of Manufacturing Processes, Elsevier, 2021.

Petrak M, Rattan A, Olson R, Kozub J, How to design parts for metal 3D printing, Precision ADM, HUBS Knowledge Base, Web address: https://www.hubs.com/knowledge-base/how-design-parts-metal-3d-printing/

Podroužek, J., et al., Bio-Inspired 3D Infill Patterns for Additive Manufacturing and Structural Applications. 2019. 12(3): p. 499.

Protolabs Inc, Direct Metal Laser Sintering Capabilities, Accessed Online 14/09/2020, Web Address: https://www.meddeviceonline.com/doc/direct-metal-laser-sintering-capabilities-0001

PumpkinSpace, Power and Energy, Accessed 09/09/2021, https://www.pumpkinspace.com/store/c28/Power_%26_Energy.html.

RabeloI S, OmonteII S, VieiraII S, JansenII W, SeraidarianII P, Morse taper internal connection implants: would abutment reseating influence retention, Brazilian Journal of Oral Sciences, 2015.

Rathod, M.K. and J. Banerjee, Thermal stability of phase change materials used in latent heat energy storage systems: A review. Renewable and Sustainable Energy Reviews, 2013. 18: p. 246-258.

Reiss, P., New methodologies for the thermal modelling of CubeSats. 2012.

Remacle, P., Study of a cooling system for a CubeSat infrared detector, in Faculty of Applied Sciences. 2018, University of Liege.

Righetti G, Savio G, Meneghello R, Doretti L, Mancin S, Experimental study of phase change material (PCM) embedded in 3D periodic structures realized via additive manufacturing, International Journal of Thermal Sciences 153 (2020).

Rodrigues H, Gaspar F, Fernandes P, Mateus A, Constructions: Proceedings of the International Conference on Automation Innovation in Construction (CIAC-2019), Leiria, Portugal, 2020, Springer Nature

Ronneberg T, Davies C, Hooper P, Revealing relationships between porosity, microstructure and mechanical properties of laser powder bed fusion 316L stainless steel through heat treatment, Elsevier, Materials and Design 189 (2020), https://doi.org/10.1016/j.matdes.2020.108481.

Roth A, 2012, Vacuum Technology, Third Edition, Elsevier.

Rubitherm, Data Sheet RT55, Version: 09.10.2020, Rubitherm Technologies GmbH, Web: www.rubitherm.com

Savage, C.J., Spacecraft Systems Engineering. 2011: John Wiley & Sons, Ltd.

Sheikholeslami, M., Solidification of NEPCM under the effect of magnetic field in a porous thermal energy storage enclosure using CuO nanoparticles. Journal of Molecular Liquids, 2018. 263: p. 303-315.

Sheldahl. Product Bulletin Aluminum Coated (One Side) FEP 2020 14/05/2020]; Available from: https://www.sheldahl.com/sites/default/files/2017-09/Radiator%20SSM_0.pdf.

Shamberger, P.J. and N.M. Bruno, Review of metallic phase change materials for high heat flux transient thermal management applications. Applied Energy, 2020. 258: p. 113955.

Shamvedi, D., et al., 3D Metal printed heat sinks with longitudinally varying lattice structure sizes using direct metal laser sintering. Virtual and Physical Prototyping, 2018. 13(4): p. 301-310.

Sharma, S.D. and K.J.I.J.o.G.E. Sagara, Latent heat storage materials and systems: a review. International Journal of Green Energy, 2005. 2(1): p. 1-56.

Shinde, P., et al. Active thermal control system for CubeSat. in 30th Florida Conference on Recent Advances in Robotics. 2017.

Silva V, Cardoso J, 'Computational Fluid Dynamics Applied to Waste-to-Energy Processes: A Hands-On Approach', Butterworth-Heinemann, 16 June 2020

Sola A, Nouri A, Microstructural porosity in additive manufacturing: The formation and detection of pores in metal parts fabricated by powder bed fusion, Journal of Advanced Manufacturing and Processing, 2019 https://doi.org/10.1002/amp2.10021.

Soro, N., et al., Investigation of the structure and mechanical properties of additively manufactured Ti-6Al-4V biomedical scaffolds designed with a Schwartz primitive unit-cell. Materials Science and Engineering: A, 2018. 745.

Stratasys, 2021, FDM Thermoplastic Filament ULTEM 1010 Resin Data Sheet.

TCPoly. Technical Data Sheet Ice9 Flex. 2019 03/06/2020]; Available from: https://tcpoly.com/wp-content/uploads/2019/09/TDS_ice9_Flex.pdf.

Thiagarajan N, 2017, A Novel Approach to Development of a Thermal Capacitor, Electronics Cooling, Web address: https://www.electronics-cooling.com/2017/02/novel-approach-development-thermal-capacitor/

TMT. Thermal Storage Units. 2020 27/05/2020]; Available from: https://ef1847f1-554c-4a0a-94a3-c51893ab9a0a.filesusr.com/ugd/4ab2a3_259014515dd144139406f21943c49119.pdf.

Ueno, A., K. Yamada, and H. Nagano. Study on a Functional Thermal Control Systems for High-power Micro-satellite. 2017. 47th International Conference on Environmental Systems.

Vander Voort, G.F., 2000. Copper Color metallography. Advanced materials & processes, 158(1), pp.36-36.

Velez C, Khayet M, Ortiz de Zarate JM, Temperature-dependent thermal properties of solid/liquid phase change even-numbered n-alkanes: n-Hexadecane, n-octadecane and n-eicosane, Elsevier Applied Energy 143, 2015.

Vincent C, Silvain JF, Heintz JM, Chandra N, Effect of porosity on the thermal conductivity of copper processed by powder metallurgy, Journal of Physics and Chemistry of Solids, Elsevier, 2020.

Vyavahare, S., et al., Fused deposition modelling: a review. Rapid Prototyping Journal, 2019. ahead-of-print.

Walton D, Oxygen Free High Conductivity Copper Explaioned, Published 25/07/2017 https://www.linkedin.com/pulse/oxygen-free-high-conductivity-copper-explained-denzil-walton.

Wei, G., et al., Selection principles and thermophysical properties of high temperature phase change materials for thermal energy storage: A review. Renewable and Sustainable Energy Reviews, 2018. 81: p. 1771-1786.

White G, Collocott S, 1984, Heat Capacity of Reference Materials: Cu and W, J. Phys. Chem. Ref. Data, Vol. 13, No.4.

Whitehead S, Triply Periodic Minimal Surfaces, Wordpress, Posted on 02/2019, Web Address: https://wewanttolearn.wordpress.com/tag/millipede/.

Wilson, M., D. Hengeveld, and B. Taft. Advanced Manufacturing of Flexible Oscillating Heat Pipes for Next-Generation Thermal Straps. 2017. 47th International Conference on Environmental Systems.

Wu, J., et al., Infill optimization for additive manufacturing—approaching bone-like porous structures. 2017. 24(2): p. 1127-1140.

Xiao S, Jiang X, Li X, Contact Stress Analysis of Tapered Interference Fit for the Cantilevered Axle, 3rd International Conference on Material, Mechanical and Manufacturing Engineering, 2015

Yamada, K. and H. Nagano, Development of a heat storage panel for micro/nano-satellites and demonstration in orbit. Applied Thermal Engineering, 2015. 91: p. 894-900.

Yamada, K., et al. Heat storage panel using a phase-change material encapsulated in a high-thermal conductivity CFRP for micro satellites. 2014. 44th International Conference on Environmental Systems.

Young, J., S. Inlow, and B. Bender. Solving Thermal Control Challenges for CubeSats: Optimizing Passive Thermal Design. in 2019 IEEE Aerospace Conference. 2019.

Yu, G.-C., L.-Z. Wu, and L.-J. Feng, Enhancing the thermal conductivity of carbon fiber reinforced polymer composite laminates by coating highly oriented graphite films. Materials & Design, 2015. 88: p. 1063-1070.

Zhao, C., et al., Numerical study of melting performance enhancement for PCM in an annular enclosure with internal-external fins and metal foams. International Journal of Heat and Mass Transfer, 2020. 150: p. 119348.

Zhao C, Opolot M, Liu M, Bruno F, Mancin S, Flewell-Smith R, Hooman K, Simulations of melting performance enhancement for a PCM embedded in metal periodic structures, International Journal of Heat and Mass Transfer, Volume 168, 2021.

Zhang, C., et al., Numerical study on heat transfer enhancement of PCM using three combined methods based on heat pipe. Energy, 2020. 195: p. 116809.

Appendix A: Numerical Modelling Sensitivity Analysis

Mesh Size Study

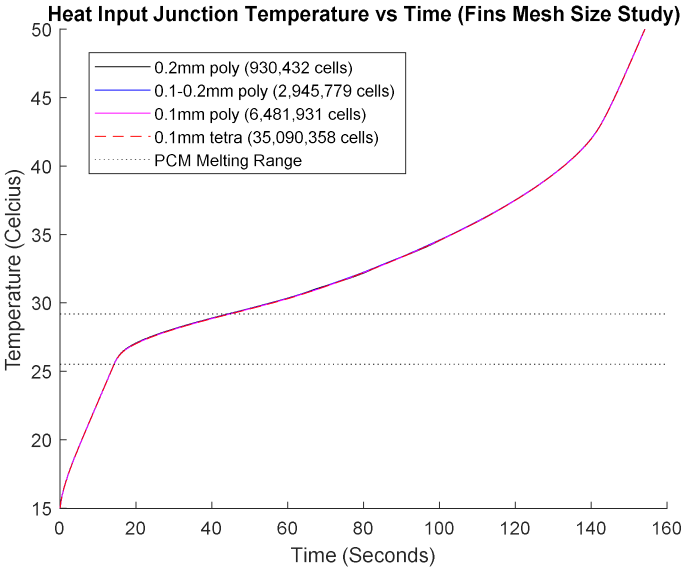

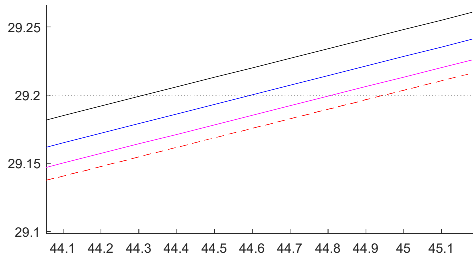

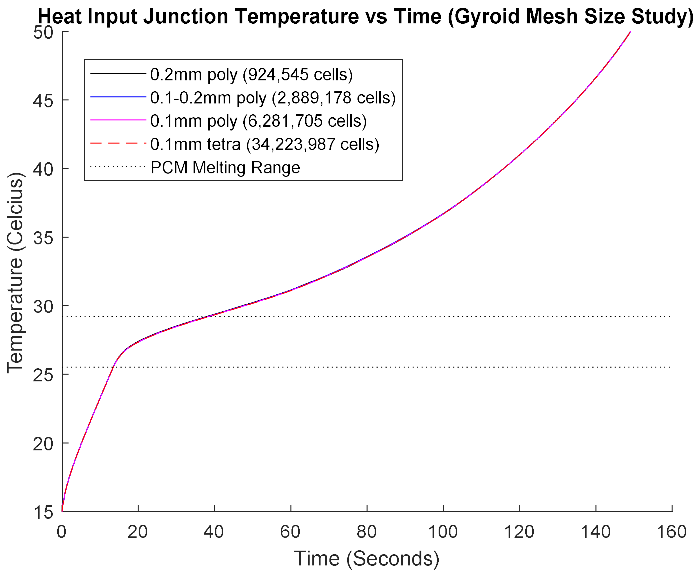

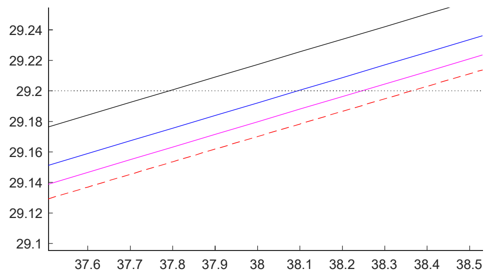

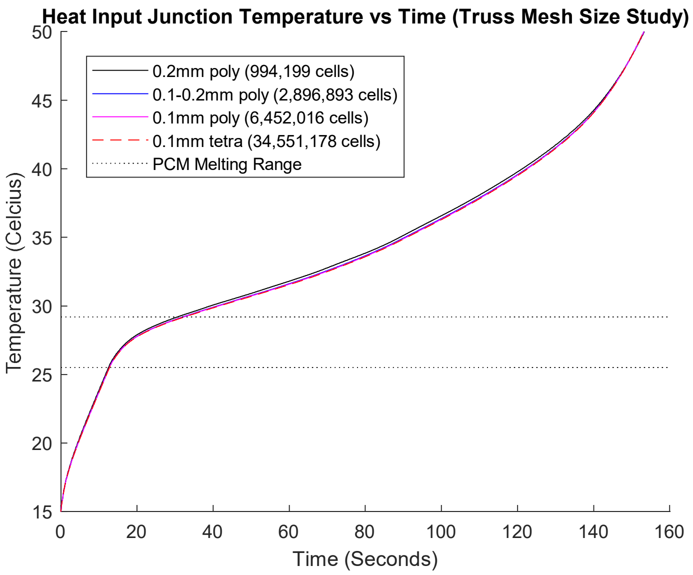

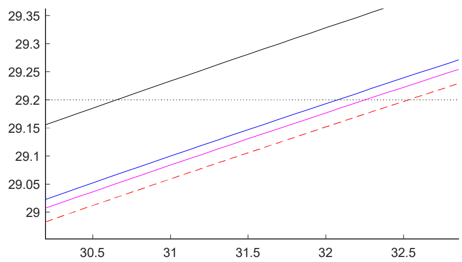

Timestep Study

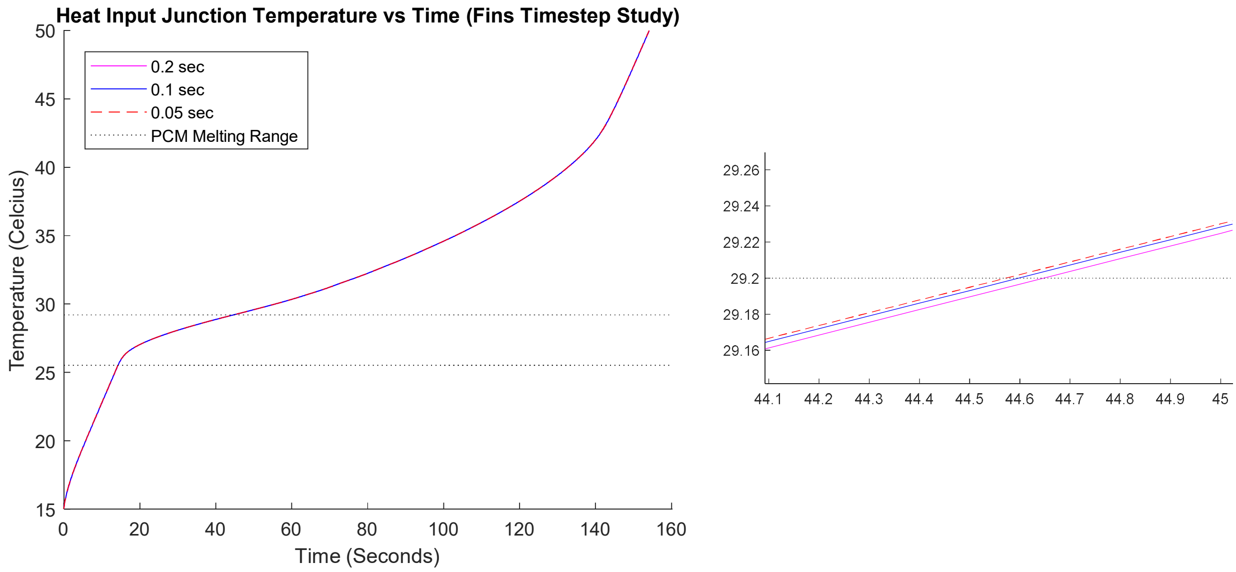

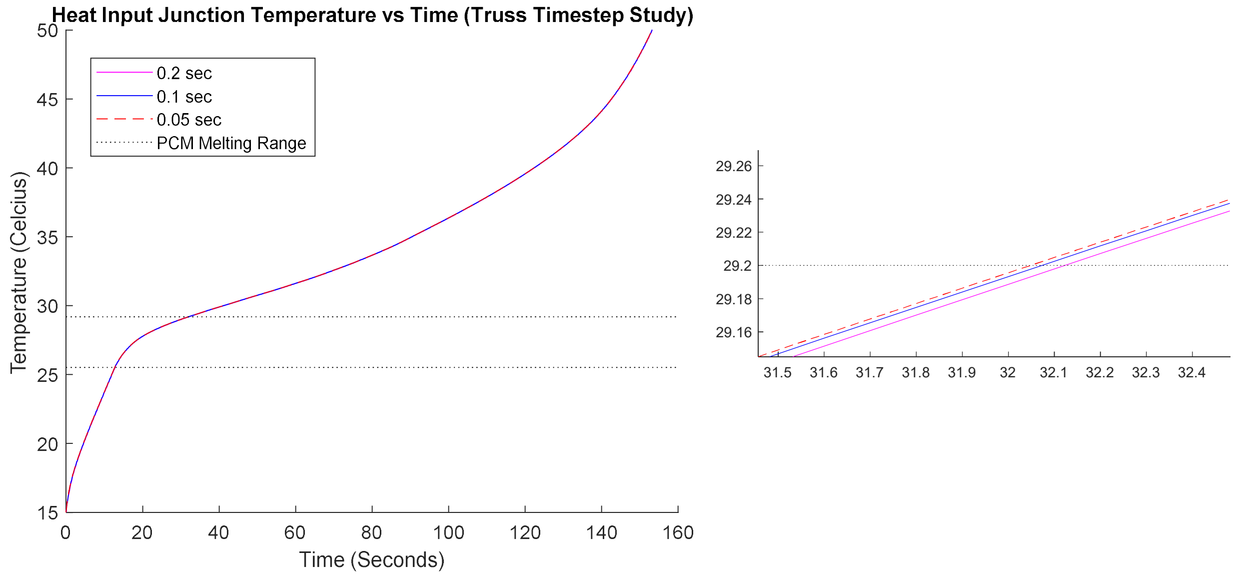

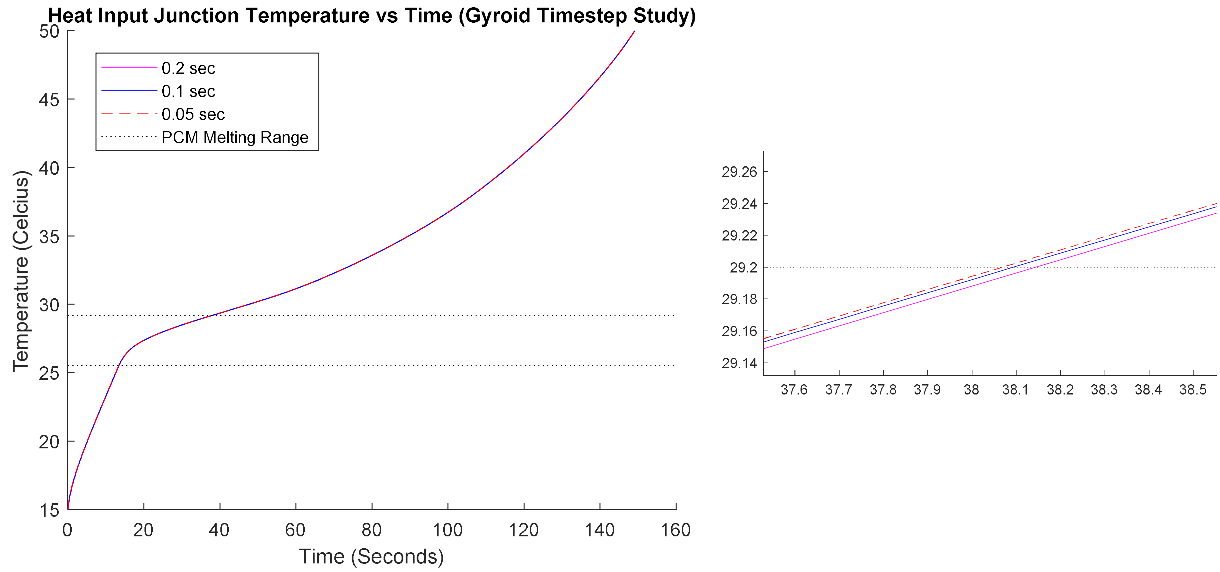

Convergence Study

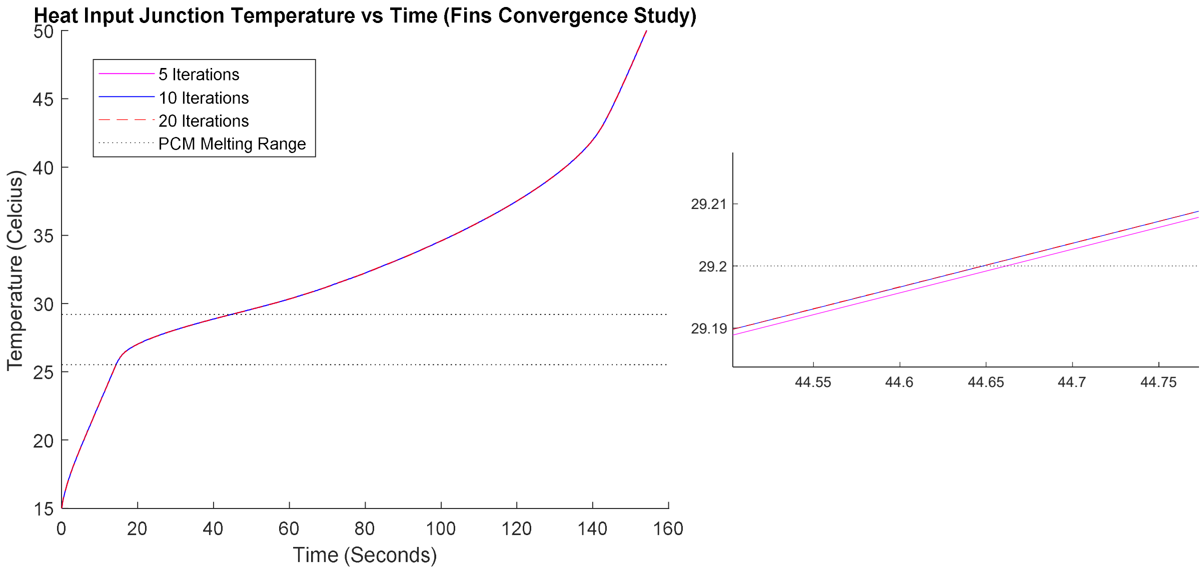

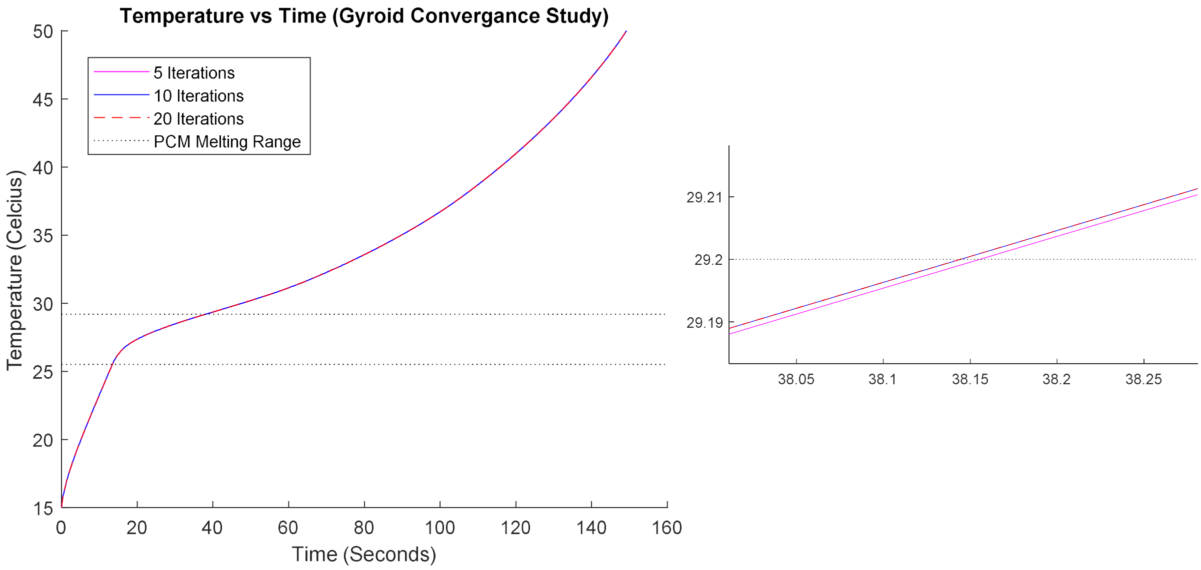

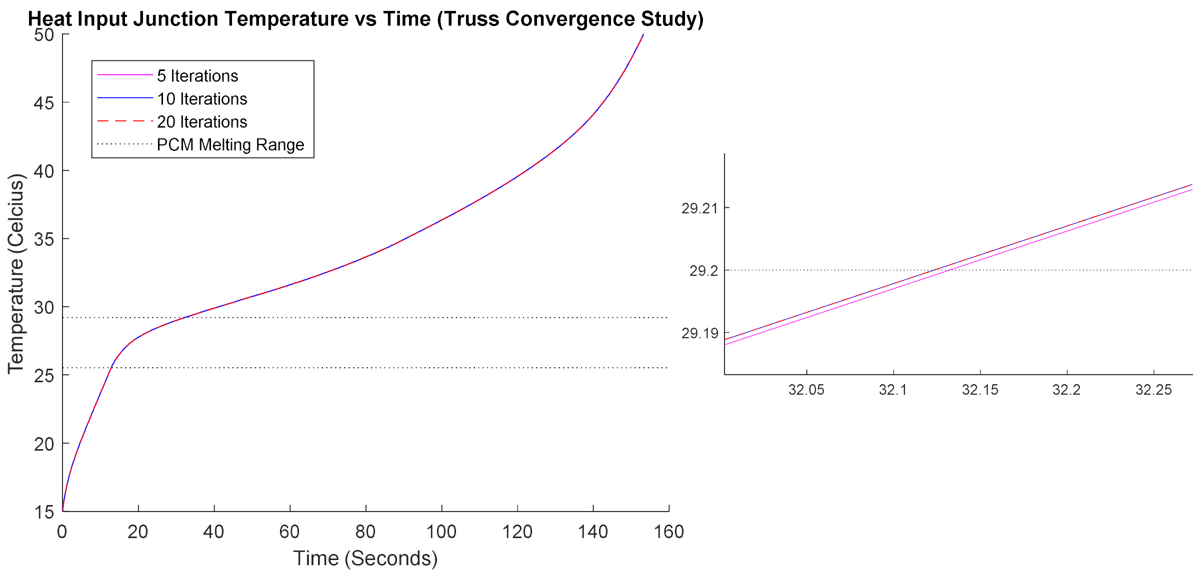

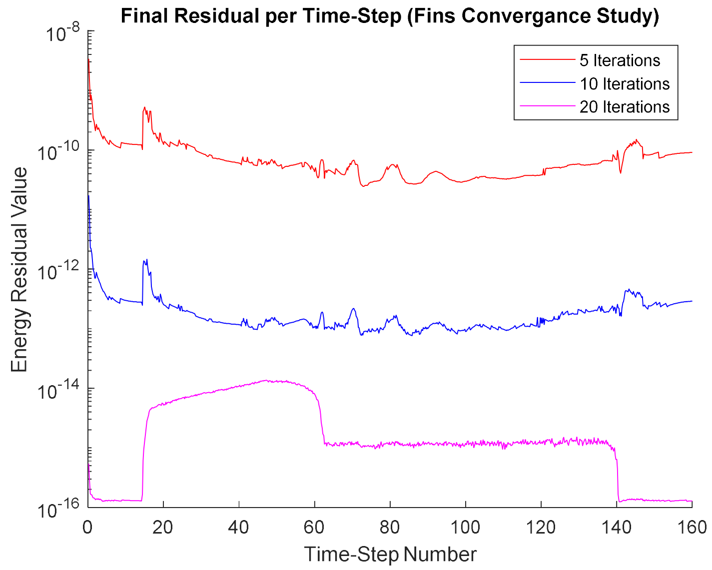

Final Residual per Time-Step (Fins Convergance Study)
5 Iterations
10 Iterations
20 Iterations
Energy Residual Value
Time-Step Number

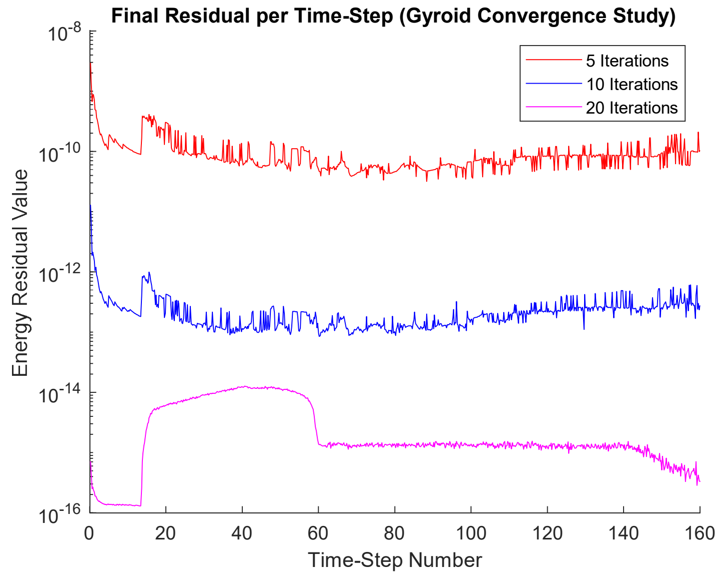

Final Residual per Time-Step (Gyroid Convergence Study)
5 Iterations
10 Iterations
20 Iterations
Energy Residual Value
Time-Step Number

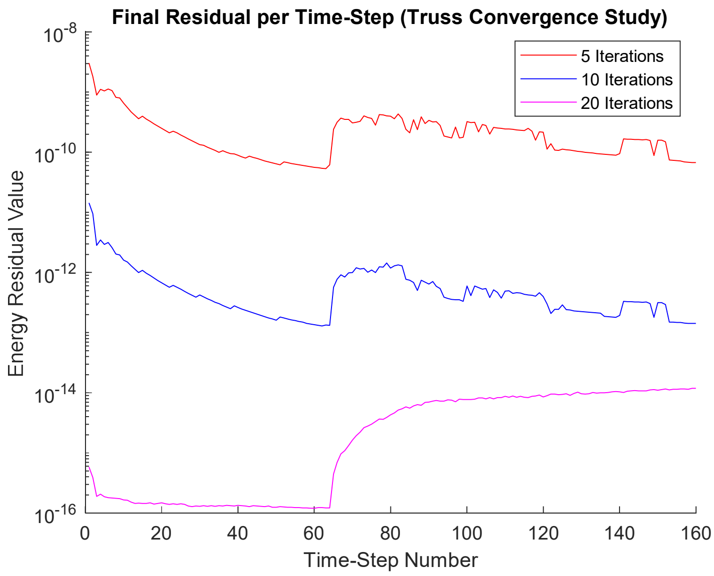

Final Residual per Time-Step (Truss Convergence Study)
5 Iterations
10 Iterations
20 Iterations
Energy Residual Value
Time-Step Number

Appendix B: Padua Model Estimated Parameters

Natural Convection Heat Loss

Noting, heat transfer coefficients for natural convection in free stream air range from 2.5 to 25W/m^{2}K (*Kosky et al., 2013*).

Heat transfer coefficient (h_c) was calculated using the Equation below, where Nu is the Nusselt number, k is the air thermal conductivity and L is the characteristic length (Cengel, 2002).

$$h_c = \frac{Nu\, k}{L}$$

Nusselt number for the natural convection - vertical and horizontal surfaces, was calculated using the equation below, where Ra is the Rayleigh number (Cengel, 2002).

Vertical Plate, $Nu = 0.59\; Ra^{0.25}$

Horizontal Plate, $Nu = 0.54\; Ra^{0.25}$

Rayleigh number was calculated using the equation below, where g is gravity, β is the thermal expansion coefficient, ΔT is the temperature difference, L is the characterictic length, ρ Density, α thermal diffusivity, μ dynamic viscosity (Cengel, 2002).

$$Ra = \frac{g\, \beta\, \Delta T\, L^3\, \rho}{\alpha\, \mu}$$

Characteristic length was calculated using L = A/P, where A and P are the area and the perimeter of the surface. Using free stream air of 292.8 K, the following thermophysical properties or air were used (Engineering toolbox, Air at 1 atmosphere pressure, 20C).
β = 3.4e-3 1/K, ρ = 1.204 kg/m^3, α = 21.70e-6 m^2/s, μ = 18.13e-6 N s/m^2, k = 25.87e-3 W/m·K

Vertical Walls

For the vertical walls, using a ΔT of 60C and a characteristic length of 0.01, a h_c of 13.5 was calculated

Horizontal Walls

For the horizontal wall, using a ΔT of 60C and a characteristic length of 0.01, a h_c of 12.5 was calculated

Contact Resistance

The thermal contact resistance as a function of contact pressure is provided below for aluminium contacts.

For the boundary between the heater block and heat sink, a nominal contact resistance of 0.001 $m^2 \cdot C/W$ was applied. The contact resistance assumed a smooth-rough aluminium contact with a low contact pressure.

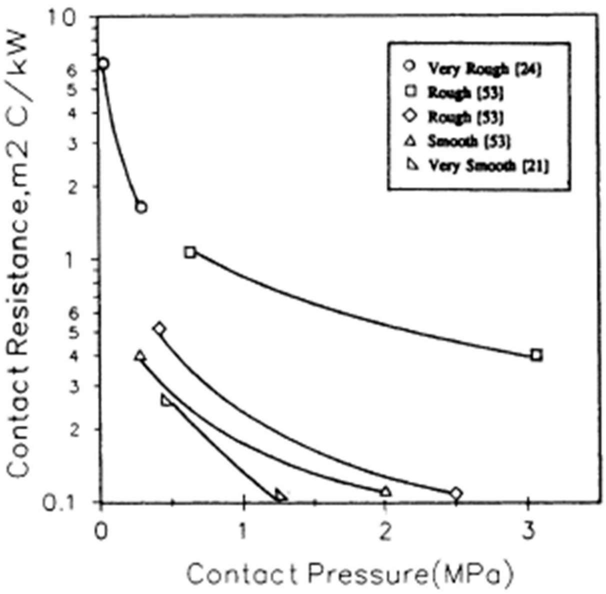

Thermal contact resistance as a function of contact pressure for aluminium contacts

(Fletcher, 1993)

Appendix C: Quarter Models of Base Size TCE Structures

<u>**Direct Cooling Quarter Models – Gyroid**</u>

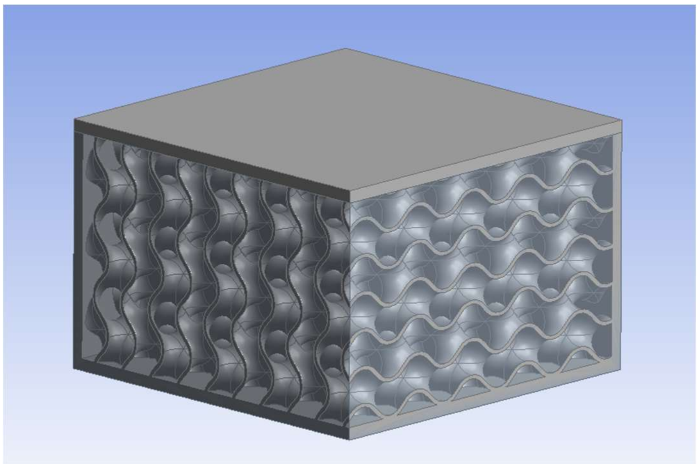

Wall thickness 0.3 mm

Gyroid base size 6.0 mm

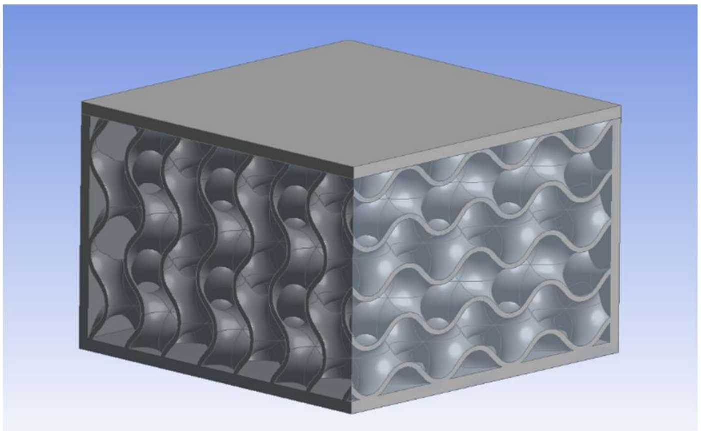

Wall thickness 0.4 mm

Gyroid base size 8.0 mm

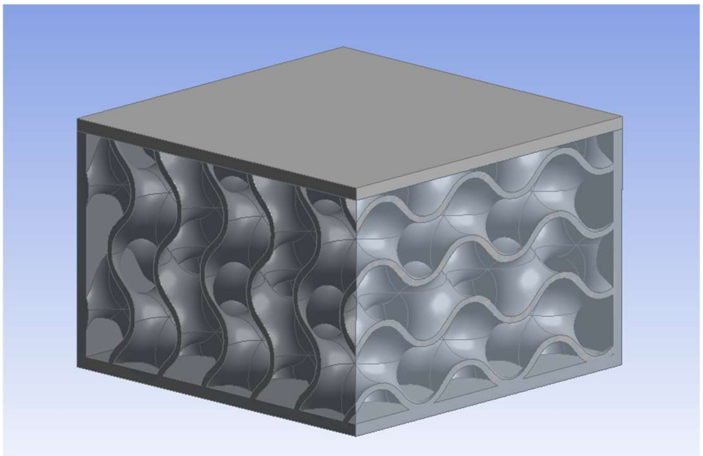

Wall thickness 0.5 mm

Gyroid base size 10.0 mm

__**Direct Cooling Quarter Models – Truss**__

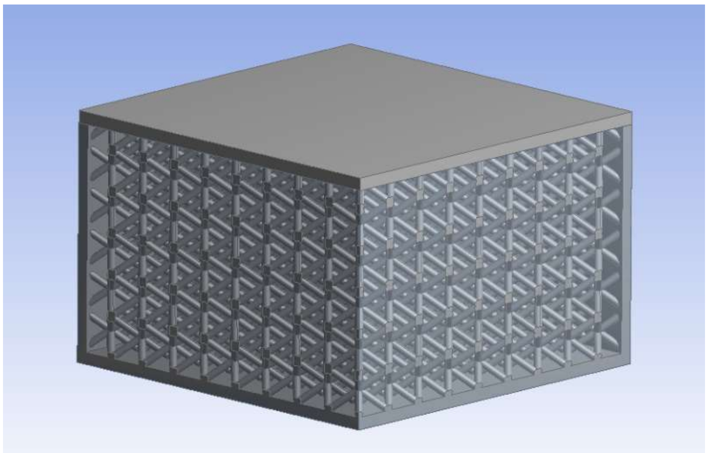

Radial thickness 0.3 mm

Cube base size 3.3 mm

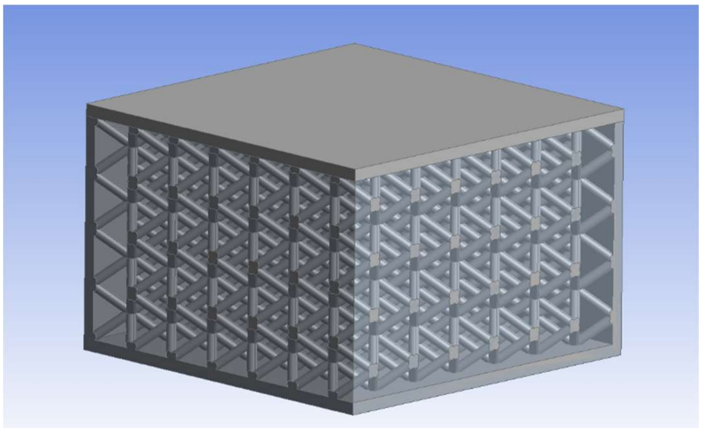

Radial thickness 0.4 mm

Cube base size 4.5 mm

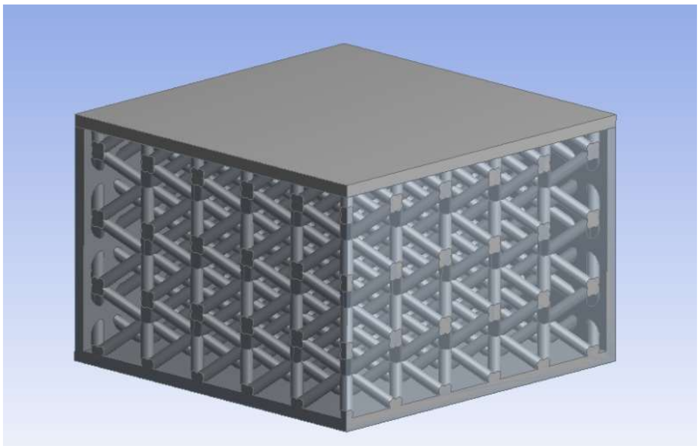

Radial thickness 0.5 mm

Cube base size 5.5 mm

__Direct Cooling Quarter Models – Fins__

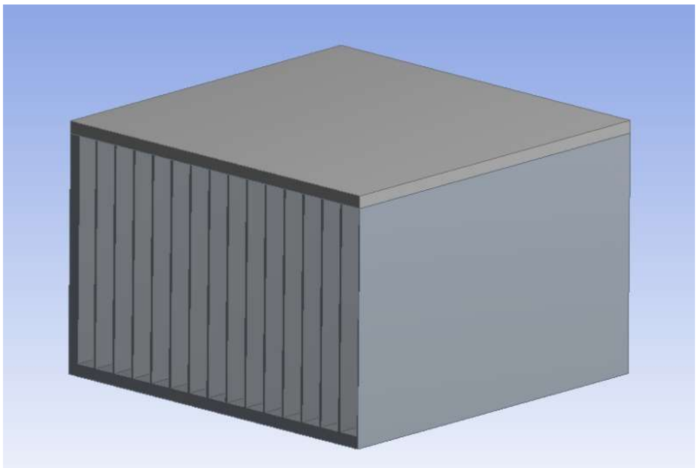

Wall thickness: 0.3 mm

Fin Spacing: 1.95 mm

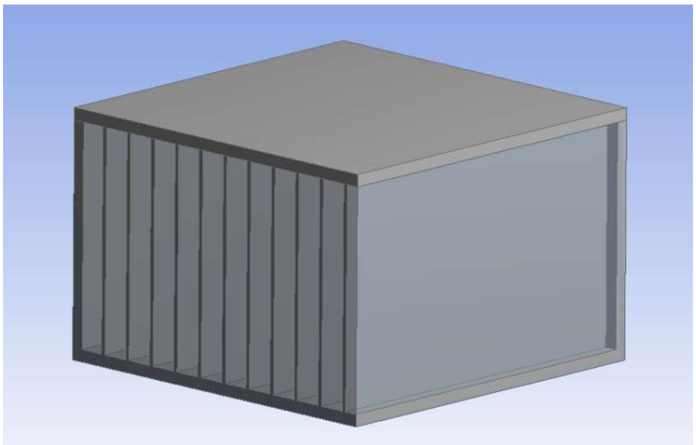

Wall thickness 0.4 mm

Fin Spacing 2.55 mm

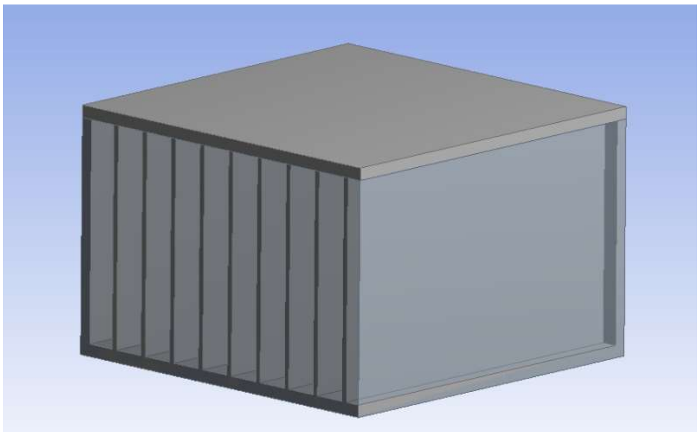

Wall thickness 0.5 mm

Fin Spacing 3.1 mm

Heat Pipe Cooling Quarter Models – Gyroid

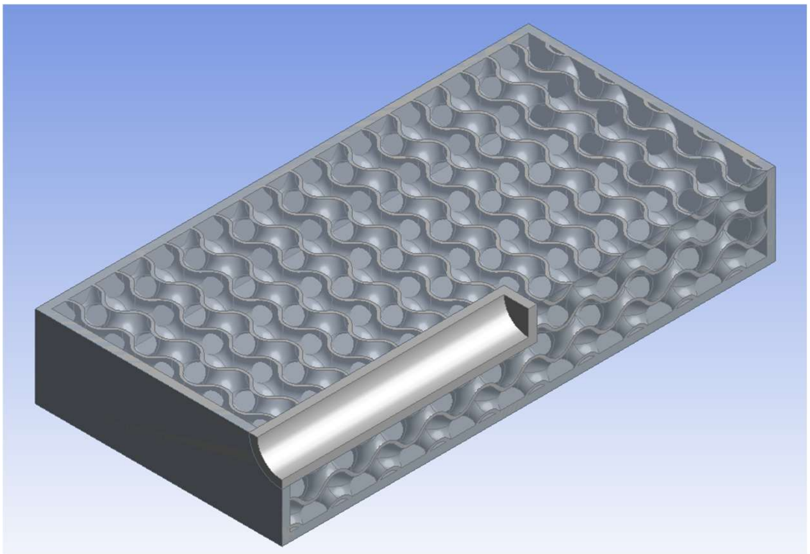

Wall thickness 0.3 mm

Gyroid base size 6.0 mm

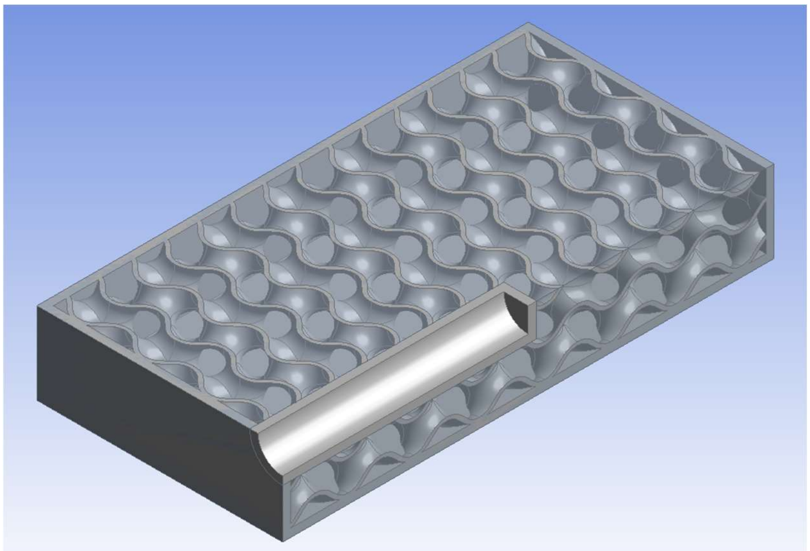

Wall thickness 0.4 mm

Gyroid base size 8.0 mm

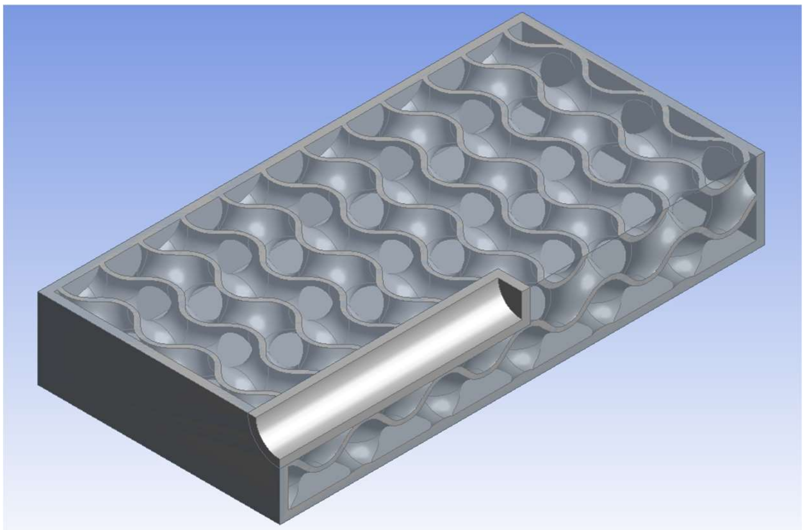

Wall thickness 0.5 mm

Gyroid base size 10.0 mm

Heat Pipe Cooling Quarter Models – Truss

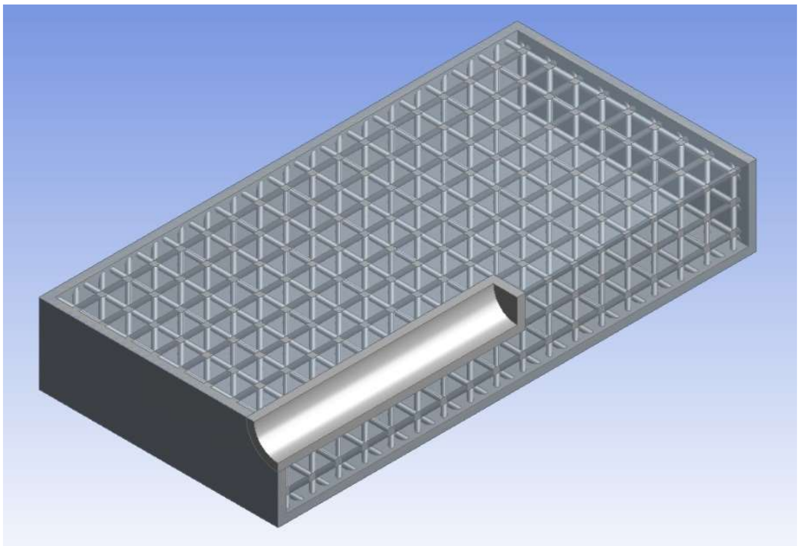

Radial thickness 0.3 mm

Cube base size 3.3 mm

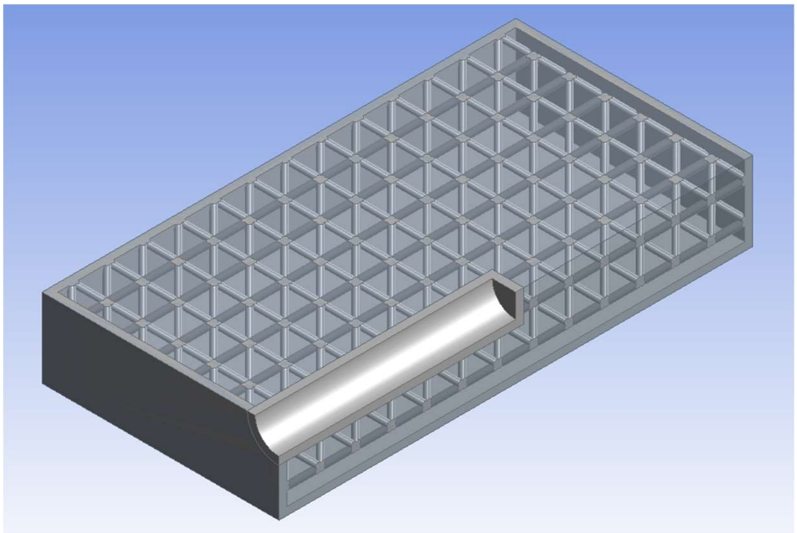

Radial thickness 0.4 mm

Cube base size 4.5 mm

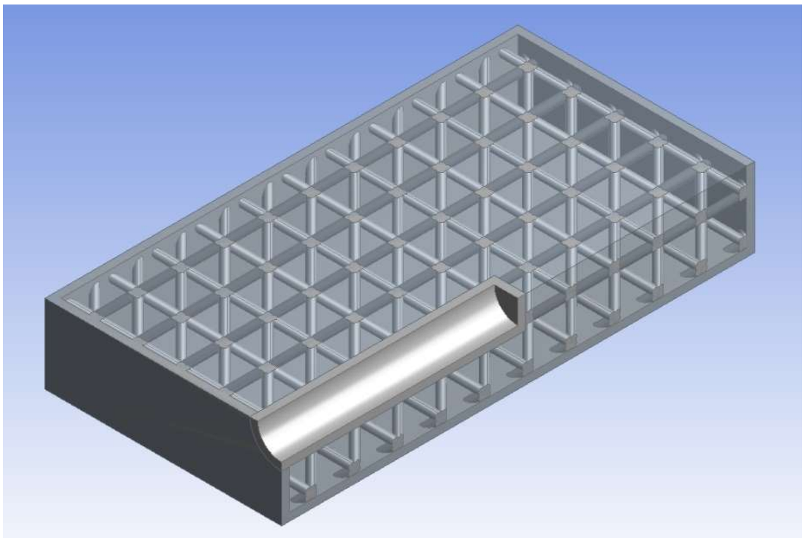

Radial thickness 0.5 mm

Cube base size 5.5 mm

Heat Pipe Cooling Quarter Models – Fins

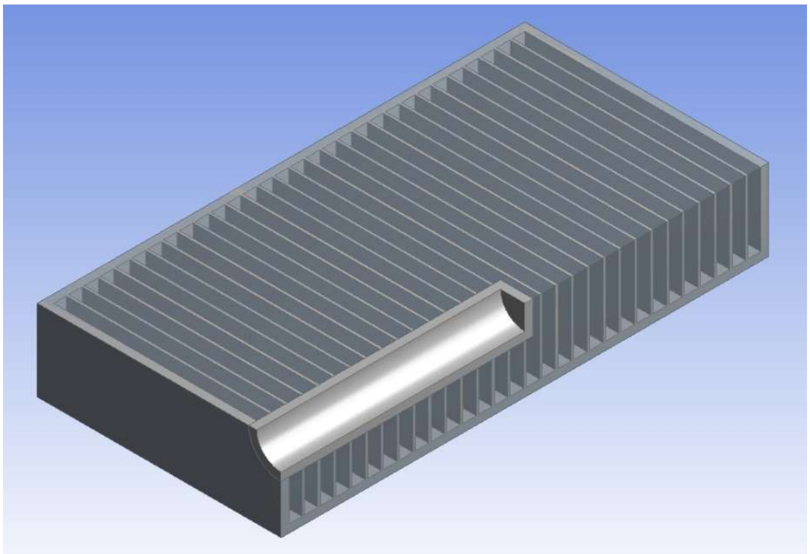

Wall thickness 0.3 mm

Fin Spacing 1.95 mm

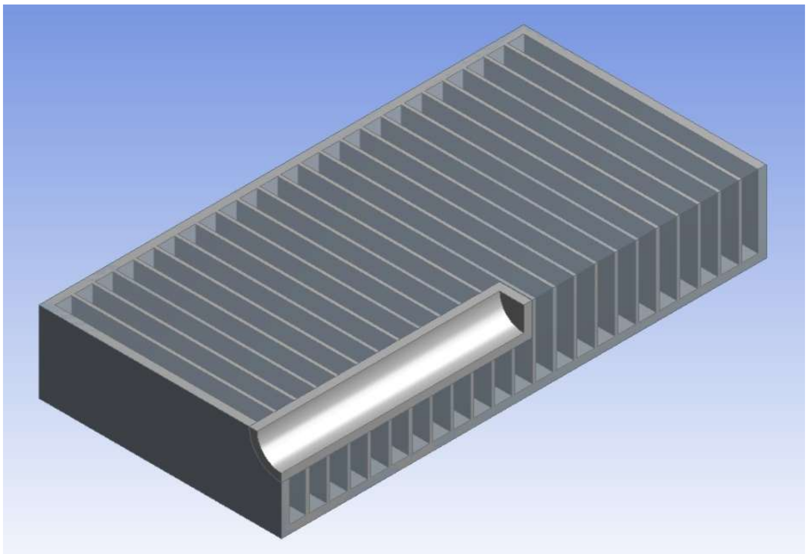

Wall thickness 0.4 mm

Fin Spacing 2.55 mm

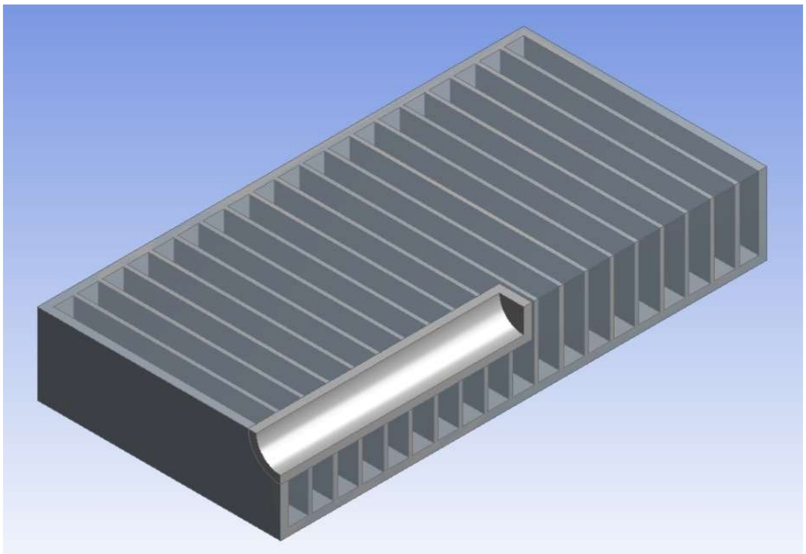

Wall thickness 0.5 mm

Fin Spacing 3.1 mm

Appendix D: BMD Copper Porosity Images

Toolpath Porosity – Top View (1)

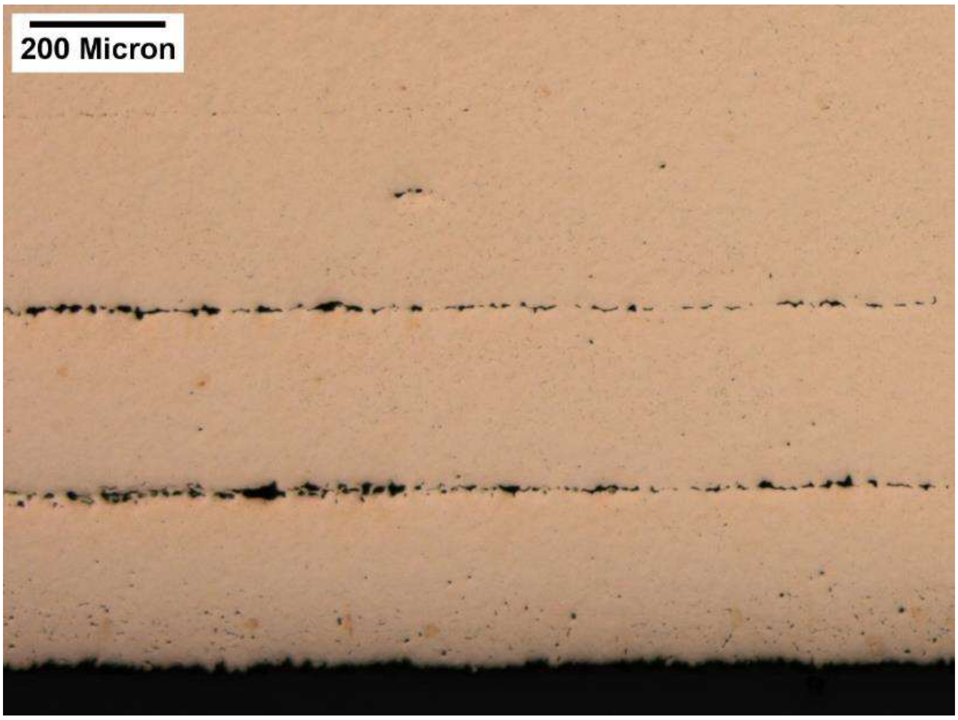

Toolpath Widths

Measurement	Distance (Micron)	Toolpaths	Toolpath Width
1	807.732	3	269.244
2	266.582	1	266.582
3	530.558	2	265.279
4	807.642	3	269.214
5	258.651	1	258.651
6	522.607	2	261.3035
		Average	**265.05 Micron**

Porosity Gaps

Measurement	Distance (Micron)
1	30.088
2	25.664
3	29.217
4	24.779
5	26.995
6	32.743
Average	**28.25 Micron**

Toolpath Porosity – Top View (2)

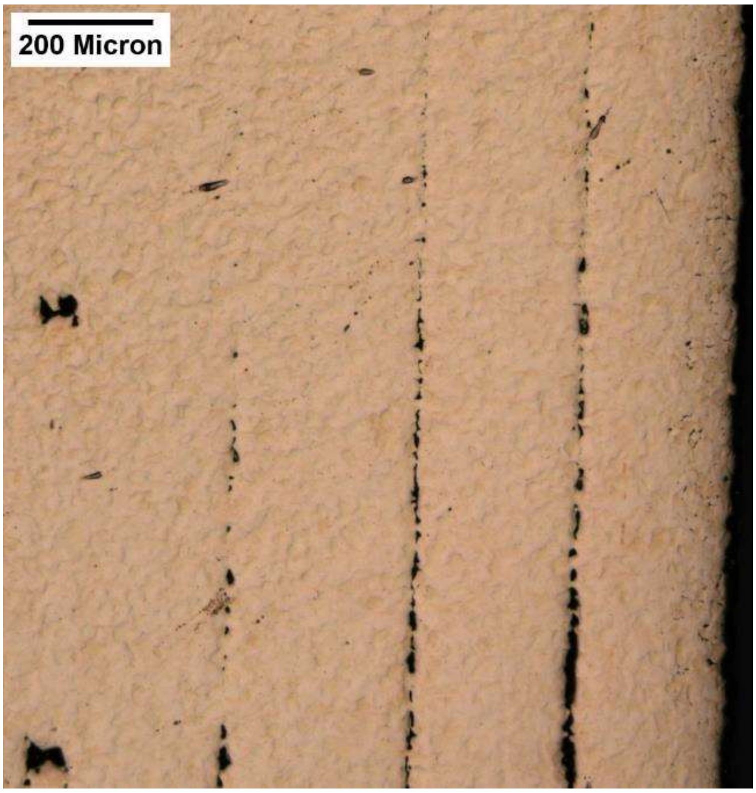

Toolpath Widths

Measurement	Distance (Micron)	Toolpaths	Toolpath Width
1	772.633	3	257.544
2	556.947	2	278.474
3	1013.877	4	253.469
4	559.586	2	279.793
5	789.219	3	263.073
6	770.769	3	256.923
		Average	**264.88 Micron**

Porosity Gaps

Measurement	Distance (Micron)
1	27.063
2	34.22
3	37.346
4	25.574
5	24.649
6	36.751
Average	**30.93 Micron**

Toolpath Porosity – Side View (1)

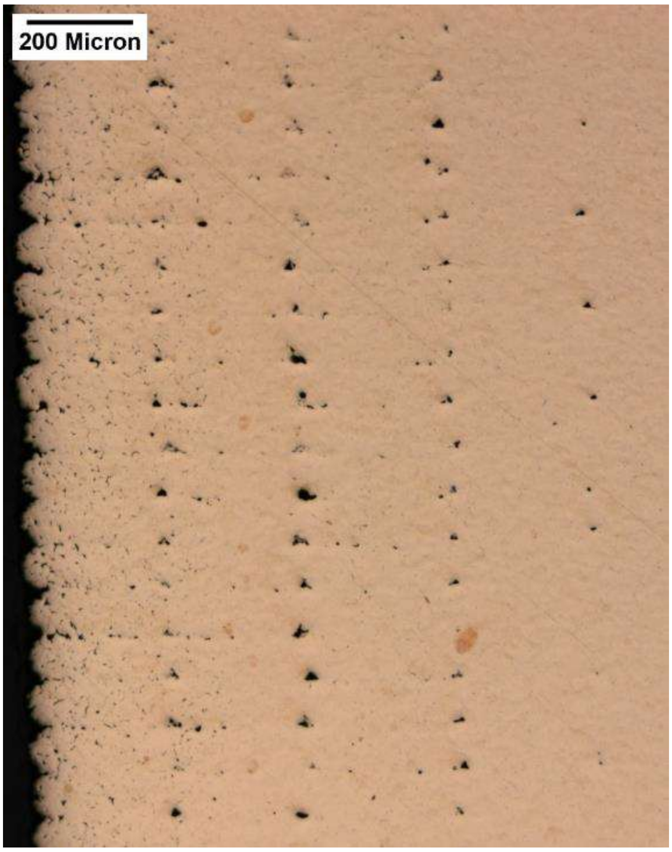

Toolpath Heights

Measurement	Distance (Micron)	Toolpaths	Toolpath Height
1	768.149	9	85.350
2	937.322	11	85.211
3	1528.428	18	84.913
4	1525.961	18	84.776
5	1449.264	17	85.251
		Average	**85.10 Micron**

Porosity Gaps

Measurement	Distance (Micron)
1	22.874
2	22.891
3	16.716
4	17.595
5	21.119
Average	**20.24 Micron**

Porosity Measurements

Measurement	Porosity (%)
1	1.44
2	1.342
3	1.332
4	1.453
5	1.483
Average	**1.41**

Toolpath Porosity – Side View (2)

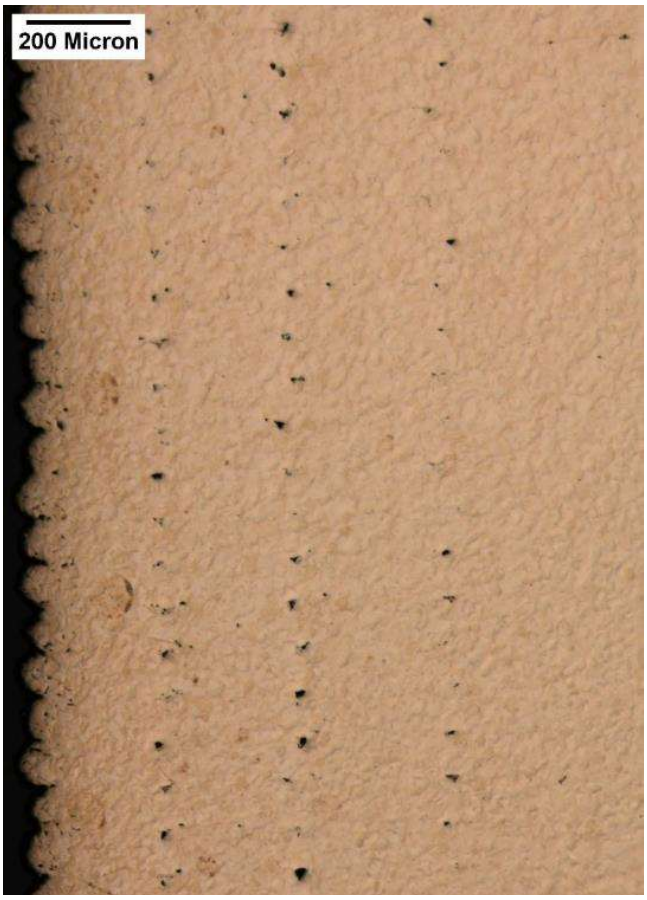

Toolpath Heights

Measurement	Distance (Micron)	Toolpaths	Toolpath Height
1	1620.262	19	85.277
2	513.639	6	85.607
3	1008.877	12	84.073
4	685.716	8	85.715
5	1360.846	16	85.053
		Average	**85.14 Micron**

Porosity Gaps

Measurement	Distance (Micron)
1	23.77
2	17.617
3	21.114
4	19.375
5	18.041
Average	**19.98 Micron**

Porosity Measurements

Measurement	Porosity (%)
1	1.251
2	1.496
3	1.314
4	1.426
5	1.286
Average	**1.35**

Micro Porosity – Vertical Sample

Image	Porosity (%)
1	0.932
2	1.252
3	0.948
4	0.977
5	0.995
6	1.255
7	0.986
8	1.278
9	0.795
10	0.876
Average	**1.03**
Min	**0.80**
Max	**1.28**

Image 1

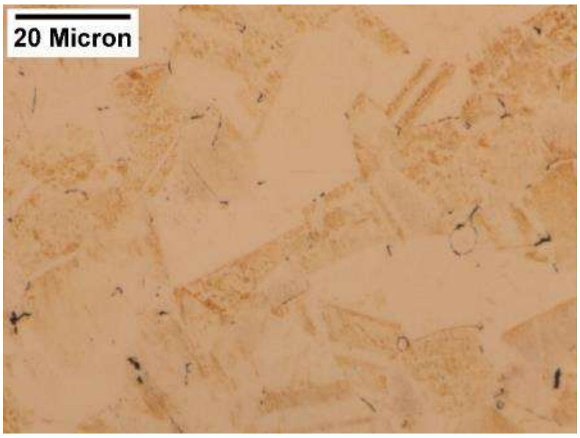

Image 2

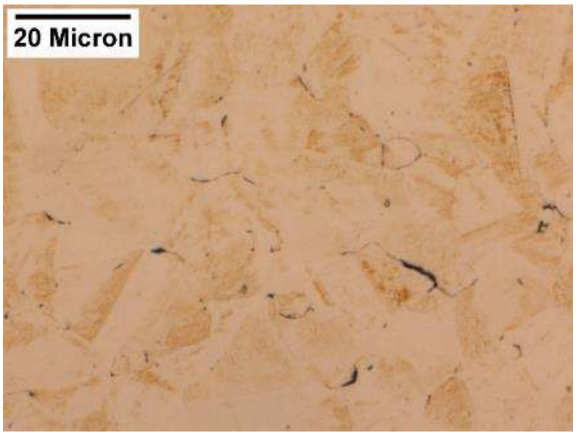

Image 3

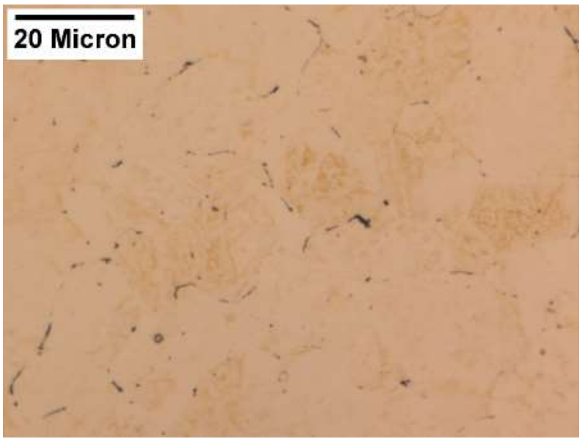

Image 4

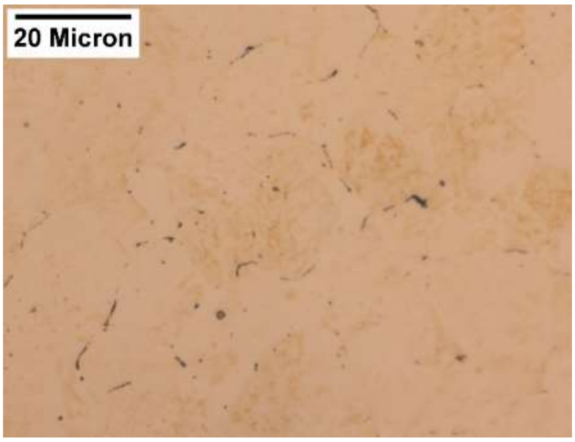

Image 5

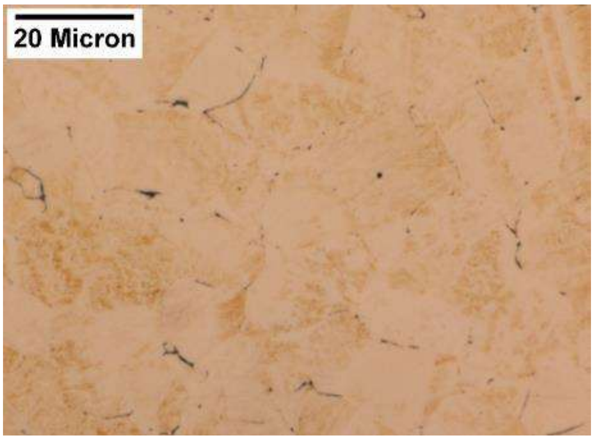

Image 6

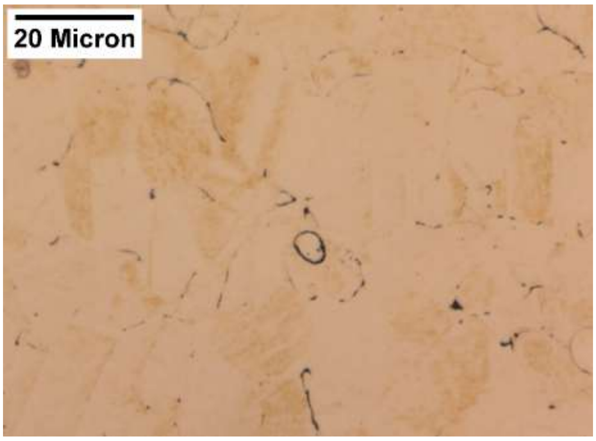

Image 7

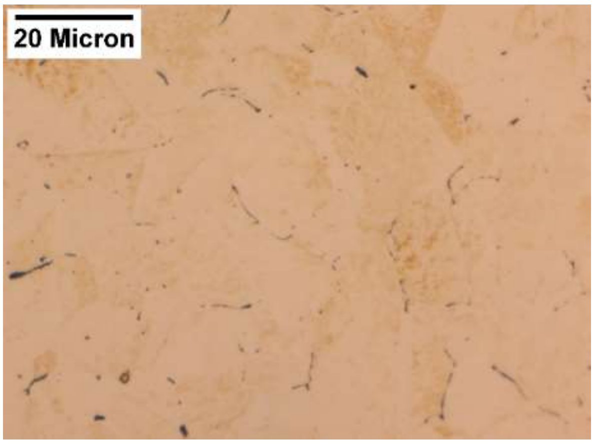

Image 8

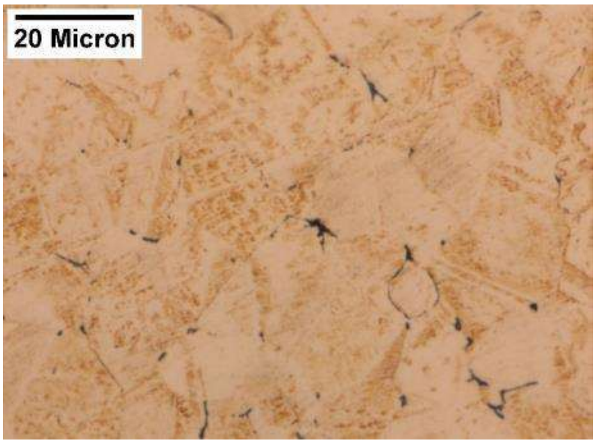

Image 9

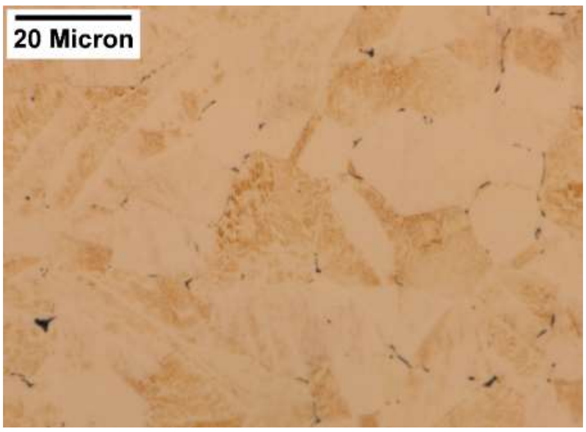

Image 10

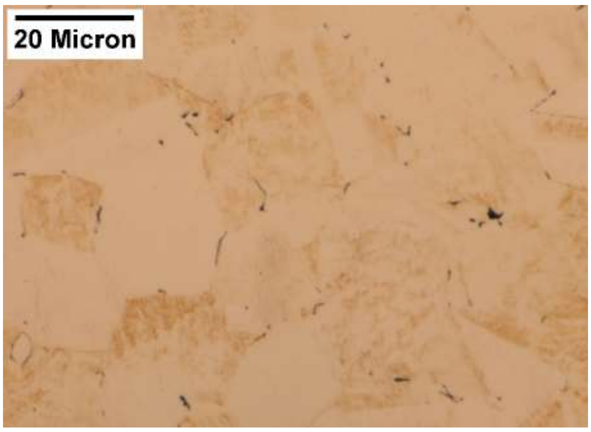

Micro Porosity – Horizontal Sample

Image	Porosity (%)
1	0.844
2	0.883
3	0.911
4	0.899
5	1.136
6	1.256
7	1.048
8	0.785
9	0.876
10	0.722
Average	**0.95**
Min	**0.72**
Max	**1.26**

Image 1

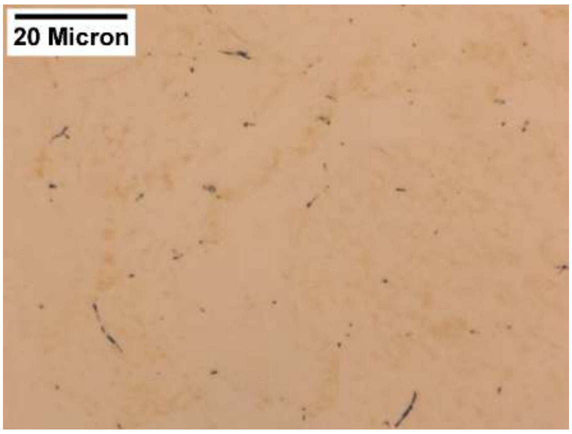

Image 2

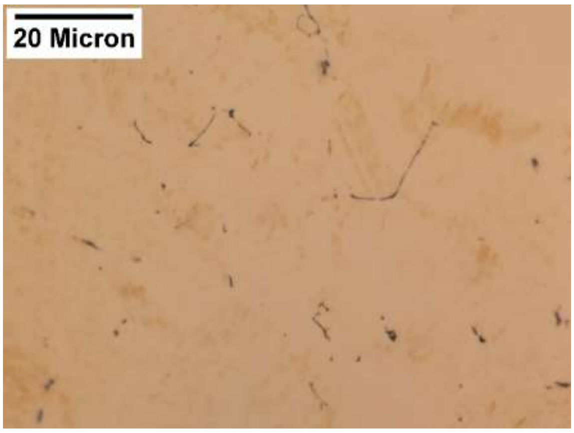

Image 3

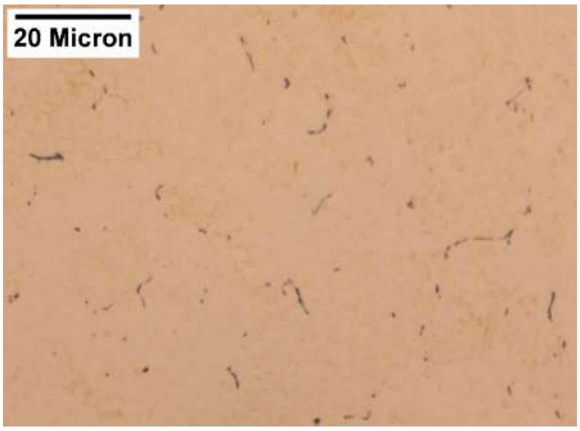

Image 4

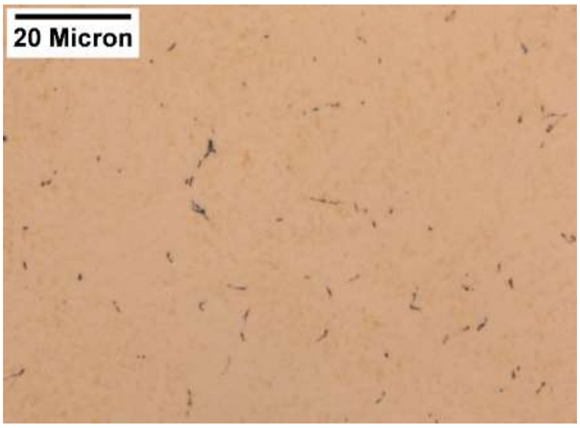

Image 5

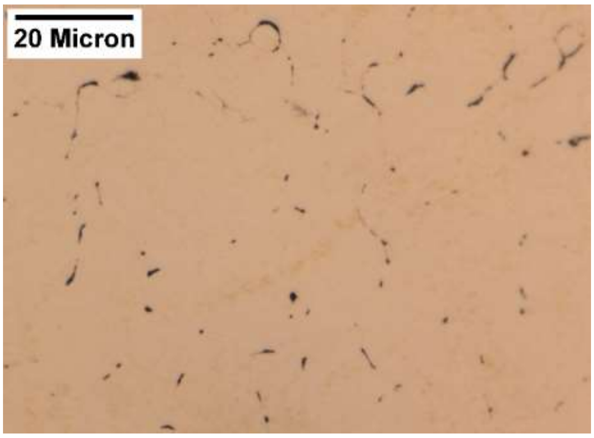

Image 6

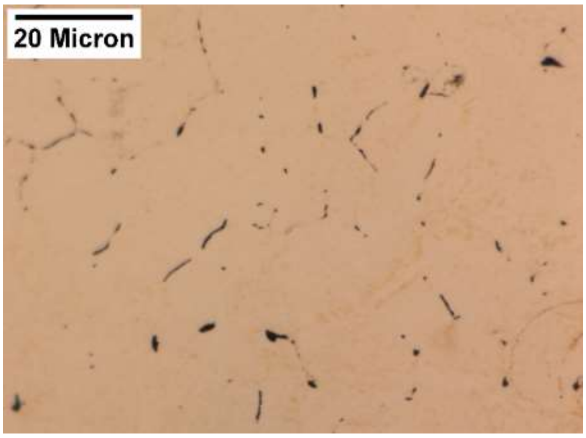

Image 7

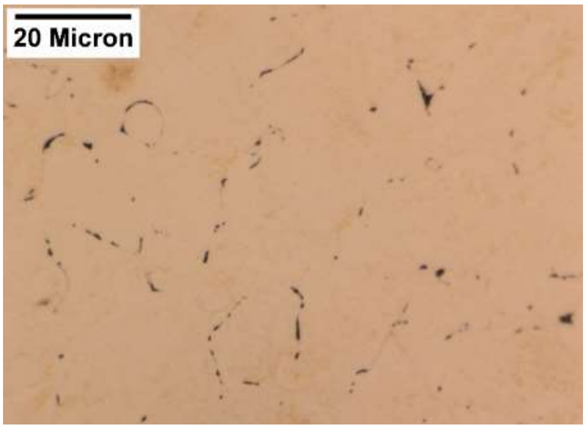

Image 8

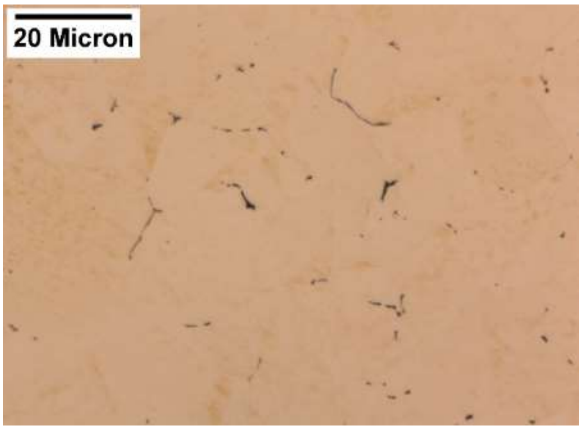

Image 9

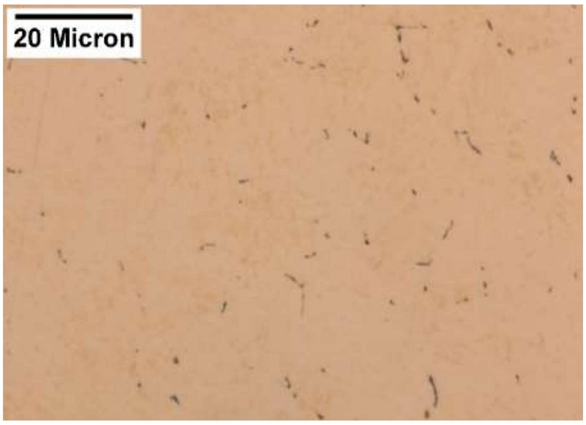

Image 10

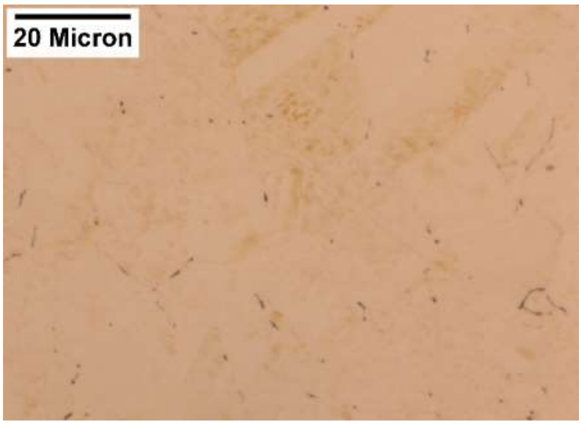

Appendix E: SEM EDS Measurements

Electron Image 1

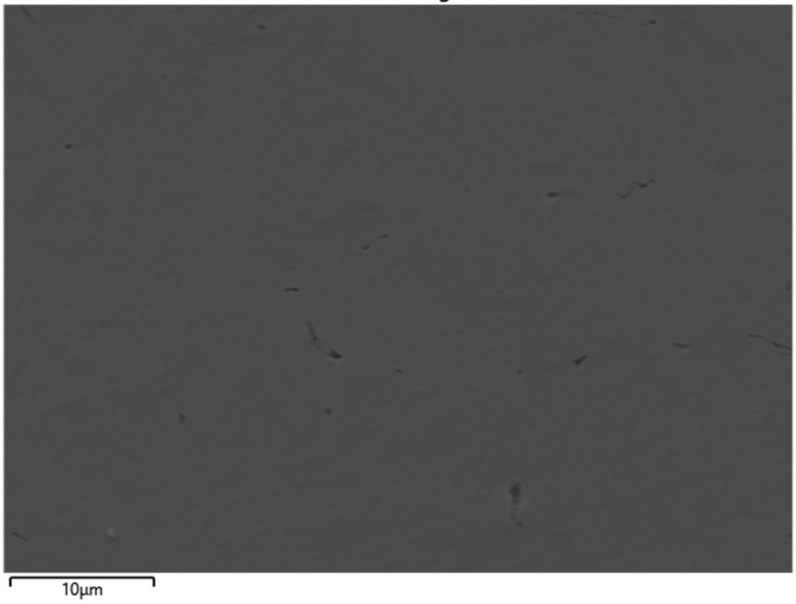

EDS Layered Image 1

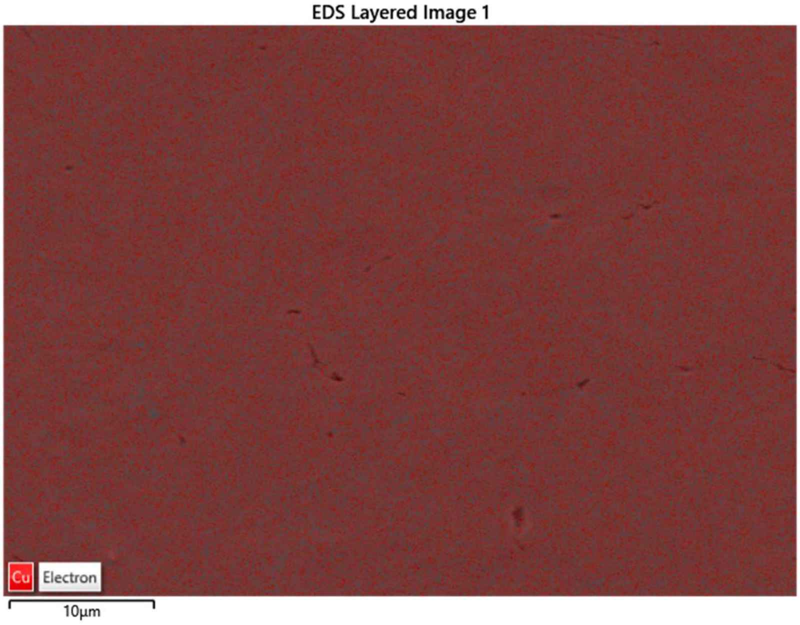

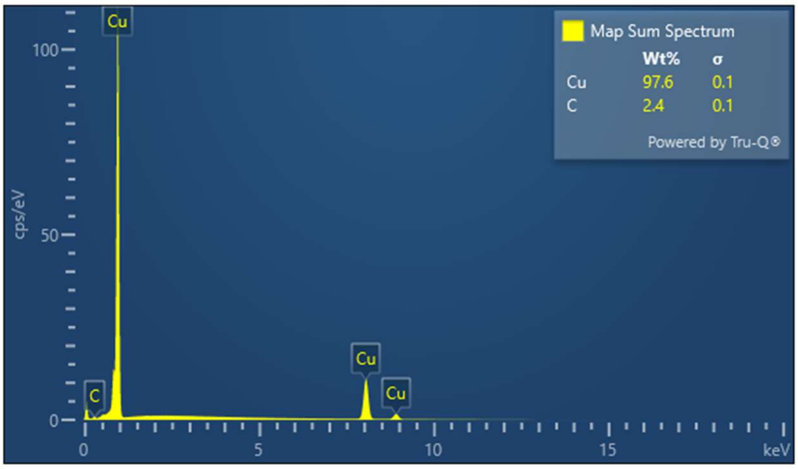

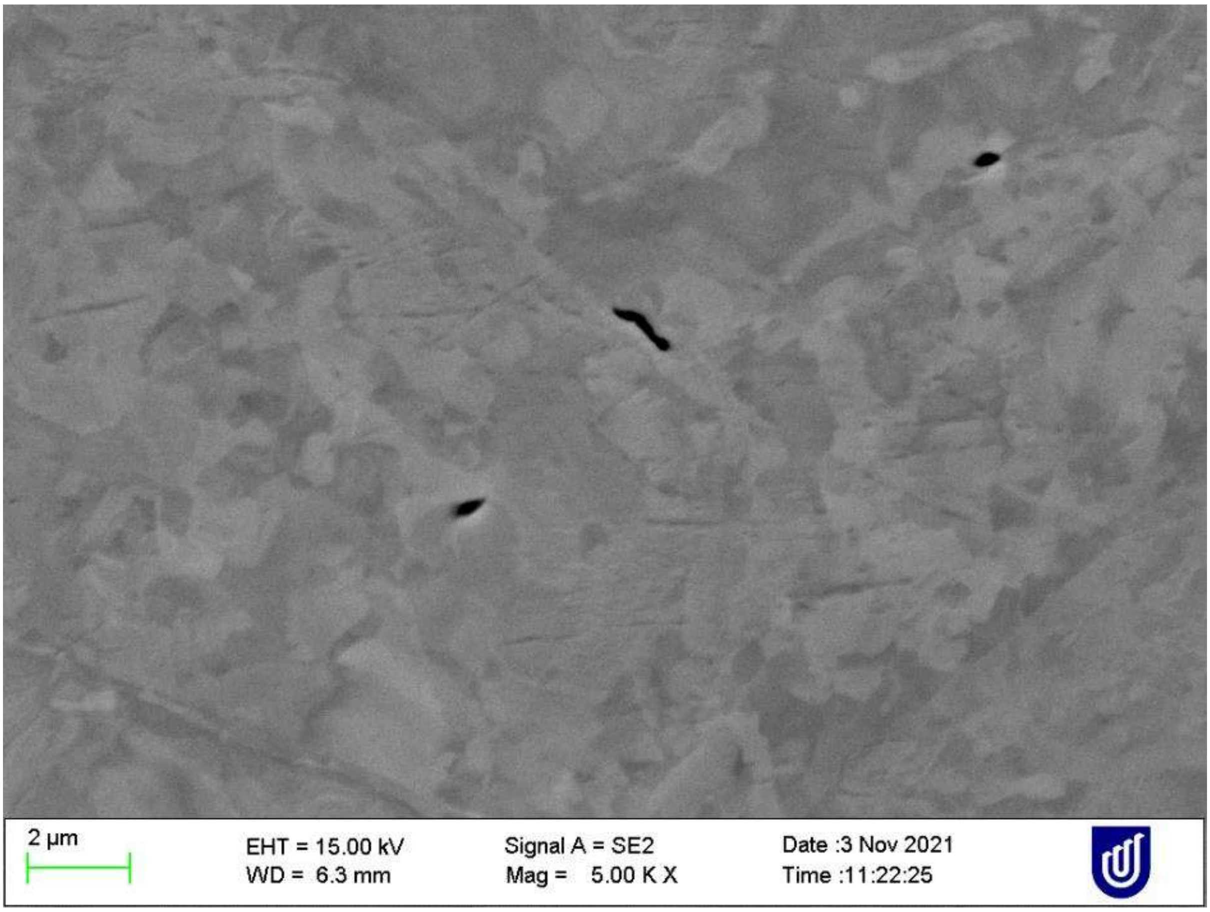
2 µm
EHT = 15.00 kV
WD = 6.3 mm
Signal A = SE2
Mag = 5.00 K X
Date :3 Nov 2021
Time :11:22:25

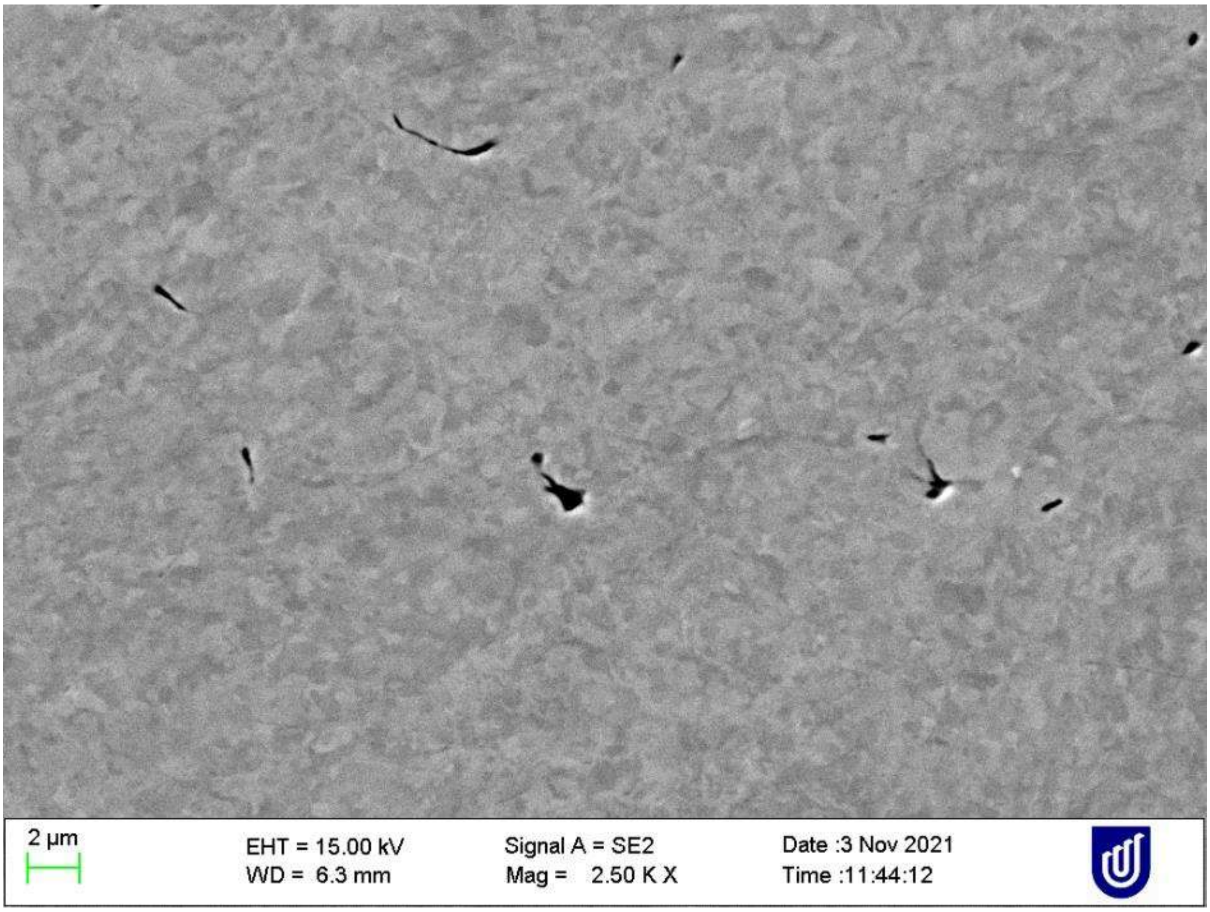
2 µm
EHT = 15.00 kV
WD = 6.3 mm
Signal A = SE2
Mag = 2.50 K X
Date :3 Nov 2021
Time :11:44:12

Appendix F: BMD Copper Cylinder Weight Measurements

Three measurements for the submerged weight and weight in air were performed for each sample - horizontal and vertical.

Ultrapure water with very low levels of impurities was utilised for the submersion, which was obtained from the ELGA PURELAB Classic water purification unit. The water was allowed to reach room temperature prior to the measurements.

	Measurement No.	Weight in Air W_g (g)	Submerged Weight W_a (g)	Density (g/cm^3)
Horizontal Sample	1	83.18	73.57	High: 8.65 **Ave: 8.64** Low: 8.63
	2	83.17	73.56	
	3	83.18	73.56	
Vertical Sample	1	83.18	73.51	High: 8.59 **Ave: 8.58** Low: 8.57
	2	83.19	73.52	
	3	83.19	73.51	

$$\rho = \frac{W_g}{W_g - W_a}\rho_w$$

W_g - weight of the test sample in air

W_a - apparent weight of the test sample in water

ρ_w - water density

The measured temperature of the water was 23°C and the density of water used was 0.998 g/cc (*Engineering ToolBox, 2003*).

Appendix G: BMD Copper DSC Outputs

BMD Copper Sample 1

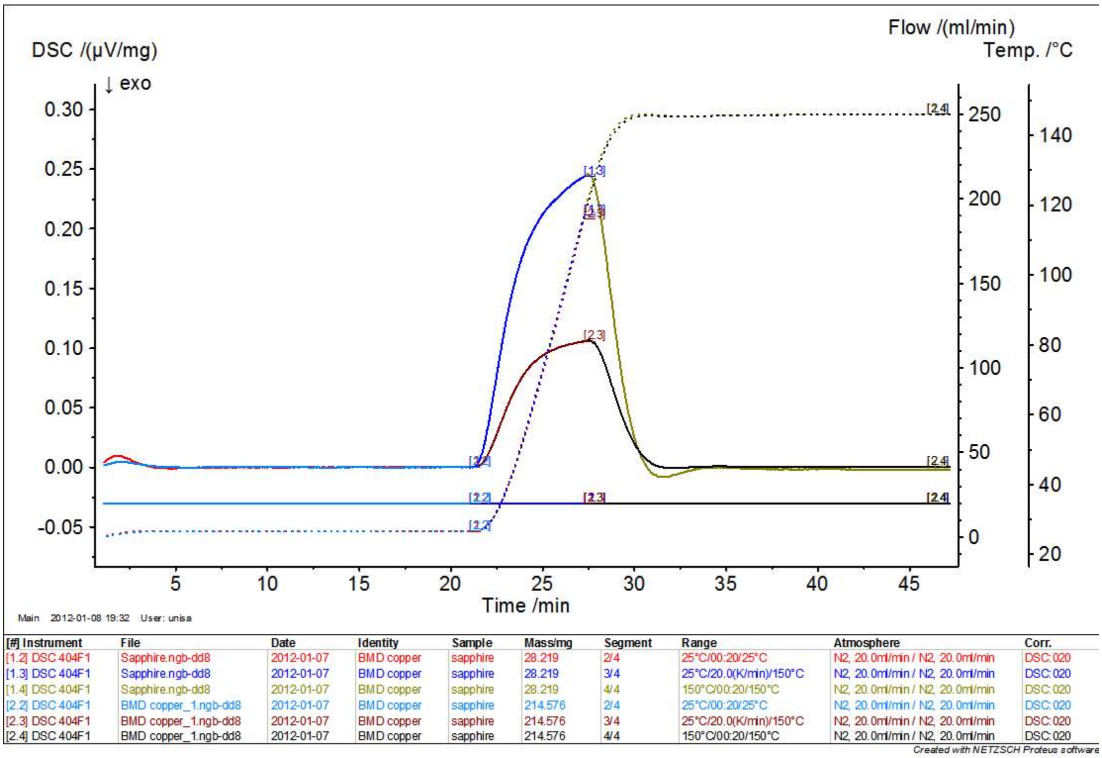

BMD Copper Sample 2

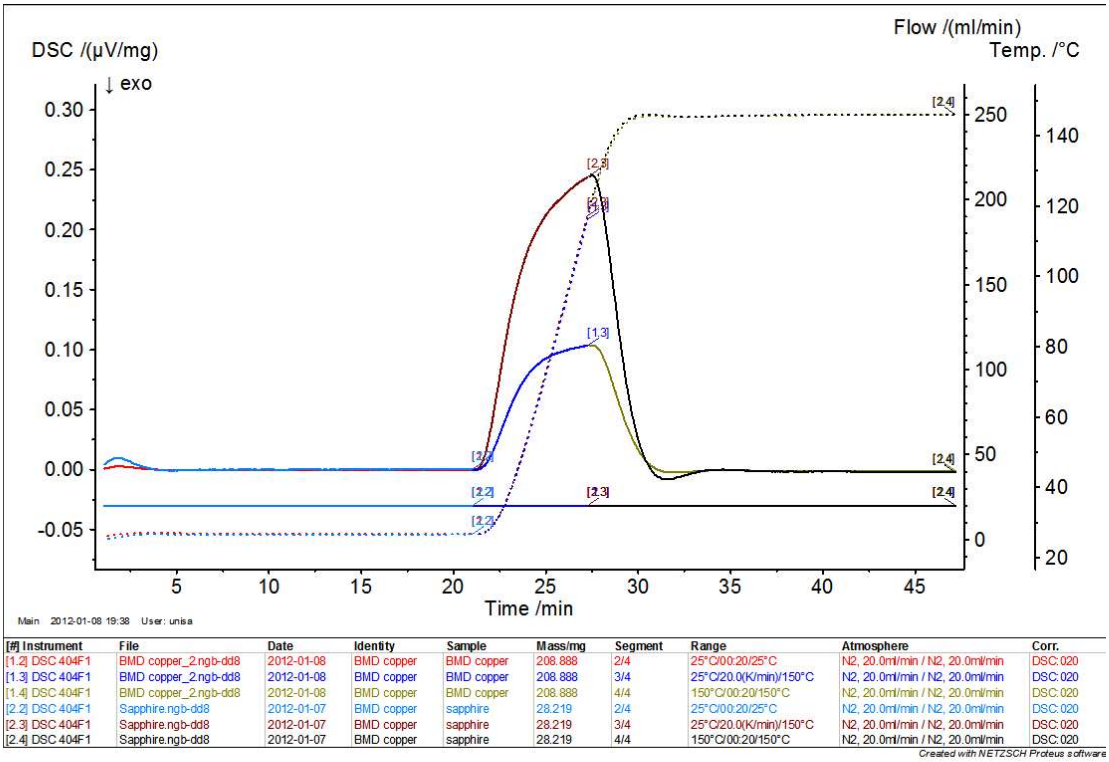

Sample Weights (mg)

BMD Copper 1	BMD Copper 2	Sapphire Disc	Sample Crucible	Ref Crucible
214.576	208.888	28.219	79.995	74.253

Appendix H: BMD Copper Thermal Effusivity Values

<u>Copper Reference Sample Test</u>

#Sensor Serial: H846
#Test ID: MTPS-Ref-High Metals-2021-10-21-02:58:54P
#Instrument: C-Therm Trident
#Calibration: High Metals
#Material:
Copper
#Contact Agent: Water

#k Status: Pass
#Effusivity Status: Pass

#Average Thermal Conductivity (W/mK): 384.550554850279
#Thermal Conductivity %RSD: 0.825501288575625

	Valid	Conductivity W/mK	Error %	R Squared	Delta T degC	Temperature degC
1	TRUE	383.3608	3.508485	0.993576	467.3704	24.09604
2	TRUE	387.5354	2.457749	0.995198	472.1764	24.08791
3	TRUE	384.2802	3.277061	0.993324	468.4225	24.06439
4	TRUE	379.3822	4.509902	0.994285	462.8468	24.08961
5	TRUE	388.1942	2.291915	0.995343	472.9413	24.10732

The RSD value was checked for each test to ensure that the RSD limit was not exceeded. The RSD limit for the high thermal conductivity metals calibration was 2.5%.

The sensor temperature was also checked to ensure that the sensor adequately equilibrated with the environment. The sensor temperature was not to vary by more than 0.2°C between successive tests.

The lab temperature needed to be kept between 19°C - 27°C (C-Therm, 2020). The lab temperature for the testing was 24°C.

Horizontal Sample Test 1

#Average Effusivity: 33934.7857746797 Ws^(1/2) / Km^2
#Effusivity RSD: 2.45519803022661%

	Valid	Effusivity Ws^(1/2) / Km^2	R Squared	Delta T degC	Temperature degC
1	TRUE	34434.15	0.995469	451.9026	25.0173
2	TRUE	34281.34	0.996887	450.0141	24.90664
3	TRUE	34922.73	0.995681	457.9222	24.83643
4	TRUE	34365.21	0.996976	451.0448	24.8019
5	TRUE	32404.58	0.997598	426.8629	24.79016
6	TRUE	34688.92	0.996351	455.0356	24.7573
7	TRUE	33240.16	0.992884	437.1672	24.74844
8	TRUE	33141.19	0.996608	435.946	24.73527

Horizontal Sample Test 2

#Average Effusivity: 33883.4015123486 Ws^(1/2) / Km^2
#Effusivity RSD: 1.60560761451634%

	Valid	Effusivity Ws^(1/2) / Km^2	R Squared	Delta T degC	Temperature degC
1	TRUE	33322.76	0.996415	438.1945	24.99369
2	TRUE	34631.29	0.99617	454.3319	24.95952
3	TRUE	33710.22	0.996282	442.9706	24.92174
4	TRUE	33402.36	0.99649	439.1719	24.87277
5	TRUE	33771.92	0.995578	443.7299	24.87294
6	TRUE	33259.18	0.995836	437.4072	24.90355
7	TRUE	34716.53	0.995972	455.3788	24.8307
8	TRUE	34252.96	0.994334	449.6611	24.82383

Horizontal Sample Test 3

#Average Effusivity: 34450.246121265 Ws^(1/2) / Km^2
#Effusivity RSD: 1.51842615414445%

	Valid	Effusivity Ws^(1/2) / Km^2	R Squared	Delta T degC	Temperature degC
1	TRUE	33973.09	0.997708	446.2097	24.8346
2	TRUE	34641.97	0.994361	454.458	24.79524
3	TRUE	34648.02	0.993054	454.5327	24.80085
4	TRUE	34111.69	0.993705	447.9173	24.78195
5	TRUE	33876.78	0.995135	445.0199	24.77827
6	TRUE	34995.56	0.994494	458.818	24.76849
7	TRUE	33955.82	0.99553	445.9939	24.75283
8	TRUE	35399.05	0.993015	463.7935	24.74352

Vertical Sample Test 1

#Average Effusivity: 33271.6024733391 Ws^(1/2) / Km^2
#Effusivity RSD: 2.23567430747812%

	Valid	Effusivity Ws^(1/2) / Km^2	R Squared	Delta T degC	Temperature degC
1	TRUE	34474.78	0.998199	452.4116	25.24239
2	TRUE	34024.65	0.996825	446.8528	25.04068
3	TRUE	33508.67	0.995372	440.4866	24.97015
4	TRUE	32125.31	0.995851	423.4232	24.92309
5	TRUE	32585.71	0.998513	429.1001	24.88064
6	TRUE	32558.14	0.997164	428.7594	24.85965
7	TRUE	33447.39	0.994906	439.7263	24.84402
8	TRUE	33448.16	0.99465	439.7356	24.84037

Vertical Sample Test 2

#Average Effusivity: 33167.553659006 Ws^(1/2) / Km^2
#Effusivity RSD: 1.79181499549523%

	Valid	Effusivity Ws^(1/2) / Km^2	R Squared	Delta T degC	Temperature degC
1	TRUE	32485.43	0.996502	427.865	24.92855
2	TRUE	34152.12	0.9981	448.4189	24.8656
3	TRUE	32459.13	0.998032	427.5382	24.86313
4	TRUE	33386.03	0.996214	438.9697	24.85036
5	TRUE	33222.94	0.995524	436.9566	24.80327
6	TRUE	33533.32	0.997717	440.7847	24.80205
7	TRUE	32468.87	0.996789	427.6552	24.7735
8	TRUE	33632.6	0.996478	442.0071	24.7445

Vertical Sample Test 3

#Average Effusivity: 33078.7990984894 Ws^(1/2) / Km^2
#Effusivity RSD: 1.82070788602461%

	Valid	Effusivity Ws^(1/2) / Km^2	R Squared	Delta T degC	Temperature degC
1	TRUE	32648.94	0.997913	429.8655	24.46821
2	TRUE	33993.07	0.997065	446.4393	24.35287
3	TRUE	33598.88	0.996234	441.5768	24.33082
4	TRUE	33234.65	0.995674	437.0835	24.30157
5	TRUE	32615.06	0.996474	429.4414	24.29101
6	TRUE	32036.94	0.992983	422.3099	24.25277
7	TRUE	33587.77	0.997027	441.4374	24.26277
8	TRUE	32915.07	0.997407	433.1406	24.26393

Appendix I: Contact Pressure Calculations

Cylindrical Base Radii

Interface Radius, R = 0.005 m

Aluminium Inner Radius, ri = 0.004 m

Copper Outer Radius, ro = 0.006 m

Aluminium Material Properties

Young's modulus, E = 69 GPa

Poisson's ratio, μ = 0.33

References: *(Atlas Steels, 2013); (Alliance LLC, 2022)*

Copper Material Properties

Young's modulus, E = 63.2 GPa

Poisson's ratio, μ = 0.36

Young’s modulus based on BMD Copper 37% Elongation, compared to Copper HC 20% Elongation

References: *(Desktop Metal, 2020); (Connex, 2020); (Engineering Toolbox, 2022)*

Appendix J: Test Results

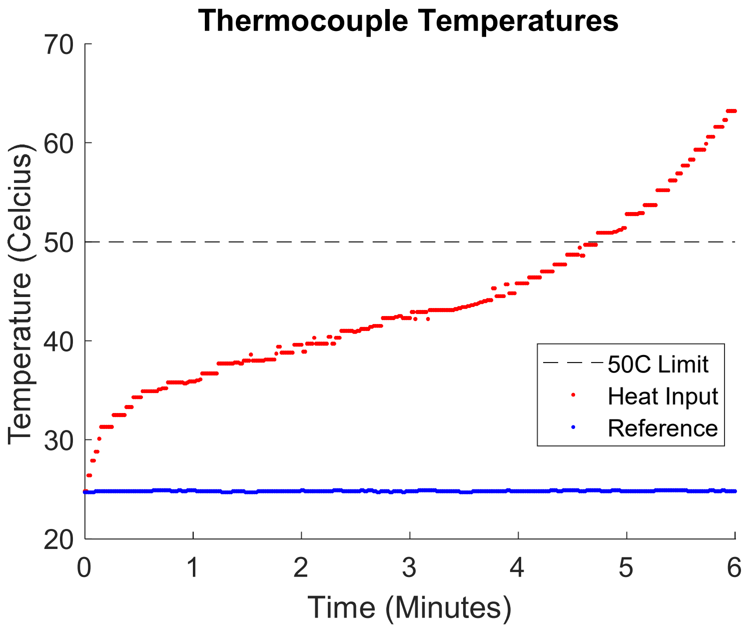

*Average reference temperature 24.8°C

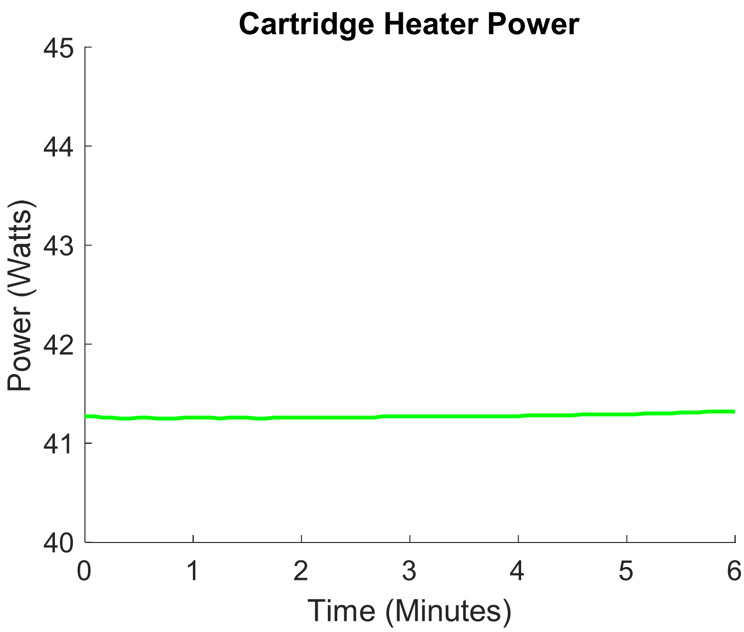

*Average heat load 41.3 W